2022

Intraplate Volcanism in our Solar System; Searching for Terrestrial Analogues for the Moon and Mars

Willcocks, Francesca

Copyright Statement

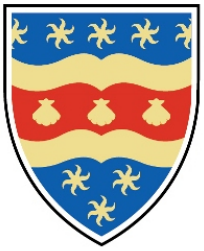

UNIVERSITY OF PLYMOUTH

Intraplate Volcanism in our Solar System; Searching for Terrestrial Analogues for the Moon and Mars

by

Francesca Willcocks

A thesis submitted to the University of Plymouth

in partial fulfilment for the degree of

RESEARCH MASTERS

School of Geography, Earth and Environmental Sciences

October 2021

Acknowledgements:

I would like to say a HUGE thank you to Dr Natasha Stephen and Dr Stephen Grimes for their endless help, advice and support throughout the year, both academically and personally. The efforts you went to to make the year as normal as possible throughout COVID (even if it meant spending entire days on zoom so I could remotely use the SEM), as well as the knowledge and opportunities you have given me have been invaluable and I couldn't have asked for better supervisors.

I'd also like to say a massive thank you to all the lab techs at the Plymouth Electron Microscopy Centre, particularly to Lorelei for kindly giving up her time to train me in sample prepping and helping with remoting into the SEM, and Jen who was always around to help with any questions I had no matter how silly they were, it has been incredibly appreciated. Lastly, I'd like to thank my friends Lauren, Lauryn and Kayla who let me crash at theirs when I was down in Plymouth finishing off my thesis, I owe you guys a pint.

Author's Declaration:

At no time during the registration for the degree of Master of Research has the author been registered for any other University award without prior agreement of the Doctoral College Quality Sub-Committee.

Work submitted for this research degree at the University of Plymouth has not formed part of any other degree either at the University of Plymouth or at another establishment. This study was self-funded.

A programme of advanced study was undertaken, which included taught modules: GEOL5001 Geoscience Frontiers: Research and Communication and GEOL5003 Advanced Analytical Techniques.

Presentations at conferences:

Presented as a poster at the Royal Microscopy Society's Microscopy and Microanalysis in Geological and Archaeological Sciences 2021 conference.

Word count of main body of thesis: 25,336

Signed……

Date: 28/10/21

Francesca Willcocks Intraplate Volcanism in Our Solar System; Searching for Terrestrial Analogues for the Moon and Mars

Abstract:

Basalt volcanism has played a huge role in the shaping of rocky bodies throughout our Solar System, including Earth, the Moon and Mars. Intra-plate volcanism has produced millions of cubic kilometres of basaltic lava on Earth, forming the likes of the Deccan Volcanic Province and Columbia River Flood Basalts, and through orbital and lander missions, flood lavas have also been identified on the Moon and Mars. These remote observations were also confirmed by lunar field observations and samples taken during the Apollo and Luna missions and an intraplate origin inferred due to their one-plate nature. The lack of direct samples for these bodies (particularly for Mars), however, has meant geochemical studies comparing these basalts to Earth have been limited. In this study, petrological and geochemical data for Lunar (basaltic breccias) and Martian (lherzolitic and olivine-phyric Shergottites) meteorites were obtained using non-destructive analysis - Scanning Electron Microscopy - and compared to terrestrial analogues of intra-plate origin (from Hawaii, New Mexico and Northern Ireland (ESA01-A)) in a search for accurate terrestrial analogues for the Moon and Mars. These analogues are important for testing components and *in situ* resource utilisation of spacecraft across these planetary bodies, in addition to giving indications of how these lavas may have formed. Whilst official analogue ESA01-A has displayed similarities across bulk geochemistry to Martian Shergottites, other field samples have proven to be more similar to the petrological and geochemical observations seen in olivine-phyric Martian

Shergottites, and, as a result, could make for a more accurate chemical analogue for Martian volcanism.

Table of Contents

List of Figures:

List of Tables:

1.0. Introduction

1.1. Aims and Objectives

The aim of this project is to use geochemical analysis of terrestrial basalts, as well as Lunar and Martian basaltic meteorites, to decipher if any of the terrestrial samples would make accurate geological analogue samples for basalts on these planetary bodies.

The main objectives throughout this project are to carry out geochemical and petrological analyses on terrestrial basalts of an intraplate origin (from Kilauea (Hawaii), New Mexico and Northern Ireland), using Scanning Electron Microscopy (SEM) at Plymouth Electron Microscopy Centre, UK. In particular, the bulk and individual mineral geochemistry will be analysed, alongside mineral abundances and petrological textures across samples. The same analyses will then be carried out on both Martian meteorite and Lunar meteorite samples (belonging to the University of Plymouth). The data collected will be processed before being interrogated to identify any similarities and differences between their petrology and geochemistry, deciphering the geological formations of the terrestrial, Martian and Lunar samples chosen, and determining the viability of these terrestrial samples for potential Martian and Lunar analogues.

Terrestrial geological analogue samples aim to replicate either the geotechnical, chemical and/or petrological characteristics of other planetary bodies, therefore comparing the chemical (bulk and individual mineral chemistry) and petrological features (texture, modal mineralogy and mineral phases present) of terrestrial

basalts (Foucher et al., 2021; ESA, 2021) to their Martian and Lunar counterparts will provide an insight into accuracy as geological analogues for use in future Lunar and Martian space mission preparations. Having analogue materials for these planetary bodies are important in the testing of components on spacecraft and *in situ* utilisation of samples on the Lunar and/or Martian surface. They can also provide resources for research developments in the field of planetary science. Uses of terrestrial analogue samples are explained in Chapter 5.4.

1.2. Basaltic Volcanism across our Solar System

Across our solar system, basaltic igneous activity has played a large role in shaping terrestrial and extra-terrestrial bodies. This type of activity has been found on at least 7 planetary bodies (O'Hara, 2000), three of which being the Earth, the Moon and Mars. One type of basaltic activity interpreted to have occurred on all three of these planetary bodies is of intraplate tectonic origin, likened to mantle plume related volcanism extruding products such as flood basalts.

Mantle plume volcanism on Earth is often prolonged and can be responsible for the formation of sea mounts and island chains such as Hawaii, with extrusion events capable of exceeding millions of years in duration (White, 2016). This type of volcanism (and associated flood basalt lavas) is an example of primary crustal formation on Earth (Carlson, 1991), and produces lavas compositionally representative of near surface magmatism both on Earth and other planetary bodies (Self *et al.,* 2015).

The origin of mantle plumes is thought to be caused by instability at the base of the mantle, within the thermal boundary layer (Kiefer, 2013), with the plumes themselves being a secondary result of mantle convection (White, 2016). There are two main processes that can cause mantle plume volcanism, both occurring in solely intraplate settings (Self *et al.,* 2015), and both highlighted by Silver *et al.,* (2006). The first process is a result of a subsurface mantle plume increasing the temperature of shallower mantle to exceed its solidus temperature (Figure 1a). The second process, however, is a result of lithospheric thinning, (caused by lithosphere stretching or convective instability and lithospheric delamination), followed by associated pressure reduction and intersection of the local geotherm with the solidus of the mantle material (Figure 1b). Both processes involve mantle melting at great depths (can occur >110 km (White & McKenzie, 1995)) and high temperatures (Self *et al*., 2015), (up to 1600°C (Jennings *et al.,* 2019)), before the transportation of magma through the crust and emplacement onto the surface.

The conditions during these processes differ greatly to the conditions associated with lithospheric thinning and decompression melting at Mid-Ocean Ridges (MORs). Here, partial melting occurs at shallower depths (~85-50 km depth (Condie, 2016)) and lower temperatures (between 1315-1350 °C (Jennings *et al.,* 2019)) within the upper mantle, causing upwelling of melt and subsequent volcanism at Mid-Ocean Ridges (Macdougall, 1988). Additionally, the mechanism for intraplate volcanism at subduction zones differs greatly to the previous tectonic settings described, and is the result of fluids in the subducting slab being released that then flux into the mantle wedge (Bourdon *et al.,* 2003). This results in metamorphic reactions and the exceeding of the wet solidus, causing partial

melting in the mantle wedge (Bourdon *et al.,* 2003), followed by transportation of melt through the crust within a magmatic arc and subsequent volcanism.

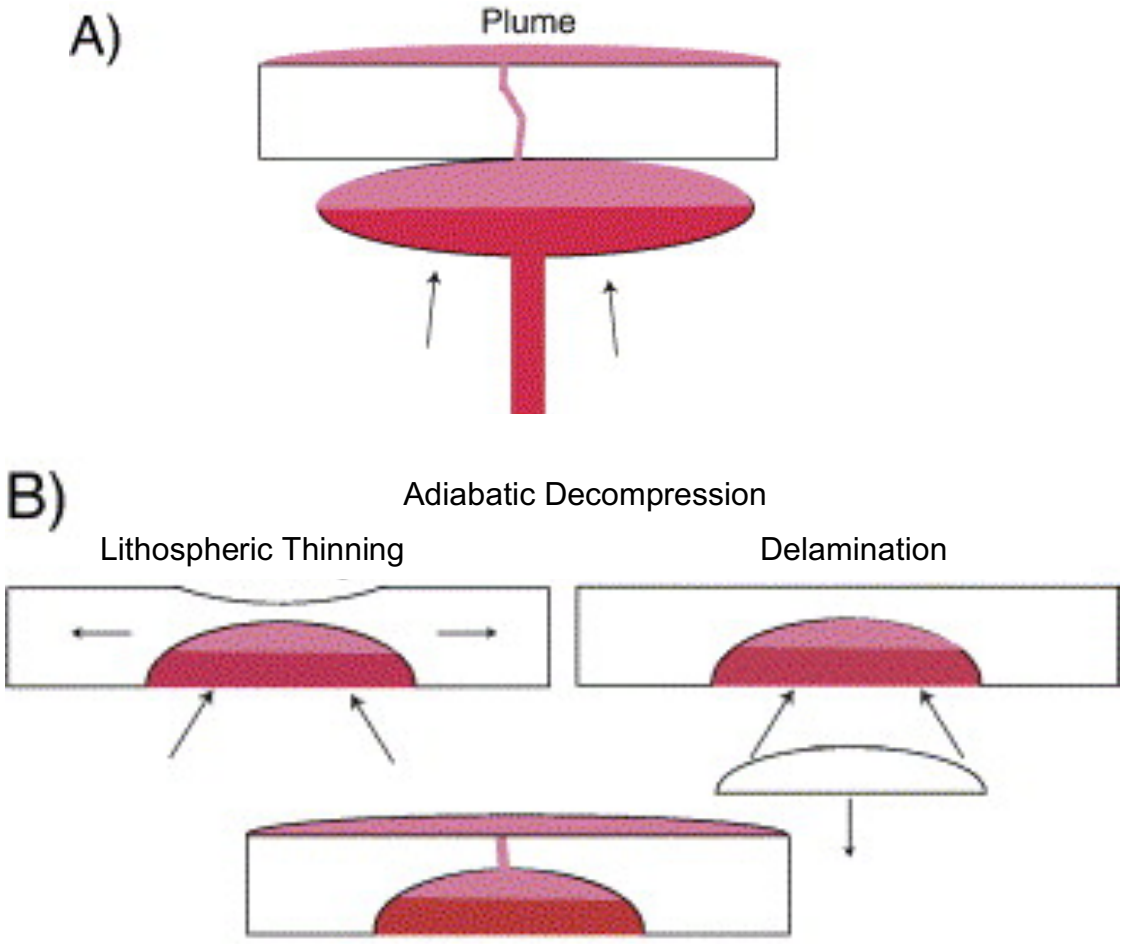

Figure 1 - a) Diagram displaying the formation of flood basalts due to a subsurface mantle plume, b) Diagram displaying the formation of flood basalts due to lithospheric thinning (Source: Silver et al., 2006)

As well as production of island chains (both oceanic and continental), intraplate volcanism can also be responsible for much larger volcanic events; the eruption of flood basalts. Flood basalts are Large Igneous Provinces (LIPs), typically covering millions of cubic kilometres, that are erupted over a relatively short period (often <3 million years), (Carlson, 1991), and have the ability to reach up to 40km thickness (Self *et al.,* 2015). Depending on the setting of their formation

flood basalt provinces are named differently, with those forming on continental crust being deemed ‘flood basalt provinces’, whilst those on oceanic crust are characterised as ‘oceanic plateaus’, (O’Hara, 2000; Self *et al.,* 2015). A map of all flood basalt provinces present on Earth can be seen in Figure 2.

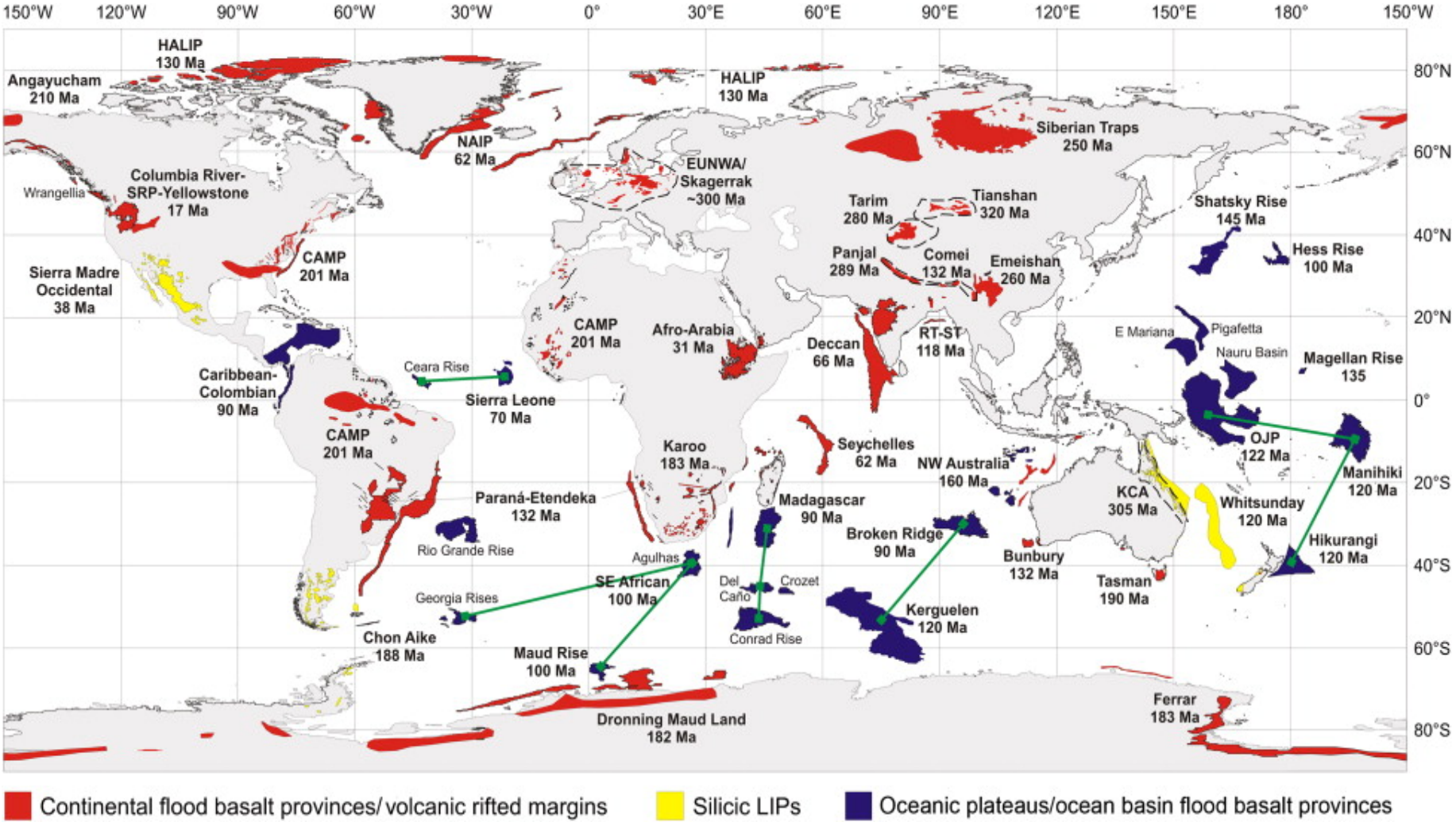

Figure 2 - A map displaying all Large Igneous Provinces across Earth (Source: Self et al., 2015)

Flood basalts can be associated with mass extinctions or continental breakup (Silver *et al.,* 2006), with high extrusion rates and low viscosities allowing for the sheer volume of lava erupted. On Earth, at least 8 of the largest flood basalt provinces have been formed in the last 250Ma (producing a combined total of ~1.5km^3 per annum of new crustal material), and forming the likes of the Deccan Volcanic Province (DVP), India and the Columbian River Flood Basalts (CRFB), America (Carlson, 1991). The Siberian Traps is another example of these provinces, and is the largest sub-aerial LIP on Earth (Self *et al.,* 2015).

Flood basalt provinces commonly consist of sequences of igneous rock that can vary in geochemical and geophysical characteristics. The differing formation of continental flood basalts (CFB) in comparison to Mid-Ocean Ridge Basalt (MORB) settings (where two lithospheric plates are moving apart under extension, allowing for the formation of new oceanic crust), results in a geochemical variation between the basalts produced, with differences being more prevalent within minor and trace elements (Macdougall, 1988). CFB also tend to have a higher diversity of major elements, including higher Fe, Ti, P and K content than MORB. This is thought to be the result of differing source regions, as well as the fractional crystallisation of plagioclase, olivine and clinopyroxene within the melt occurring at lower pressures (Macdougall, 1988). Both CFB and MORB are generally tholeiitic in nature, however, alkalic CFB differentiates can occur (exhibiting varying degrees of crustal contamination and differing source regions), (Macdougall, 1988).

Tholeiitic and alkaline lavas can be distinguished by their concentration of Na_2O, K_2O and SiO_2 (McSween *et al.,* 2006), but also exhibit differing oxygen fugacity's,

with tholeiitic lavas being reduced whilst alkaline lavas are oxidised (Vermeesch & Pease, 2021). These lavas can also be divided by their tectonic settings, where tholeiitic lavas are found in MOR settings where there has been minimal crustal contamination, whilst alkaline lavas are found in subduction zones where mixing of magma source regions occurs owing to the dehydration of the subducting slab. CFB lavas often comprise of clinopyroxenes, Fe-Ti oxides, olivine and plagioclase (the most dominant phenocryst phase).

1.3. Previous studies and Interpretations

The interpretation of basaltic volcanism on the Moon and Mars, and their comparison to the flood basalts we see on Earth, has predominantly been based on surface morphologies in these provinces observed by satellites. A study carried out by Keszthelyi and McEwen, (2007), compared flood lavas (identified by their compositional spectral signature) found on Mars to those already known on Earth based upon the features seen in aerial imaging from the Mars Global Surveyor and NASA's Thermal Emission Imaging System (THEMIS) aboard NASA's Mars Odyssey spacecraft. It was found through this study that there are physical similarities between flood basalts on Earth and Mars, with both displaying similar physiographic effects. There were also some differences interpreted from the satellite data, with Martian flood lavas found to be more platy-ridged basalts as opposed to terrestrial inflated pahoehoe flood lavas more commonly identified on Earth.

Additionally, Keszthelyi *et al.,* (2006), used imagery of both Mars, as well as Io – one of Jupiter's moons – to compare the morphology and flow rates of flood lavas visible to those on Earth. Lava flow morphology of Io was analysed using captures from the 'Voyager' – taken in 1979 – and 'Galileo' – taken between December 1995 and September 2003 – spacecrafts. The information analysed from these images allowed for the interpretation of flood lavas on Io to be fed by narrow lava tubes, with lava between 1999 and 2000 forming at a rate of 50 m^2s^{-1}. In this study, Martian flood lavas were also analysed using NASA's THEMIS images, and followed the same interpretations from Keszthelyi and McEwen, (2007), identifying these flood lavas to display a more 'platy-ridged' morphology. Further interpretations were made comparing this morphology to pahoehoe lavas (based on a comparison to the 1783-84 Laki Flow Field in Iceland - a morphological analogue for Martian flood lavas identified by Keszthelyi et al., (2000)). This study concluded all the lavas analysed were flood lavas of diverse modes of formation. Effusion rates were interpreted for all three planetary bodies (with Io experiencing effusion rates of 50-500 m^3s^{-1}, whilst Mars and Earth displayed effusion rates of ~10^6 m^3s^{-1} and ~5000m^3s^{-1} respectively), as well as the emplacement methods of each of the flood lavas.

Orbital imagery has also been used to study Lunar flood basalts. A study by Whitten & Head III (2013) used imagery from the Lunar Reconnaissance Orbiter's Lunar Orbiter Laser Altimeter (LOLA) to simulate flood volcanism during secondary crust formation in the Lunar Highlands; volcanism that saw the eruption of the Lunar Mare. Here, a three-stage sequence of basin infilling that may have seen the eruption of these flood basalts (discussed more in Chapter 2.2) was constructed, beginning with the infilling of large individual craters

(exceeding 20 km in diameter), followed by a breach of these crater rims and formation of 'intercrater' plains. The final stage sees the expansion of flood basalt deposits before their halt resulting from regional topographic variations. Previous studies have also highlighted potential morphological terrestrial analogues for Lunar flood basalts, for example, a study by Schaber (1973) found the area and volumetric extent of the CRFB (2 x 10^5 km^2 and 2 x 10^5 km^3 respectively) is strikingly similar to that of the Eratosthenian age flood lavas in the Lunar Mare Imbrium basin.

Whilst comparisons of Lunar and Martian surface morphology using satellite imagery have been long studied, there is still little known about the geochemical similarities and differences these flood basalts relative to those on Earth. Geochemical comparisons between samples from the Moon and Mars are limited due to the relative lack of direct samples that can allow for accurate comparisons of *in situ* lavas to those on Earth. Whilst we have samples from the Moon retrieved during the Apollo, Luna and more recently China's Chang'e 5 missions (in addition to Lunar meteorites), to date, there are no direct return samples from Mars. As a result, we often rely on meteorites (which have been randomly ejected from the Martian surface), as the best match to analyse the geochemical histories of Martian basalts.

A meteorite is defined as a fairly small, natural object that has fallen to Earth's surface from space, after surviving passage through Earth's atmosphere (Alexander, 2021). There are two types of meteorite: Undifferentiated meteorites called Chondrites (that are pre-planetary, forming within the proto-planetary disc ~4.56 Gyr ago), and differentiated meteorites from differentiated planetary bodies

such as large asteroids and planets). Differentiated meteorites can be divided into achondrites, iron and stony-iron meteorites. Primitive achondrites fall between chondrites and achondrites, exhibiting bulk compositions similar to chondritic meteorites, whilst displaying igneous and/or metamorphic textures more common in achondrites (Hibiya *et al.,* 2018)), see Figure 3.

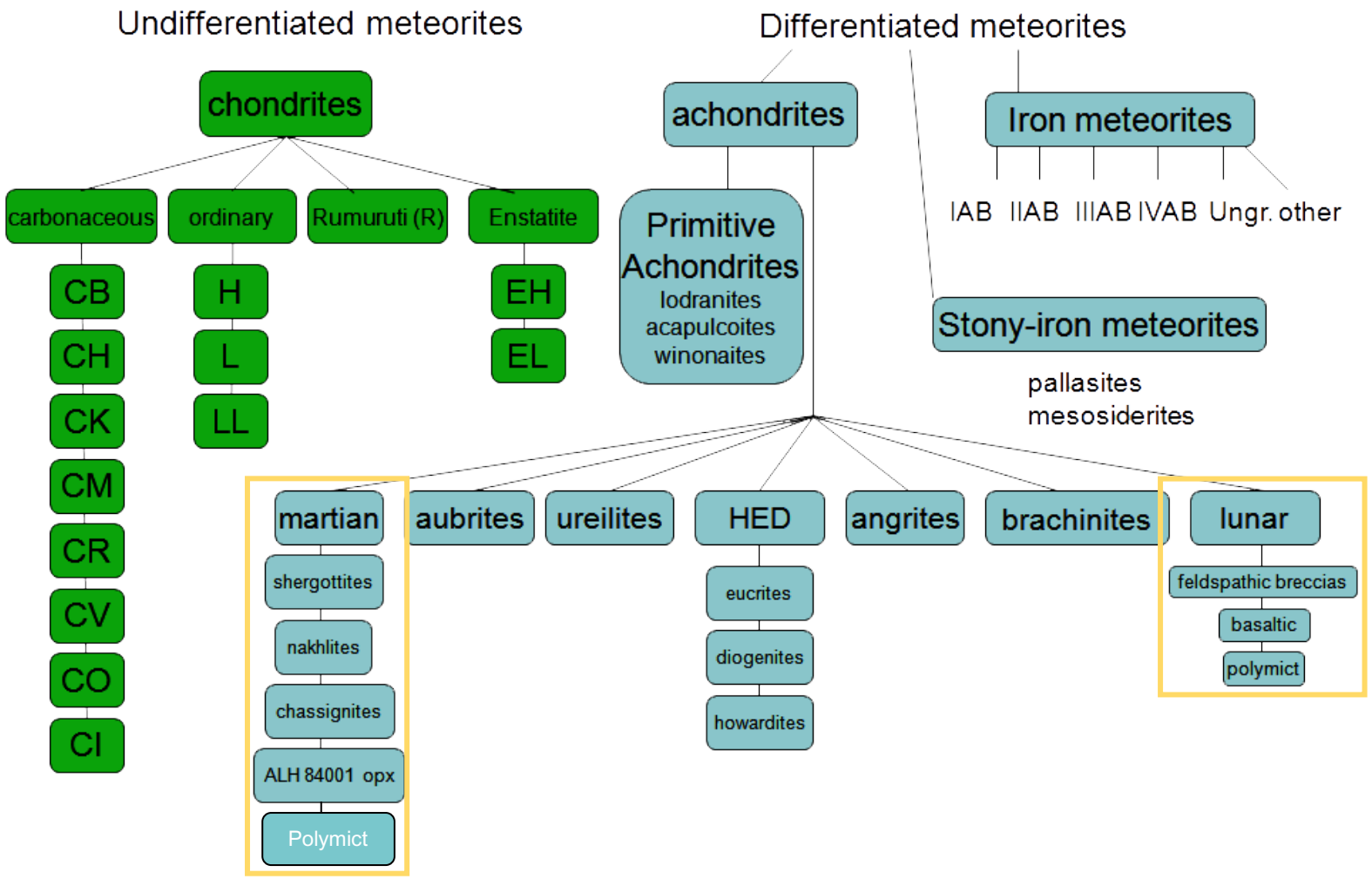

Figure 3 - Diagram displaying the different classifications of meteorites, with both Martian and Lunar meteorites highlighted by the yellow boxes (After Evans, 2016)

Achondrites can be classified into different groups respective to which planetary body they originate from, for example, Lunar and Martian meteorites. Lunar meteorites are generally grouped into three types: feldspathic breccias, basaltic meteorites or polymict meteorites. At the time of this project, a minimum of 154 Lunar meteorites have been found on Earth, with 96 being categorised as feldspathic breccias (Korotev, 2021). Feldspathic breccias (Figure 4) are more representative of the Lunar highland basalts, demonstrating a dominantly anorthositic composition (Jones, 2003), and an incredibly brecciated nature due to a period of intense collisions (known as the Late Heavy Bombardment, Chapter 2.2).

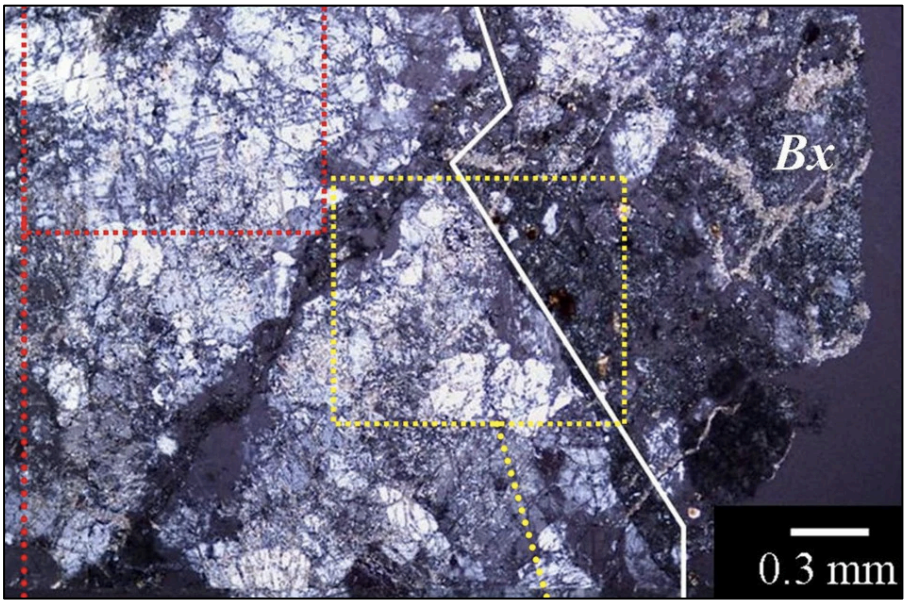

Figure 4 - Optical image of a Lunar feldspathic breccia Dhofar 489, with the brighter, white minerals representing anorthite, Bx = Breccia Matrix (Source: Nagaoka et al., 2014)

Additionally, 15 of the 154 known Lunar meteorites represent largely unbrecciated basaltic samples, interpreted to represent the Lunar Mare – extensive dark basaltic extrusions that are likened to terrestrial flood basalts (see

Chapter 2.2). The remaining basaltic meteorites are basaltic breccias – representing breccias of predominantly basaltic lithologies (The Meteoritical Society, 2021). These breccias are inferred to be largely representative of the Lunar Mare basalts (Jones, 2003), despite being extensively brecciated due to the Late Heavy Bombardment (Figure 5).

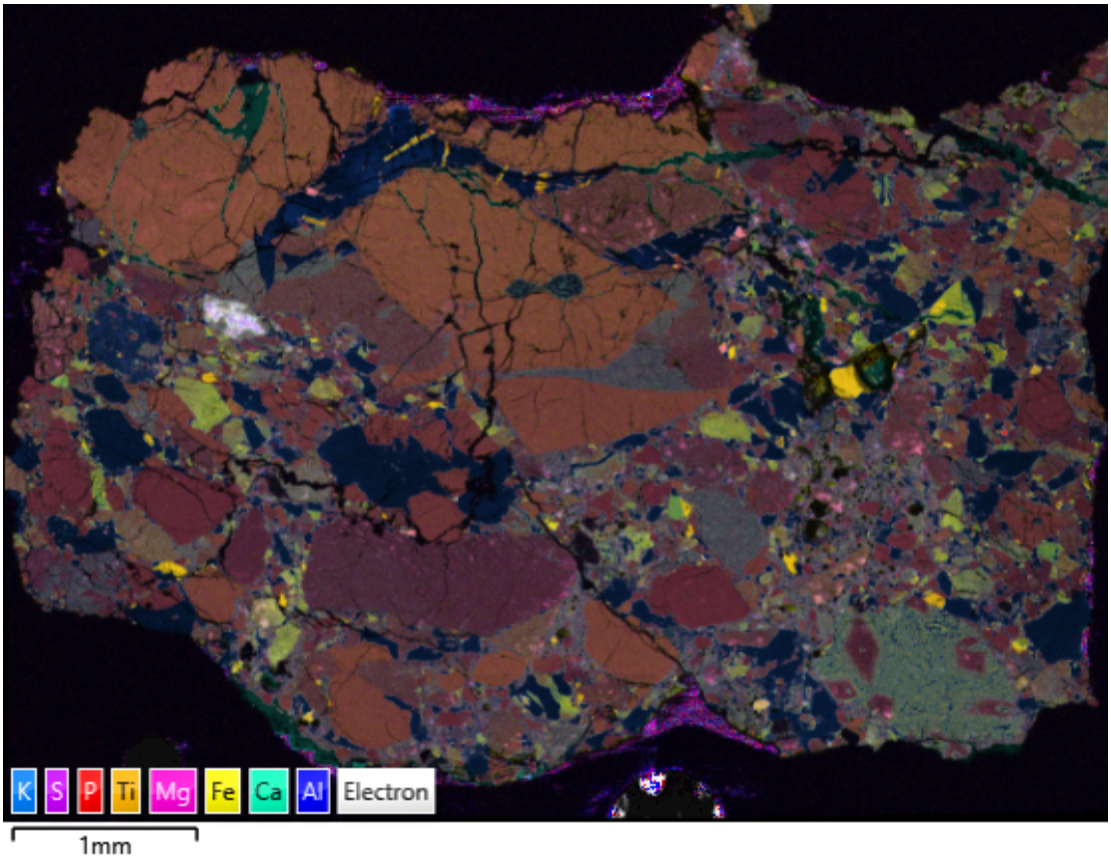

Figure 5 - EDS map of Lunar Mare breccia NWA3160. This sample was used in this project (Chapter 4.2.1)

Martian meteorites can be separated into five groups – the crystalline Shergottite, Nahklite and Chassignite (known collectively as SNC meteorites) and Orthopyroxenites (ALH 84001), (Evans, 2016), alongside the Martian breccias (Agee *et al.,* 2013). Of the SNC meteorites, Shergottites are the most common (comprising 152 of the 169 known Martian meteorites to date (Irving, 2021)), and can be divided into three main groups: Basaltic (Figure 6), poikilitic and olivine-

phyric shergottites (Figure 7), based on mineralogy and textures (Udry *et al*., 2020). Basaltic shergottites consist of mostly pyroxene (Udry *et al*., 2020), and exhibit an absence of olivine within a basaltic, gabbroic (Filiberto *et al.,* 2018) or diabasic texture (Krot *et al*., 2014). Poikilitic shergottites, unlike basaltic shergottites, display cumulate textures, predominantly of olivine-pyroxene composition (Filiberto, 2017). Olivine-phyric shergottites are the most common of the three, exhibiting olivine-porphyritic textures (Goodrich, 2002) and representing more extrusive rocks (Howarth *et al.,* 2014). Shergottite meteorites are generally inferred to be between 150-575 Myr old (Smith *et al.,* 2018). There are two Shergottites (NWA 7635 and NWA 8159) that are 2.4 Gyr old and ~2.3 Gyr old respectively (Udry *et al*., 2020). Unlike the prior Shergottites mentioned, NWA 7635 is an olivine-plagioclase-phyric Shergottite, whilst NWA 8159 is an augite-basalt (Udry *et al*., 2020).

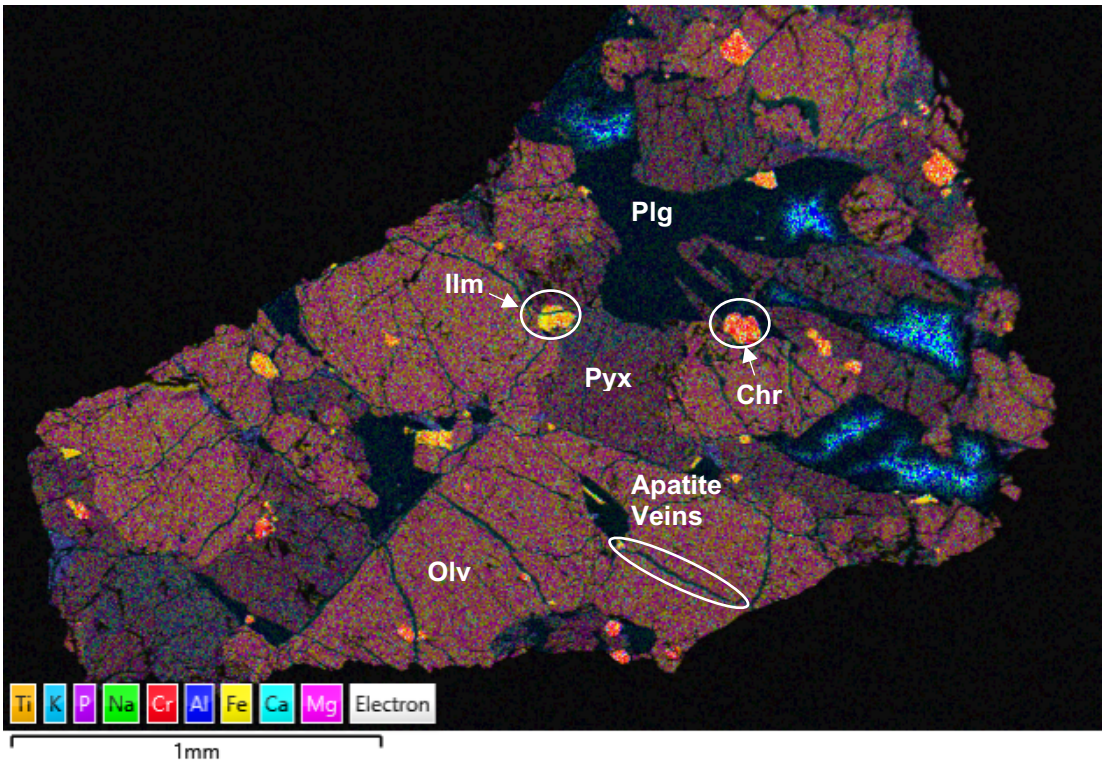

Figure 6 - EDS image of NWA7397 (one of two grains, poikilitic Shergottite), at 40x magnification, displaying an example of the cumulate nature in some

Shergottite samples, with Olv = Olivine, Pyx = Pyroxene, Plg = Plagioclase and Ilm = Ilmenite

Unlike shergottites, Nahklites and Chassignites are cumulate in nature (Filiberto, 2017). Nahklites comprise 14 of the 169 known Martian meteorites, and are clinopyroxenites comprising of ~70-80% augite and 10% olivine (Mezger *et al*., 2013). Only three known Martian meteorites have been classified as Chassignites, with all examples bearing a dunitic composition (almost exclusively olivine) in cumulative textures alongside accessory pyroxene, feldspar and oxides (Mezger *et al*., 2014). Both Nahklites and Chassignites share similar ages (~1.3 Ga), with both being older than Shergottites (Smith *et al.,* 2018). Nahklite and Chassignites are also thought to have similar formation processes (Udry *et al*., 2020). Orthopyroxenites fall outside of the SNC bracket, with only one meteorite (ALH 84001) making up this group. This meteorite is the oldest of all of the known Martian meteorites (~4.1 Gyr old (Lapen *et al*., 2010)), and is brecciated, with a dominantly orthopyroxene composition (Smith *et al.,* 2018).

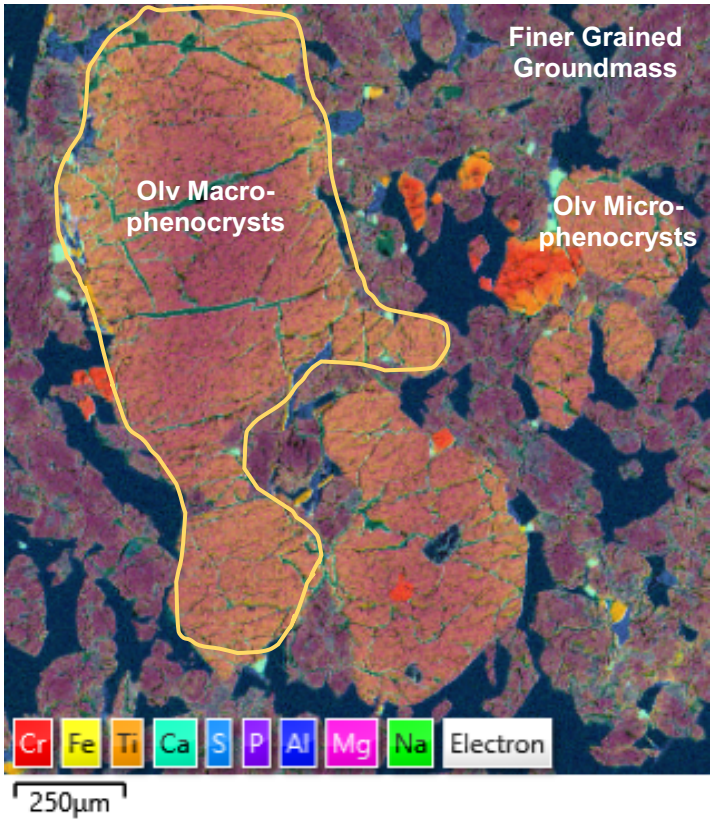

Figure 7 - EDS image of Dhofar019 (75x magnification), an olivine-phyric Shergottite, displaying the porphyritic texture of olivine macro- and micro-phenocrysts

The planetary body from which a meteorite was derived can be interpreted through oxygen isotope data (Figure 8). When plotting $\delta^{18}O$ ppm vs $\Delta^{17}O$ ppm for samples from each planetary body, Lunar meteorite data roughly plots on the same line as terrestrial samples (~0.00 ppm). This can be explained by the giant impact hypothesis, with the Moon being a natural satellite of accreted material derived from the proto-Earth (this is discussed further in Chapter 2.2). Additionally, using the same graph, Martian meteorites can be distinguished due to their higher $\Delta^{17}O$ content (~0.3 ppm), with their $\delta^{18}O$ ppm vs $\Delta^{17}O$ ppm ratio being the only result for an achondritic meteorite that falls above the terrestrial sample line (Figure 8).

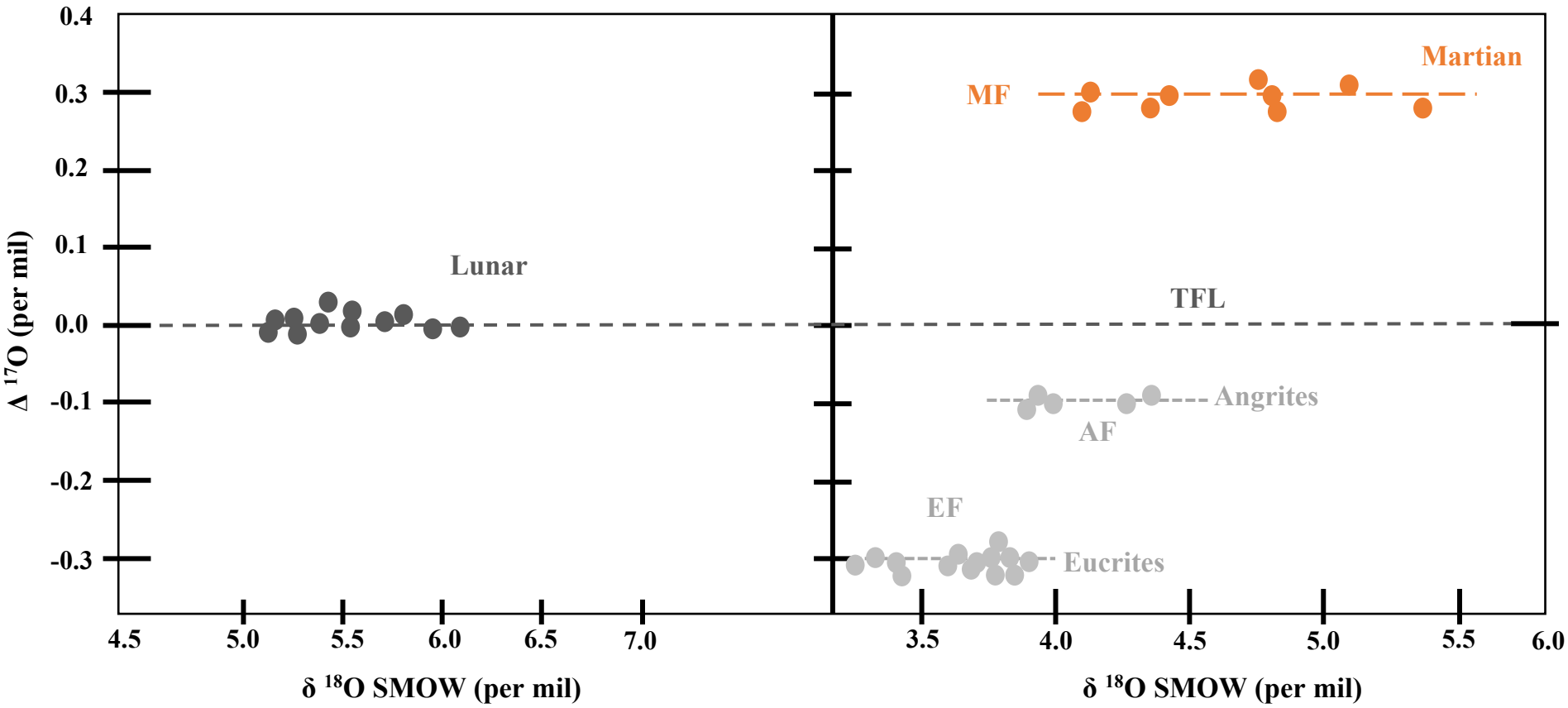

Figure 8 - Graph displaying how the isotope values from meteorites can inform on where the meteorite may have come from. Oxygen isotope data for Lunar meteorites fall on the same line as those of Terrestrial samples (black dashed line), whilst oxygen isotopes data for Martian meteorites fall above Terrestrial samples. Oxygen isotope data characteristic of remaining achondritic meteorite groups fall below Terrestrial samples (Source: Drake & Righter, 2002)

Martian meteorites can also be distinguished through noble gas concentrations within glasses in the meteorite (McSween Jr, 2015). Glasses within Martian meteorites consist of the same concentration of gases (such as ^{132}Xe, ^{84}Kr, ^{36}Ar) as recorded in the Martian atmosphere during the Viking 1 and 2 missions from 1976-1982 and 1976-1980 respectively (NASA, 2021), shown in Figure 9. The matching of these two data sets indicates that these meteorites originated on Mars, with the gases being trapped within shock melted glass on ejection from the Martian surface (Bogard & Johnson, 1983).

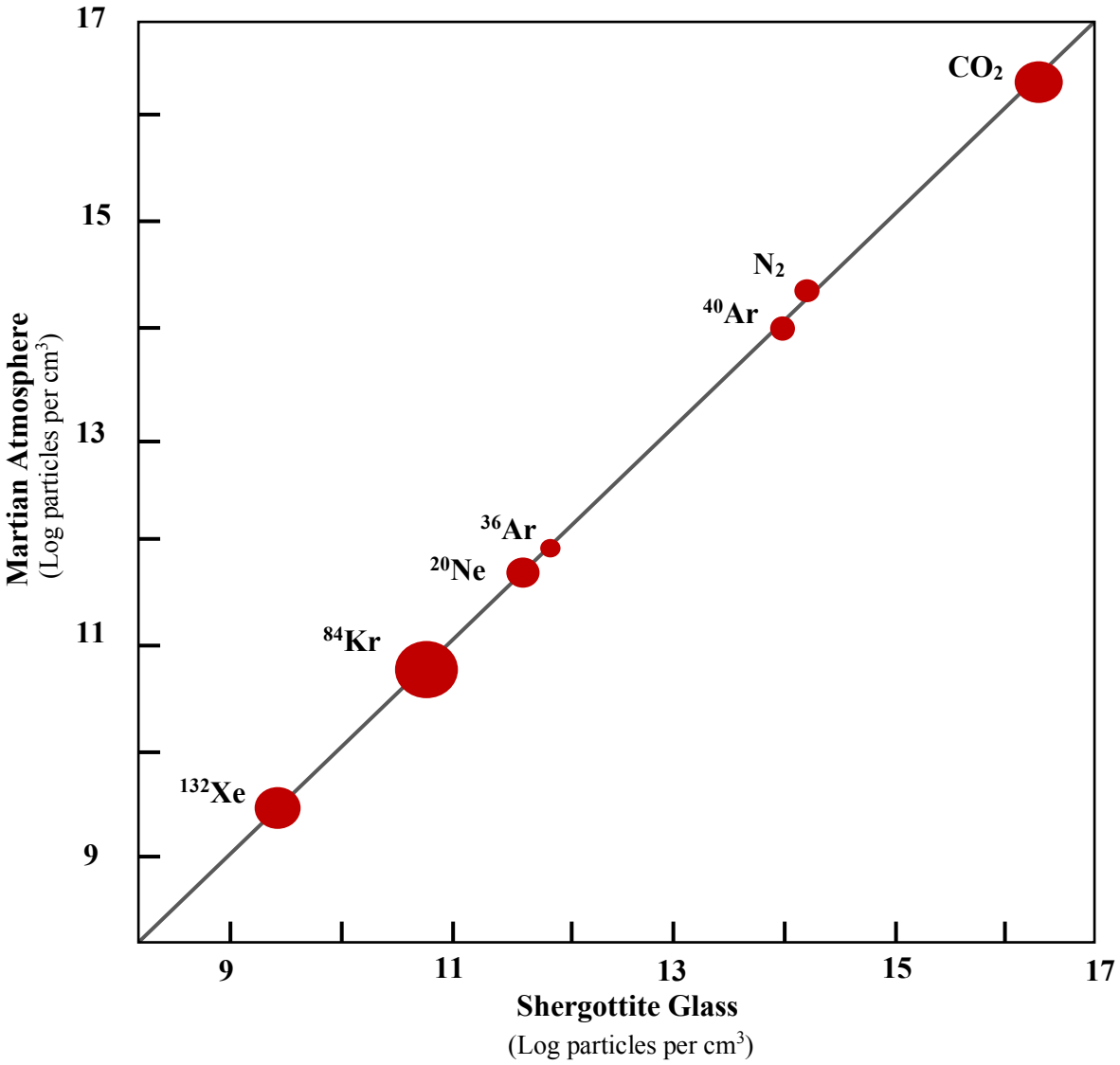

Figure 9 - Graph displaying the isotopic concentrations of glass in Shergottite meteorites in comparison to Martian Atmosphere concentrations recorded by the Viking 1 and 2 missions (Source: Pepin, 1985)

As opposed to the studies previously mentioned, by Keszthelyi and McEwen, (2007), and Keszthelyi *et al.,* (2006), Ruzicka *et al.,* (2001), utilised the study of Lunar and Martian meteorites (alongside the Vesta asteroid, known as the HED meteorites parent body). Comparative geochemical analyses were carried out on these meteorites to determine the similarities and differences between the basalts, with the aim to provide insight on the origin of the Moon. Through these geochemical analyses, they found that in all four planetary bodies the basalt source regions had low abundance in alkali elements (with Mars and Earth being less depleted in these elements than the HED asteroid and the Moon). It was also found that the Moon and Earth had few similarities between basalt source regions. From their analysis, the most likely origin for the Moon is the 'giant impact hypothesis' with the impactor having a large influence in the composition of the moon.

Whilst the comparison of geochemical analyses in these planetary bodies is similar to the methodology of this study, the context will differ. In this study, not only will the geochemical similarities and differences across meteorites from the Moon and Mars be explored, but these will then be compared to terrestrial samples from Hawaii, New Mexico, and Northern Ireland, as well as to literature data for the CRFB and the DVP on Earth to determine if their geochemical histories (and hence their formations) are similar. Additionally, deducing the similarities and differences between petrology and geochemistry across samples from these planetary bodies will allow for identification of any Terrestrial samples that may represent accurate geological analogues for the Moon or Mars.

2.0. Planetary Formation

To understand the processes that may have been responsible for the formation of basalts on the Moon and Mars, the formation, evolution and ages of volcanism on these planetary bodies, along with that on Earth, must be understood. The following section will describe the current understanding with respect to each of these planetary bodies.

Geological time is named differently on each planetary body. Figure 10 below is an illustration after Williams (2001) highlighting the geological time scales for the Earth, Moon, and Mars respectively, including the names for each of their eons as well as their associated ages, for which relative sample and meteorite ages have been annotated.

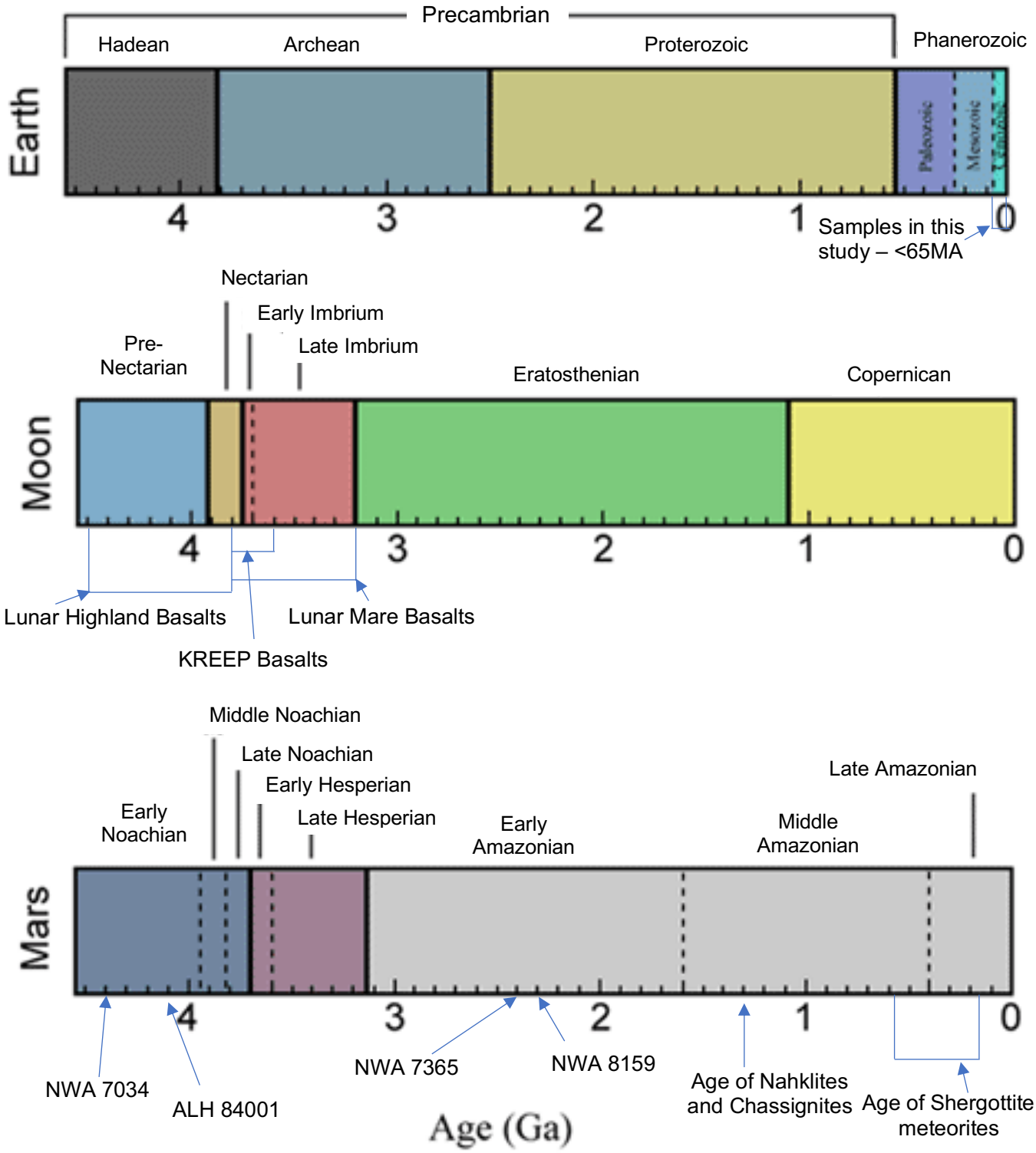

Figure 10 - Illustration displaying the geological timescales for Earth, Mars and the Moon (After Williams, 2021)

2.1. Formation and Evolution of Earth

The Earth is the third of four terrestrial planets within our Solar System, forming ~4.56Gyr ago (Pfalzner *et al.,* 2015). The current understanding of the Solar System's formation is by inferred condensation and hot accretion (over 10-100 Ma, Nikishin, (2011)) of solid matter (dust) within a proto-planetary disk that was shed off a solar nebula and, aided by heat, formed chondrules. Further accumulation of material through continued collisional processes resulted in the formation of planetesimals (Smith *et al.,* 2018). Gravitational fields developed by these planetesimals after reaching a critical size allowed for their growth to form proto-planets (Smith *et al.,* 2018), and their distribution into orbits (Brasser, 2013).

Following accretion, large scale collisions occurred (Oschmann *et al.*, 2002), with one giant impact occurring on the differentiated proto-Earth ~4.5 Ga (Albarède, 2009), which is thought to be responsible for the formation of the Moon (Chapter 2.2), (Albarède, 2009). This giant impact is inferred to mark the beginning of the Hadean eon (Figure 10), when the main accretion phase of Earth had ended (Nisbet & Fowler, 2011). Collisions on Earth and their associated impact heating, resulted in the outer layer of the proto-Earth becoming a magma ocean, with differentiation of the magma ocean occurring due to the sinking of heavier, metallic elements in the magma to form a liquid metallic core, and the lighter, silicate material remaining to comprise the mantle (Nikishin, 2011). During this time, water that wasn't incorporated into the magma ocean created a vapour-gas proto-atmosphere around the body.

Solidification of the liquid iron outer core by cooling, freezing, and sinking of heavier metallic Fe and Ni produced a solid inner core, with lighter elements rising within the crystallising outer core to form a surrounding liquid (Driscoll, 2019). It was inferred by Stixrude *et al*., (2020) that heat flow from the metallic core increased during the cooling of the global magma ocean, with this and the convection induced by crystallisation of the inner core resulting in the formation of the core dynamo (Frost *et al.,* 2021). The dynamo phenomenon has been inferred to involve the rotation of the solid inner core relative to the mantle, encompassed by a current through the liquid outer core (de Paor, 2001). The rotation and subsequent current within the inner and outer core are responsible for Earth's magnetic field.

Cooling of the Earth's surface ~4.4-4.3 Gyr ago (within the Hadean eon) saw the creation of a solid crust over the global magma ocean, on which volcanic eruptions occurred and precipitation of water produced a world ocean. Following this, around 4.3-4.0 Ga the newly formed lithosphere split into tectonic plates, thought to be initiated by mantle upwelling and eruption of more dense, ultrabasic lavas causing subduction of lithosphere into the asthenosphere (Nikishin, 2011).

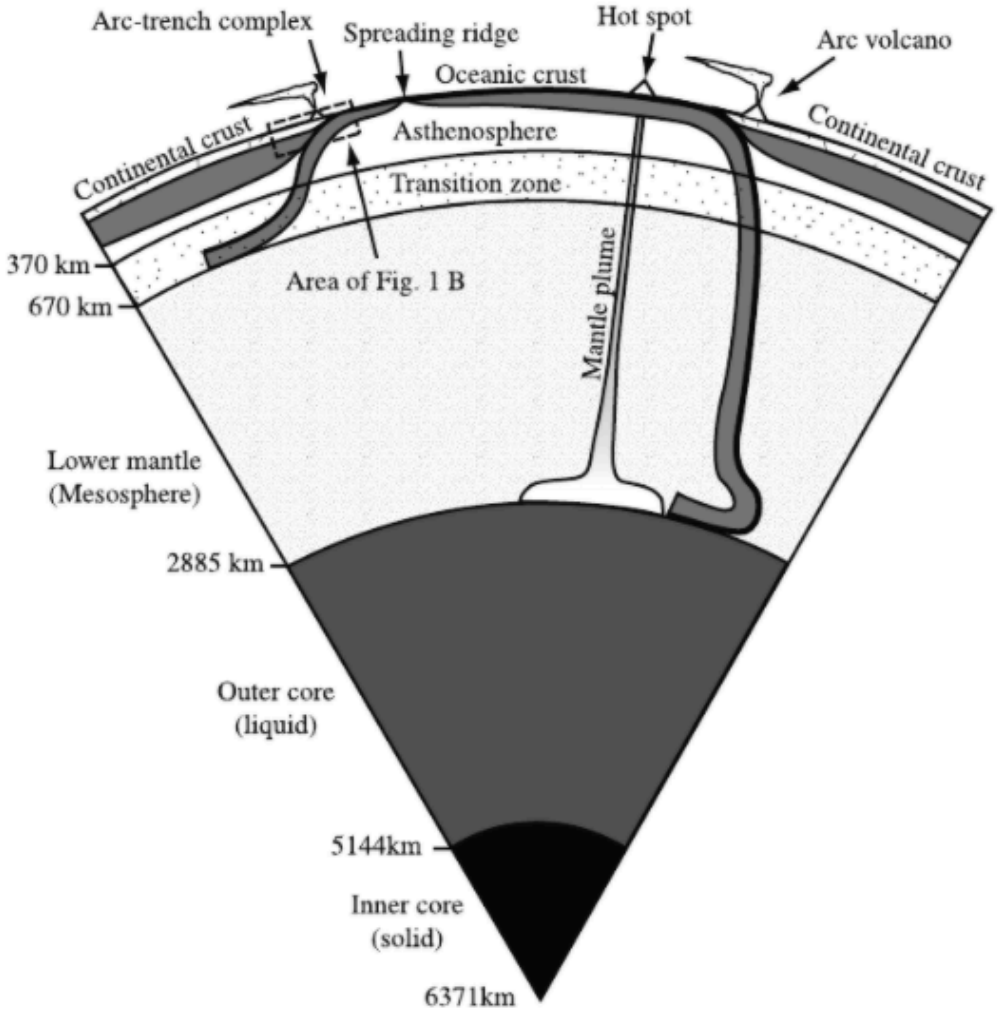

Figure 11 - Diagram displaying the internal structure of the Earth, the layers that comprise Earth and their associated depths (Source: Stern, 2002).

Present-day Earth has a 12,472 km diameter, with a geological structure comprising of a solid inner core reaching (6371 km depth) and the liquid outer core (5144-2885 km depth), lower mantle (2,885-670 km), a transition zone between the lower mantle and asthenosphere (670-370 km depth), the asthenosphere (less dense than the lithosphere, between 100-370 km depth), and lithosphere (comprising the crust and the uppermost mantle, 0-100 km depth), all inferred by the use of seismic tomography (Figure 11), (Stern, 2002).

Terrestrial volcanism has occurred since the Hadean, with Earth being the only planetary body of the three in this study (Earth, Moon and Mars) that is known to still be experiencing volcanic activity today (a comparison of volcanism duration on all three of these planetary bodies can be seen in Figure 15). Unlike both the Moon and Mars, plate tectonics play a huge role in the types of volcanism we see on Earth and the subsequent products of these events. Volcanism on Earth occurs at subduction zones (through magmatic arcs and back arc basins), constructive plate margins (such as MORs), and through intraplate volcanism (of which will be the main focus of this study), Figure 11.

2.2. Formation and Evolution of the Moon

The retrieval of direct Lunar samples through the Apollo, Luna and Chang'e 5 missions provided an insight into the geological conditions of known areas of the Lunar surface. Through the study of these samples, it was discovered that the Moon shows a deficit in both Fe and volatile material. This observation alongside the interpretation of an early molten Moon provided insight into its formation, and subsequently gave rise to the giant impact hypothesis (Halliday, 2012; Canup, 2019).

The current and widely accepted understanding for the formation of the Moon is the derivation from a giant impact (occurring ~4.5 Gyr ago (Albarède, 2009) on the differentiated proto-Earth, during the Moon's Pre-Nectarian epoch (see Figure 10)) and towards the end of the accretionary stage of planetary formation (Lunine, 2006; Halliday, 2012). A Mars-sized impacting body has been inferred to have

obliquely collided with the proto-Earth (Lunine, 2006), resulting in the subsequent disk of material that remained in Earth's orbit and eventually accumulated to form a single moon. During the impact, chemical mixing between both the proto-Earth and the impacting body occurred (Gross & Joy, 2016).

Previous theories for the formation of the Moon include a 'small-impact collisional ejection' theory, involving the formation of a disk of material ejected from the proto-Earth by multiple smaller planetesimal collisions (Ruzicka *et al.,* 2001). As well as this, both an independent formation theory for the Moon (where the Moon formed as its own body before being captured by Earth's gravitational field), and a theory for co-formation of the Moon alongside the Earth (with both accumulating from the same source material) have also been proposed (Canup, 2019). The giant impact hypothesis, however, is currently the favoured theory, as it accounts for the overall lack of Fe within the Moon in comparison to the bulk Fe content on Earth, as well as the rapid initial spin that the Earth is inferred to have experienced in its early evolution (Canup, 2014). Additionally, the resultant force from a giant impact could also account for the deficit of volatiles that has been inferred on the Moon (Canup, 2019).

The rapid accretion of the material disk (produced from the giant impact) resulted in the formation of a global magma ocean (GMO) on the newly formed Moon (Elardo, 2016). As the GMO cooled, differentiation occurred within the magma (Figure 12), with the denser pyroxene and olivine mineral phases sinking and accumulating from the base of the mantle, up, forming a cumulate layer (Albarède, 2009). Once ~75-80% of the GMO had crystallised (Gross & Joy, 2016), the less dense plagioclase mineral phase (anorthite in composition),

floated to the surface and formed an anorthite rich crust (one that is now representative of the 4.5-3.8 Gyr old Lunar Highland basalts). Residual liquids left over during this differentiation process are inferred to have remained between the newly formed anorthite crust and cumulate layer, later forming the 3.8-3.6 Gyr old KREEP basalts.

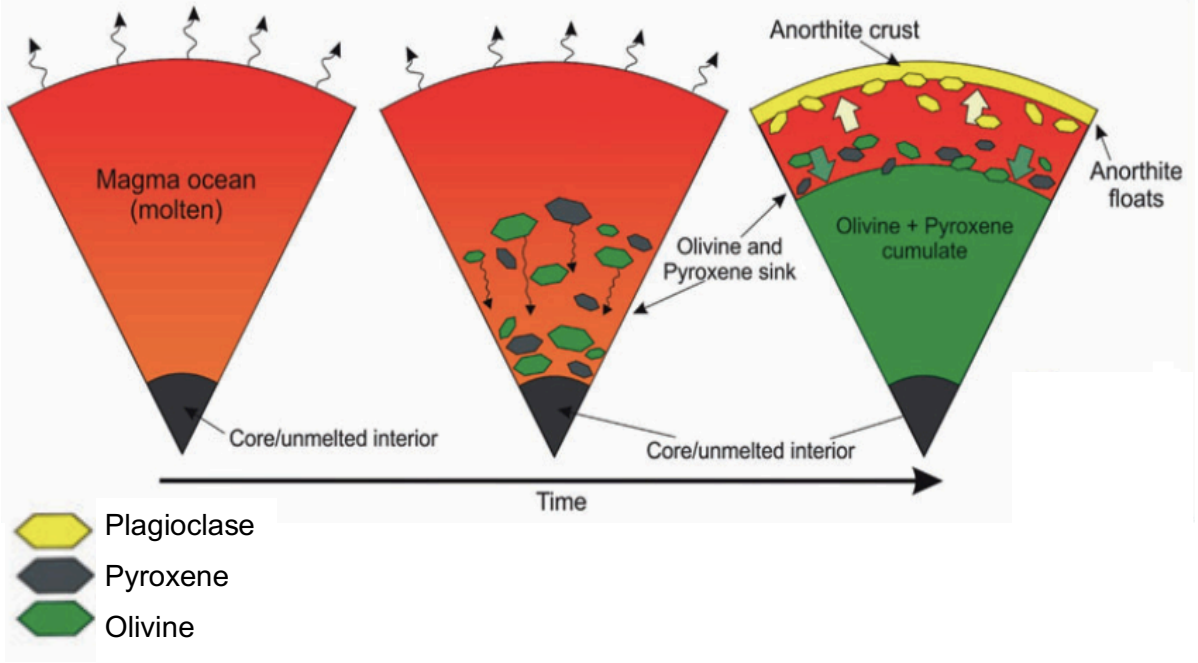

Figure 12 - Schematic displaying the differentiation process for the molten, global magma ocean present on the Moon after the giant-impact (Source: Gross & Joy, 2016)

Following the accretion of the Moon, a period of heavy collisions occurred between 4.5 and 3.9 Gyr ago (Pre-Nectarian - Nectarian, see Figure 10). This period included a relatively short but more intense period (known as the Late Heavy Bombardment (LHB)) taking place at ~3.9 Ga (Koeberl, 2003). The LHB is believed to have occurred due to small planetary bodies within the inner solar system becoming destabilised (Albarède, 2009), a process thought to have been induced by the migration of the giant planets in the outer solar system (Fassett &

Minton, 2013). These periods of intense collisions gave rise to the substantial cratering visible on the surface of the Moon within the Lunar Highlands. Following the LHB, volcanism of the Lunar Mare took place, peaking ~3.8-3.2 Gyr ago (Head III & Wilson, 1992), but continuing until 1 Gyr, (Spudis, 2015) and covering a total of ~17% of the Lunar surface. This unit is the youngest on the Moon, therefore, likely marks the end of volcanism on the Moon (Spudis, 2015).

The Lunar Mare have been found to comprise of three varying basalt compositions: Low-Ti, very low-Ti, and high-Ti basalts (Carlson, 2019), with the production of the Lunar Mare basalts having an inferred intraplate origin (Albarède, 2009) resulting from partial melting of mantle cumulates that earlier differentiated in the GMO (Figure 12), (Albarède, 2009; O'Hara, 2000; Taylor, 1982). Additionally, the variation in geochemistry is thought to be as a result of compositional heterogeneity in the Lunar interior (Taylor, 1982), likely forming during the cooling of the GMO (Carlson, 2019).

Through analysis of meteorites and samples retrieved during the Apollo, Luna and Chang'e 5 missions, Lunar Mare lavas have been identified as more reduced compared to Earth, demonstrating an alkali-poor composition that is alike terrestrial tholeiitic lavas (O'Hara, 2000). Samples collected during Apollo 11 and 17 also exhibit low SiO_2 content, falling within the alkaline lavas on a TAS diagram (Figure 34). Storey (1973) suggested the lack of Na, K and lower Si content across Lunar samples could be the result of mass volatile loss during liquid magma extrusion into a vacuum environment, therefore may not wholly representative of pre-eruption compositions. This lack of Na, K and lower Si,

however, is thought to be the cause of the extremely low viscosities inferred for Lunar Mare basalts in the Imbrium Basin (Shaber, 1973).

Inferred variations in the magma transport, accumulation and eruption of these Lunar Mare basalts have been identified by their asymmetry across the nearside and farside of the Moon (Figure 14). This asymmetry is the inferred result of differing topographies and crustal thicknesses observed by NASA's Lunar Orbital Laser Altimeter (LOLA), (Figure 13), and the Gravity Recovery and Interior Laboratory (GRAIL), (Head III & Wilson, 1992; Zhu *et al.,* 2019). The variation in magma accumulation was interpreted by Solomon, (1975) to be due to the density contrast of the lower density anorthite crust and the higher density Lunar Mare magmas below. The decreasing density towards the Lunar surface meant hydrostatic forces (induced by thickness variations of the crust) helped drive Lunar Mare magmatism, with the thinner nearside crust meaning Lunar Mare basalts preferentially pooled on this side, concentrating in regions of local thickness heterogeneity (such as impact basins). The combination of larger thickness and already decreasing density towards the surface meant on the farside, Lunar Mare magmas likely stalled before reaching the Lunar surface, and relied on hydrostatic forces induced by the deepest impact basins to rise to the surface (Head III & Wilson, 1992).

Interpretations by Head III & Wilson, (1992) found that it was during the differentiation and formation of Lunar lithosphere (mentioned earlier) that the nearside-farside thickness asymmetry formed, occurring during the Pre-Nectarian period and lasting ~630 Ma. The origin of this asymmetry is still poorly understood and has previously been regarded as the result of GMO

crystallisation (Ohtake *et al.,* 2012). More recently, however, formation of this asymmetry is inferred to be the result of a second large impact on the Lunar surface, responsible for an excess of ^{128}W isotope compositions on the Moon compared to Earth's present-day bulk silicate compositions (Zhu e*t al.,* 2019).

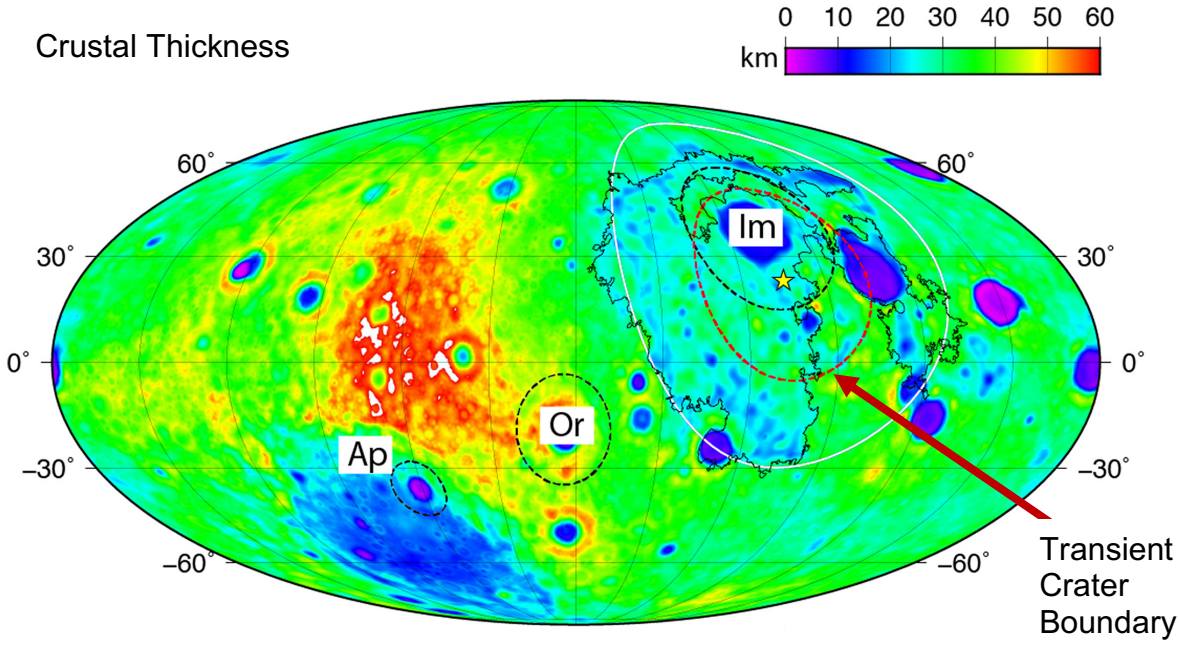

Figure 13 - Image taken by the LOLA spacecraft, displaying the crustal thickness variations across the nearside (right of centre) and farside (left of centre). Red dashed circle = boundary of transient crater exhibiting a radius of 850km (Source: Zhu et al., 2019)

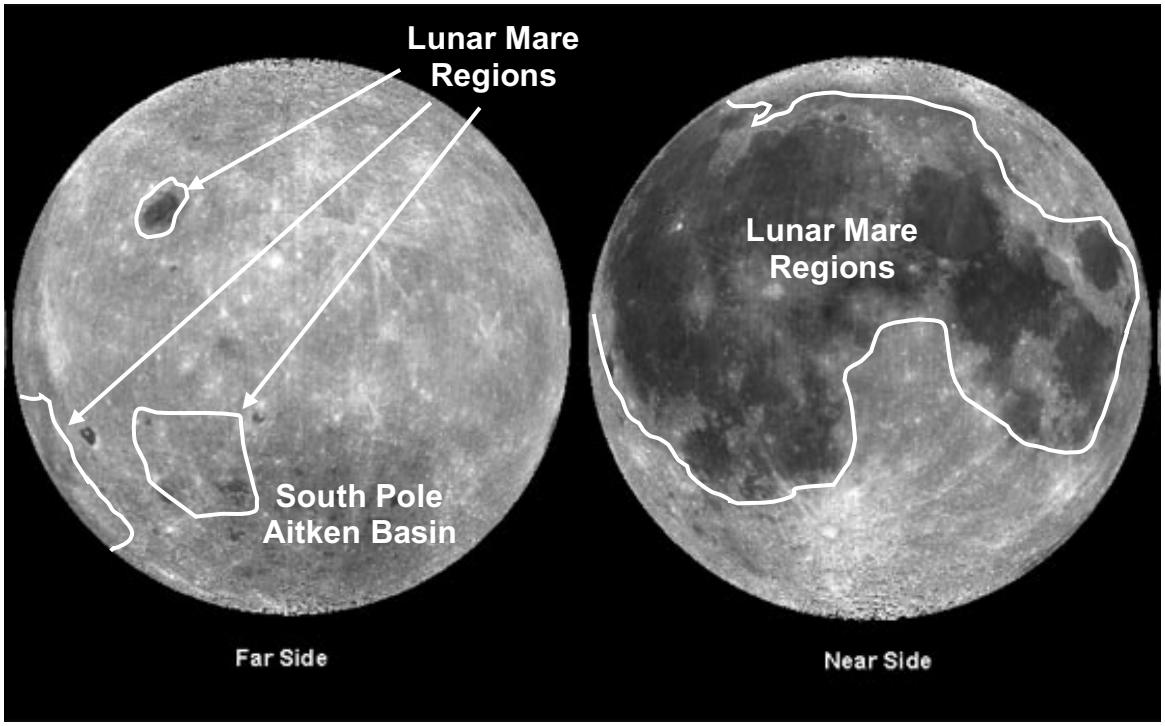

Figure 14 - Images taken from the Clementine 1 spacecraft, displaying the variation in Lunar Mare deposits (darker areas) across the nearside and farside of the Moon, regions of the Lunar Mare have been taken after Lemelin et al., (2013), (NASA Photojournal, 1998b) images – PIA00302 (nearside) and PIA00304 (farside)

During the peak of Lunar Mare volcanism ~3.8-3.2 Ga (Spudis, 2015; Head III & Wilson, 1992), global volumetric expansion is thought to have occurred, encouraging further Mare volcanism (Head III & Wilson, 1992). The previous infilling of basins has been inferred to instigate isostatic load and subsequent subsidence of lithosphere causing extensional environments that saw the formation of linear rilles of Lunar Mare basalts associated with the Lunar Mare basins (Head III & Wilson, 1992; Mullis, 1993). Extensional features observed on the Moon (such as normal faults and graben and rift structures) are all thought to have formed during this period of global extension (Mullis, 1993). By the Eratosthenian period (Head III & Wilson, 1992), the global thermal state of the

Moon has been inferred to have become more compressive (a subsequent result of cooling and contraction of the Moon). The change in tectonic regime and associated crustal thickening is likely to have been responsible for the slowing of Mare volcanism during this period, occurring from 3.2 – 1.1 Ga (Head III & Wilson, 1992).

Altogether, volcanism on the Moon in comparison to both the Earth and Mars was relatively short lived, with the total duration of volcanism occurring from ~4.5-1 Ga before becoming a stagnant body. As a result, volcanism on the Earth and Mars reaches much younger ages in comparison to the Moon. A diagram of this timescale compared to Earth and Mars can be seen in Figure 15.

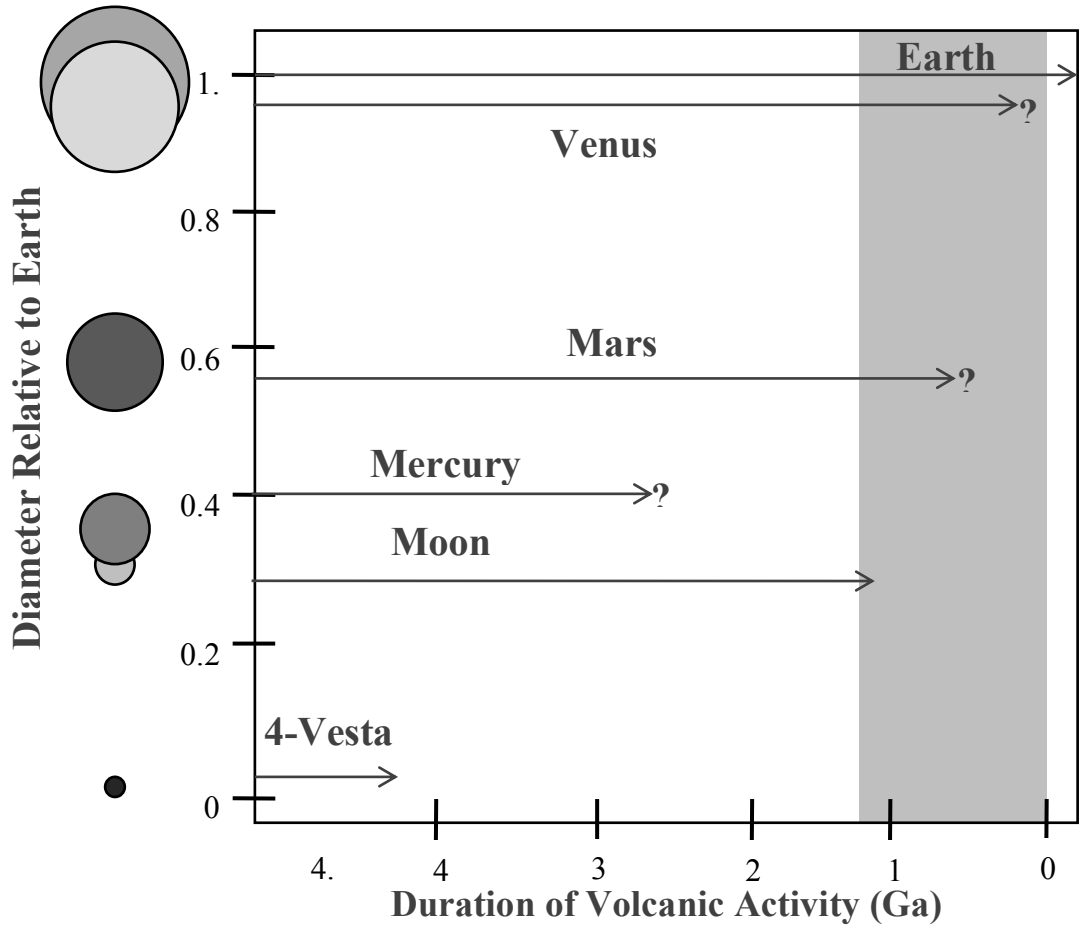

Figure 15 - Diagram displaying the overall age of volcanism on Earth, Moon and Mars (as well as the age of volcanism on 4-Vesta and Venus), (After McSween, 1999)

2.3. Formation and Evolution of Mars

Studies focused on developing an understanding of the formation and evolution of Mars have been limited due to the lack of targeted, direct samples from the Martian surface. Despite this, the study of meteorites, and the observations of both orbiter and lander spacecraft (such as the Mars rovers, NASA's InSight, MAVEN and Viking missions) carried out by NASA, the former Soviet Union Programme, ESA and the Indian Space Research Organisation, (that have landed on the planet or carried out flybys) have allowed for the research into the formation and evolution of Mars since solar system formation (Howell, 2021). The use of satellite imagery in particular aided the categorisation of Martian geological time into epochs (Figure 10), with epochs separated into categories based off of impact crater densities on the Martian surface. In this classification scheme, surfaces covered in a higher crater density are older in age (Hartmann & Neukum, 2001).

Mars is the second smallest terrestrial planet in our Solar System, with a diameter of 6772 km (Albrède, 2009). Unlike Earth, Brasser (2013) inferred that Mars' accretion was rapid, lasting ~2 Myr, compared to the 10-100 Myr time frame for Earth. The study of Martian meteorites also indicate that Mars differentiated rapidly within ~10 Ma during accretion (Righter & O'Brien, 2011; Mezger *et al*., 2013), with isotope geochemistry of Martian SNC meteorites suggesting differentiation into a layered structure of a core, mantle and crust (Forget & Hauber, 2015). This interpretation is also supported by recent findings of NASA's InSight mission indicating a three-layered interior structure of Mars (Witze *et al.*, 2021). Additionally, SNC meteorites may indicate the presence of an early-

Martian GMO (interpreted to have formed by either decay of radioactive isotopes generating heat, or impact melting during prolonged accretion). The GMO allowed for the sinking of metallic elements from silicate mantle to form the metallic core (Mezger *et al*., 2013). This metallic core has been inferred to be partially-molten, with sulphur content capable of lowering the core's melting point, creating a subsequent lack of a magnetic field generation, (Franz *et al.,* 2019), (a field that is believed to have been absent since ~4 Ga (Mezger *et al.,* 2013)). The sulphur content of Mars' core has been debated, with Mezger *et al.,* (2013), deducing a sulphur content of 16% (similar to studies by Stewart *et al.,* (2007) – between 10.6-16.2 wt% - and Rivoldini *et al.,* (2011) – 16 $\pm$ 2%). Other studies have produced estimations of sulphur content much higher, for example, Khan & Connolly (2008) which estimated a content of >20 wt%. There are more recent studies, however, that have deduced an estimation with an upper limit of ~8 wt% S (Shahar *et al.,* 2015).

One model for the formation of Mars' GMO discussed by Mezger *et al.,* (2013) suggests crystallisation of the Martian mantle beginning from the base, up, a process that is estimated by Shergottite Nd isotopes to have occurred ~4.52 Gyr ago (Mezger *et al.,* 2013). This process instigated mantle overturning ~100 Ma post-solar system formation, caused by a density imbalance of more-dense Fe-rich cumulates situated over less dense Mg-rich cumulates (Mezger *et al*., 2013). During the mantle overturn, adiabatic compression induced melting and upwelling of mantle cumulates, segregating garnet and possibly being responsible for the formation of early Martian crust. The Martian crust consists of one plate, and lacks any evidence for present-day plate tectonics, although an inferred presence of a magnetic field between 4.5-4.0 Ga indicates that plate tectonic-like processes

may have been present during this period, with convection processes required to maintain a geodynamo (Carr, 2006). A schematic for the crystallisation of the GMO can be seen in Figure 16.

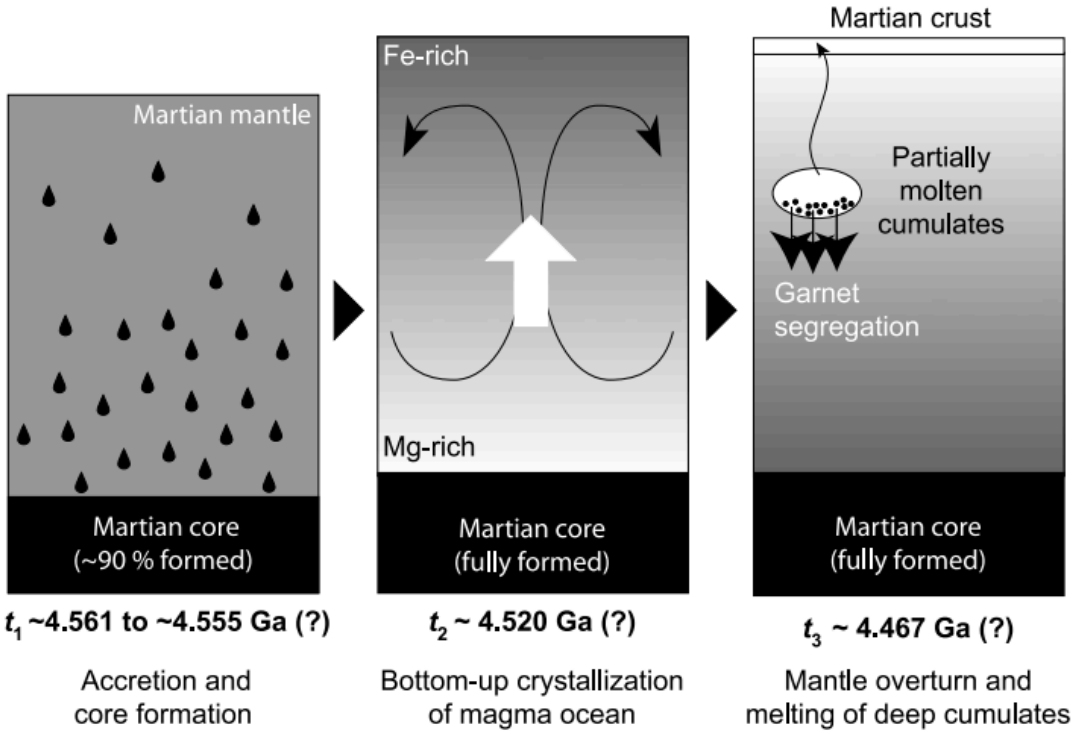

Figure 16 - Schematic displaying the formation of the layered core-mantle-crust sequence on early Mars, with the settling of metallic elements occurring, followed by the crystallisation of the GMO, which then induced mantle overturn. (Source: Mezger et al., 2013)

The current understanding of Martian volcanism is the occurrence of volcanic eruptions early in the planet's formation (Carr, 2006), up to as recent as 10-200 Myr ago (Hughes *et al*., 2019). A diagram displaying the duration of Martian volcanism relative to Earth and the Moon can be seen in Figure 15. Two provinces on Mars, Tharsis and Elysium, have been identified as the largest

areas of magma production on the planet (Mitchell & Wilson, 2003), with both representing the longest-lived volcanism on Mars (Platz *et al.,* 2014).

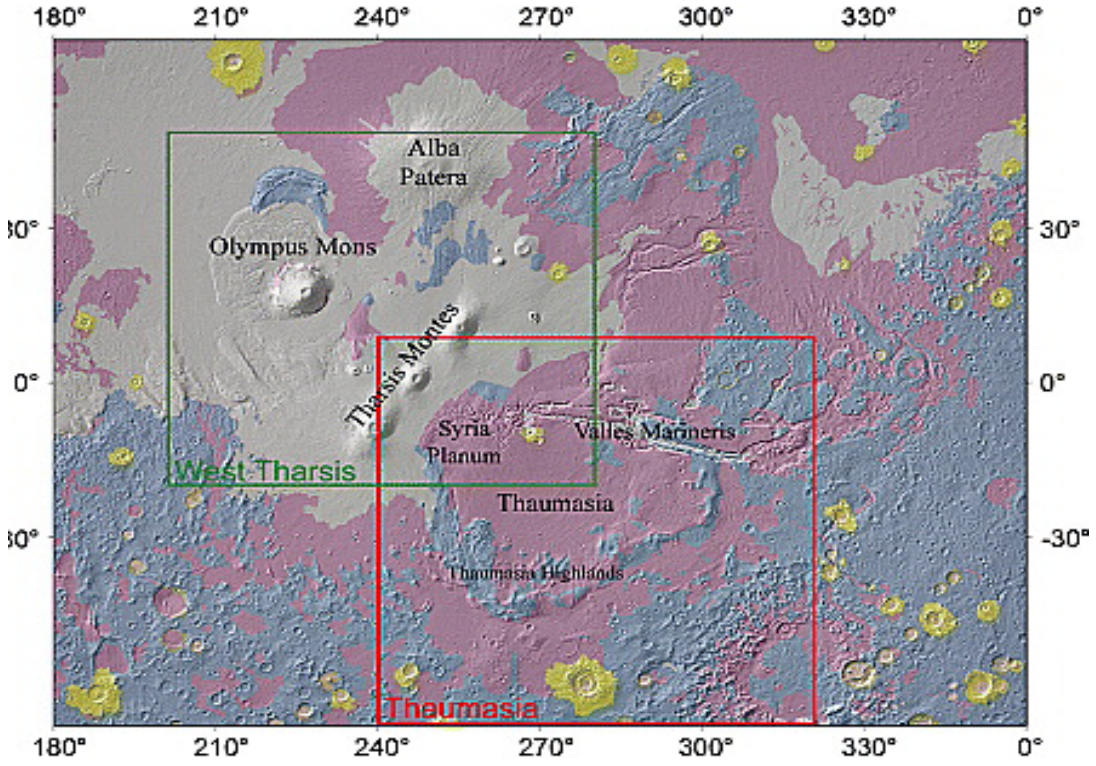

Figure 17 - Map displaying the aerial extent of the Tharsis volcanic province where blue = Noachian volcanism, purple = Hesperian volcanism and grey = Amazonia volcanism (Source: Williams et al., 2008)

Tharsis (Figure 17) is the largest of the two provinces, and is home to Olympus Mons – the largest volcano in our solar system. It has been deduced that volcanism at Tharsis occurred during the Noachian Epoch (Figure 10), ~3.71 Gyr ago, and continued into the Amazonian Epoch (3.37-present), (Platz *et al*., 2014), exhibiting flows as recent as 10-200 Myr old (Hughes *et al*., 2019). The majority of material that comprises the Tharsis volcanic province, however, was erupted during the early Hesperian Epoch (3.71-3.61 Ga). The discovery of 10-200 Myr

old lava flows means Tharsis may still be volcanically active, and over its lifetime has produced ~3 x 10^8 km^3 of magma in total (Platz *et al*., 2014).

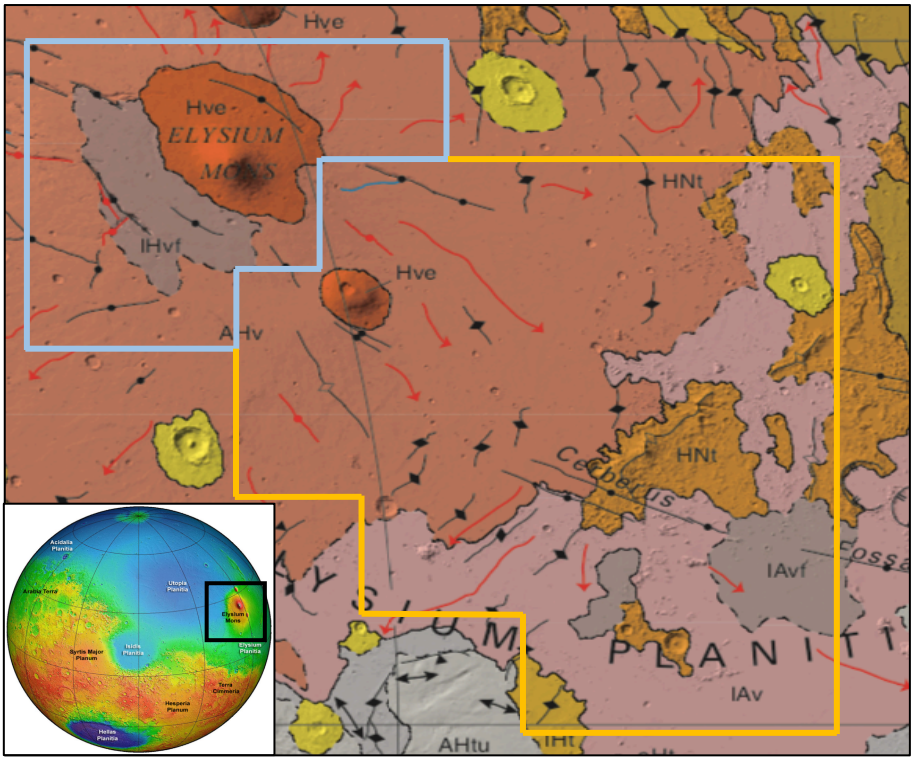

Figure 18 - Map displaying the aerial extent of the Elysium province, with blue outlining NW area of Elysium, and orange outline the SE area of Elysium (encompassing Elysium Planitia), Scale: 1000's km (Source: Susko et al., 2017)

Elysium (Figure 18) is a smaller (minimum of ~3.5 x 10^6 km^3), province in comparison to Tharsis, and home to Elysium Mons, with the formation of Elysium rise occurring at an estimated ~4.1 Ga (Platz *et al*., 2014). To the SE of Elysium is Elysium Planitia which is often included within the broader Elysium volcanic province they are inferred to share the same magma source. The majority of Elysium's volcanic activity is thought to have occurred within the Amazonian Epoch, between 2.5 - 1 Ga (Platz *et al*., 2014), with ~12 eruptions interpreted over the past 500 Myr.

Volcanism on Mars is complex, and its intraplate origin is believed to be responsible for a variety of landforms observable through satellite imagery, most of which are large shield volcanoes (Carr, 2006). This volcanism has been predominantly recognised as basaltic in nature through the Mars Global Surveyor Thermal Emission Spectrometer (TES), with this data identifying two groups of volcanic rocks (largely limited by their latitudes) exist on Mars, with group 1 representing basalt and dominating the lower latitudes of Mars. Group 2 has previously been identified as andesite (and was supported by chemical analyses collected by Mars Pathfinder (McSween *et al.,* 1999)), however, further research has suggested this group actually comprises of weathered basalt (interpreted by matching of spectral data to those of terrestrial samples, and a lack of andesitic compositions across Martian meteorites), (Wyatt & McSween, 2002).

Through meteorite observations, orbital and lander missions, both tholeiitic and alkalic lavas have been identified on Mars (Chevrel *et al*., 2014; Sautter & Payre, 2021). Mildly-alkaline lavas were identified through Alpha Particle X-Ray spectroscopy (APXS) observations by the Spirit rover within Gusev crater. As well as this, strongly alkaline lavas identified by the Curiosity rover in Gale crater – examined by the rover's laser induced break-down spectroscopy instrument ('Chemcam') and APXS (McSween *et al*., 2006; McSween, 2015; Schmidt *et al.,* 2014). Two clasts within polymict breccia NWA 7034 also demonstrated an alkali composition (Filiberto, 2017). These compositions differ to the tholeiitic compositions exhibited by Martian Shergottites, Nahklites and Chassignites. Studies such as Sautter & Payre, (2021) suggested the presence of these alkalic lavas could be due to processes such as low degree partial melting in a primitive or metasomatized mantle source, fractional crystallisation of oxidised basaltic

magma in the presence of water or crustal contamination through assimilation of crustal rocks. A possible metasomatized mantle source for these alkalic lavas was also supported by Schmidt *et al*., (2014), and Filiberto, (2017). The ages of alkalic basalts at Gusev (~3.65 Ga) and Gale (<3.86 Ga) crater are significantly older than the young Shergottites (McCubbin *et al.,* 2016), therefore, this alkalic volcanism could be more representative of fairly ancient volcanism, and suggests global magmatic evolution over Mars' history (McSween, 2015).

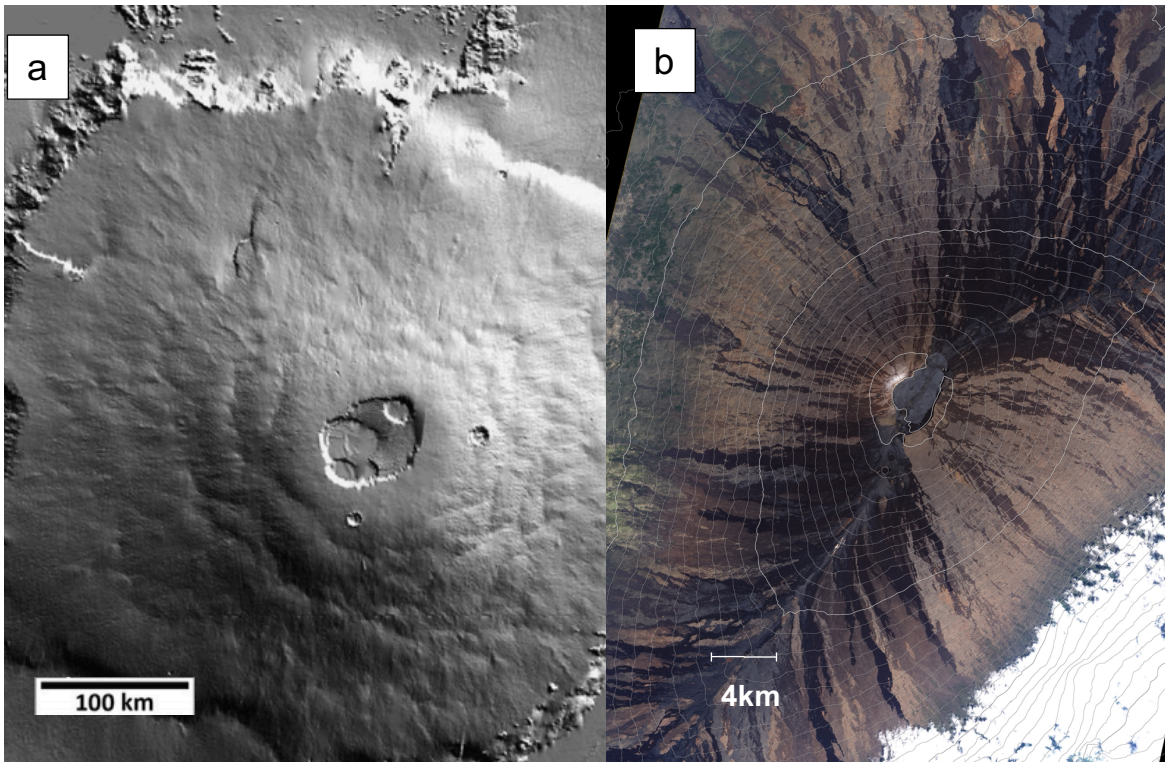

Figure 19 - a) Aerial image of Olympus Mons, Tharsis, b) Aerial image of the Mauna Loa, Hawaii (Source: Zimbelman et al., 2015; Nasa Earth Observatory, 2006 respectively)

Landforms on the Martian surface have been likened to those on Earth, just at a larger scale. Steep sided domes, for example, as well as highland paterae (the only evidence for explosive volcanic activity on Mars, exhibited in the form of low

relief and very shallow sloped volcanoes such as Alba Patera, Zimbelman *et al.,* (2015)) have all also been identified on Mars (Platz *et al.,* 2014). Large shield volcanoes on Mars such as Olympus Mons, (reaching a diameter of 500km, Figure 19a, and baring similar morphology to the likes of the Mauna Loa in Hawaii (Figure 19b)) occur at a much larger scale to shield volcanoes on Earth (Zimbelman *et al.*, 2015). Summit calderas are also present on some large shield volcanoes on Mars, such as Olympus Mons, Elysium Mons and the three Tharsis Montes in the Tharsis region (Zimbelman *et al.*, 2015). Elysium Mons is also an example of conical volcanoes on Mars similar to those seen on Earth. In addition to these volcanoes, extensive volcanic plains have been observed on the Martian surface, and are inferred to represent effusive emplacement of lava flows on Mars in the Late-Amazonian. Martian imagery since the Viking-era of Mars missions have identified low shield volcanoes and fissures as potential sources for some of these volcanic plains (Zimbelman *et al.,* 2015).

3.0. Methodology

3.1. Sample Acquisition

For the acquisition of terrestrial samples for this study, it is important that the samples chosen were analogous in geological setting for both Lunar and Martian basalts. For this to be the case, those selected must be of intraplate tectonic origin (deriving from flood basalt volcanism and/or mantle plume association). This is due to the lack of plate tectonics present on both of these planetary bodies (Knapmeyer-Endrun & Kawamura, 2020). As a result, four terrestrial samples

have been chosen, with two being from Kilauea (Hawaii). The first Hawaiian sample was collected in 2013 (Hawaii 2), with the other being a fresher sample collected in 2017 (Hawaii 1). Both Hawaiian samples were collected on the flanks of Kilauea by Dave Frank from the University of Hawaii. A sample from New Mexico (America) has been acquired, taken off of Route 54, 79 miles from the White Sands Monument and thought to be associated with the Sierra Madre Occidental igneous province. New Mexico was collected by Dr Natasha Stephen, and belongs to the University of Plymouth. Finally, a sample belonging to the European Space Agency's analogue collection, retrieved from Craig's Quarry within County Antrim, Northern Ireland, has been selected.

For Lunar samples, this project has focused on the identification and subsequent use of basaltic clasts within a Lunar Mare breccia (NWA3160) owing to the limited availability of loan Apollo or Luna basalts at this time. This Lunar Mare breccia was acquired from the University of Plymouth's meteorite collection due to their similarity to the Lunar Mare. A more plagioclase-rich impact melt breccia (NWA11444) was also analysed to identify any basaltic clasts that could be compared to terrestrial analogues. Feldspathic breccias were not used due to their larger similarity to the Lunar Highlands (Jones, 2003).

Finally, the Martian meteorites acquired for analysis were also from the University of Plymouth's meteorite collection. Shergottite meteorites were specifically chosen for this study due to the cumulate nature of Nahklites and Chassignites making them less alike basaltic rocks on Earth (Ruzicka *et al.,* 2000). Additionally, of the three Shergottite meteorites chosen, two were olivine-phyric (due to their similarity to extrusive basalts on Earth (Howarth *et al.,* 2014; Filiberto, 2008;

Filiberto *et al.,* 2018)), with the remaining sample being cumulate in texture (selected for comparison). Meteorite samples, particularly from Mars, were chosen preferentially to surface data (collected from rovers and satellite imagery), as they have been found to differ slightly to observations of the immediate Martian surface studied by satellites and rovers (for example, the identification of andesite that has since been determined as weathered basalt, discussed in Chapter 2.3). As a result, these meteorites may be more likely to appear at larger quantities on these planetary bodies, and therefore, provide better insight into the analogue requirements for testing of *in situ* utilisation (discussed further in Chapter 5.4). In total, nine samples were chosen (all of which can be seen in Table 1).

To provide further geochemical comparisons to terrestrial and Lunar basalts, openly accessible data from four literature sources has been used, Table 1. For terrestrial samples, bulk geochemistry data from both the DVP and the CRFB has been utilised owing to lack of sample availability for these provinces. Additionally, openly accessible data from the literature has been sourced for Apollo Lunar samples (Lofgren & Lofgren, 1981), including bulk geochemistry data for high-Ti Lunar basalts from Apollo 11 and 17 (as high-Ti basalts are only accessible on Earth in the form of basaltic fragments in feldspathic/ feldspathic-mare meteorites (Xue *et al.,* 2019)). Data for the remaining Apollo missions (3-4 samples from each mission) has also been utilised to compare bulk geochemistry for low-Ti basalts that are less brecciated.

Samples Used for Analysis

Planetary Body	Sample	Location
Earth	Hawaii 1	Kilauea Basalt (2013)
	Hawaii 2	Kilauea Basalt (2017)
	ESA01-A	County Antrim, Northern Ireland
	New Mexico	New Mexico, Sierra Madre Occidental
Mars	NWA7397	*Meteorite*
	NWA1110	*Meteorite*
	Tissint	*Meteorite*
Moon	NWA3160	*Meteorite*
	NWA11444	*Meteorite*
Supplementary Data	Author(s)	Location
	Basu *et al.,* 2020	Deccan Traps
	Lofgren & Lofgren, 1981	Apollo 11, 12, 14, 15, 16 and 17 data
	Hooper & Hawkesworth, 1993	Columbia River Flood Basalt Province
	Sano *et al*., 2001	Deccan Traps

Table 1 - A table of all samples collected and analysed at the University of Plymouth, as well as the literature data utilised in this project

Figure 20 - a) Sample photo for Hawaii 1, b) Sample photo for Hawaii 2, c) Sample photo for ESA01-A, d) Sample photo for New Mexico, e) Sample photo for NWA7397 (Source: Stoeckli, 2013), f) Sample photo for NWA1110 (Source: Armstrong, 2010), g) Sample photo for Tissint (Source: Auricular, 2012), h) Sample photo for NWA 3160 (Source: Edwards, 2007), i) Sample photo for NWA11444

3.2. Sample Preparation

Once samples were acquired, sample preparation was carried out to ensure that all samples selected were ready for SEM analysis. The sample preparation process can be seen below (Figure 21). This work flow is described in more detail within the following section.

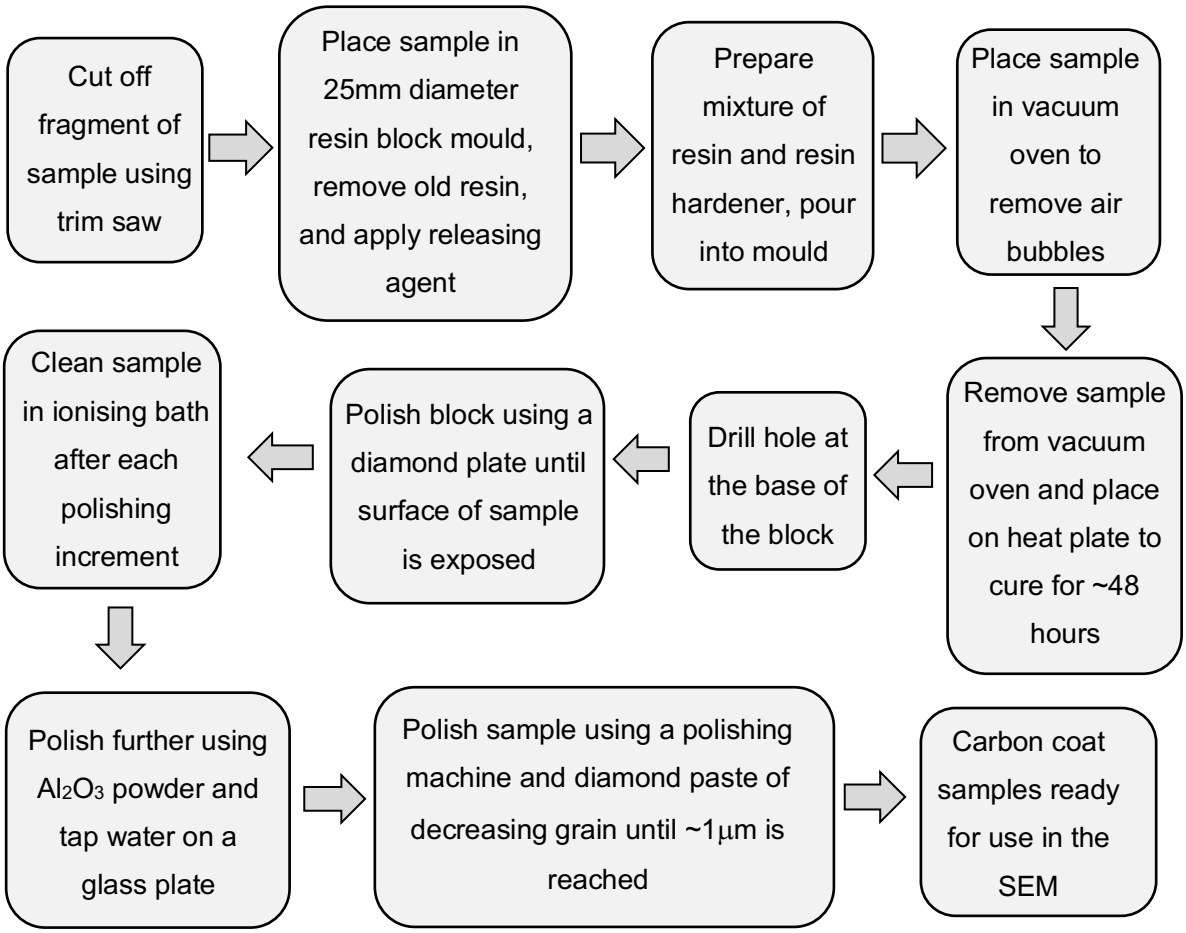

Figure 21 - Flow chart displaying the process of sample preparation used for this project

On samples Hawaii 1, Hawaii 2, New Mexico, and NWA11444 sample preparation involved mounting and polishing fragments in resin blocks for SEM analysis. Fragments of terrestrial samples were cut using a trim saw, before being placed in 25mm resin block moulds. The mould was prepared by removing excess resin from previous use, and wiping a releasing agent around the lid and body of the mould to ensure easier removal once the resin had cured. A mixture of EPO FLO resin and resin hardener was created at a ratio of 3.3:1, and poured over the sample into the mould. The mould was placed inside a vacuum oven to remove any air bubbles. When removal of air bubbles began to slow (~10 minutes in the vacuum oven), the sample was then removed and left on a hotplate to cure for ~48 hours. Once cured, the resin block was polished, starting by polishing in circular motions onto a diamond plate of ~12μm grain. This process was then repeated using a combination of Al_2O_3 powder (9μm grain) and tap water onto a glass plate. The samples were then rinsed and washed in an ionising bath before being polished using polishing machines that required diamond paste and diamond lubricant, polishing at increments 6μm, 3μm and 1μm respectively. Between each machine the sample was washed in the ionising bath. After each sample was prepared, the polished blocks were carbon coated. To do this, the samples were placed in a Quorum Q150T Coating System and underwent carbon coating using a current of 50 Amps, producing a 10 nm layer carbon coat.

3.3. Data Acquisition

Petrological and geochemical observations of major elements on each sample were made using a JEOL-7001 field emission SEM equipped with Oxford

Instruments AZtec software and an X-Max 50mm^2 EDS detector. The analyses were done at Plymouth Electron Microscopy Centre, located at the University of Plymouth (UK). Before being loaded into the SEM, samples were mounted in specimen holders and secured with copper tape, offset distance of the sample was measured using a 30cm ruler. Standard settings for geological analysis were used, however, samples analysed with different settings applied will be specified. The standard settings used were a probe current of 9nA, an acceleration voltage of 20kv, and a working distance of 10mm. Backscattered Electron Images (BEI) were taken at each site. These consisted of one frame images taken at a 1024-pixel resolution, and a 20μs pixel dwell time.

Chemical mapping was carried out on all samples using the EDS detector. These were done at individual sites, as well as Large Area Maps (LAMs) of the whole sample. Most EDS maps produced were using standard settings of 1024-pixel resolution, at an acquisition time of 3 frames. Pixel dwell time remained at 100μs across all maps. An increased resolution and acquisition time, however, was used at higher magnifications (images where varying settings were used will be specified throughout this study). Magnification also varies at different sites across the samples analysed, and this will also be highlighted throughout. When producing LAMs, each sample was analysed under the same settings, at a resolution of 1024 pixels, and an acquisition time of three frames. Magnification of LAMs varied for each sample and is highlighted where required.

3.4. Data Processing and Presentation

SEM data was processed using Oxford Instrument's AZtec software. This software allowed identification of minerals by their chemical compositions retrieved using EDS, and comparisons of compositions across minerals. Once this was completed, the geochemical data for each mineral was normalised, transferred to a Microsoft Excel workbook and put into tables (see Appendix 4, 8 and 9) where calculations of the average and standard deviations of each dataset were made. The error numbers for each of the datasets are the calculated standard deviation results for oxides in each sample. Standard deviations for individual mineral compositions were calculated where n=>7, with all data in Appendices 4, 8 and 9 being included. For bulk geochemistry, standard deviations were carried out where n=3, with spectra collected from a whole LAM being utilised alongside sites of representative texture and mineral abundances. For Lunar samples, the brecciated nature meant minimal sites were representative of the whole rock, therefore only the LAM was used for bulk geochemistry values.

Data plots were then created to present the data collected. The pyroxene quadrilateral plots (see Appendix 1-3), and plagioclase triangular plots (see Appendix 5-7) created for this study were produced using the openly accessible 'Tri-Plot Excel Spreadsheet' by Graham & Midgely, (2000). For the plagioclase plots, anorthite, albite and orthoclase percentages were calculated using the Gabbrosoft (2011) mineral calculator. Both plots were then drawn up on Adobe

Illustrator, with Libbey & Williams-Jones (2016) being used for reference for the plagioclase triangular plots.

4.0. Results

The following section discusses the results collected for each of the samples analysed, beginning with the terrestrial samples. Both petrological and geochemical observations will be highlighted, with the process being repeated for the Martian and Lunar samples. These results will then be discussed further in section 5.0.

4.1. Terrestrial Samples

4.1.1. Hawaii 1

Hawaii 1 displays a vesicular, porphyritic texture of olivine and plagioclase, within a very fine-grained groundmass consisting of both plagioclase and pyroxene (Figure 22a). Some vesicles were infilled, displaying a similar composition to the groundmass. There are three distinguishable mineral phases present (with abundances estimated visually for all samples). Abundances were as follows: plagioclase – 20% abundance, pyroxene – 8% abundance and olivine – 6% abundance – with the remaining 66% comprising of groundmass). No accessory minerals were detected. When plotted on a TAS diagram, the bulk geochemistry of Hawaii 1 is representative of a ‘Basalt’ (Figure 23), comprising of 50.56 $\pm$ 0.36

wt% SiO_2, 2.42 ± 0.07 wt% Na_2O and 0.43 ± 0.01 wt% K_2O. Additionally, a Mg# of 48.00 indicates that Hawaii 1 is an evolved basalt.

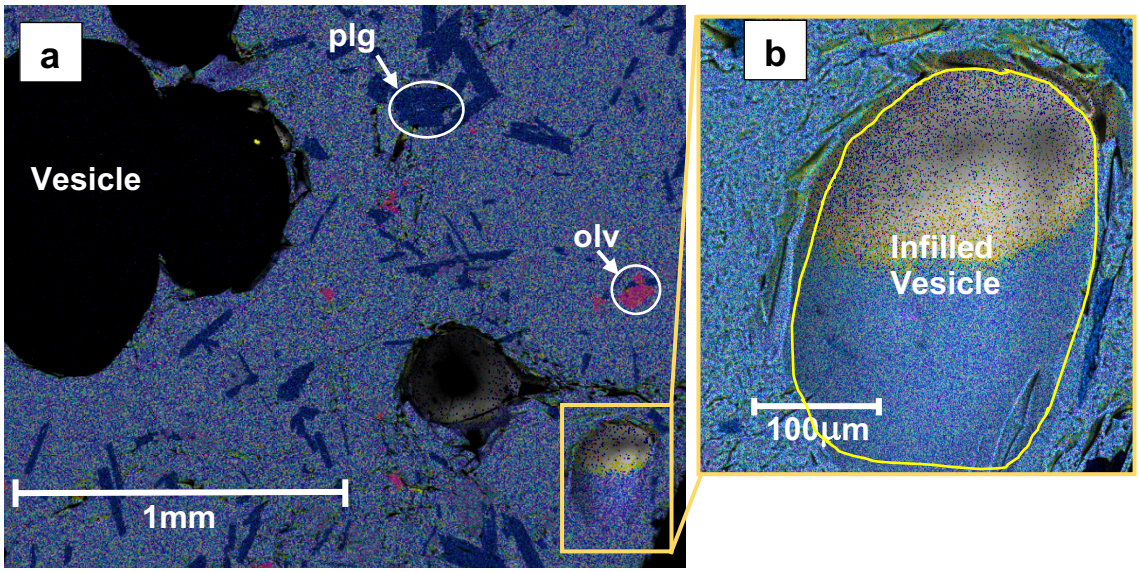

Figure 22 - a) Representative EDS image of Hawaii 1 taken at 43x magnification, displaying a porphyritic texture with plagioclase ('plg') and olivine ('olv') phenocrysts surrounded by groundmass, b) EDS image (taken at 220x magnification) of an infilled vesicle showing the same composition as the surrounding groundmass. Both images share the following key: Yellow = Iron, Teal = Calcium, Navy Blue = Aluminium, Pink = Magnesium, Green = Sodium

Within Hawaii 1, plagioclase is present as laths, as well as in the groundmass, with grain sizes across Hawaii 1 (alongside all samples analysed in this study) displayed in Table 4. Geochemically, plagioclase ranged from An_{53-79} (Appendix 5a & 8a). Plagioclase phenocrysts don't display any zoning.

Across Hawaii 1, pyroxene is present as subhedral-anhedral micro-phenocrysts, as well as within the groundmass. Geochemically, all pyroxenes in Hawaii 1 are Ca-rich and have been identified as augite, with compositions ranging from $Wo_{36-43}En_{34-42}Fs_{18-24}$ (Appendix 1a & 4a). These also displayed no zoning. Finally,

olivine within Hawaii 1 was scarce, only occurring as subhedral phenocrysts, with compositions ranging from $Fo_{67-77}Fa_{23-33}$.

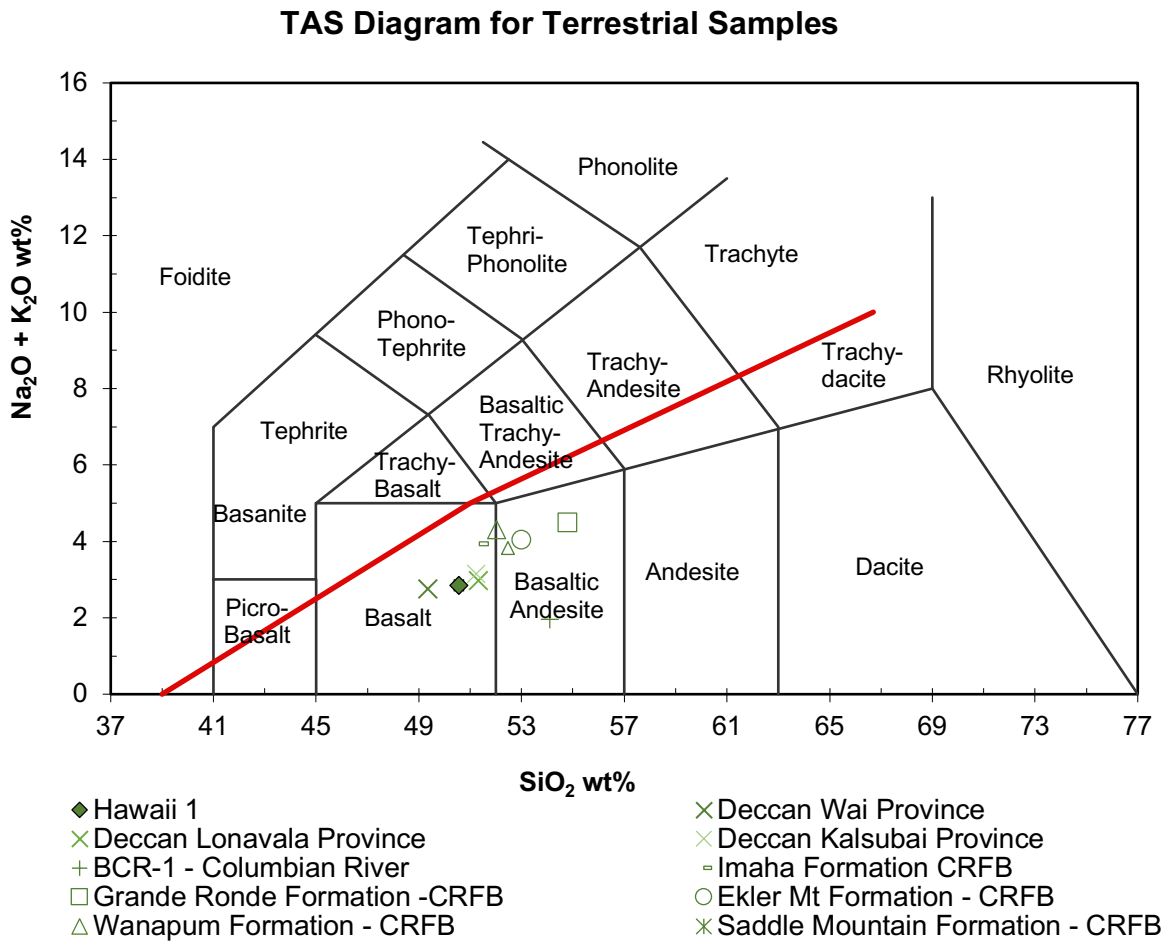

Figure 23 - TAS diagram displaying the representative rock type for Hawaii 1 as 'Basalt' when comparing SiO_2 wt% against Na_2O + K_2O wt%. Key: Green = Terrestrial sample. Bulk geochemical data for DVP and CRFB are also plotted for comparison (Source: Basu et al., 2020 & Hooper & Hawkesworth, 1993 respectively)

4.1.2. Hawaii 2

Similar to Hawaii 1, Hawaii 2 has a vesicular, porphyritic texture of olivine and plagioclase phenocrysts, Figure 24a. There are no infilled vesicles in Hawaii 1. It

also contains a very fine-grained groundmass predominantly composed of plagioclase and pyroxene. Additionally, the groundmass of Hawaii 2 displays a Type 1-a symplectic texture of andesine and orthopyroxene at high magnifications (2500x), (Figure 24b). There are four mineral phases present within this sample (with estimated abundances as follows: plagioclase – 60%, olivine – 13%, and spinel – 2%, with the remaining 25% consisting of groundmass – including the pyroxene mineral phase). When plotted on a TAS diagram, the bulk geochemistry of Hawaii 2 is representative of a 'Trachy-Basalt' (Graph 25), with a composition of 51.36 ± 0.28 wt% SiO_2, 4.03 ± 0.13 wt% Na_2O and 1.25 ± 0.16 wt% K_2O. Hawaii 2 is also representative of an evolved basalt, with a Mg# of 45.77.

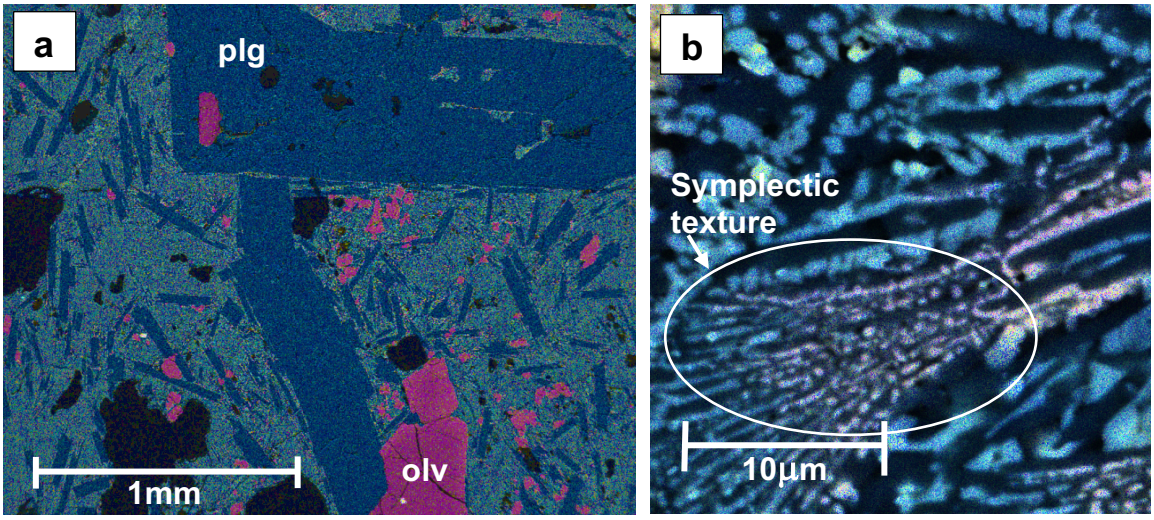

Figure 24 - a) Representative EDS image of Hawaii 2 taken at 40x magnification, displaying a fine grained, porphyritic texture with plagioclase and olivine phenocrysts. b) EDS image of Hawaii 2 groundmass taken at 2500x magnification, displaying a symplectic texture. Both images follow the same key: Yellow = Iron, Teal = Calcium, Navy Blue = Aluminium, Pink = Magnesium, Green = Sodium

Similar to Hawaii 1, Plagioclase in Hawaii 2 is also present as laths, although they are much larger in Hawaii 2 (see Table 4). These plagioclase phenocrysts display no zoning, but are encompassed by reaction rims of pigeonite composition. Geochemically, plagioclase across ranges from An_{50-68} (Appendix 5b & 8b).

Olivine also appears as euhedral-subhedral phenocrysts in Hawaii 2, with occasional larger phenocrysts (up to 723μm) resulting in a large variation in grain sizes (Table 4). The larger phenocrysts display weak zoning of increasing FeO towards the rims. Geochemically, Fo-rich olivine is dominant across the sample with compositions ranging across $Fo_{44-67}Fa_{33-56}$. When weakly zoned, some olivine phenocrysts become more Fa-rich towards the rims. Finally, chromite is present in Hawaii 2 displaying grains that are euhedral in shape.

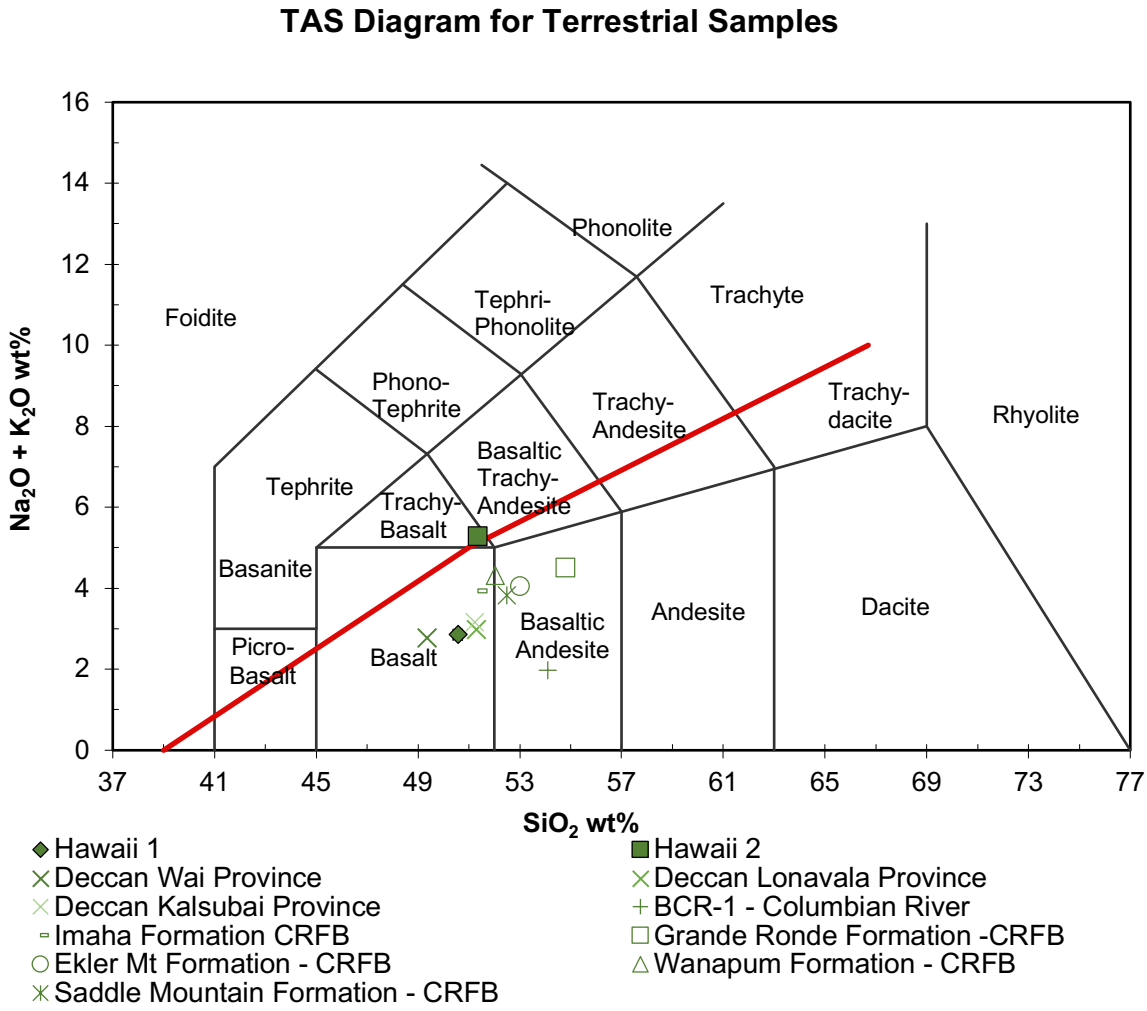

Figure 25 - TAS diagram displaying the representative rock type for Hawaii 1 as 'Basalt' and Hawaii 2 as 'Trachy-Basalt', when comparing SiO_2 wt% against Na_2O + K_2O wt%. Key: Green = Terrestrial sample, error bars are smaller than some points. Bulk geochemical data for DVP and CRFB are also plotted for comparison (Basu et al., 2020 & Hooper & Hawkesworth, 1993)

4.1.3. ESA01-A

ESA01-A is a fine-grained basalt that is non-vesicular, and is mostly aphyric in texture with occasional olivine micro-phenocrysts reaching maximum grain sizes of ~250μm (Figure 26a). A subophitic texture is displayed between plagioclase

and pyroxene phases, with plagioclase encompassing pyroxene across the sample (Figure 26a). Grain sizes for all samples analysed are displayed in Table 4. There are five mineral phases observed within this sample (with estimated abundances as follows: plagioclase – 60%, olivine – 15%, pyroxene – 15%, spinel – 8% and apatite – 2%). When plotted on a TAS diagram, ESA01-A is found to have a bulk geochemistry representative of a 'Basalt' (Figure 27), with a composition of 47.44 ± 0.69 wt% SiO_2, 3.39 ± 0.16 wt% Na_2O and K_2O below detection limit (BDL). The sample is also representative of an evolved basalt, comprising of a Mg# of 49.23.

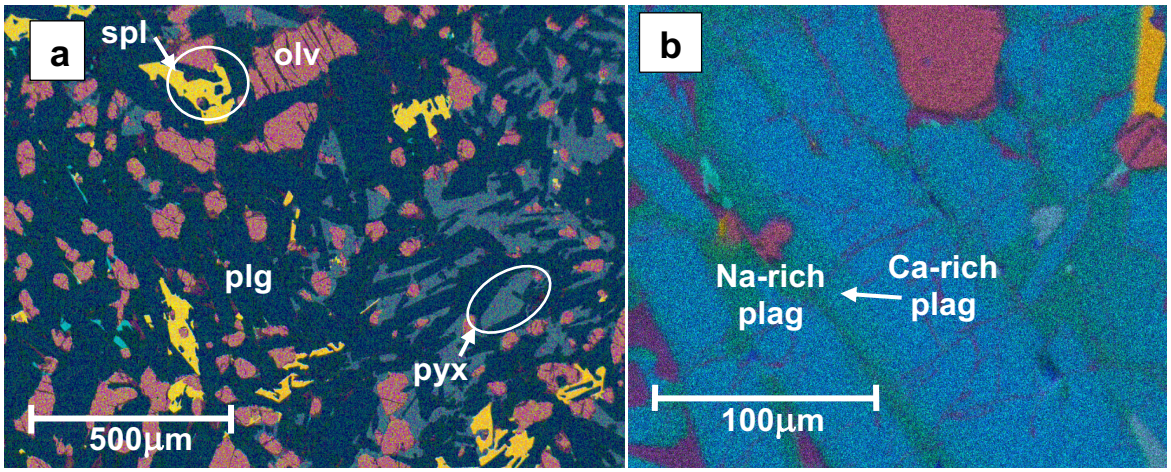

Figure 26 - a) EDS image of ESA01-A taken at 75x magnification displaying an overall aphyric texture and a euhedral texture of the spinel mineral phase (spl). Also present is a subophitic texture between both plg and pyx across the sample, b) EDS image taken at 350x magnification, displaying zoning within plagioclase. Plagioclase displays a dominantly calcic composition becoming more sodic towards the rims. Both Figures have the same key, where Yellow = Iron, Orange = Titanium, Teal = Calcium, Navy Blue = Aluminium, Pink = Magnesium and Green = Sodium

Plagioclase across ESA01-A is present as laths, displaying an intercumulus sub ophitic texture. These are also strongly zoned (visible in both BEI and EDS images, Figure 26b), becoming more sodic towards the rims. Geochemically, plagioclase compositions range from $An_{16\text{-}100}Ab_{BDL\text{-}79}Or_{BDL\text{-}16}$ across the sample. The range in plagioclase compositions can be seen in Appendix 5c & 8c.

Pyroxene is anhedral and of an intercumulus nature. Zoning is not visible within these grains. Geochemically, pyroxenes are Ca-rich, with all pyroxenes being identified as diopside ($Wo_{47\text{-}50}Ens_{26\text{-}31}Fs_{21\text{-}26}$), (Appendix 1b & 4b). Zoning is also absent in olivine across ESA01-A. Olivine is euhedral-subhedral shape and is Fa-rich, ranging from $Fo_{32\text{-}44}Fa_{56\text{-}68}$. Finally, the spinel mineral phase is present as ilmenite, with inclusions of olivine, pyroxene and plagioclase occurring within ilmenite grains. Spinel grains are euhedral and intercumulus in nature, moulding around plagioclase laths (Figure 26a), and occasional displaying diffuse grain boundaries.

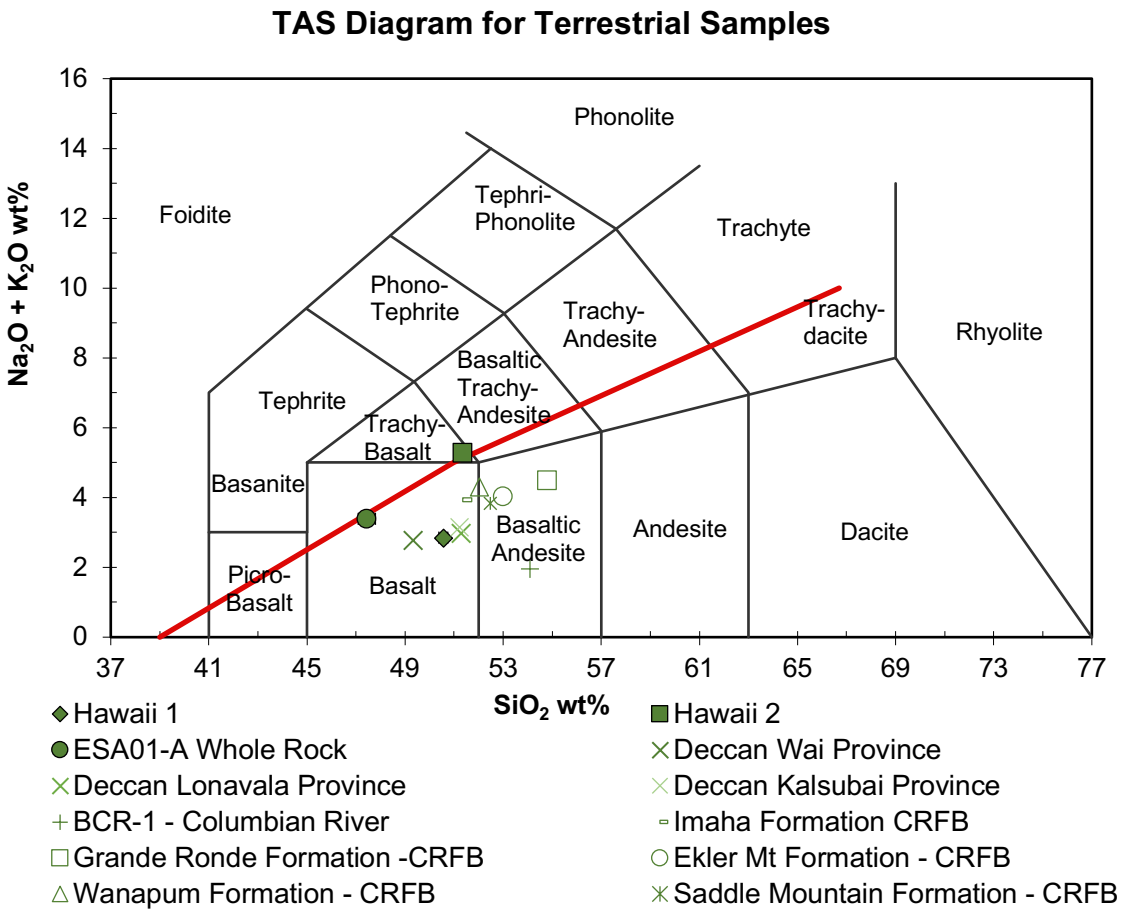

Figure 27 - TAS diagram displaying the representative rock type for Hawaii 1 as 'Basalt', Hawaii 2 as ''Trachy-Basalt' and ESA01-A as 'Basalt', when comparing SiO_2 wt% against $Na_2O + K_2O$ wt%. Key: Green = Terrestrial sample, error bars are smaller than some points. Bulk geochemical data for DVP and CRFB are also plotted for comparison (Source: Basu et al., 2020 & Hooper & Hawkesworth, 1993 respectively)

4.1.4. New Mexico

New Mexico is a fine-grained, vesicular sample, displaying a porphyritic texture of both macro- and micro- phenocrysts of olivine (Figure 28a). There are three dominant mineral phases present within this sample (with estimated abundances as follows: plagioclase – 30%, olivine – 20% and spinel – 10%). The remaining

40% is comprised of a spinifex groundmass, where pyroxene is present as platy crystals alongside plagioclase. Pyroxene is also present within the groundmass and as dendritic reaction rims around plagioclase and olivine micro-phenocrysts (Figure 28b). New Mexico is representative of a 'Basaltic-Trachy Andesite' when plotted on a TAS diagram (Figure 29), with an average ~51.72 ± 0.08 wt% SiO_2, ~4.18 ± 0.07 wt% Na_2O and ~1.36 ± 0.07 wt% K_2O. A Mg# of 40.72 also means the sample is representative of an evolved basalt.

Plagioclase is present as laths across the sample, but also as laths within a spinifex groundmass. Geochemically, plagioclase range from An_{43-65} across the sample, with no zoning visible. A broad range of pyroxene compositions are present in the groundmass relative to the previous terrestrial samples, ranging from $Wo_{2-47}En_{3-38}Fs_{41-92}$. (Appendix 1c & 4c).

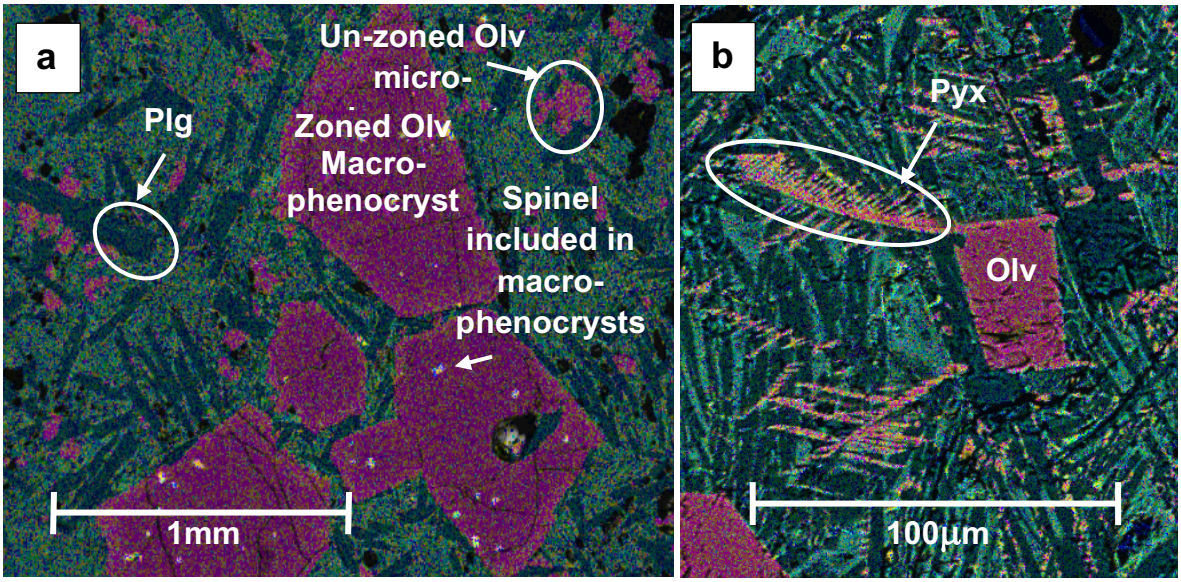

Figure 28 - a) EDS image taken at 40x magnification, displaying the porphyritic nature of New Mexico with macro-phenocrysts of olivine and surrounding micro-phenocrysts of both olivine and plagioclase. b) EDS image (taken at 350x magnification) of dendritic pigeonite in the groundmass. Key: Yellow = Iron,

Orange = *Titanium*, *Teal* = *Calcium*, *Navy Blue* = *Aluminium*, *Pink* = *Magnesium* and *Green* = *Sodium*

Olivine, on the other hand, comprises both micro- and macro-phenocrysts across this sample. Normal zoning occurs within the olivine macro-phenocrysts, displaying Fo-rich centres ($Fo_{60-69}Fa_{31-40}$) that progressively become more Fa-rich towards the rims ($Fo_{56-67}Fa_{33-44}$), (Figure 30 and 31). No zoning is present within the micro-phenocrysts, with their compositions more representative of the Fa-rich rims seen within the macro-phenocrysts ($Fo_{55-63}Fa_{37-45}$), (a comparison of MgO wt% vs FeO wt% across both micro- and macro-phenocrysts can be seen in Figure 32). Spinel occurs as both chromite and magnetite within the sample and are typically euhedral-subhedral in shape, with chromite often included within the olivine macro-phenocrysts.

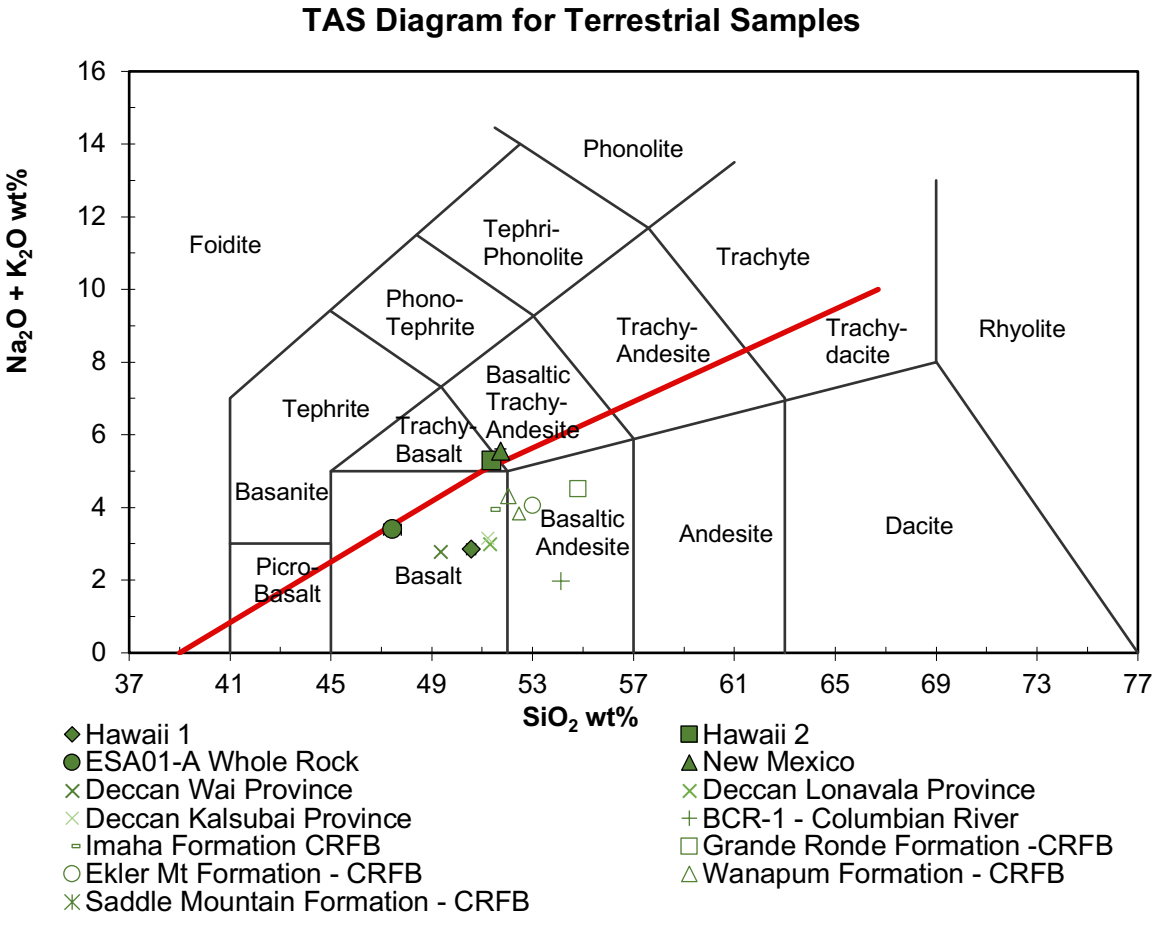

Figure 29 - TAS diagram displaying the representative rock type for Hawaii 1 as 'Basalt', Hawaii 2 as 'Trachy-Basalt', ESA01-A as 'Basalt', and New Mexico as a 'Basaltic Tracy-Andesite' when comparing SiO_2 wt% against Na_2O + K_2O wt%. Key: Green = Terrestrial sample, error bars are smaller than some markers. Bulk geochemical data for DVP and CRFB are also plotted for comparison (Source: Basu et al., 2020 & Hooper & Hawkesworth, 1993 respectively)

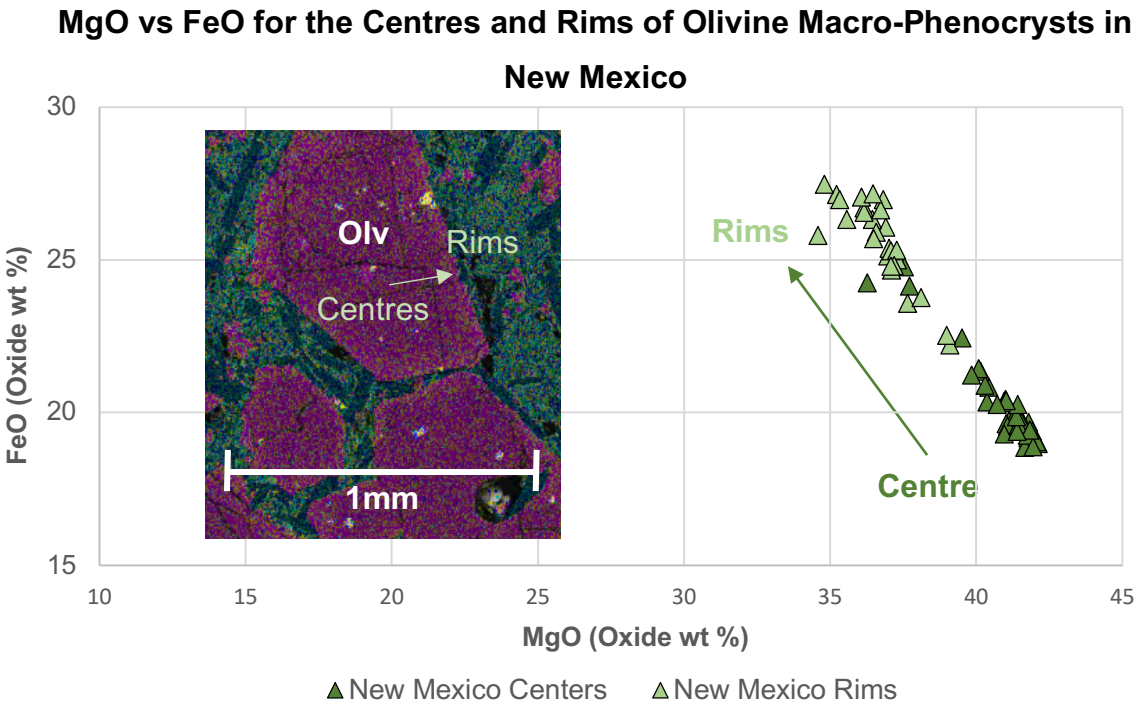

Figure 30 - (Left), EDS image taken at 40x magnification, displaying an example of the zoned macro-phenocrysts of olivine in New Mexico. Figure 31 - (Right), Harker diagram comparing MgO wt% vs FeO wt% for both the centres and the rims of olivine macro-phenocrysts in New Mexico. The graph shows a linear trend of decreasing MgO content towards the rims of the olivine macro-phenocrysts, where the concentration of FeO from between 18.86-24.87 ± 3.12 wt% FeO in

the olivine centres of macro-phenocrysts to between 22.22-27.16 ± 2.73 wt% FeO at the rims. Key: Green = Terrestrial sample.

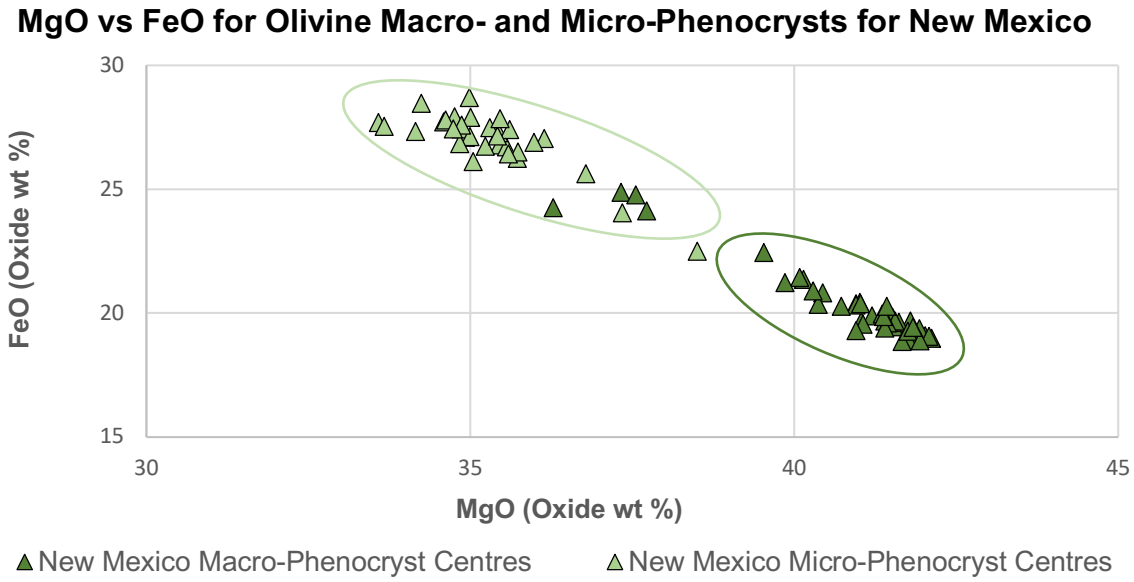

Figure 32 – Harker diagram displaying MgO wt% vs FeO wt% for both olivine macro- and micro-phenocrysts in New Mexico. This graph displays a linear trend, and shows that macro-phenocrysts within this sample are richer in MgO content (36.27-42.11 ± 1.33 wt% MgO) than the surrounding micro-phenocrysts (20.95-38.50 ± 2.67 wt% MgO). Key: Green = Terrestrial sample.

4.2. Lunar Samples

4.2.1. NWA3160

NWA3160 is a Lunar Mare breccia, that comprises of several angular clasts and a variety of textures (see large area map, Figure 33). The sample is mostly fine grained; however, the grain sizes of minerals vary across each clast. There are at least 7 mineral phases present across the whole sample (with estimated abundances as follows: plagioclase – 15%, pyroxene – 50%, olivine – 25%, as

well as minor spinel, carbonate, apatite and pyrrhotite). The sample is heavily fractured, with calcite and apatite often infilling these fractures. Additionally, melt inclusions largely composed of pyroxene and plagioclase are occasionally present in olivine (Figure 33). Comprising of 45.28 wt % SiO_2, 0.29 wt% K_2O and Na_2O below detection limit, the whole rock of NWA3160 plots as a 'Basalt' on a TAS diagram (Figure 34), representing similar bulk compositions to those of the Apollo 16 basalts (Figure 34). Additionally, this sample has a Mg# of 62.02 representing a lesser evolved basalt.

Across NWA3160, plagioclase compositions ranged across $An_{0\text{-}100}$ with Ab and Or present but often below detection limit (Appendix 7a & 8jj, Figure 33). Despite a variation in plagioclase composition, there was no zoning visible within this mineral phase in any clast. Across the sample, pyroxene compositions were mostly representative of either pigeonite and augite, with hedenbergite and enstatite present in smaller amounts (Appendix 3a, 4f & 4g). Compositions ranged across $Wo_{0\text{-}44}En_{BDL\text{-}59}Fs_{26\text{-}98}$ across the sample.

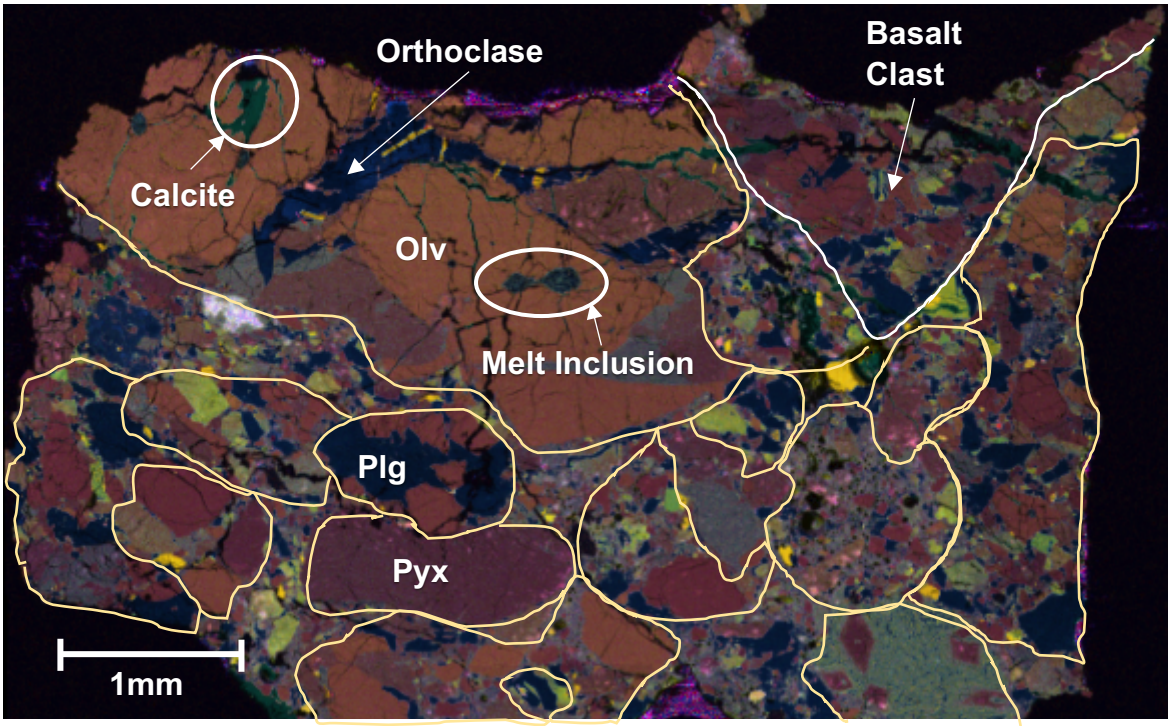

Figure 33 - EDS image taken at 100x magnification, displaying a large area map of NWA3160. This image displays the heavily brecciated nature of this sample, with individual clasts outlined in yellow, and an identified basalt clast highlighted with white. A melt inclusion present within olivine. Calcite, plagioclase and pyroxene are also present within the sample. The image follows the following key: Yellow = Iron, Orange = Titanium, Teal = Calcium, Navy Blue = Aluminium, Pink = Magnesium and Green = Sodium, Red = Phosphorous, Purple = Sulphur

Olivine compositions across the whole rock vary greatly, with some clasts comprising of Fo-rich olivine, whilst others are Fa-rich. Compositions range from $Fo_{36-64}Fa_{36-64}$ across the whole sample. Spinel was mainly present as chromite alongside ilmenite across NWA3160, with both phases occurring as euhedral grains. Pyrrhotite was also present within the sample. Due to the brecciated nature of this sample, it is difficult to compare the whole sample to basalts from Earth. Additionally, the breccia may not be representative (both petrologically or

geochemically) for the Lunar Mare. This is indicated by the bulk geochemistry of NWA3160 being most similar to Apollo 16 basalts (Figure 34), with the Apollo 16 Lunar module landing in central Lunar Highlands (Apollo Field Geology Investigation Team, 1973). As a result, basalt clasts were searched for as, individually, they may be geochemically and petrologically more representative of the Lunar Mare. One basalt clast was identified within NWA3160 (see Figures 33 and 35), and this study will focus on observations for this clast in context for the Lunar Mare.

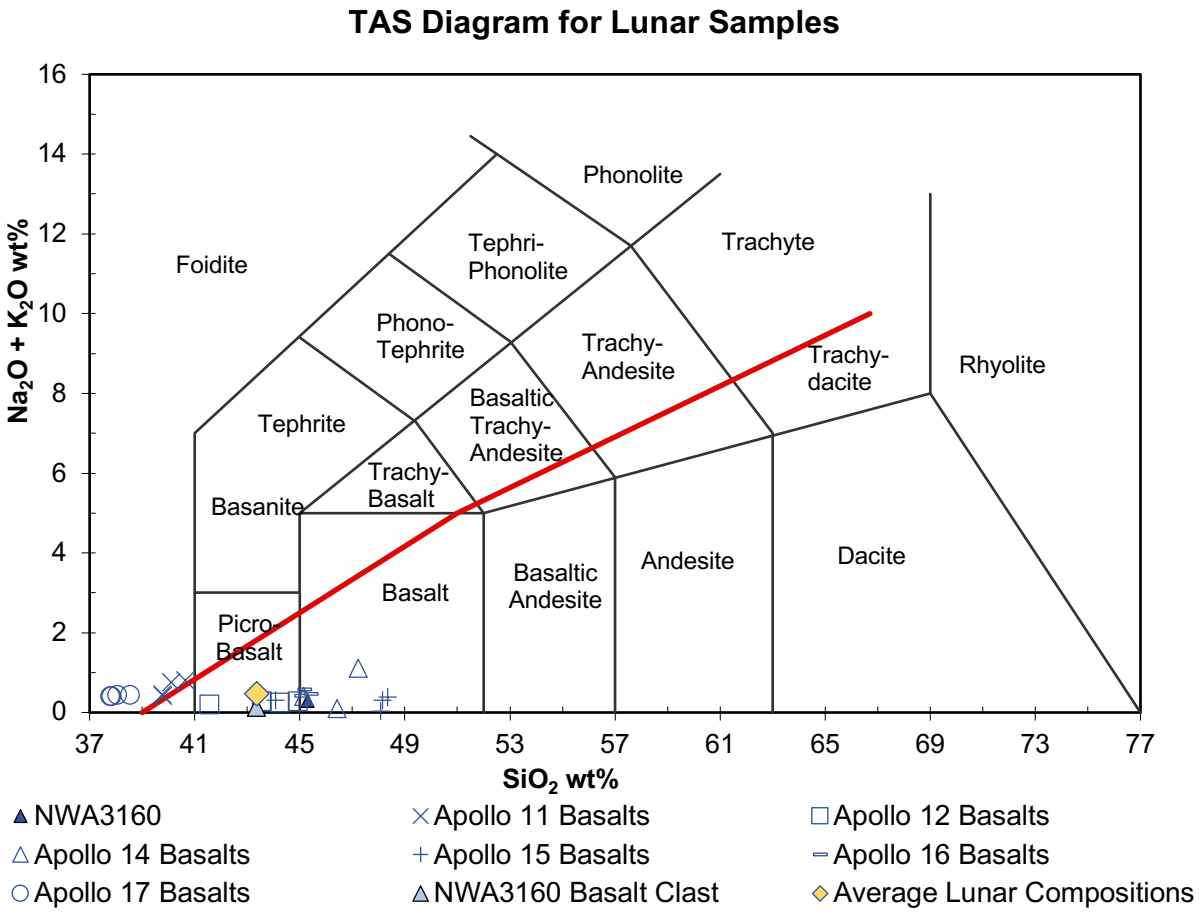

Figure 34 - TAS diagram displaying the representative rock type for NWA3160 (whole sample) as a 'Basalt' and the representative rock type for the basalt clast within NWA3160as a pico-basalt, when comparing SiO_2 wt% against $Na_2O + K_2O$ wt%. Error bars smaller than marker. Key: Blue = Lunar samples. Apollo data for this graph was sourced from Lofgren & Lofgren (1981), with the 'Average Lunar

Compositions' representing the average compositions of Apollo data within this dataset.

Basalt Clast within NWA3160

Across the basalt clast in NWA3160 (Figure 33), olivine and pyroxene are the most dominant minerals, with plagioclase present in low abundances (estimated abundances are 33%, 55% and 10% respectively). Occasional grains of ilmenite and pyrrhotite are also present, comprising the remaining 2% of estimated abundances. Overall, the bulk geochemistry for this basalt clast can be seen in Table 2, with the sample plotting as a pico-basalt on a TAS diagram (Figure 34).

Table of Bulk Geochemical Data for Basalt Clast in NWA3160

Data in Wt% Oxide	SiO_2	MgO	Al_2O_3	K_2O	CaO	FeO	Cr_2O_3	TiO_2	MnO
Basalt Clast	43.33	16.30	9.62	0.14	10.17	19.11	0.42	0.63	0.26

Table 2 - Bulk geochemical data for the basalt clast in NWA3160, with all data in wt% oxide

Unlike the whole sample for NWA3160, the bulk geochemistry of the basalt clast within NWA 3160 compared to average bulk compositions for Apollo 11-17 basalts (Table 3), is most representative of the Apollo 12 basalts (Table 3), with this observation also being made for NWA3160 'basalt' by Ziegler *et al.,* (2006). This interpretation is due to the high FeO content displayed by Apollo 12 samples (averaging at ~21.55 wt% oxide, Table 3), and the clast (19.11 wt% oxide), but also the higher MgO content across the Apollo 12 samples (averaging at ~15.53

wt% oxide, Table 3) and the basaltic clast (~16.30 wt% oxide, Table 2). Additionally, the lack of Na_2O across the bulk geochemistry of this clast may also indicate crystallisation from a plagioclase poor source region (Ziegler *et al.,* 2006).

Table of Bulk Geochemical Data for Lunar Mare Basalts from Apollo Missions

Data in Wt% Oxide	SiO_2	TiO_2	Al_2O_3	FeO	MnO	MgO	CaO	Na_2O	K_2O	P_2O_5	S	Cr_2O_3
Apollo 11	40.07	11.28	9.24	19.39	0.26	7.51	10.95	0.44	0.17	0.14	0.19	0.35
Apollo 12	43.57	2.70	7.28	21.55	0.29	15.53	7.93	0.20	0.05	0.07	0.06	0.81
Apollo 14	46.25	2.15	14.92	14.33	0.21	9.50	11.11	0.48	0.22	0.17	0.09	0.35
Apollo 15	47.16	1.81	9.13	20.24	0.28	9.79	10.03	0.30	0.04	0.07	0.07	0.62
Apollo 16	45.20	0.45	25.81	4.97	0.07	7.91	14.85	0.41	0.08	0.10	0.04	0.15
Apollo 17	38.05	13.11	8.57	18.96	0.27	9.47	10.26	0.37	0.06	0.06	0.17	0.52

Table 3 - Bulk geochemical data for samples from Apollo missions 11-17 (data are averages across 4-5 samples from each mission, taken from Lofgren& Lofgren, (1981), Apollo 12 basalts highlighted in yellow.

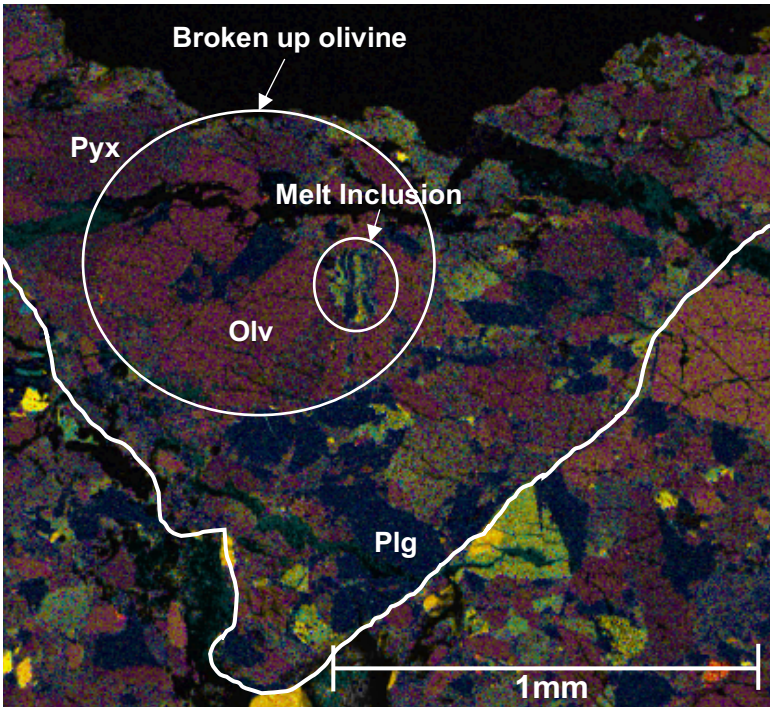

Figure 35 - A higher magnification image (43x magnification) EDS image of the basalt clast in NWA3160, displaying the olivine, pyroxene and plagioclase present within the clast. This is shown alongside a melt inclusion (highlighted by a white circle). The image follows the following key: Yellow = Iron, Orange = Titanium, Teal = Calcium, Navy Blue = Aluminium, Pink = Magnesium and Green = Sodium, Red = Phosphorous, Purple = Sulphur

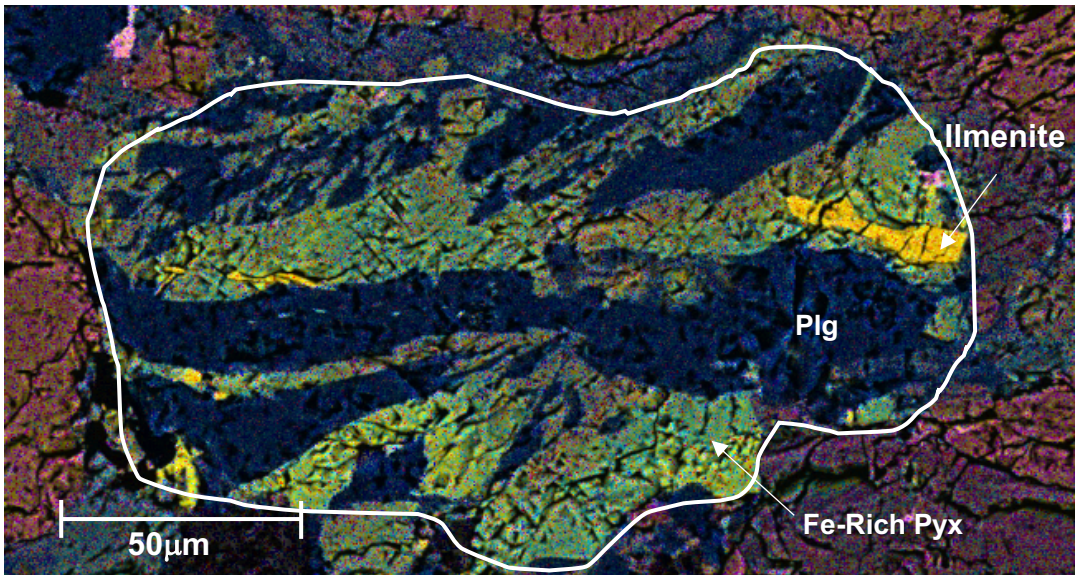

Figure 36 - High magnification (550x magnification) image of the melt inclusion present in olivine within the basalt clast

The basaltic clast is fine grained in nature, with olivine that appears as phenocrysts and within the groundmass, exhibiting varying grain sizes (Table 4). Olivine is anhedral in shape and displays no zoning. Across the clast, olivine is predominantly Fo-rich in composition (ranging between $Fo_{38-60}Fa_{40-62}$). Within one of the olivine grains is a rounded, crystalline melt inclusion (Figure 36), dominated by Ca-rich plagioclase (anorthite) and Fe-rich pyroxene (averaging at $Ens_{11}Wo_{19}Fs_{70}$ across the inclusion (Figure 37)). A single, euhedral grain of ilmenite is also present within this inclusion. Due to the Ca-rich and Fe-rich nature of this melt inclusion, it has been inferred that it is comprised of trapped residual melt rich in Ca and Fe. This melt is inferred to have been trapped within the lava flow, with its crystallised nature indicating slow cooling (Chen *et al.,* 2019).

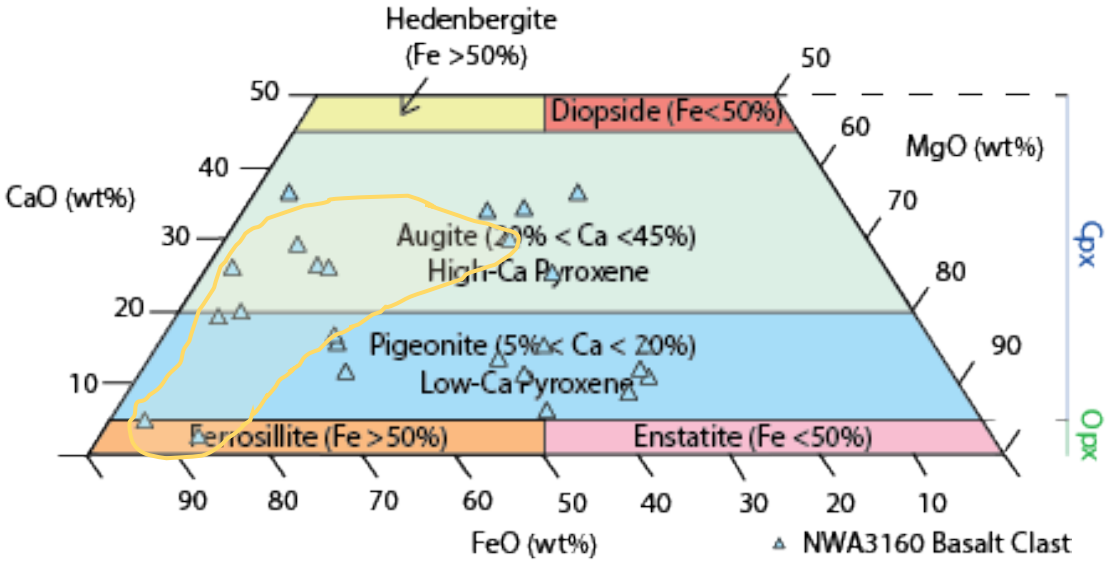

Figure 37 - Quadrilateral plot displaying the varying pyroxene compositions across the basalt clast in NWA3160. Compositions within the melt inclusion have been highlighted in yellow. Further data for these compositions can be seen in Appendix 4h

Additionally, pyroxene occurs sub-anhedrally across the basaltic clast at grain sizes similar to olivine (Table 4). Pyroxene compositions vary largely ($Wo_{0-56}Ens_{2-43}Fs_{17-92}$, see further in Figure 37), consisting of Fe/Mg-rich and Ca-poor compositions (mainly pigeonite with occasionally orthopyroxene present), as well as Fe/Ca-rich and Mg-poor compositions (augite). The varying pyroxene compositions are present as distinct pyroxene grains similar to what is observed in NWA7397 (Chapter 5.2), and are not as a result of zoning. Plagioclase across the clast displays anorthite compositions, similar to the bulk plagioclase compositions of the entire NWA3160 meteorite. Compositions within the clast specifically range from $An_{89-100,}$ Ab is present but below detection limits (Figure 38). Finally, the clast also displays heavy fracturing, specifically across olivine grains, that are likely shock related (Valencia *et al.,* 2019).

In previous studies, NWA3160 has been found to comprise of two distinct lithologies, deemed 'Breccia' and 'Basalt' by Ziegler *et al.,* (2006), (a BSE image of their section of NWA3160 can be seen in Figure 39). When comparing textural observations in the basalt clast found in this study to those discussed in the official classification of NWA3160 and Ziegler *et al.,* (2006), the clast has been found to fit within the 'Breccia' lithology. Due to only a single basaltic clast being identified within this study, whilst geochemical differences between these two lithologies may be minor (Ziegler *et al.,* 2006), the data for this basalt (as well as petrological observations) are limited and may not be representative of the larger scale Lunar Mare basalts. As a result, this sample will not be discussed further in this study.

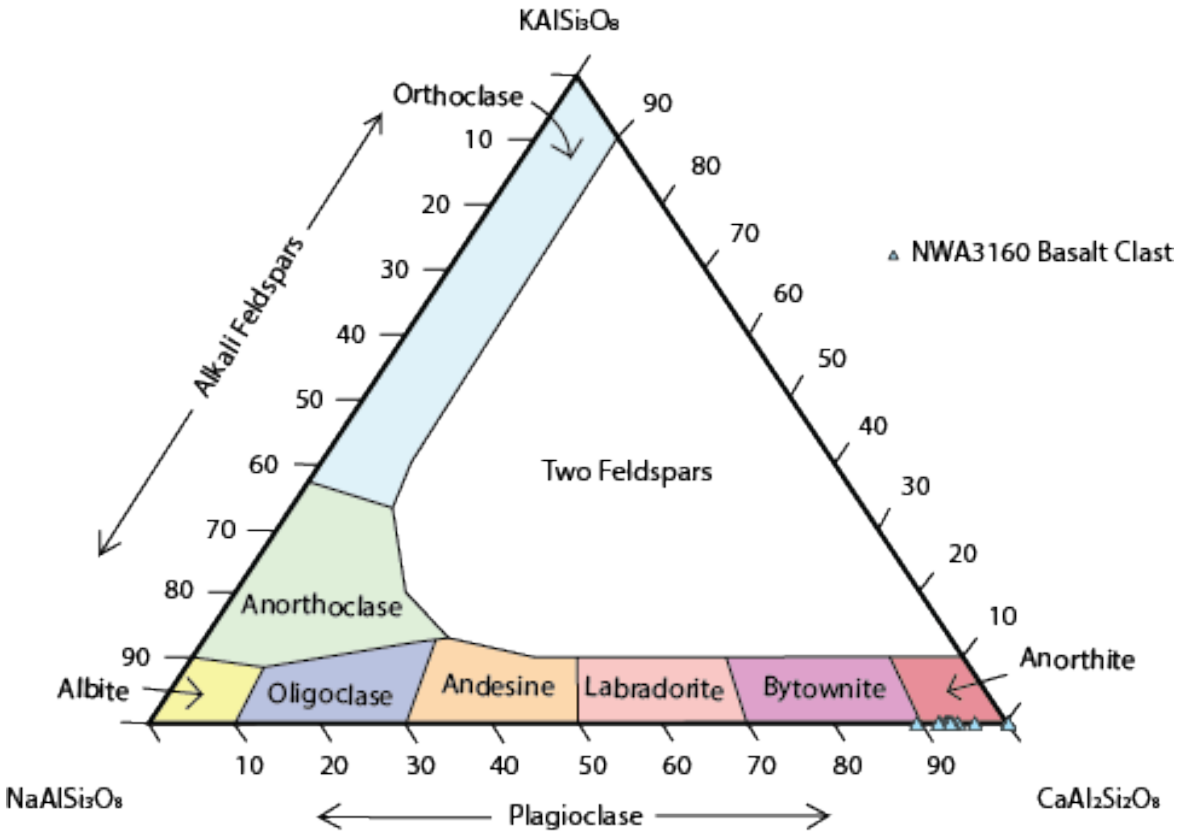

Figure 38 - Triangular plot displaying plagioclase compositions across the basalt clast in NWA3160, further data for these compositions can be seen in Appendix 4k. All data in wt% oxide.

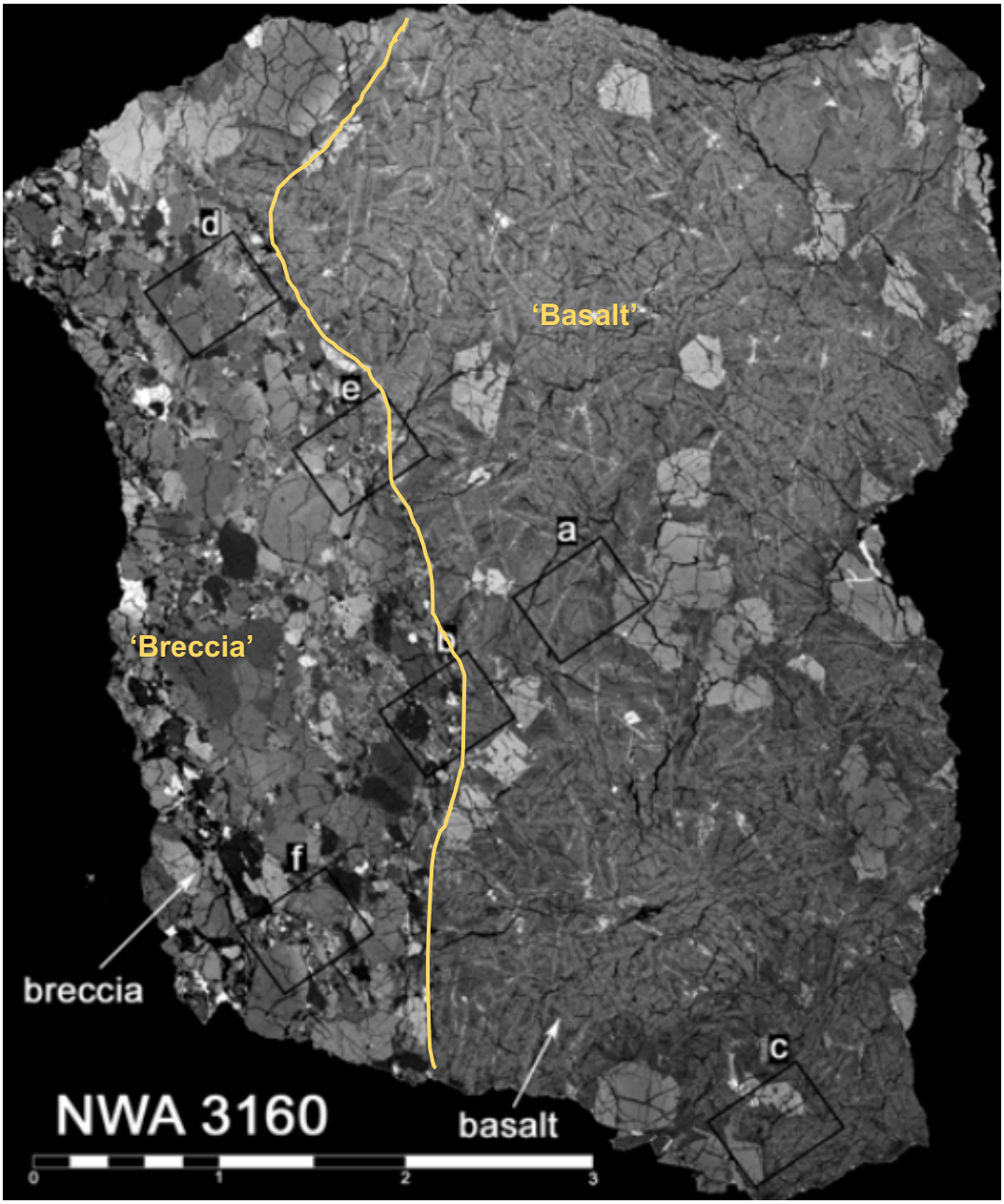

Figure 39 - BSE image displaying the section of NWA3160 studied by Ziegler et al., (2006) displaying the textural variation in both lithologies, scale bar = mm's

4.2.2. NWA11444

NWA11444 is an impact melt breccia, comprising of multiple clasts of varying lithologies. Clast A in particular (Figure 40a), is a noticeably different lithology to the remainder of the sample, and in places is surrounded by a pseudotachylyte (Figure 40b). Aside from Clast A, NWA11444 is very fine-grained, with the groundmass comprised predominantly of plagioclase. Clast A, on the other hand, has a groundmass composed of both pyroxene and olivine. There are 5 main mineral phases present within the sample (with estimated abundances as follows: plagioclase – 70%, pyroxene – 15%, olivine – 10%, spinel and calcite – remaining 5%). Additionally, this sample is fractured, with calcite often infilling these fractures. Comprising of 44.21 wt% SiO_2, 0.31 wt% Na_2O and K_2O below detection limits, NWA11444 plots as a 'Pico-Basalt' on a TAS diagram (Figure 41). Additionally, this sample has a Mg# of 58.00, representing a moderately evolved basalt.

Plagioclase across NWA11444, including Clast A, ranges from $An_{96\text{-}100}Ab_{BDL}Or_{0\text{-}3.7}$ in composition (Appendix 7b & 8l), displaying no zoning or compositional differences across the sample. Additionally, when appearing as phenocrysts, plagioclase is subhedral-euhedral in shape. Pyroxene compositions, on the other hand, vary across clasts within NWA11444. Similar to NWA3160, most pyroxenes within NWA11444 are either augite (Ca-rich, $Wo_{21\text{-}47}En_{14\text{-}42}Fs_{16\text{-}64}$) or pigeonite (Fe/Mg-rich, $Wo_{4\text{-}23}En_{26\text{-}70}Fs_{23\text{-}68}$) in composition (further data can be seen in Appendix 3b, 4i & 4j).

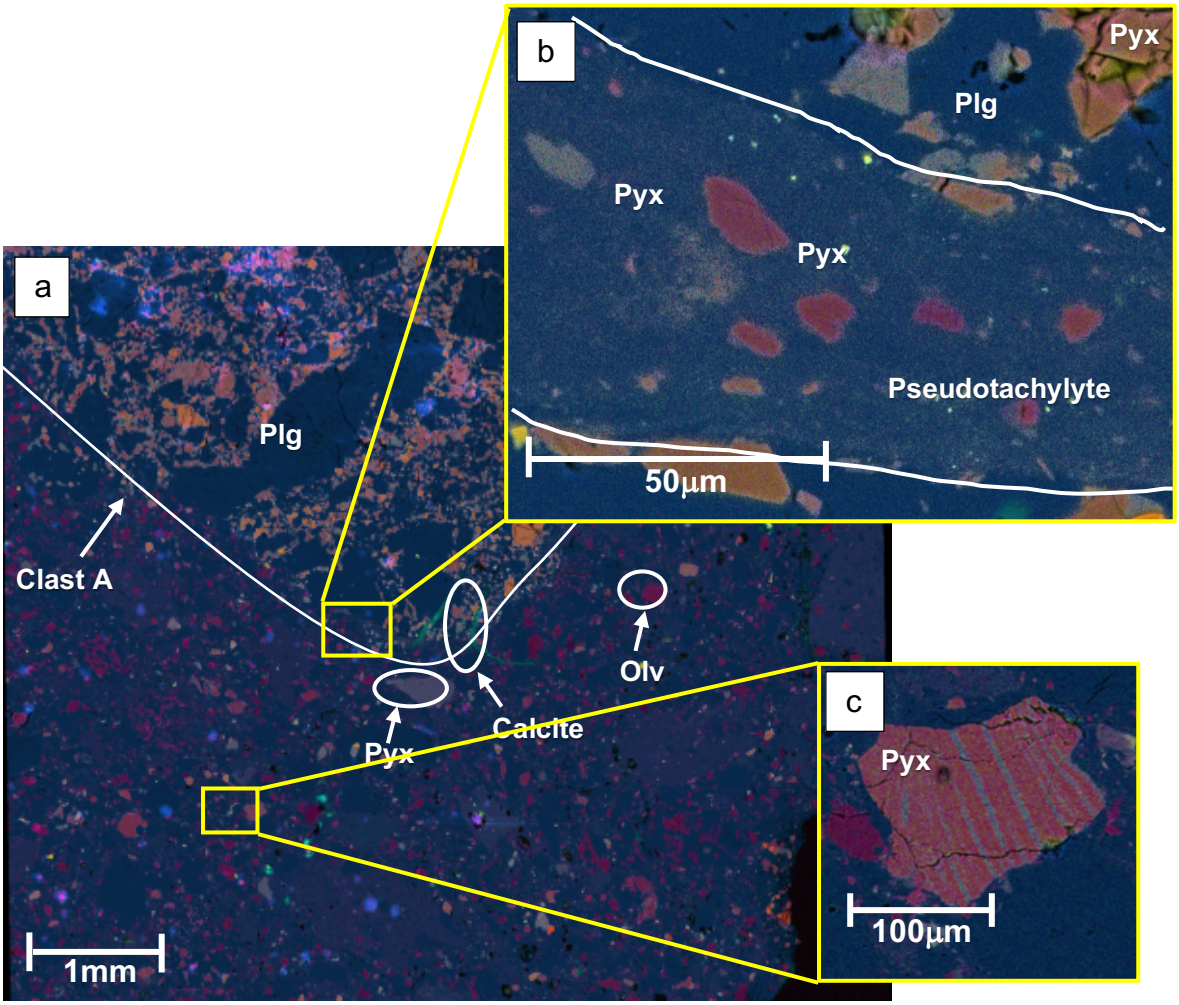

Figure 40 - a) EDS large area map (100x magnification) of NWA11444, displaying Clast A and the overall brecciated nature of the sample. The sample is predominantly plagioclase, alongside the presence of olivine, pyroxene, spinel and calcite filled veins. b) An EDS image taken at a higher magnification (850x) of the pseudotachylyte running close to the boundary of Clast A and the rest of the sample. c) An EDS image taken from the Figure 40a of pyroxene exsolution present in a pyroxene phenocryst within NWA11444. The phenocrysts itself is Fe/Mg-pyroxene, whilst the lamellae produced from this exsolution is more Ca-rich. Figures A, B and C follow the same key: Yellow = Iron, Orange = Titanium, Teal = Calcium, Navy Blue = Aluminium, Pink = Magnesium and Green = Sodium, Red = Phosphorous, Purple = Sulphur

As well as this, some pyroxene phenocrysts display exsolution lamellae (Figure 40c), with the lamellae comprising of Ca-rich pyroxene in comparison to the whole Fe/Mg-rich phenocryst. Compositional zoning is also exhibited within pyroxenes in Clast A, with these grains displaying Fe/Mg-rich centres and Ca-rich rims. Olivine, within Clast A, appears as groundmass material alongside pyroxene, however, outside of Clast A it is present as phenocrysts. Compositions of these olivine crystals also differ greatly across NWA11444, varying from $Fo_{23-82}Fa_{18-77}$. As well as this, spinel is present as chromite, alongside Fe-Ni metal grains that are anhedral in shape.

Across NWA11444, whilst clasts with varying lithologies were identified, no basaltic clasts were found. This could be due to its brecciated nature and due to its meteorite origin meaning it was not taken *in situ.* As a result, multiple lithologies such as Lunar regolith, Lunar Highlands basalts etc. may have been included in the sample, whilst exhibiting a lack of Lunar Mare basalts. The sample won't be discussed further due to the lack of representation of Lunar Mare basalts allowing for poor comparison to the terrestrial analogues within this study.

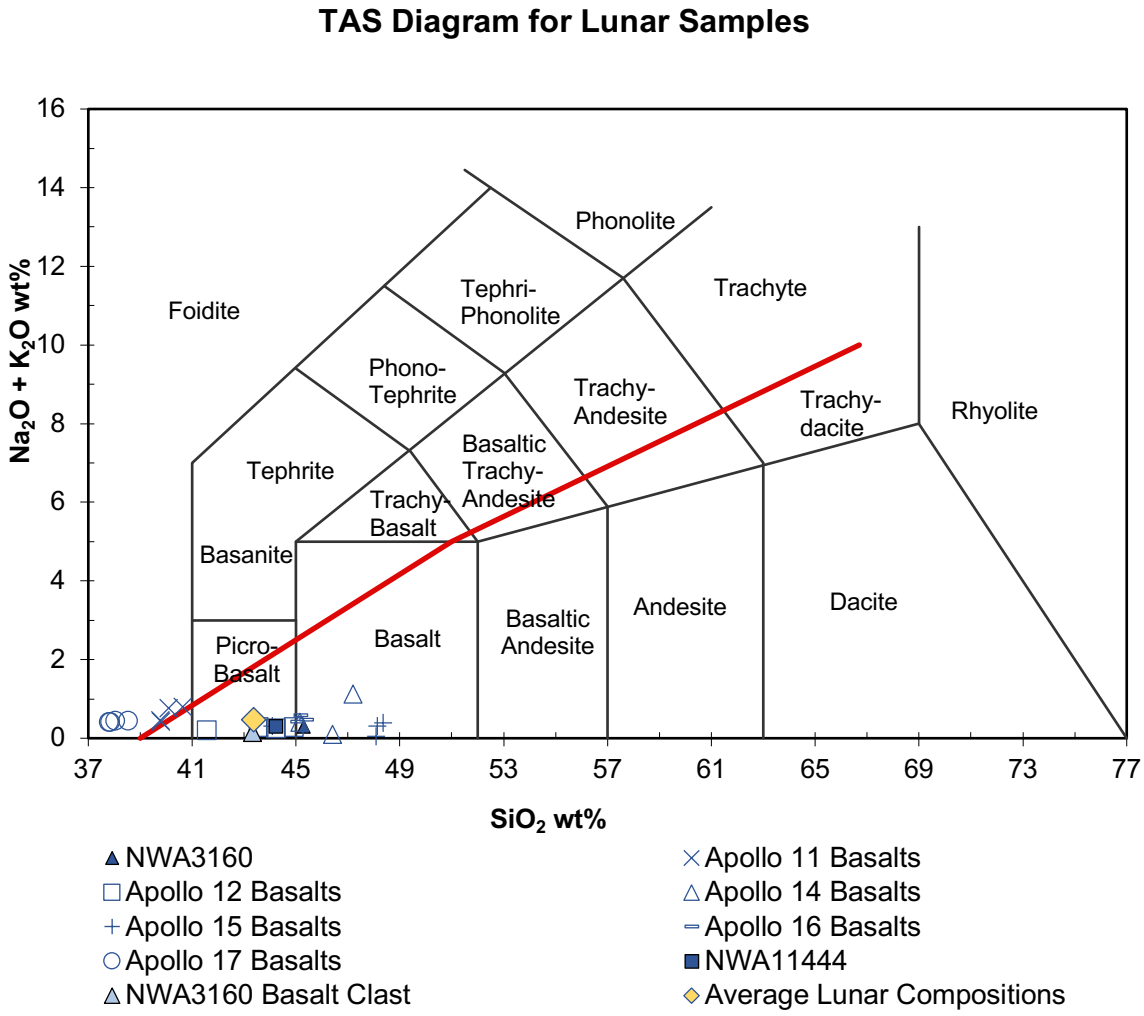

Figure 41 - TAS diagram displaying the representative rock type for NWA3160 as 'Basalt', and NWA11444 as 'Pico-Basalt', when comparing SiO_2 wt% against $Na_2O + K_2O$ wt%. Key: Blue = Lunar sample, error bars smaller than some points. Apollo data for this graph was sourced from Lofgren & Lofgren (1981), with the 'Average Lunar Compositions' representing the average compositions of Apollo data within this dataset.

4.3. Martian Samples

4.3.1. NWA7397

NWA7397 is a poikilitic Shergottite and comprises of two grains, with both representing cumulate rocks and displaying a non-poikilitic texture (a large area map of Grain 1 can be seen in Figure 42a). There are five visible mineral phases present within the sample (with estimated abundances as follows: plagioclase – 15%, olivine – 40%, pyroxene – 30%, spinels – 10%, carbonates/apatite – 5%). Olivine and pyroxene are heavily fractured, with most fractures infilled with calcite or apatite. Merrillite is also present as accessory minerals alongside spinel. When plotted on TAS, NWA7397 is representative of a 'picro-basalt' (Figure 43), with an average of 41.69 $\pm$ 0.28 wt% SiO_2, 1.05 $\pm$ 0.08 wt% Na_2O and K_2O below detection limit. The sample also has a Mg# of 58.08, representing a moderately evolved basalt.

Across both grains, plagioclase ranges across $An_{35-58}Ab_{39-62}Or_{2-7}$ in compositions (Appendix 6a & 8g), with no zoning present and displaying an anhedral shape. It is likely that plagioclase in this sample (as well as in the later Martian meteorites analysed) was shock-transformed to maskelynite (Howarth *et al*., 2014; McSween, 2015), however, this can't be observed using SEM. Pyroxene is present as distinct angular grains of Ca-rich and Fe/Mg-rich pyroxene (Figure 42b), with the associated Mg#'s of Fe/Mg-rich pyroxene (or Ca-poor pyroxene) also indicating a non-poikilitic pyroxene (Mg# = <70, Howarth *et al*., (2014)). A graph displaying the chemical variation when comparing MgO wt% vs CaO wt% between these pyroxenes can be seen in Figure 44). Subsequently, the

compositions for the pyroxenes vary from pigeonite to augite, with values ranging across $Wo_{9-28}Ens_{37-52}Fs_{33-49}$ (further data can be seen in Appendix 2a, 4d & 4e).

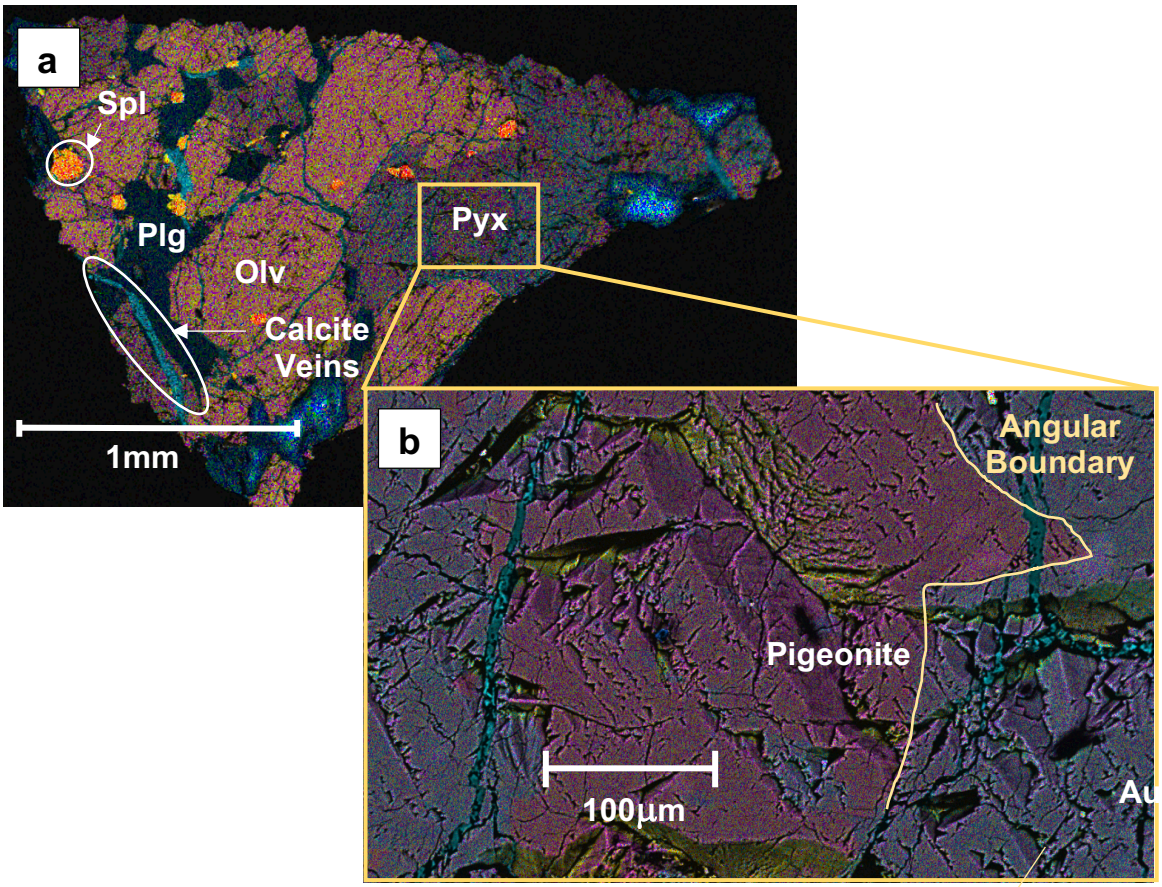

Figure 42 - a) Representative EDS image of grain 1 in NWA7397 taken at 37x magnification, displaying a cumulate texture comprising of olivine, pyroxene, plagioclase, spinel and carbonate mineral veins. b) Higher magnification (250x magnification) EDS image of grain 1, showing the distinct grains present in pyroxene, separated by angular boundaries. Key: Yellow = Iron, Orange = Titanium, Teal = Calcium, Navy Blue = Aluminium, Pink = Magnesium and Green = Sodium, Red = Chromium

Olivine occurs at larger sizes across grains in comparison to both plagioclase and pyroxene (Table 4), and, unlike the pyroxene crystals, shows no zoning. Additionally, olivine is distinctly Fe-rich (ranging across $Fo_{41-49}Fa_{51-59}$), and are

often sub-euhedral in shape. Additionally, olivine grains across the sample are often rounded in nature. Finally, spinel across NWA7397 is widely associated with olivine, often present as inclusions. This mineral phase occurs as chromite, Ti-rich chromite and ilmenite in NWA7397 and is sub-euhedral in shape.

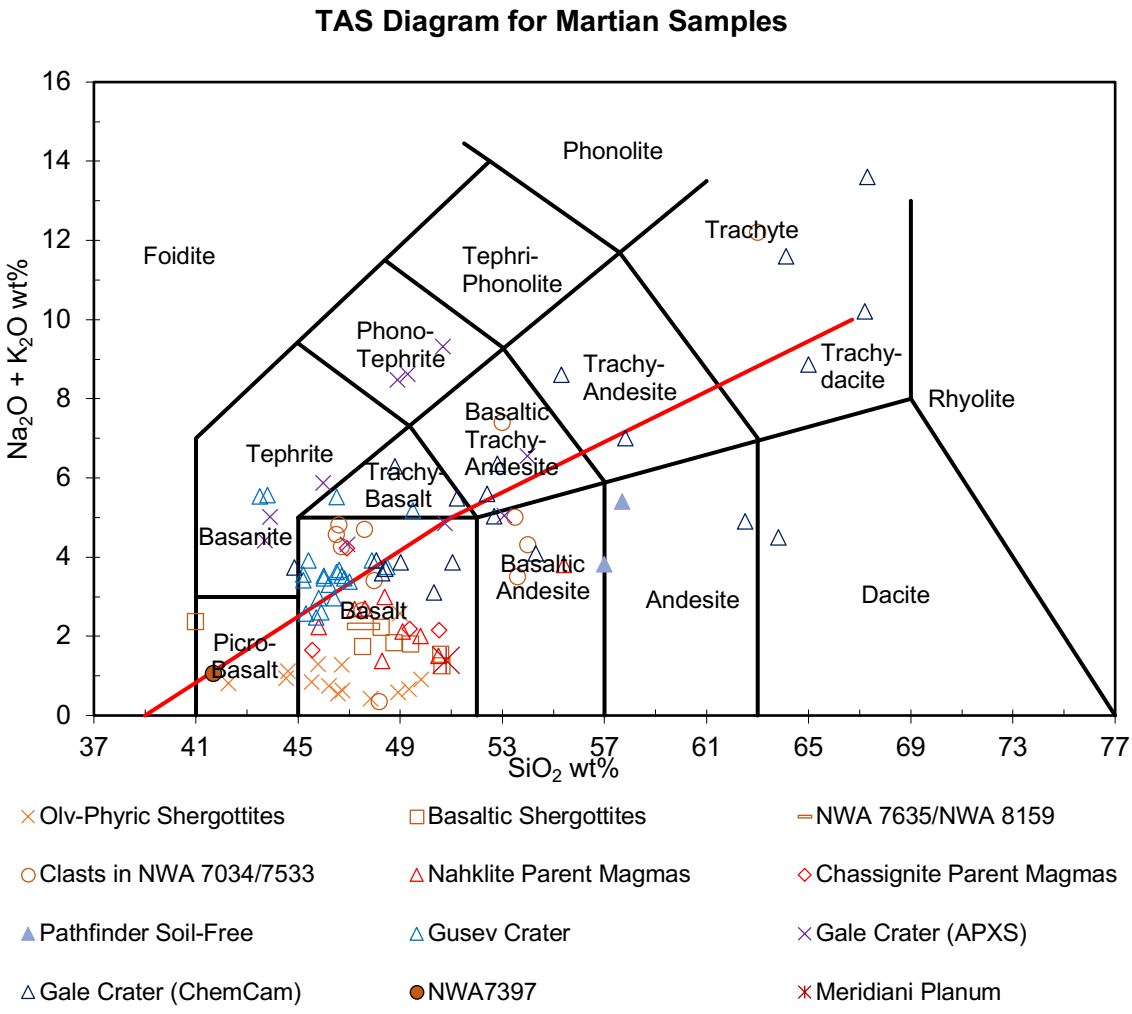

Figure 43 - TAS diagram displaying the representative rock type for NWA7397 as a 'Pico-Basalt' when comparing SiO_2 wt% against Na_2O + K_2O wt%. Key: Orange = Martian samples. For context Martian surface compositions from Gusev and Gale crater, Meridiani Planum and other Martian meteorite data from Filiberto, (2017) has also been plotted on this graph.

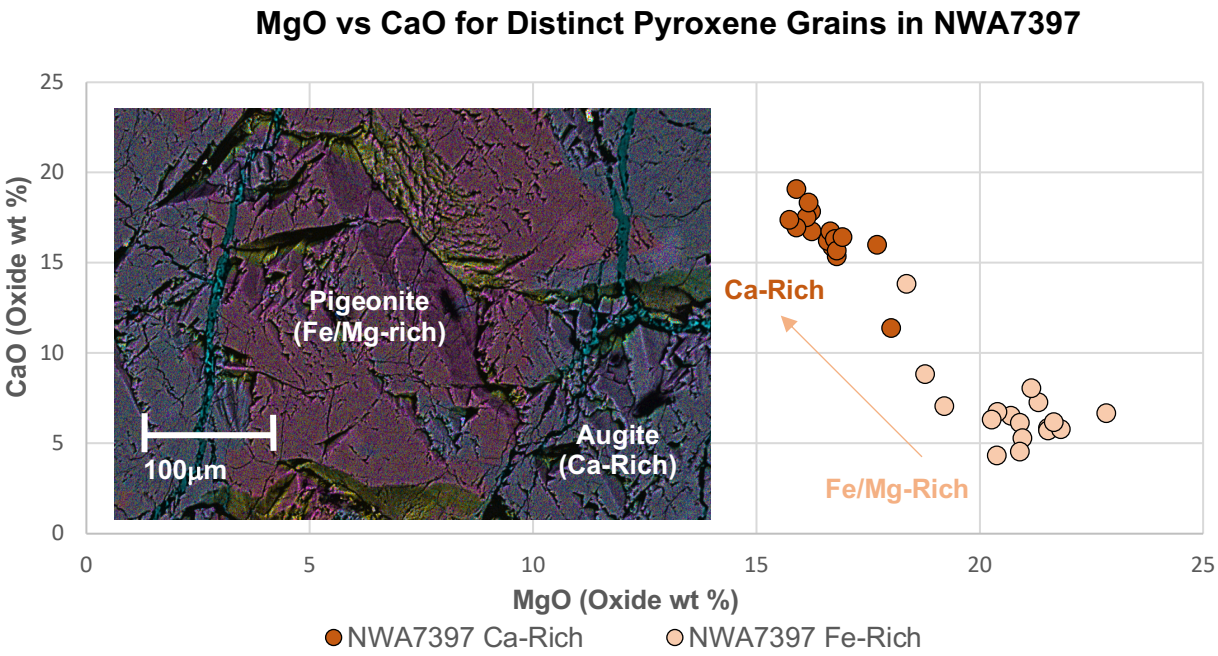

Figure 44 - Harker diagram comparing MgO wt% vs CaO wt% for the distinct pyroxene grains visible in NWA7397. The graph shows clustering of Fe/ Mg-rich pyroxene (with an average composition of ~20.75 wt% MgO, ~18.55 wt% FeO and ~6.75 wt% CaO), and Ca-Rich pyroxene (with an average composition of ~16.59 wt% MgO, ~13.04 wt% FeO and ~16.46 wt% CaO).

4.3.2. NWA1110

NWA1110 is an olivine-phyric Shergottite, displaying an olivine-porphyritic texture (with both macro- (referred to as 'macro-phenocrysts' prior to further discussion in Chapter 5.2) and micro-phenocrysts, Figure 45). The sample exhibits a fine-grained groundmass comprising of both pyroxene and plagioclase. There are six mineral phases present within the sample (with estimated abundances as follows: plagioclase – 35%, pyroxene – 40%, olivine – 20%, spinel, pyrrhotite and apatite – that combined comprise 5%). When plotted on a TAS diagram, NWA1110 has

a bulk geochemistry of a 'basalt' (Figure 46), comprising of 46.92 ± 2.41 wt% SiO_2, 3.16 ± 0.21 wt% Na_2O and 0.35 ± BDL wt% K_2O. Published bulk geochemical data for NWA 1068 (paired with NWA 1110) for comparison can be seen in Chapter 5.4, Table 7. Additionally, NWA1110 has a Mg# of 52.58, representing a moderately evolved basalt.

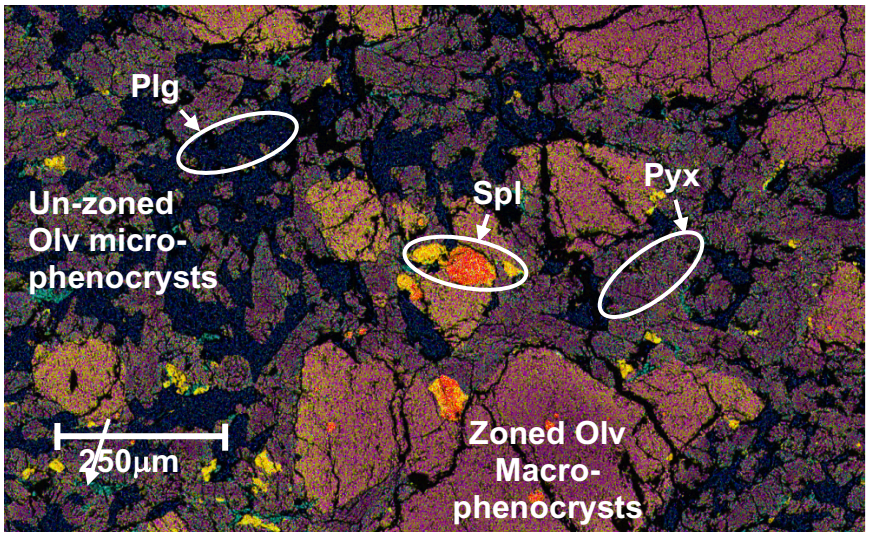

Figure 45 - Representative EDS image of NWA1110 taken at 250x magnification 5390 resolution, displaying a porphyritic texture comprising of olivine macro- and micro- phenocrysts, a pyroxene/plagioclase groundmass and spinel. Key: Yellow = Iron, Orange = Titanium, Teal = Calcium, Navy Blue = Aluminium, Pink = Magnesium and Green = Sodium, Red = Chromium

Anhedral plagioclase (now maskelynite) is present within the groundmass of NWA1110, ranging across $An_{30\text{-}62}Ab_{35\text{-}57}Or_{BDL}$ (Appendix 6b & 8h). Additionally, no zoning is visible within this plagioclase. As well as plagioclase, pyroxene is also present within the groundmass of this sample and displays compositional zoning of Fe/Mg-rich (pigeonite) and Ca-rich (augite) pyroxene (the variation of geochemistry within pyroxene in this sample stretches across $Wo_{6\text{-}29}En_{5\text{-}53}Fs_{33\text{-}}$

85 and can be seen in App endix 2c & 4f). Across the sample, the finer grained pyroxenes exhibit compositional zoning that appears irregular/patchy, however, where larger pyroxene grains are present, continuous normal zoning is exhibited.

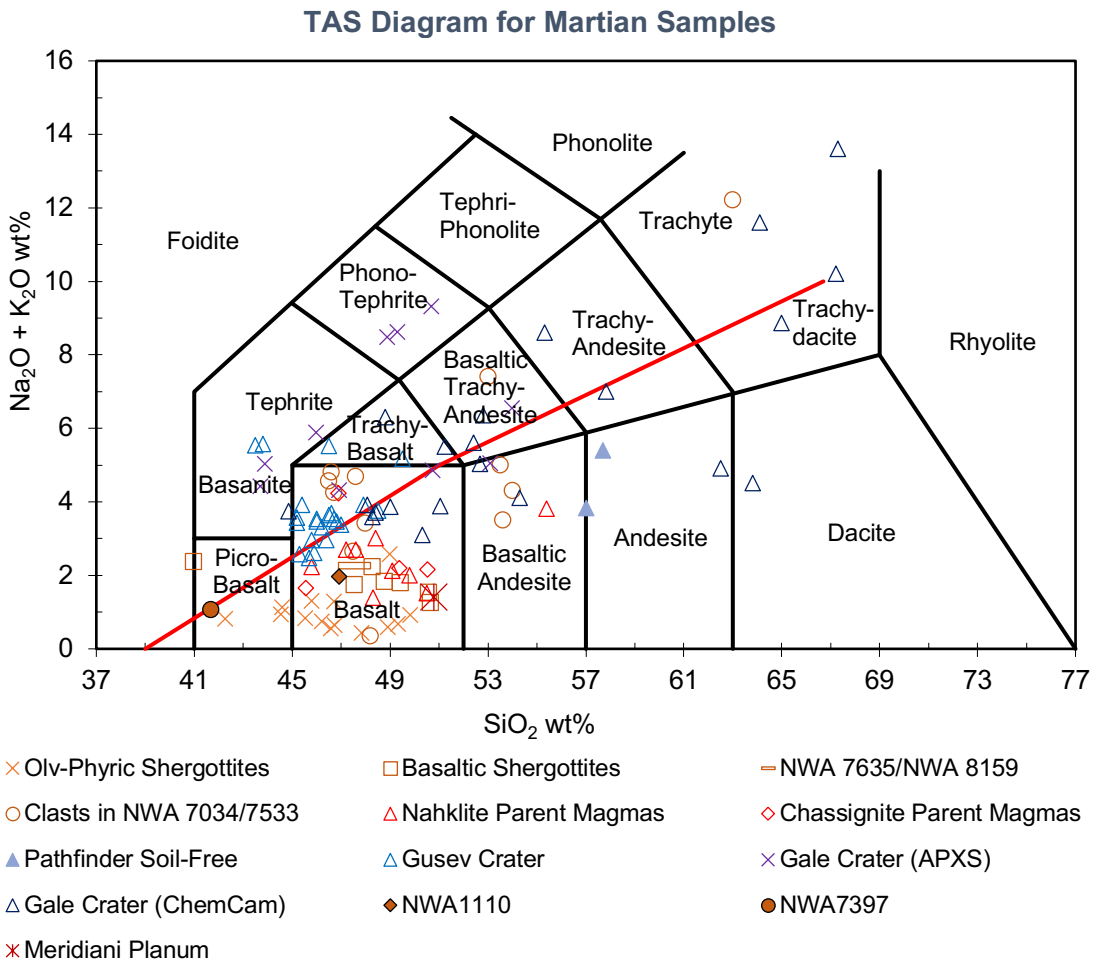

Figure 46 -TAS diagram displaying the rock type for NWA7397 as a 'Pico-Basalt' and NWA1110 as 'Basalt'. Key: Orange = Martian samples. For context Martian surface compositions from Gusev and Gale crater, Meridiani Planum and other Martian meteorite data from Filiberto, (2017) has also been plotted on this graph.

Olivine is present as both micro- and macro-phenocrysts across NWA1110. These macro-phenocrysts are anhedral in shape and appear slightly corroded, with their predominantly Mg-rich core also appearing to have an anhedral shape

(Figure 47). Additionally, macro-phenocrysts of olivine are normally zoned, with MgO concentration decreasing and FeO concentration increasing from centres ($Fo_{42-57}Fa_{43-58}$) to rims ($Fo_{31-48}Fa_{52-69}$) (the chemical difference between the centres and rims can be seen in Figure 48 and Figure 49). Olivine micro-phenocrysts, however, are more similar in composition to the rims of the olivine macro-phenocrysts, with a range of $Fo_{26-43}Fa_{57-74}$ across the sample, see Figure 50.

Spinel is also present as accessory minerals within NWA1110. Chromite is present as subhedral-euhedral grains mostly within olivine macro-phenocrysts, and generally when in contact with the groundmass, display normal zoning of chromite to Ti-rich chromite. Smaller grains of ilmenite and Ti-rich chromite are also present within the groundmass. These minerals occur alongside pyrrhotite.

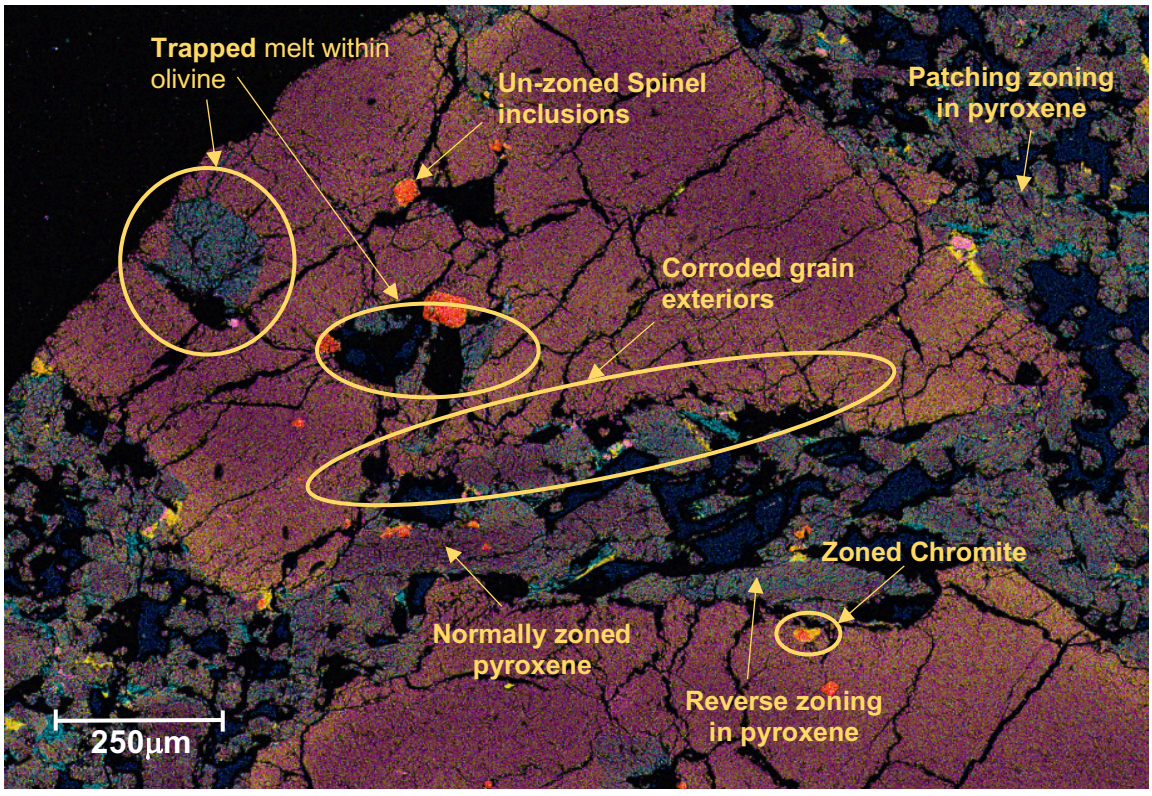

Figure 47 - EDS image (taken at 250x magnification) displaying the anhedral nature of olivine, the trapped melt within the olivine 'macro-phenocrysts' and

corroded grain exteriors. You can also see the patchy zoning of pyroxene in the sample, with occasional larger pyroxene grains that are normally zoned. Zoned chromite grains in contact with the groundmass are also visible in this figure. Key: Yellow = Iron, Orange = Titanium, Teal = Calcium, Navy Blue = Aluminium, Pink = Magnesium and Green = Sodium, Red = Chromium

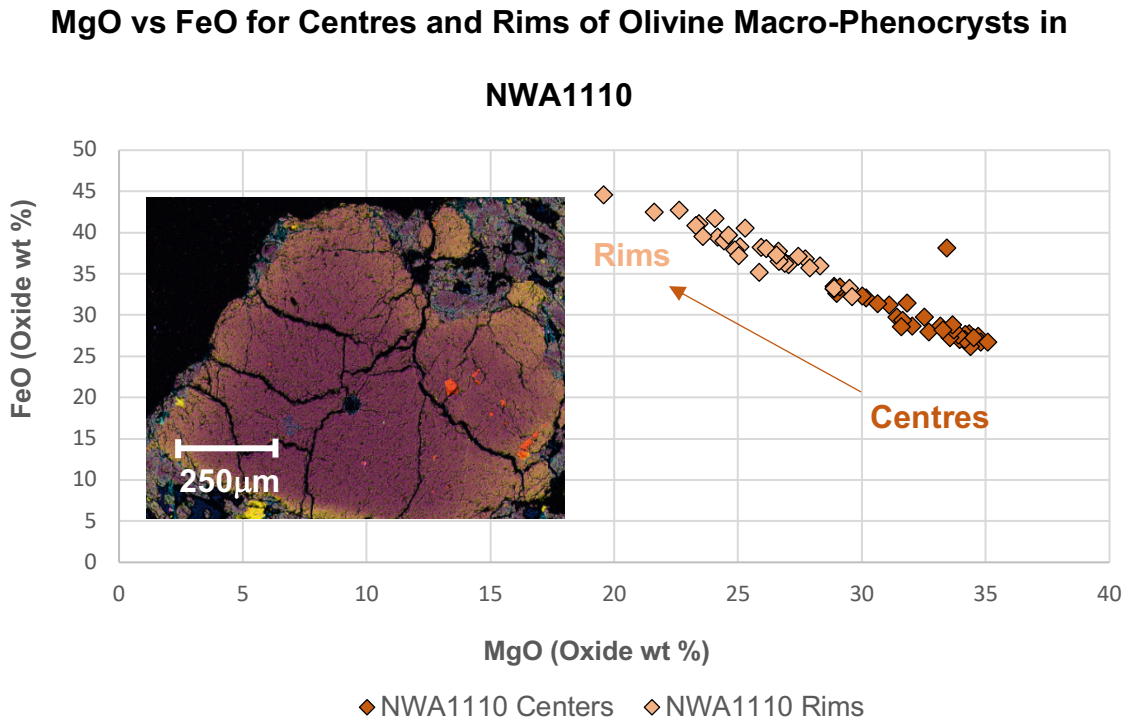

Figure 48 – (Left), EDS image (taken at 250x magnification) displaying an example of olivine zonation present within NWA1110. Figure 49 - (Right), Harker diagram comparing MgO wt% vs FeO wt% for both the centres and the rims of olivine macro-phenocrysts in NWA1110. Spot data displayed on the graph has been taken from all sites across the sample. The graph shows a linear trend of decreasing MgO content towards the rims of the olivine macro-phenocrysts, where the concentration of FeO increases (from between 26.69-37.03 ± 2.97 wt% FeO in the olivine centres of macro-phenocrysts to between 32.18-44.52 ± 2.88 wt% FeO at the rims).

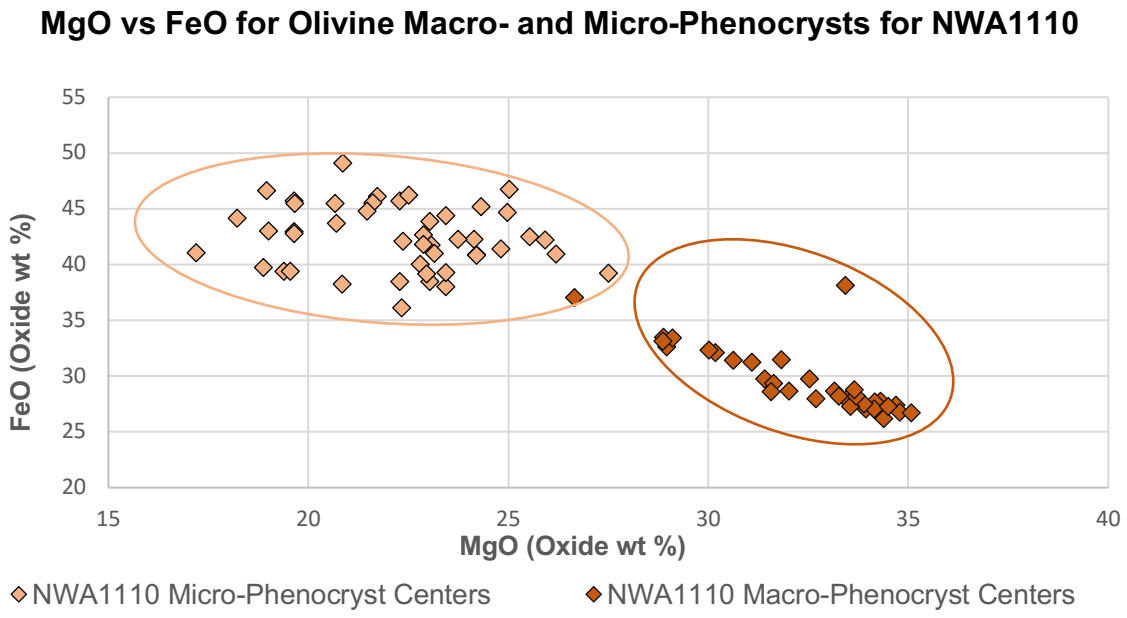

Figure 50 - Harker diagram comparing MgO wt% vs FeO wt% for olivine macro- and micro-phenocryst centres in NWA1110. This graph shows that macro-phenocrysts within this sample are richer in MgO content (26.66-35.07 ± 2.14 wt% MgO) than the surrounding micro-phenocrysts (17.20-27.05 ± 2.36 wt% MgO). Orange = Martian

4.3.3. Tissint

Tissint is an olivine-phyric Shergottite consisting of a fine-grained groundmass and a porphyritic texture of macro- (named macro-phenocrysts prior to further discussion in Chapter 5.2) and micro-phenocrysts, all surrounded by a fine-grained groundmass of an intercumulus nature (Figure 51). Five mineral phases are present within this sample (with estimated abundances as follows: plagioclase – 30%, pyroxene – 40%, olivine – 20%, spinels, ilmenite and pyrrhotite – 10% combined). Comprising of 46.35 ± 0.12 wt % SiO_2, 0.97 ± 0.06

wt% Na_2O and K_2O below detection limits, Tissint plots as a basalt on a TAS diagram (Figure 52). Published bulk geochemical data for Tissint for comparison can be seen in Chapter 5.4, Table 7. Additionally, this sample has a Mg# of 59.00, representing a moderately evolved basalt.

Plagioclase (now maskelynite) across Tissint is anhedral in shape representing a more intercumulus texture, and ranges across $An_{60\text{-}68}Ab_{31\text{-}39}Or_{BDL}$ in composition (Appendix 6c & 8i) with no zoning present. These grains also occasionally host inclusions of Fe/Mg-rich pyroxene (Figure 51). This mineral phase comprises of intergrowths alongside pyroxene, of which is compositionally normally zoned with Fe/Mg-rich (pigeonite) centres and Ca-rich (augite) rims (Figure 51). Pyroxene compositions range from $Wo_{9\text{-}25}Ens_{34.12\text{-}53}Fs_{38\text{-}59}$ across the whole sample (Appendix 2b, 4g & 4h). The zoning exhibited by pyroxene appears more regular than that shown by NWA1110, with better defined cores and rims. Despite this, the smaller pyroxene grains display zoning that is patchier in nature, with some that are almost completely augite in composition. Pyroxene is also sub-anhedral in shape.

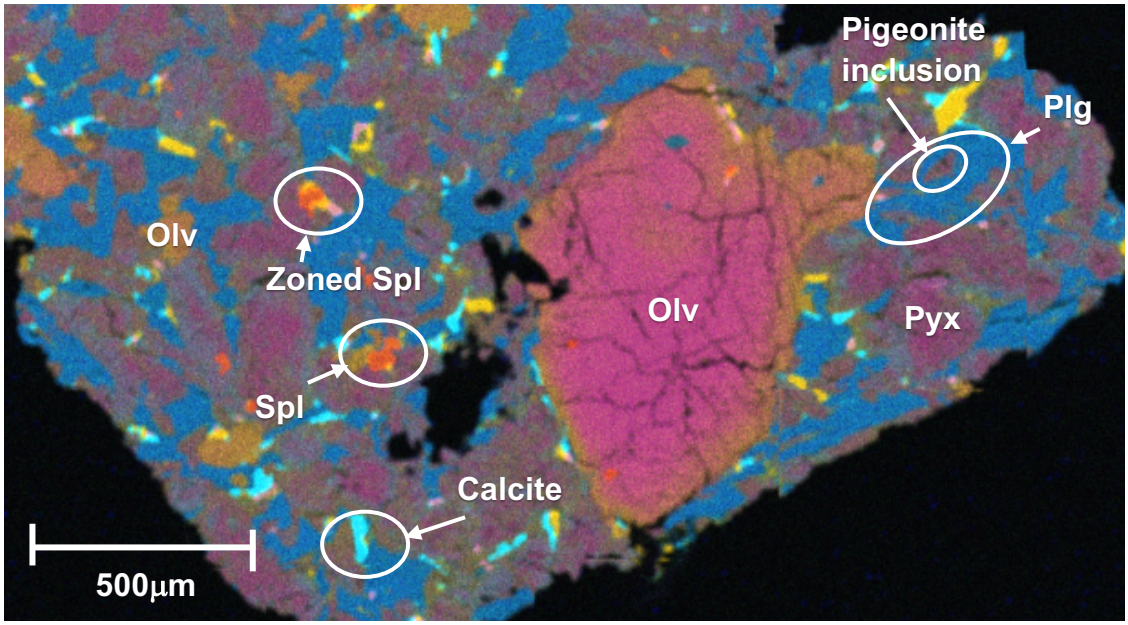

Figure 51 - Representative EDS image of Tissint (taken at 200x magnification) displaying a porphyritic texture of olivine macro- and micro- phenocrysts, spinel, and a groundmass of pyroxene and plagioclase. Accessory minerals of apatite are also present. Key: Yellow = Iron, Orange = Titanium, Teal = Calcium, Navy Blue = Aluminium, Pink = Magnesium and Green = Sodium, Red = Chromium

Similar to NWA1110, the macro- and micro-phenocrysts within Tissint are olivine in composition. The macro-phenocrysts are subhedral in shape with irregular rims and are normally zoned, displaying Mg-rich centres ($Fo_{43-66}Fa_{34-57}$) that gradually become more Fe-rich ($Fo_{33-62}Fa_{38-67}$) towards the rims (a difference visible in Figure 53 and Figure 54). Olivine micro-phenocrysts, however, display a composition more similar to the Fe-rich rims of the macro- phenocrysts ($Fo_{24-63}Fa_{37-76}$), Figure 55. Finally, spinel is present in Tissint as both chromite and ilmenite accessory minerals, alongside apatite. Additionally, chromite grains occasionally display normal zoning from chromite to Ti-rich chromite.

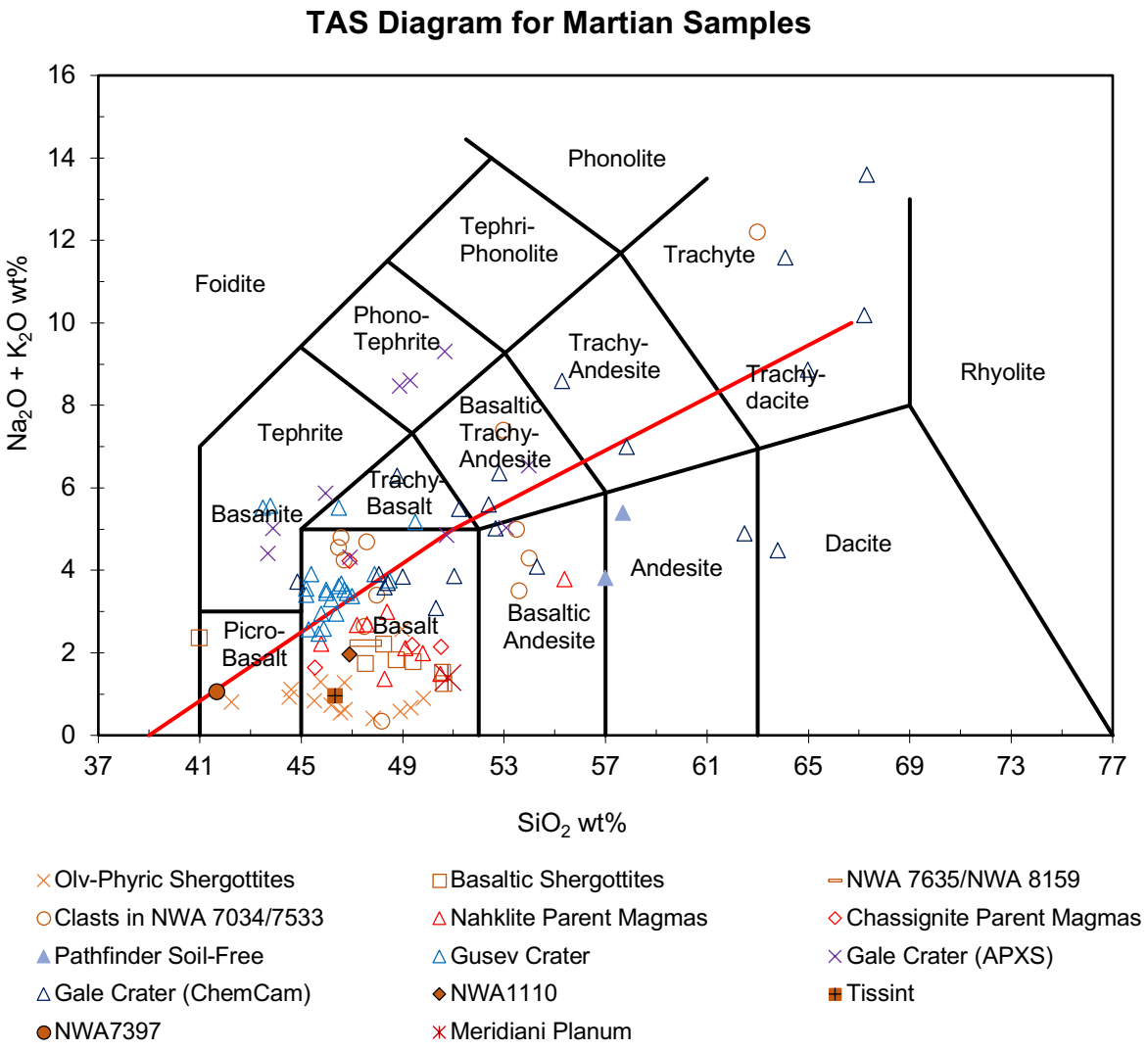

Figure 52 - TAS diagram displaying the representative rock type for NWA7397 as a 'Pico-Basalt', NWA1110 as 'Basalt' and Tissint as 'Basalt' when comparingSiO_2 wt% against $Na_2O + K_2O$ wt%. Key: Orange = Martian samples. For context Martian surface compositions from Gusev and Gale crater, Meridiani Planum and other Martian meteorite data from Filiberto, (2017) has also been plotted on this graph.

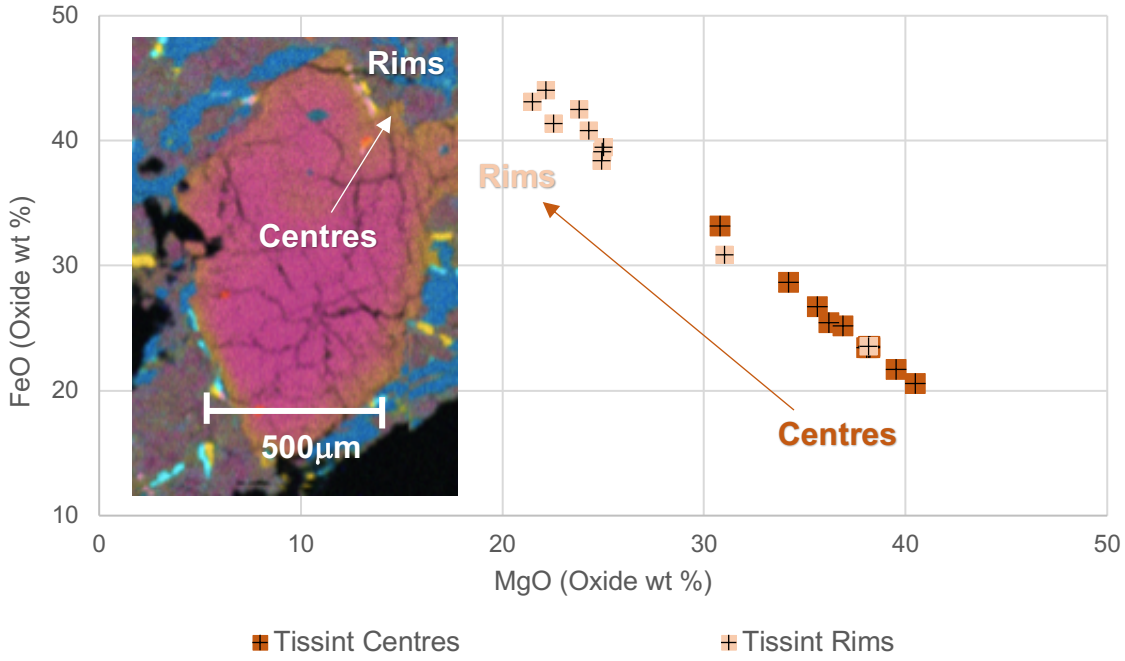

Figure 53 - (Left), EDS image (250x magnification) of a zoned olivine 'macro-phenocryst' within Tissint, displaying a Mg-rich core and Fe-rich rim. towards the rims can be seen. Figure 54 – (Right) Graph displaying the MgO vs FeO wt% content of both olivine 'macro-phenocryst' centres and rims. A liner trend of increasing FeO wt% content towards the rims can be seen.

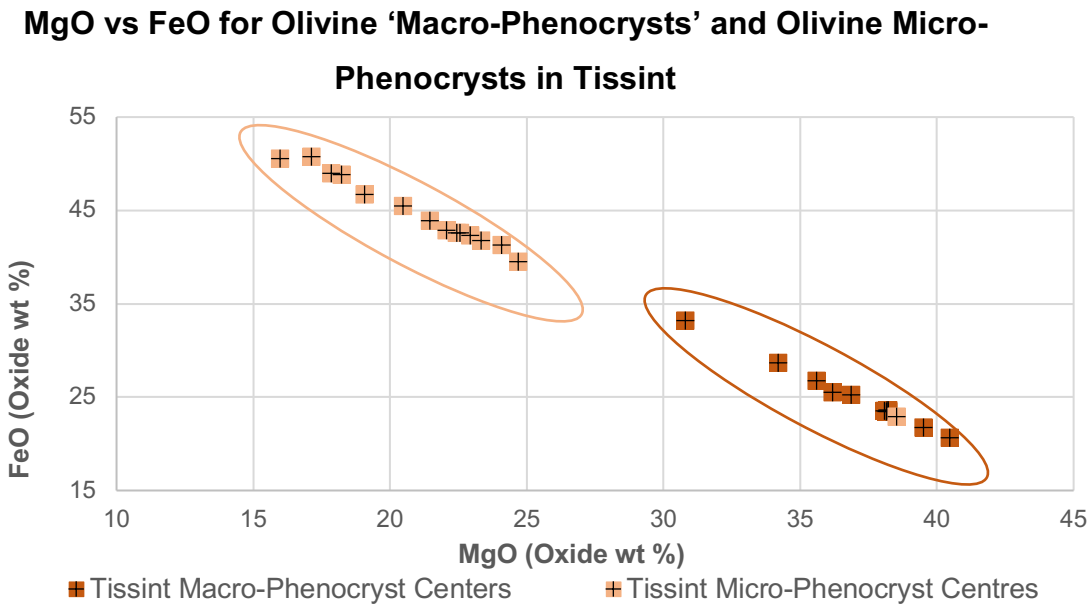

Figure 55 - Graph displaying the linear trend of FeO wt% content and MgO wt% within olivine 'macro-phenocrysts' and olivine micro-phenocrysts within Tissint

Grain Sizes of All Samples Analysed in this Study

Sample	Mineral	Grain Size	Sample	Mineral	Grain Size
Hawaii 1	Plagioclase	~250-300μm	**Tissint**	Plagioclase	~250μm
	Pyroxene	~200μm		Pyroxene	~280μm
	Olivine	~100μm		Olivine	~580μm (Macro), ~157μm (Micro)
Hawaii 2	Plagioclase	0.1-2mm		Spinel	~100μm
	Olivine	~100-723μm		Carbonates	<100μm
	Spinel	~33μm	**NWA3160**	Plagioclase	~200-685μm
ESA01-A	Plagioclase	~22-171μm		Pyroxene	~200-1370μm
	Pyroxene	~30-201μm		Olivine	0.35-1.54mm
	Olivine	~27-250μm		Carbonate	<250μm
	Spinel	~117μm		Spinel	<100μm
New Mexico	Plagioclase	~161-574μm		Pyrrhotite	~75μm
	Pyroxene	Groundmass	**NWA11444**	Plagioclase	<200μm-2250μm
	Olivine	~843μm (Macro), ~142μm (Micro)		Pyroxene	30-509μm
	Spinel	~40μm		Olivine	30-170μm
NWA7397	Plagioclase	~241μm		Carbonate	~600μm length (fractures)
	Pyroxene	~332μm		Spinel	<50μm
	Olivine	~623μm	**NWA3160 (Basalt Clast)**	Plagioclase	100-282μm
	Spinel	~130μm		Olivine	100-395μm
	Carbonates	~130μm		Pyroxene	60-280μm
NWA1110	Plagioclase	<120μm		Spinel	~70μm
	Pyroxene	<132μm			
	Olivine	~685μm (Macro), ~257μm (Micro)			
	Spinel	~60μm			
	Carbonates	~50μm			
	Pyrrhotite	~54μm			

Table 4 - Table displaying all of the grain sizes for each mineral phase in every sample analysed during this study, with a single value representing average grain sizes. Grain sizes were determined using the measuring function on Oxford

Instrument's AZtec Software on randomly selected mineral grains, before averaging across the measured minerals.

5.0. Discussion

Within the following section, observations made in Chapter 4.0 for Earth and Mars will be discussed in the context of their inferred geological formations, and compared to identify if any of the terrestrial samples will make for accurate analogues for Mars. Lunar samples will not be discussed due to their limited geochemical and petrological data to compare to terrestrial samples, owing to the lack of basaltic clasts within NWA3160 and NWA11444 (explained in Chapter 4.2).

5.1. Geological Formation of Terrestrial Samples

5.1.1. Hawaii 1 and Hawaii 2

Kilauea is a basaltic shield volcano (Macdonald, 1949), reaching an elevation of 1,222m (USGS a, 2021) and situated towards the SE of Hawaii - the youngest of 8 volcanic islands that make up the Hawaiian island chain. These 8 islands are home to ~15 volcanoes, and are a small part of a much larger chain of seamounts and volcanic islands – comprising of >100 volcanoes and stretching ~6,100km across the north Pacific Ocean, (USGS b, 2021; Jiang *et al.,* 2021), recording 70 million years of volcanic activity (Poland *et al.*, 2014). Ages of the Hawaiian Islands increase towards the NW of the chain, with their formation thought to be

the result of a fixed subsurface mantle plume causing partial melting of the deep mantle and subsequent formation of the Hawaiian hotspot (Jiang *et al.,* 2021). Intraplate volcanism due to this mantle plume caused the formation of these volcanic islands, with lithosphere migration above the hotspot responsible for the chained distribution.

The magma plumbing system of Kilauea, Figure 56, is inferred to consist of two magma reservoirs (Poland *et al.,* 2011), that combined are recognised as the summit reservoirs (Pietruska *et al.,* 2018). Both reservoirs are situated below the summit region of Kilauea, and are hydraulically linked through intrusive activity such as dikes. The smaller of the two reservoirs (Halema'uma'u magma body (Pietruska *et al*., 2018)), is located 1-2km beneath the caldera centre (Poland *et al*., 2014), however, the larger reservoir (South Caldera magma body) is located >3km below Kilauea's southern caldera. Magma from the summit reservoirs can be erupted at the summit or transported laterally by shallow dikes (~3km deep (Poland *et al.,* 2014)), to two linked rift zones (the East Rift Zone (ERZ) - ~3km deep, and the Seismic South Western Rift Zone (SSWRZ) - ~3km deep), (Poland *et al.*, 2014; Pietruska *et al*., 2018). Of the two rift zones, the ERZ is the most active (displaying continuous activity since 1982, (Poland *et al.*, 2014)), receiving more magma from Kilauea's summit. Kilauea also comprises of a Volcanic South Western Rift Zone (VSWRZ), situated at ~1km depth, and displays more fissures and eruptive vents than the SSWRZ.

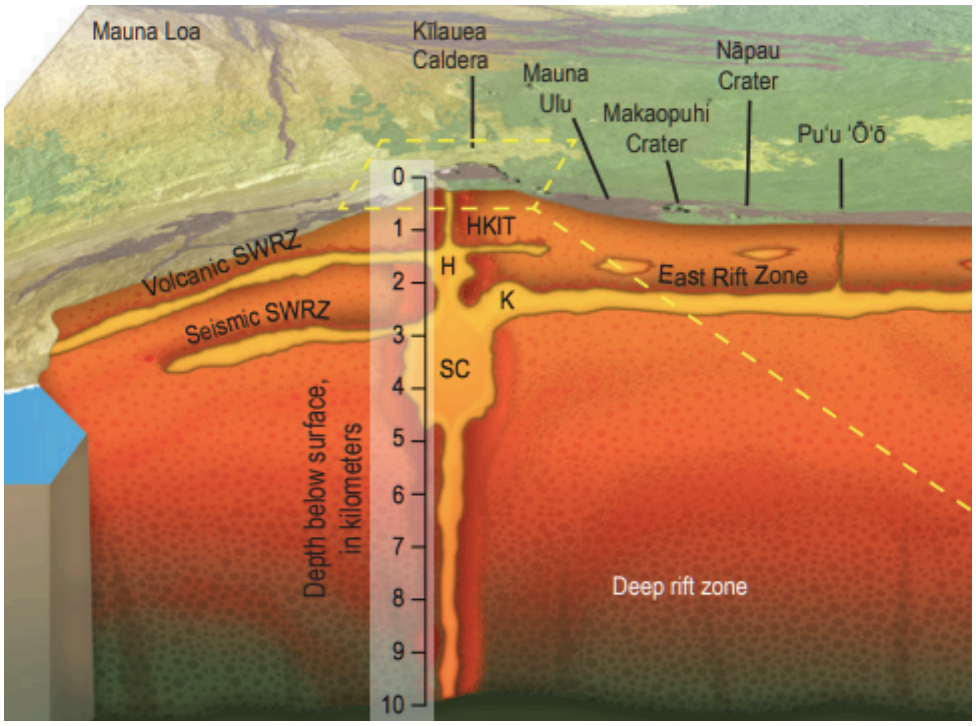

Figure 56 - Diagram displaying the magma plumbing system of Kilauea, Hawai'i. (Source: Poland, 2014). SC = Southern Caldera magma body, H = Halema'uma'u magma body.

The crystallisation of magma stored within the summit reservoir is inferred to be olivine controlled, a process also seen in some rift zones, producing basalts exceeding 6.8 wt% MgO (Wright & Fiske, 1971). This involves the removal and settling of olivine crystals during magma ascent and crystallisation, causing a gradient of olivine accumulation towards the base of the reservoir, and a deficit of olivine towards the top (Wright, 1971). Unlike the summit reservoirs, magmas erupted within both the ERZ and SSWRZ can also be differentiated, characterised by a MgO concentration of <6.8 wt%. This is due to the lateral transport of magma to the adjacent rift zones, where it is then stored and subject to magmatic differentiation until eruption. Differentiation processes such as filtration of liquid from a static crystal mush have been identified by Wright &

Fiske, (1971) as most likely to occur within the Kilauea rift zones, often occurring due to pressure changes within the magma plumbing system and involving the removal of minerals that aren't olivine. Eruption events at rift zones often leave magma behind in the reservoir, allowing for further crystallisation and differentiation in the rift zone.

Both Hawaii 1 and Hawaii 2 exhibited MgO concentrations below those of the olivine-controlled summit magmas, averaging at ~6.09 ± 0.38 wt% and ~4.17 ± 0.15 wt% respectively (Appendix 9a & 9b). Whilst Hawaii 1 remains below the 6.8 wt% MgO (characteristic of the olivine-controlled crystallisation), the scarcity of olivine within the sample relative to Hawaii 2 (only ~6% abundance with a maximum grain size of ~100μm (Table 4)) suggests that the crystallisation process was olivine-controlled, with the sample experiencing olivine removal before eruption (Wright, 1971). Moreover, if the magma was olivine-controlled, Hawaii 1 must have undergone less differentiation relative to Hawaii 2 to cause a MgO content below 6.8 wt% rather than the ~4.17 ± 0.15 wt% in Hawaii 2. It has been inferred that this magma underwent olivine-controlled crystallisation within the ERZ, before the occurrence of a final filter pressing of residual liquid from the olivine rich crystal-liquid mush within the magma prior to eruption (Wright & Fiske, 1971); a mush produced by gravity settling. This differentiated residual liquid then infilled some vesicles present within the magma in the lava flow after eruption, producing the infilled vesicles visible in Chapter 1.4.1 (Anderson Jr *et al.,*1984).

In contrast to Hawaii 1, Hawaii 2 displays a greater abundance of olivine (~13%, reaching a maximum grain size of 723μm (Table 4)), and, with a considerably low

MgO concentration, is indicative of a differentiated rift zone magma. Wright (1971), also suggested that a MgO this low indicates a silicate phase must have crystallised in equilibrium with the melt alongside olivine (at inferred temperatures ~1185-1070°C, (Wright & Fiske, 1971)), with this observation possibly responsible for the abundance of plagioclase phenocrysts alongside olivine in Hawaii 2 compared to Hawaii 1. Additionally, there are no pyroxene phenocrysts present within Hawaii 2 (Chapter 4.1.2, Figure 24a) unlike the augite phenocrysts visible in Hawaii 1. The removal of a mineral phase other than olivine is a common process during differentiation (Wright & Fiske, 1971), and could be responsible for the removal of pyroxene within Hawaii 2. To add to this, the larger overall grain size of Hawaii 2 in comparison to Hawaii 1 (Table 4), indicates that the magma was crystallising for a longer period of time in the magma reservoir prior to eruption. Therefore, it has been inferred that Hawaii 2 is an example of a rift zone lava, where magma was laterally transported to the ERZ before remaining in the magma reservoir and undergoing extensive differentiation prior to eruption.

In this study, the porphyritic textures of both Hawaii 1 and Hawaii 2, (Chapters 1.4.1 and 1.4.2, Figures 22a and 24a respectively), suggest they both underwent two stages of cooling prior to eruption, with the first occurring within the magma reservoir, and the second upon eruption. The euhedral nature of plagioclase phenocrysts across both samples suggests that both were already present in the magma chamber prior to eruption, crystallising in equilibrium with the melt (Wright & Fiske, 1971). In addition, the vesicular nature of both samples is inferred to have developed during magma storage (Helz *et al.,* 2014), or during emplacement of the magma during eruption.

The symplectic texture present in Hawaii 2 (Chapter 4.1.2, Figure 24b) is indicative of late-stage interactions between interstitial liquid and crystal phases (Keevil *et al.,* 2020). The formation of this texture has been found between the boundaries of olivine and plagioclase primocrysts (both phases present within Hawaii 2), with a magmatic origin (Holness *et al.,* 2011). Geert-Jan *et al*., (2002), found that symplectic textures can form due to the crystallisation of orthopyroxene through partial dissolution of olivine, alongside plagioclase and clinopyroxene crystallisation, with the SiO_2 required for this available from a differentiated liquid present in intercumulus spaces.

5.1.2. ESA01-A

ESA01-A was retrieved from Craig's quarry, part of the Lower Basalt Formation of the County Antrim Basalt Plateau (within the County Antrim Lava Group) in Northern Ireland, Figure 57. The County Antrim Basalt Plateau is part of the larger North Atlantic Igneous Province (NAIP), (Wilkinson *et al.,* 2016) covering Antrim, Londonderry, Tyrone, Armagh and Down counties (Patterson *et al.,* 1954-1956). The NAIP is a LIP covering land both onshore and offshore at an area estimated 1.3×10^6 km^2. Eruption and emplacement of the province has been associated with continental rifting and crustal uplift, with the NAIP now being divided by the North Atlantic Ocean. A sub-province of NAIP, home to the County Antrim Basalt Plateau, is the British-Irish Palaeogene Igneous Province (BIPIP), a mostly basaltic province formed by intense volcanic activity, covering 10,788 km^2.

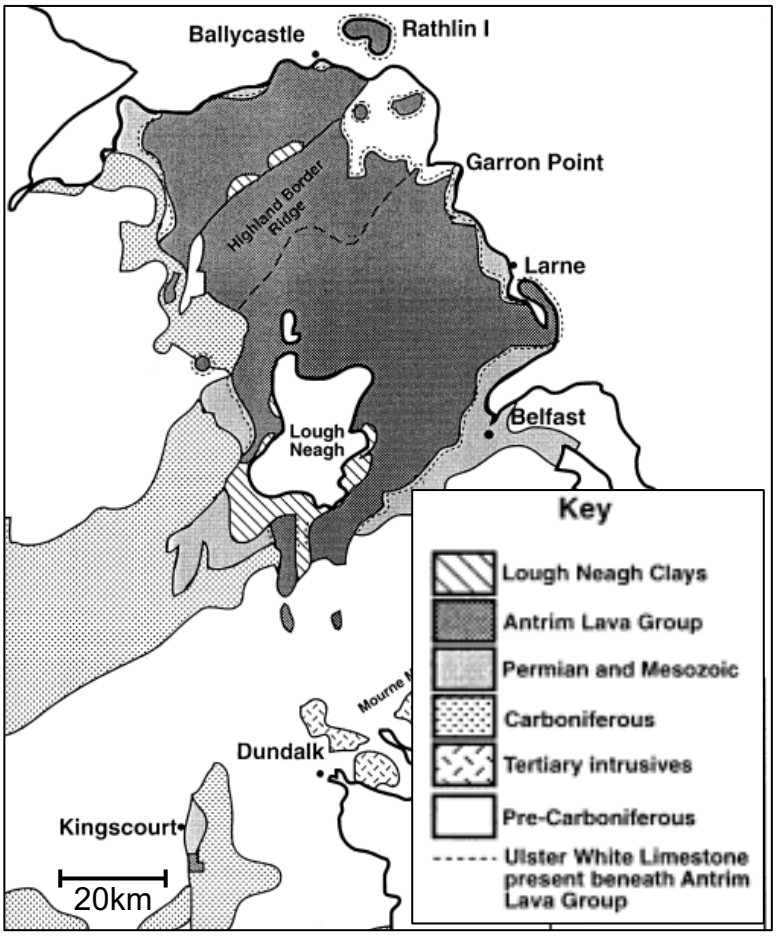

Figure 57 - Map displaying the location of the County Antrim Lava Group (Source: Simms, 2000)

Within the BIPIP, the County Antrim Lava Group has been separated into three groups: The Lower Basalt Formation (62-63 Ma in age, and representing the first cycle of volcanic activity), Inter-basaltic Basalt Formation (61.3 Ma in age, consisting of a 30m layer of laterites formed by dormancy and weathering, covering lavas from the Lower Basalt Formation), and the Upper Basalt Formation (a sequence of olivine tholeiite lavas that are 59 Ma in age, representing the second cycle of volcanic activity and covering the Upper Maastrichtian limestones towards the north of Northern Ireland (Ganerød *et al.,* 2010). The Lower Basalt Formation of the Antrim Lava Group are thought to be

basaltic flood lavas that are deemed as uniform across the whole formation (Brooks *et al*., 2016). A series of dikes and dolerite plugs reside through the Antrim lavas, with their presence thought to be feeder dikes for upper lava flows (Tomkeieff, 1940).

Volcanism of the County Antrim Lava Group is thought to be as a result of a shield lava complex (Tomkeieff, 1940), associated with the magma sourced from the larger scale, SE margin of the deep, proto-Icelandic plume that was responsible for the formation of the entire NAIP (Wilkinson *et al*., 2016; Ganerød *et al*., 2010). This event occurred during the Palaeogene, with both extrusive and intrusive activity occurring through areas of weakness in the crust, prior to continental rifting ~52Ma. The magma storage system for the shield lava complex that saw the formation of the County Antrim Lava Group is thought to have been fed by basalt/doleritic plugs (Tomkeieff, 1940).

Similar to porphyritic textures in Hawaii 1, and Hawaii 2, the presence of occasional micro-phenocrysts in ESA01-A suggests two phases of cooling, with the euhedral nature of these micro-phenocrysts indicating a crystal presence in the magma storage system prior to eruption (Wright & Fiske, 1971). Additionally, ESA01-A lacks a vesicular texture, an observation characteristic of the lower basalt formation in the Antrim Lava Group (Tomkeieff, 1940), specifically within the middle zone of the flow (Tomkeieff, 1934). The crystallisation of olivine micro-phenocrysts must have occurred relatively quickly, resulting in their small grain size, before eruption and crystallisation of the pyroxene/plagioclase groundmass. Additionally, the diopsidic nature of pyroxene across ESA01-A (Chapter 4.1.3), indicates that the crystallisation of this mineral phase occurred relatively soon

after olivine crystallisation (Poldervaart & Hart, 1951). The sub-ophitic nature of plagioclase and pyroxene crystals within ESA01-A (a texture also identified by Patterson, 1950) is an example of the intergrowth within a poikilitic texture, and potentially grew within a crystal-mush setting, seeing the crystallisation of the interstitial liquid between olivine micro-phenocrysts (Barnes *et al.*, 2016). Additionally, the simple, compositional zoning visible in plagioclase within ESA01-A (Chapter 4.1.3, Figure 26b, Appendix 5c), is a product of intra-crystal diffusion of anorthite to albite as continuous crystallisation progresses (Yang et al., 2019; Deer *et al.,* 2013). The lack of zoning in olivine and pyroxene within the sample, and the lack of reaction rims surrounding these phases, suggests that, unlike in New Mexico (see below), zoning in plagioclase is a crystallisation product rather than magma recharge and magma mixing. Crystallisation has also been inferred by Tomkeieff (1940), as cause for differentiation in the associated magma-type for the lower basalt formation. Gravity settling of more dense minerals (such as olivine) as a result of fractional crystallisation may then have occurred, resulting in a Mg# of 49.23 (Chapter 4.3). This is a process highlighted by Walker, (1959) and Tomkeieff (1934) as potentially responsible for production of both olivine-rich and olivine-poor basalts at the County Antrim lava group.

From these observations, it has been inferred that the olivine crystallised first as micro-phenocrysts within the magma storage system, with some gravity settling occurring during this process resulting in the olivine-poor and olivine-rich basalts seen across the lava group. Following this, magma was erupted within an effusive eruption (identified by the lack of ash within the field (Tomkeieff, 1940)), through shield volcanoes that are now recognised in the area as basalt/dolerite plugs (Tomkeieff, 1940). Further crystallisation occurred post-eruption within the lava

flow, with basalts in the middle zone of the lava flow being responsible for basalts of the likes of ESA01-A (due to the lack of vesicles present, mentioned above). The location within the lava flow would allow for a low temperature to be maintained, and for pyroxene and plagioclase to crystallise as intercumulus growth within the crystal-mush setting in the flow between the previously crystallised olivine micro-phenocrysts. Normal zoning occurred within plagioclase during the cooling of this lava flow, with its preservation due to the low crystallisation temperatures (Deer *et al.,* 2013). The moulding of spinel and apatite crystals to plagioclase within ESA01-A (Chapter 4.1.3, Figure 26a), a feature also highlighted by Tomkeieff (1940), indicates it too crystallised from intercumulus melt, with the inclusions of olivine and plagioclase within the spinel suggesting it was one of the last mineral phases to crystallise.

5.1.3. New Mexico

The Sierra Madre Occidental is mid-Cenozoic in age (Cameron *et al.,* 1989), and situated in western North-America, extending southwards from the USA border to the Trans-Mexican volcanic belt (Demant *et al.,*1989), Figure 58. The province formed in association with evolution of western North America and the subduction of the Farallon plate, displaying sequences of orogenic andesites and ignimbrites, commonly overlain by the basaltic andesites known as the Southern Cordilleran Basaltic Andesite (SCORBA) suite – a suite first recognised in New Mexico (Cameron *et al.,* 1989).

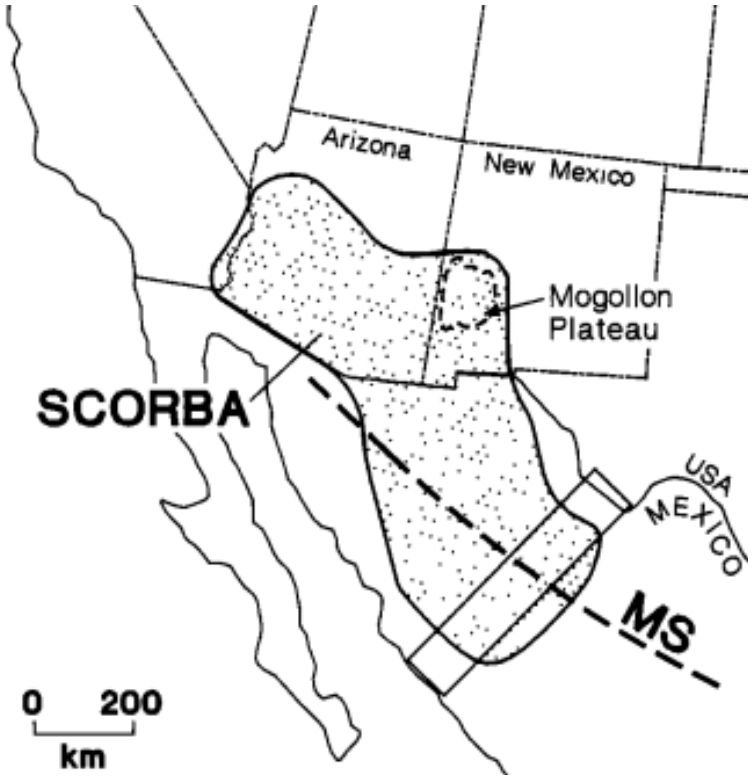

Figure 58 - Diagram displaying the location of SCORBA lavas across Western North America (Source: Cameron et al., 1989)

The SCORBA lavas are 32-17 Ma in age and are most common in New Mexico, southern Arizona, Sorona and Chihuahua. It has been inferred that the SCORBA suite was erupted from a broad shield volcano situated on a major rift fault, with volcanism reaching its peak ~21 Ma. This volcanism event was associated with Cordilleran magmatism and may be linked to an interpretation by Ferrari *et al.,* (2007) as 'post-ignimbritic transitional mafic volcanism', where basaltic lava erupted during and after each pulse of ignimbrite eruption. Magma was stored in a magma plumbing system prior to this eruption (Cameron *et a.,* 1989). The volcanic setting has been interpreted as intraplate in origin within an intra-rift arc setting (Figure 59), formed in a tectonic sequence comprised of three stages: a compression stage (seeing the sub-horizontal subduction of the Farallon plate

under the North American plate), an early phase extensional regime (seeing the steepening of Farallon plate subduction and associated slab-pull causing lithospheric delamination), and a late stage extensional phase (seeing the formation of the basin and range topography visible across western North America (Cameron *et al.,* 1989; Ward *et al.,* 2017). The intra-rift arc setting was inferred due to the lack of continuous arcs present during major SCORBA volcanism, as well as a lack of distinction in geochemistry within $^{87}Sr/^{86}Sr$ rations that are common of basalts erupted in back arc settings (Cameron *et al.,* 1989).

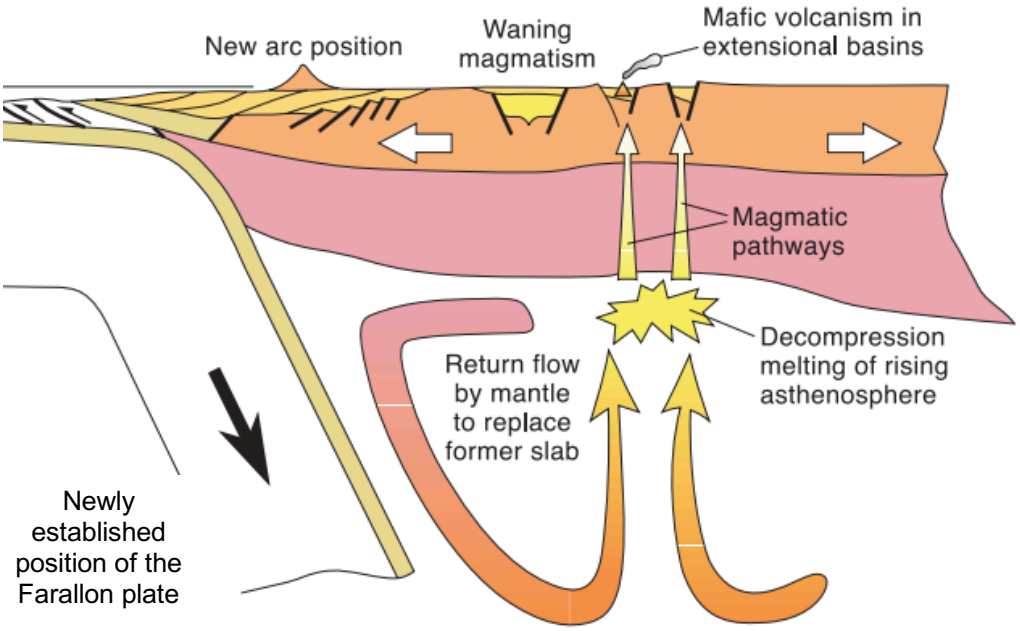

Figure 59 - Diagram displaying the inferred geological setting during the eruption of SCORBA and PRE-SCORBA basalts in New Mexico. Steepening of the subducting Farallon plate allowed for asthenospheric mantle to mix with mantle wedge material, this material then rose through decompression melting and transported through dikes before erupting in extensional basins (Source: Chapin et al., 2004).

The SCORBA suite comprises a sequence of basalts and basaltic andesites, as well as interlayered rhyolite ignimbrites characteristic of bimodal silicic volcanism that is thought to be influenced by the dehydration of the subducting Farallon plate. As well as this, the suite has also been likened to the CRFB, specifically the Grande Ronde basalt formation (Cameron *et al.,* 1989). Whilst both were intraplate in origin, however, they were formed in different environments, with the SCORBA suite erupting in an environment less extensional than CRFB due to its intra-rift arc setting.

Geochemically, SCORBA suite samples in New Mexico contained SiO_2 concentrations of between 47-61 wt%, representing a basaltic andesite composition and plotting with Hawaiian alkalic basalts on a TAS diagram (Cameron *et al.,* 1989). Stratigraphically below the SCORBA suite are more silicic lavas (>60% SiO_2) and rare mafic lavas that are present as both basalts and basaltic andesites, these rare lavas are known as PRE-SCORBA (Cameron *et al.,* 1989). Bulk compositions displayed by New Mexico in this study comprise of ~51.72 $\pm$ 0.08 wt% SiO_2. New Mexico plots alongside Hawaii 2 on a TAS diagram (Chapter 4.1.4, Figure 29), and represents an alkaline composition unlike the tholeiitic composition represented by basaltic andesites in the SCORBA suite (Cameron *et al.,* 1989), therefore, has been deemed PRE-SCORBA in this study. This alkaline composition is likely the result of magma source region mixing resulting from dehydration of the subducting plate in the samples formation, discussed in Chapter 1.2.

PRE-SCORBA basalts and basaltic andesites are petrographically distinct, with basalts being dominantly aphyric (rarely porphyritic), whilst the basaltic andesites

are coarsely porphyritic featuring phenocrysts of plagioclase, orthopyroxene (a mineral limited to the PRE-SCORBA basalts only), augite, olivine, and Fe-Ti oxides, with a maximum grain size measuring ~2-3mm (Cameron *et al.,* 1989). SCORBA basaltic andesites, on the other hand, are commonly aphyric, with rare phenocrysts of olivine and plagioclase in addition to even rarer augite. Using these observations, the porphyritic texture seen within New Mexico (Chapter 4.1.4, Figure 28a), in addition to the presence of orthopyroxene and augite within the sample (Appendix 1c), also suggests that New Mexico is of PRE-SCORBA origin. Despite this, Cameron *et al.,* (1989) did suggest that PRE-SCORBA shows no Fe-enrichment, a process that is visible in New Mexico.

Similar to Hawaii 1 and 2, the porphyritic texture visible in New Mexico implies multiple cooling stages prior to eruption, with the large sizes of some phenocrysts indicating a longer crystallisation time at higher temperatures. This was also highlighted by Cameron *et al.,* (1989), who inferred the PRE-SCORBA magma to have risen to the surface slower than that of SCORBA, allowing for an extended crystallisation time. Similar to both of these samples, the euhedral nature of these phenocrysts indicates they were present in the magma prior to eruption. Unlike Hawaii 1 and Hawaii 2, however, New Mexico indicates three stages of cooling, displaying both macro- and micro-phenocrysts (grain sizes in Table 4) surrounded by fine-grained groundmass (Chapter 4.1.4, Figure 28a).

The normal zoning (Mg-rich cores to Fe-rich rims, Chapter 4.1.4) displayed by the macro-phenocrysts, and composition of micro-phenocrysts representing the composition of the Fe-rich macro-phenocryst rims suggests the occurrence of magma recharge, involving the introduction and mixing of a more evolved, higher

temperature, Fe-rich magma after the crystallisation of the olivine macro-phenocrysts. This was highlighted in a study by Gordeychik *et al*., (2018), which looked at growth and diffusion of olivine in basalt magmas from Shiveluch volcano. See a comparison of normally zoned phenocrysts in Gordeychik *et al.,* (2018) and New Mexico in Figures 60a and 60b. The introduction of this magma caused the outer cores of the olivine macro-phenocrysts to equilibrate with the more evolved magma, with unaffected cores indicating incomplete diffusion. The similar composition of macro-phenocryst rims to the Fe-rich micro-phenocrysts suggests the micro-phenocrysts crystallised from the higher temperature, more evolved magma responsible for the normally zoned macro-phenocrysts. Additionally, the smaller grain size of micro-phenocrysts suggests a quicker crystallisation.

Evidence for magma mixing is also indicated by Ca-poor pyroxene reaction rims/overgrowths present surrounding both plagioclase and olivine micro-phenocrysts (Chapter 4.1.4). Tsuchiyama, (1986), found that the introduction and magma mixing of a compositionally different magma (for example, one that is more evolved) or one of a different temperature resulted in the formation of pyroxene reaction rims, with these observations supporting Cameron *et* al., (1989) who interpreted the occurrence of magma mixing in PRE-SCORBA lavas.

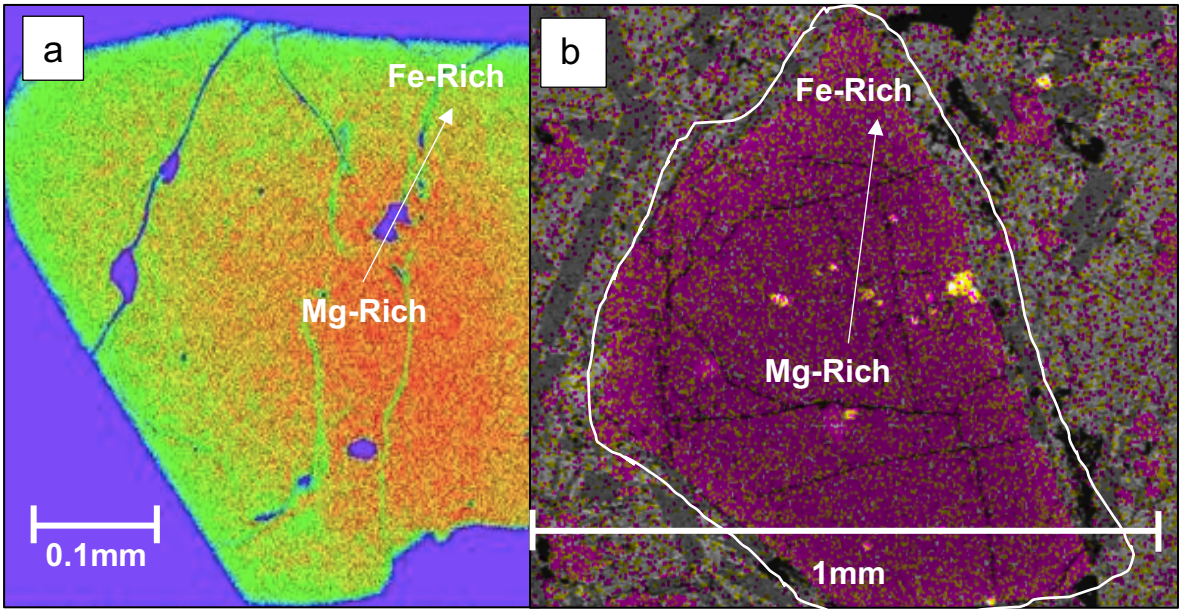

Figure 60 - a) Example of the normal zoning exhibited by olivine phenocrysts in a study by Gordeychik et al., (2018). These phenocrysts comprise of Mg-rich centres (Red), with a gradual change to Fe-Rich rims (Green), zoning also present within New Mexico and interpreted to represent magma recharge. b) Example of the normal zoning exhibited by olivine macro-phenocrysts in New Mexico (at 40x magnification), with them comprising of Mg-rich centres (pink) and Fe-rich rims (yellow). Zoning in Figure 60a is stronger than that of Figure 60b.

These observations suggest the olivine macro-phenocrysts crystallised deeper in the magma plumbing system, before the introduction of a more evolved magma resulted in magma mixing and the zoning of the olivine macro-phenocrysts, followed by the crystallisation of olivine micro-phenocrysts. It has also been inferred that plagioclase crystallisation began after the introduction of this magma, due to the lack of zoning present in these phenocrysts. Additionally, the euhedral shape of plagioclase laths exhibited by New Mexico indicates the crystallisation within a magma of <7 wt% MgO (Thompson *et al.,* 2005), therefore,

the magma mixing process of a more evolved magma may have allowed the MgO to decrease enough for these euhedral phenocrysts to form. This coincides with the bulk MgO concentration of 3.44 ± 0.57 wt% found in New Mexico (Table 7). This mixing could have occurred during the steepening of the subducting Farallon plate (see above), causing asthenospheric mantle to mix with more enriched mantle material in the opened mantle wedge, (Chapin *et al.,* 2004), and be incorporated into the magma plumbing system. Further magma recharge of a lower temperature, Fe-rich magma must have then occurred to form the Ca-poor pyroxene reaction rims around plagioclase laths and olivine micro-phenocrysts prior to eruption, this has been inferred from the lack of zoning within the plagioclase and olivine micro-phenocrysts, suggesting magma of similar composition but lower temperature was introduced. The platy pyroxene crystals and spinifex plagioclase present in the groundmass suggests that the groundmass cooled rapidly once erupted (Lowrey *et al*., 2017).

Across all the terrestrial samples analysed, ESA01-A is the most differentiated lava, displaying a lower Mg# to that of Hawaii 1, Hawaii 2 and New Mexico (Figure 61). Of these terrestrial samples, New Mexico is the only sample that exhibits magma mixing/magma recharge processes (see above). In comparison to the remaining terrestrial samples, the centres of the New Mexico olivine macro-phenocrysts represent the most primitive terrestrial magma within this study, with the more differentiated magma responsible for the formation of the rims on these macro-phenocrysts baring a more similar composition to the Hawaii 1 and Hawaii 2 lavas studied.

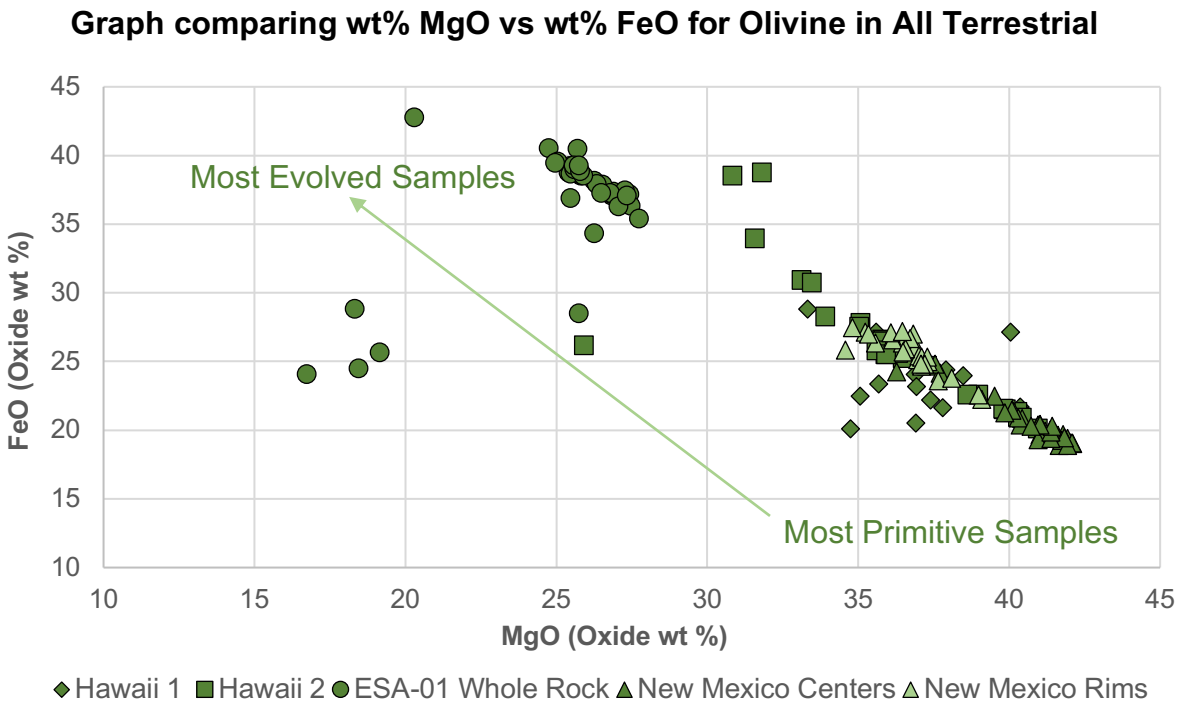

Figure 61 – Graph displaying a linear treat when plotting wt% MgO and wt% FeO contents of olivine within all terrestrial samples analysed within this project, with the highest MgO content marking the most primitive sample

5.2. Geological Formation of Martian Samples

Through the study of meteorites, particularly involving the study of Rare Earth Element (REE) and Light Rare Earth Element (LREE) patterns, three distinct source magmatic reservoirs have been interpreted to be present on Mars (Kiefer & Jones, 2015). These differing source regions are described by Taylor, (2020) as the result of the differentiating global magma ocean (discussed in Chapter 2.3) that took place in early Martian history, or the resulting magmatic activity. The reservoirs are thought to have formed within the first 50-100 million years of Mars' history, and defined by their radiogenic isotopes (Kiefer & Jones, 2015). Two of

these reservoirs are labelled the ‘Enriched’ and ‘Depleted’ reservoirs with the third being ‘Intermediate’ but can be included under the ‘Enriched’ bracket (Schulz *et al.,* 2020), with analysis of REE and LREE patterns allowing for the interpretation of which reservoirs may be the source region for some Shergottite meteorites. Enriched and depleted shergottites can also be differentiated by their ages (enriched shergottites are younger than depleted shergottites), as well as their spread in Zr/Nb ratios (enriched shergottites demonstrate a narrower spread), (Schulz *et al.,* 2020). It has been inferred that Shergottites are likely depleted in nature when first formed, with their enrichment dependent on their interaction with crust and lithospheric material (Kiefer & Jones, 2015). This agrees with the interpretation by Jones (2003) which suggested the enriched component of enriched Shergottites could be the result of crustal contamination. Of the samples studied, NWA1110 and NWA7397 are of enriched origin (Shearer *et al.,* 2007; Howarth *et al.,* 2014), whilst Tissint is inferred to be depleted in nature (Basu Sarbadhikari *et al.,* 2016).

The lack of plate tectonics on Mars (see Chapter 2.3), indicates that the volcanism displayed on Mars is intraplate in origin. Similar to terrestrial intraplate volcanism, it’s been inferred that mantle generated magma on Mars rises to the surface due to adiabatic compression (Kiefer *et al.,* 2015) and an increase in buoyancy as a result of density variations within the mantle (Carr, 2006), although a smaller gravitational acceleration on Mars lessens these forces in comparison to Earth. The general mode of magma transport through the mantle is thought to be through diapirism (Carr, 2006), with volcanism indicating some presence of mantle convection (Kiefer *et al.,* 2015; Kiefer, 2010). Self-compaction of the Martian crust (Chapter 2.3) means that as magma rises, the density of the

surrounding rock decreases, causing the magma to stall and pool out below the surface (Carr, 2006). This results in the formation of dike networks, as well as potentially allowing a magma reservoir to form (Carr, 2006). Addition of a fresher magma rising into the magma reservoir may then alter the pressure and instigate a rise of magma towards the surface (Mitchell & Wilson, 2003).

5.2.1. NWA7397

NWA7397 in this study has been found to represent the non-poikilitic lithology of this meteorite identified in a previous study by Howarth *et al.,* (2014). This was determined by the identification of merrillite, Chapter 4.2.1 (present only in the non-poikilitic lithology), and the Mg# of Ca-poor pyroxene grains observed in this study generally being <70 (Appendix 4e), and hence representing Ca-poor non-poikilitic pyroxene (Howarth *et al.,* 2014).

On average across NWA7397, the bulk FeO content is ~23.48 $\pm$ 0.02 wt% FeO. This, in addition to a Mg# of 58.08, suggests that this sample crystallised within a moderately evolved melt that had undergone differentiation prior to crystallisation. Additionally, the Fe-rich nature of olivine within this sample ($Fo_{41-49}Fa_{51-59}$), as well as the average Mg# of olivine being 58.51 also indicates differentiation of the melt prior to their crystallisation, falling outside of the equilibrium line for olivine and melt within a predicted primary Martian melt (Figure 66). The evolved nature of this melt has been inferred by Howarth *et al.,* (2014) to be the result of crystallisation of a poikilitic lithology that has previously been observed in NWA7397 prior to the crystallisation of the non-poikilitic lithology. Within this study, however, there was a lack of this poikilitic lithology, therefore,

this stage of the crystallisation process has been based on interpretations by Howarth *et al.,* (2014).

To add to this, the sub-euhedral, un-zoned nature of olivine grains provides a lack of evidence for the re-introduction of these crystals into the melt that is more similar to what is seen in olivine-phyric Shergottites (see below), (Shearer *et al.,* 2008), although the rounded nature of these grains could suggest that some resorption has occurred (Lin *et al.,* 2005). As a result, it's been inferred that these olivine grains crystallised within the melt and are not xenocrysts or antecrysts. Additionally, their larger grain size (Table 4), also suggests they crystallised deeper in the magma storage system, prior to the crystallisation of the interstitial melt. The inclusion and association of spinel grains within olivine across the sample (as opposed to the encompassing of spinel around interstitial plagioclase and pyroxene seen within ESA01-A, (Chapter 4.1.3, Figure 26a) suggests early co-crystallisation of the olivine and spinel mineral phases (Howarth *et al.,* 2014).

The anhedral grain shapes (intergrowths) exhibited by plagioclase and pigeonite (Ca-poor pyroxene) in NWA7397 (Chapter 4.2.1, and below in Figure 62), as well as the angular contact between both pigeonite and augite, indicates that these mineral phases co-crystallised alongside each other in an interstitial melt (Mikouchi & Kurihara, 2008; Gillet *et al*., 2005). Additionally, it was inferred by Howarth *et al.,* (2014), that crystallisation temperatures for this lithology range from 1100-1200°C based on the co-existence of individual grains of both Ca-poor and Ca-rich pyroxenes in the same sample (with this coexistence also present within this study). The presence of both augite and pigeonite in NWA7397 (Chapter 4.2.1) also suggests that this melt was crystallising whilst in equilibrium

with the surrounding melt (Poldervaart & Hess, 1951), also indicated by the lack of zoning present within this sample.

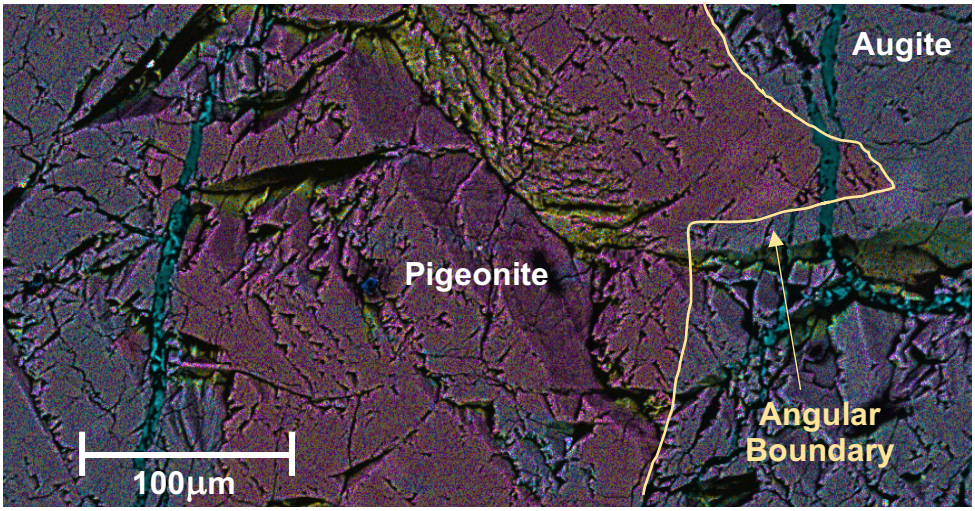

Figure 62 - EDS image (250x magnification) displaying the angular contact between distinct grains of pigeonite and augite in NWA7397, indicative of co-crystallisation of these mineral phases

The overall formation of NWA7397 can be seen in Figure 45. The formation is inferred to have begun by the pooling out of more buoyant, partially melted magma within the crust to form a staging chamber (Howarth *et al.,* 2014), as a result of decreasing density of surrounding material due to the self-compaction of the planetary body (Carr, 2006). From here, chromite and olivine within NWA7397 is thought to have crystallised, instigating the formation of the earlier formed poikilitic texture observed in other samples of this meteorite, and is inferred by Howarth *et al.,* (2014) to have crystallised from a REE-enriched parental magma. The crystallisation of the poikilitic lithology could have resulted in the fractionation of the melt, giving rise to the high-Fe content and evolved nature of the Mg# displayed within the later formed, non-poikilitic lithology of NWA7397 exhibited in this study.

Within the staging chamber, further olivine and chromite crystallisation may then have occurred from the now more fractionated, Fe-rich melt, with the depth of this crystallisation allowing for the larger, more euhedral grain characteristics displayed by olivine in the sample. Transportation of this magma to the near surface, carrying the earlier-crystallised Fe-rich olivine and chromite (Howarth *et al*., 2014) then occurred, with the magma storage system inferred by Howarth *et al.,* (2014) to be increasingly Fe-rich towards the top. If this near surface magma was more Fe-rich than the already Fe-rich olivine crystals being transported through the system, this could be responsible for the resorption indicated by the rounded nature of the olivine grains. If this is the case, the lack of zoning within these olivine grains suggests that they reached complete re-equilibrium with the more Fe-rich melt.

After transportation to the near surface, the crystallisation of the interstitial melt occurred, with the shallower crystallisation resulting in the decrease in grain size for interstitial mineral phases displayed in this study (Table 4). The interstitial Ca-poor (pigeonite) and Ca-rich (augite) pyroxene experienced co-crystallisation (indicated by the angular contacts between both pigeonite and augite grains in the sample), with their coexistence indicating crystallisation temperatures of 1100-1200°C within equilibrium conditions (Howarth *et al.,* 2014). The crystallisation of pigeonite and augite also occurred alongside plagioclase crystallisation, determined due to the angular nature of intergrowths between both pyroxenes and plagioclase in NWA7397. Pyrrhotite and merrillite were the last minerals to crystallise, and could be the result of terrestrial alteration.

Fractures infilled with calcite across the sample are likely secondary minerals from terrestrial alteration (Crozaz *et al.,* 2003).

The similar mode of formation inferred by Howarth *et al.,* (2014) for NWA7397 was also taken a step further, with Howarth *et al.,* (2014) indicating the processes that formed the poikilitic Shergottite NWA7397 could be related to the formation of enriched olivine-phyric Shergottites. In particular, their model was likened to that of Filiberto *et al.,* (2010) for NWA1068 (an olivine-phyric Shergottite that is paired with NWA1110), where the interpreted formation for NWA1068 saw the emplacement and final crystallisation of the magma on the surface/near surface (<4.3 kbar) rather than remaining intrusive (Figure 63).

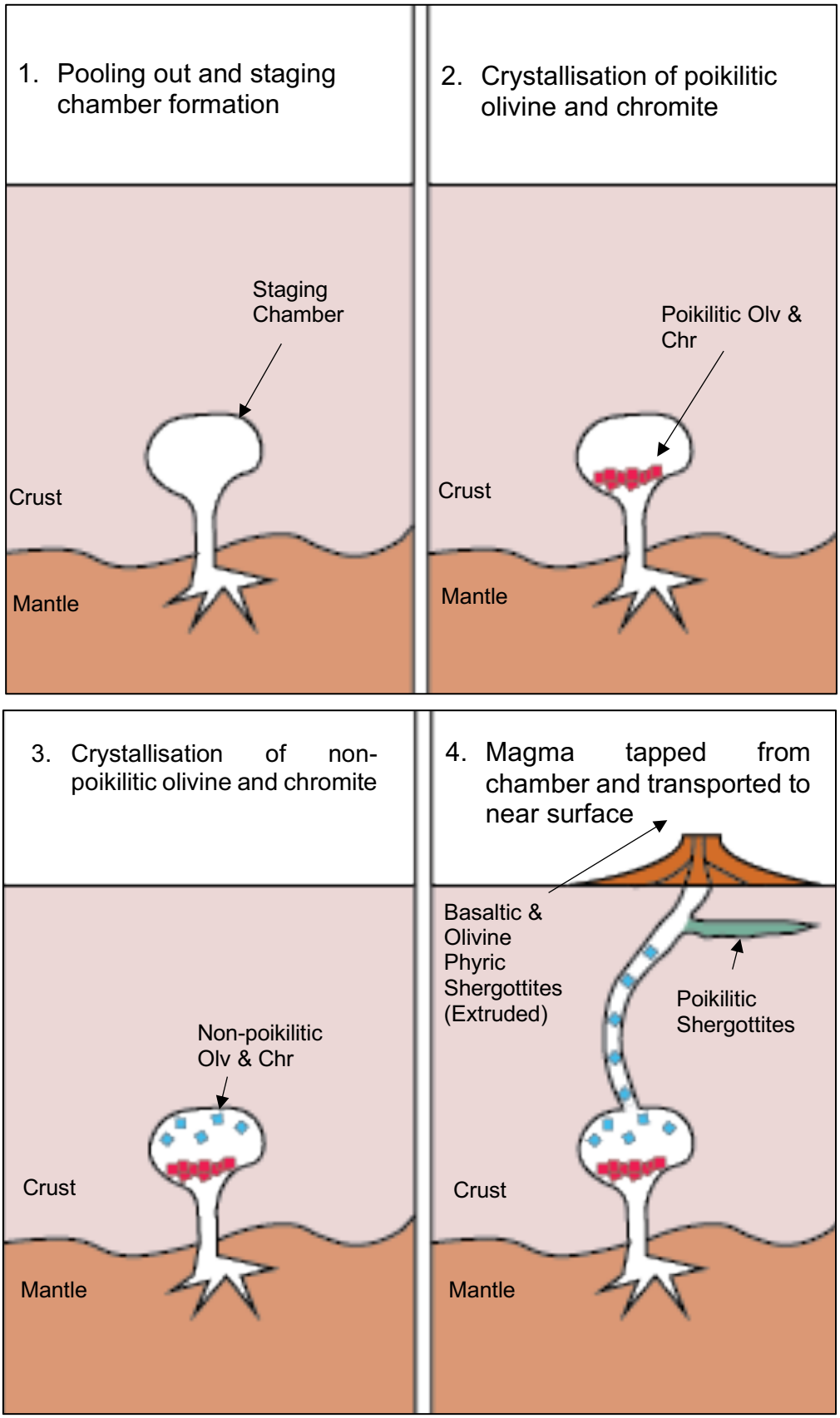

Figure 63 - Schematic after Howarth et al., (2014) illustrating the inferred formation of NWA7397 within this study

5.2.2. NWA1110

Across studies on olivine-phyric Shergottites, there have been large debates on the origin of these olivine 'macro-phenocrysts' (Shearer *et al.,* 2008), and whether they are phenocrysts, antecrysts, or xenocrysts. Whilst phenocrysts crystallise from the same melt as the bulk rock (Liu *et al.,* 2016), antecrysts represent the addition of previously accumulated cogenetic olivine within a basaltic melt, with compositions that differ from the host melt but originate from the same overall system (Liu *et al.,* 2016). These are referred to as megacrysts by Shearer *et al.,* (2008). Xenocrysts, on the other hand, originally form either from a separate melt or due to impact melting and being incorporated into the basaltic melt, and (unlike antecrysts) are not co-genetic with the bulk rock (McSween, 2015).

NWA1110 bares a large resemblance to the petrological observations and geochemical data observed in the terrestrial sample, New Mexico (discussion further in Chapter 5.5), with one of the main similarities between the two being the porphyritic texture of olivine 'macro-phenocrysts' and micro-phenocrysts. Due to its similarity to New Mexico, the presence of both olivine 'macro-phenocrysts' and micro-phenocrysts across NWA1110 were originally thought to indicate three phases of cooling during its crystallisation history, with the 'macro-phenocrysts' being phenocrysts in origin. Despite this, unlike the olivine macro-phenocrysts in New Mexico, those in NWA1110 not only enclose inclusions of spinel (particularly un-zoned chromite), but also trapped melt (Chapter 4.2.2, Figure 47), and appear more sub-anhedral in shape. The sub-anhedral grain shapes and exteriors that appear corroded (Chapter 4.2.2, Figure 47), indicates that these 'macro-phenocrysts' have experienced some resorption (Shearer *et al.,* 2008)

suggesting that they could potentially be xenocrysts (or antecrysts) that were re-introduced to the melt within the magma storage system, prior to eruption (Papike *et al.,* 2009).

The composition of augite within this trapped melt falls within the compositional range displayed by augite within the remainder of the sample (Table 5), indicating that these inclusions are from the same melt. Additionally, previous studies analysing the LREE compositions within the trapped melt in NWA1110 also found that it represents the same melt as the bulk rock (with the LREE contents of trapped melt mirroring that of the bulk rock), (Shearer *et al.,* 2008). As a result, it has been inferred that the interstitial melt responsible for the groundmass was already present and of final melt composition prior to the introduction of the olivine 'macro-phenocrysts'. From these observations, it has been inferred that the olivine 'macro-phenocrysts' within this sample are antecrysts or xenocrysts in nature.

To add to this, when plotting Mg# for the olivine 'macro-phenocryst' cores against that of the bulk rock (Figure 66), it can be inferred that NWA1110 not only falls outside of the predicted equilibrium line for olivine and melt within primary Martian magmas, but also contains excess olivine (with this excess olivine likely represented by antecrysts, or xenocrysts), (Filiberto *et al.,* 2010). Finally, analysis from previous studies on REE patterns of melt inclusions and the bulk rock, as well as zoning trajectories expressed by nickel, cobalt and manganese within olivine on this sample carried out by Shearer *et al*., (2008) determined these olivine 'macro-phenocrysts' to be co-genetic, and so demonstrating an

antecrystic origin. As a result, these ‘macro-phenocrysts’ within NWA1110 will be referred to as antecrysts for the rest of this study.

The normal zoning of these olivine antecrysts present in NWA1110 indicates that, when introduced, they were in disequilibrium with the melt (Dunham *et al.,* 2019), resulting in the normal zoning of Mg-rich cores to Fe-rich rims, seen in Chapter 4.2.2, Figure 45 (zoning that is also visible in New Mexico, see Chapter 5.1.4, Figure 60b). This has also been observed in other olivine-phyric Shergottites, such as LAR 12095 and LAR 12240, (Dunham *et al.,* 2019). Mg-rich cores (Mg# = 66.05) of these antecrysts in comparison to the cores of the olivine micro-phenocrysts in this sample (Mg# = 48.39) indicate that they must have crystallised in a much more primitive melt prior to their introduction to the melt. Observations similar to these but for another olivine-phyric Shergotitte (LAR 06319) were also made by Balta *et al.,* (2013), who also interpreted an antecrystic nature of these large olivines within LAR 06319. Additionally, the presence of these antecrysts could be responsible for the high MgO content of the bulk rock within NWA1110 alongside the higher FeO content (see Chapter 5.4, Table 7), (Larrea *et al.,* 2012).

Table of Geochemical Data for Augite in Trapped Melt and Bulk Sample, NWA1110

Spectra	SiO_2	MgO	FeO	CaO	Al_2O_3	Total
	All data in wt% Oxide					
Augite 1 (Trapped Melt)	51.51	17.32	12.77	15.86	2.55	100.01
Augite 2	47.87	16.15	22.42	11.39	2.17	100.00
Augite 3	54.62	14.43	17.63	13.32	N/A	100.00
Augite 4	56.75	16.76	13.27	10.34	2.87	99.99
Augite 5	51.42	16.54	13.53	16.12	2.38	99.99

Table 5 - Table displaying the compositions of the augite in trapped melt as well as augite in the groundmass within Site 4 of NWA1110.

The lack of zoning present in the olivine micro-phenocrysts suggests that these were in equilibrium with the melt during their crystallisation (Shearer *et al.,* 2008). Additionally, the Fe-rich nature of these micro-phenocrysts suggest that they crystallised within an already differentiated melt, with their sub-euhedral shape and larger grain size in relation to the finer grained pyroxene/plagioclase groundmass suggesting their crystallisation occurred prior to eruption. Additionally, these micro-phenocrysts compositionally overlap with the rims of the olivine antecrysts (Chapter 4.2.2), indicating the antecrysts were in disequilibrium with the melt responsible for the crystallisation of these micro-phenocrysts.

The finer grained groundmass comprising of pyroxene and plagioclase relative to olivine micro-phenocrysts (Table 4) indicates that this component crystallised

relatively quick (Papike *et al.,* 2009), and post-olivine micro-phenocryst crystallisation. Additionally, the patchy, complex zoning exhibited by pyroxene across NWA1110 could represent a shock texture as a result of impact heating, causing associated recrystallisation. This texture has also previously been interpreted to be the result of a multistaged cooling and growth phenomenon (Basu Sarbadhikari *et al.,* 2016). The recrystallisation of these finer pyroxenes could explain why some of the larger pyroxene grains remain normally zoned, whilst the smaller pyroxene grains experience the patchy more complex zoning (Chapter 4.2.2, Figure 47). The normal zoning within larger pyroxene grains is more likely a product of closed system crystal fractionation, exhibiting the evolution of Fe-rich cores to Ca-rich rims similar to that seen in Tissint (discussed below), (Basu Sarbadhikari *et al.,* 2016).

The variation of spinel compositions, as well as the presence of ilmenite in the groundmass, suggests multiple stages of crystallisation for these accessory minerals. Firstly, the chromite appearing as inclusions within the olivine antecrysts of NWA1110 (Chapter 4.2.2, Figure 47), displays a notable lack of zoning. The inclusion and association of chromite with the olivine antecrysts indicates that these chromite grains crystallised before the olivine antecrysts (Dunham *et al.,* 2019), and could have been reprocessed into the melt alongside these antecrysts later in the crystallisation history of NWA1110. The zoning present across some chromite grains in the sample largely occurs when in contact with the groundmass, indicating a disequilibrium between these grains and the surrounding, more differentiated, groundmass. Finally, ilmenite is largely concentrated within the groundmass of NWA1110, indicating a later stage crystallisation alongside the olivine micro-phenocrysts.

From these observations on the analysis of NWA1110, it has been inferred that the crystallisation history started with the ponding out of magma at the base of the crust (Filiberto *et al.,* 2010) before the early crystallisation of chromite and olivine antecrysts that are potentially cumulate in nature began (Gross *et al.,* 2011; Balta *et al.,* 2013). This crystallisation may have occurred at a greater depth and at a slower rate to give rise to a larger grain size of olivine (Balta *et al*., 2013), with antecrysts possibly residing in a cumulate pile or on the sides of the magma reservoir before being later entrained into the melt prior to eruption (Balta *et al.,* 2015). Differentiation of the magma must have occurred following the olivine antecryst's crystallisation to give rise to a more evolved, Fe-rich melt that eventually saw the crystallisation of the Fe-rich olivine micro-phenocrysts visible across the sample. This could have been as a result of fractional crystallisation and accumulation of the olivine antecrysts resulting in the fractionation of the melt, suggested to be responsible for the formation of the non-poikilitic lithology in NWA7397 (Howarth *et al.,* 2014). Additionally, this ponding out of magma was suggested by Jones (2003), to allow for crustal contamination of the magma, based on interpretations on another olivine-phyric Shergottite NWA1068 (of which is paired with NWA1110). This crustal contamination has also been suggested by Jones (2003), and is inferred to be responsible for an 'enriched' component of NWA1110 (although this was not observed in this study).

From the differentiated magma, the Fe-rich olivine micro-phenocrysts crystallised, occurring at a shallower depth to result in a smaller grain size. Finally, within the active magmatic system antecrysts that were previously crystallised may have been disrupted and introduced into this melt (Dunham *et*

al., 2019), with Balta *et al.,* (2013), suggesting this process may have occurred pre-eruption. An introduction of these Mg-rich antecrysts into the Fe-rich melt would cause the disequilibrium required for the normal zoning of these antecrysts to occur, allowing for the Fe-rich rims of these antecrysts to be of similar composition to the olivine micro-phenocrysts within the melt. Zoning of the earlier crystallised chromite grains could have also occurred at this stage. Crystallisation of the pyroxene and plagioclase interstital melt then occurred rapidly, alongside the ilmenite accessory minerals within the groundmass, likely on or very close to the Martian surface (Filiberto *et al.,* 2010). The fracturing of olivine visible across the sample is likely a secondary texture produced by shock on the sample through impacts on the Martian surface (Dunham *et al.,* 2019). A diagram for the inferred formation of NWA1110 (as well as Tissint) can be seen in Figure 67.

5.2.3. Tissint

Despite having a more euhedral-subhedral shape (as opposed to the sub-anhedral shape exhibited by olivine antecrysts in NWA1110), irregular exteriors of olivine 'macro-phenocrysts' in Tissint indicates that these could also be antecrysts in origin. As well as this, unlike NWA1110, there appears to be a sharper boundary between the cores and rims of olivine 'macro-phenocrysts' within Tissint, see Figure 64, which could represent a gap between the core crystallisation and the zoning process that formed these rims (Mari *et al.,* 2020). This sharp boundary compared to the gradual transition from core to rim in NWA1110 antecrysts indicates that Tissint underwent disequilibria diffusion more rapidly (Basu Sarbadhikari *et al.,* 2016).

The Mg-rich nature of 'macro-phenocryst' cores observed in Tissint suggests that these crystallised earlier in a more primitive melt (Mari *et al.,* 2020), with their large grain size indicating that this occurred deeper in the magma storage system. The normal zoning of Mg-rich cores (with an average Mg# of 72.52) to Fe-rich rims is further evidence for this interpretation (Mari *et al.,* 2020; Balta *et al.,* 2015), and suggests that these 'macro-phenocrysts' are actually antecrysts (also interpreted by Mari *et al.,* (2020) and Balta *et al.,* (2015)). It has also been inferred that these were in disequilibrium when reintroduced into the melt pre-eruption, evidenced by the normal zoning. As a result, the olivine 'macro-phenocrysts' in Tissint will be referred to as antecrysts for the rest of this study. Additionally, the presence of small chromite inclusions within these olivine antecrysts indicates that, similar to NWA1110, these were one of the first phases to crystallise, crystallising before and alongside the earlier crystallised olivine.

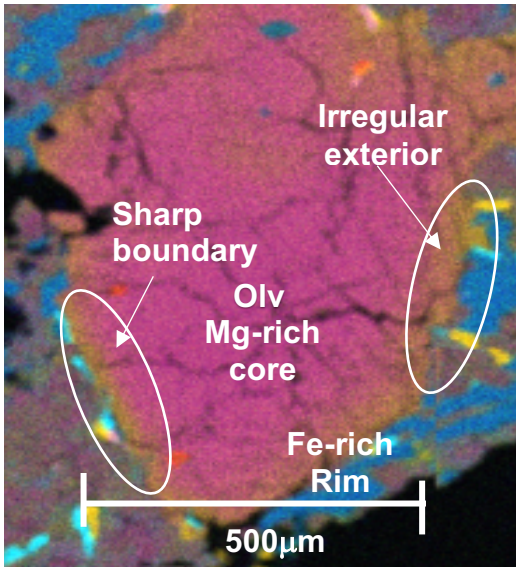

Figure 64 - EDS image (200x magnification) displaying an olivine antecryst, with the sharp boundary between Mg-rich cores and Fe-rich rims, as well as the irregular grain *exteriors highlighted by white circles. Key:* Yellow = Iron, Orange = Titanium, Teal = Calcium, Navy Blue = Aluminium, Pink = Magnesium and Green = Sodium, Red = Chromium

The lack of zoning displayed by olivine micro-phenocrysts within Tissint (Figure 65), (similar to that shown by NWA1110, Chapter 4.2.2, Figure 45), as well as a much more Fe-rich composition than those of the olivine antecryst cores (Appendix 9m & 9o), suggests that the magma must have undergone fractionation after the antecryst crystallisation. This is also indicated when comparing the Mg# cores of these antecrysts vs bulk Mg# of the sample to the suggested equilibrium line for olivine and melt within predicted primary Martian magmas (a line experimentally constrained by Filiberto & Dasgputa, (2011)). From this comparison, it can be inferred that Tissint is not representative of a primary Martian magma (Figure 66), indicating that fractionation has occurred and represented by the Fe-rich nature of the rest of the sample (post-antecryst crystallisation). This comparison is also further evidence for the antecrystic nature of the olivine antecrysts in Tissint, with the plot suggesting Tissint has accumulated excess olivine, likely in the form of these olivine antecrysts.

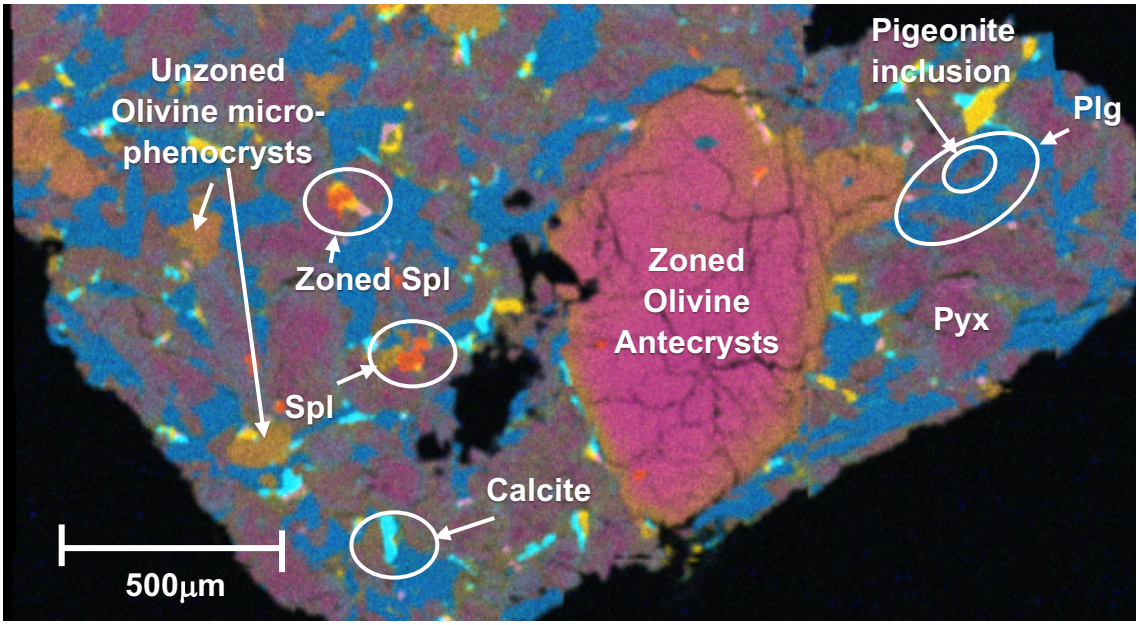

Figure 65 - EDS image (taken at 200x magnification) displaying the zoned olivine antecrysts alongside the un-zoned olivine micro-phenocrysts in Tissint. Key: Yellow = Iron, Orange = Titanium, Teal = Calcium, Navy Blue = Aluminium, Pink = Magnesium and Green = Sodium, Red = Chromium

The interpreted formation of Tissint begins with the crystallisation and accumulation of Mg-rich olivine antecrysts in the magma chamber, occurring after the pooling out and during the subsequent fractional crystallisation of magma at the base of the crust (Filiberto *et al.,* 2010) mentioned earlier in the context of NWA1110. The crystallisation of these earlier-crystallised olivine grains may be responsible for the Fe-rich, fractionated nature of the remaining melt (similar to what is inferred of the poikilitic and non-poikilitic lithology formation within NWA7397 (Howarth *et al.,* 2014)). Following the crystallisation of the Mg-rich antecrysts, magma may then have been tapped and transported shallower through the magma storage system, with the antecrysts possibly remaining in a cumulate pile or on the walls of the magma chamber prior to their later entrainment in the crystallisation history (Balta *et al.,* 2015). This must have occurred before olivine micro-phenocrysts began to crystallise due to the decrease in grain size between the antecrysts and the micro-phenocrysts, (Table 4). During a period of activity in the magmatic system, these antecrysts were then disrupted and introduced into the now fractionated melt (Dunham *et al.,* 2019), allowing for the disequilibrium relationship and subsequent normal zoning of the antecrysts with the surrounding melt.

The smaller grain size exhibited by olivine micro-phenocrysts compared to the antecrysts within Tissint (Table 4) suggests they formed at a shallower depth in the magma storage system, with their size baring large similarities to those of the plagioclase and pyroxene groundmass. Additionally, the boundary between these olivine micro-phenocrysts and pyroxenes are often anhedral in nature, indicating that these two minerals co-crystallised. These interpretations support those of Balta *et al.,* (2014), who suggested that low-Ca pyroxene crystallised

alongside Fe-rich olivine after the olivine antecrysts had been entrained into the melt. The normal zoning of pyroxenes is much more abundant than in NWA1110, and this could be accounted for by the grain size of these pyroxenes being ~100μm larger in Tissint (Table 4), requiring slower cooling times for recrystallisation of the whole crystal to occur. The normal zoning of these pyroxene grains indicates that during the crystallisation of this mineral phase, the low-Ca pigeonite crystallised first, before the evolution of pyroxene compositions to a Ca-rich, augite composition (Balta *et al.,* 2014). This zoning exhibited in Tissint has been inferred by Basu Sarbadhikari *et al.,* (2016) to be the result of close-system crystal fractionation. Patchy zoning is still observed within the finer pyroxene grains within this sample, and could be a result of impact melting and associated recrystallisation similar to NWA1110.

The inclusions of pigeonite within plagioclase grains (Mikouchi Ab *et al.,* 1999), has been observed in lithology B of another olivine-phyric Shergottite EETA 79001, and has been inferred to be the result of plagioclase crystallisation following the cease of augite crystallisation once the plagioclase field had been reached. Merrillite was one of the last phases to crystallise (Balta *et al.,* 2015), alongside ilmenite and pyrrhotite. Additionally, the fine grain sizes of all mineral phases within the groundmass indicates that this crystallisation process was relatively quick (Papike *et al.,* 2009), therefore it is inferred (similar to NWA1110), that this crystallisation occurred on or near the surface of Mars. A diagram for the inferred formation of NWA1110 and Tissint can be seen in Figure 67.

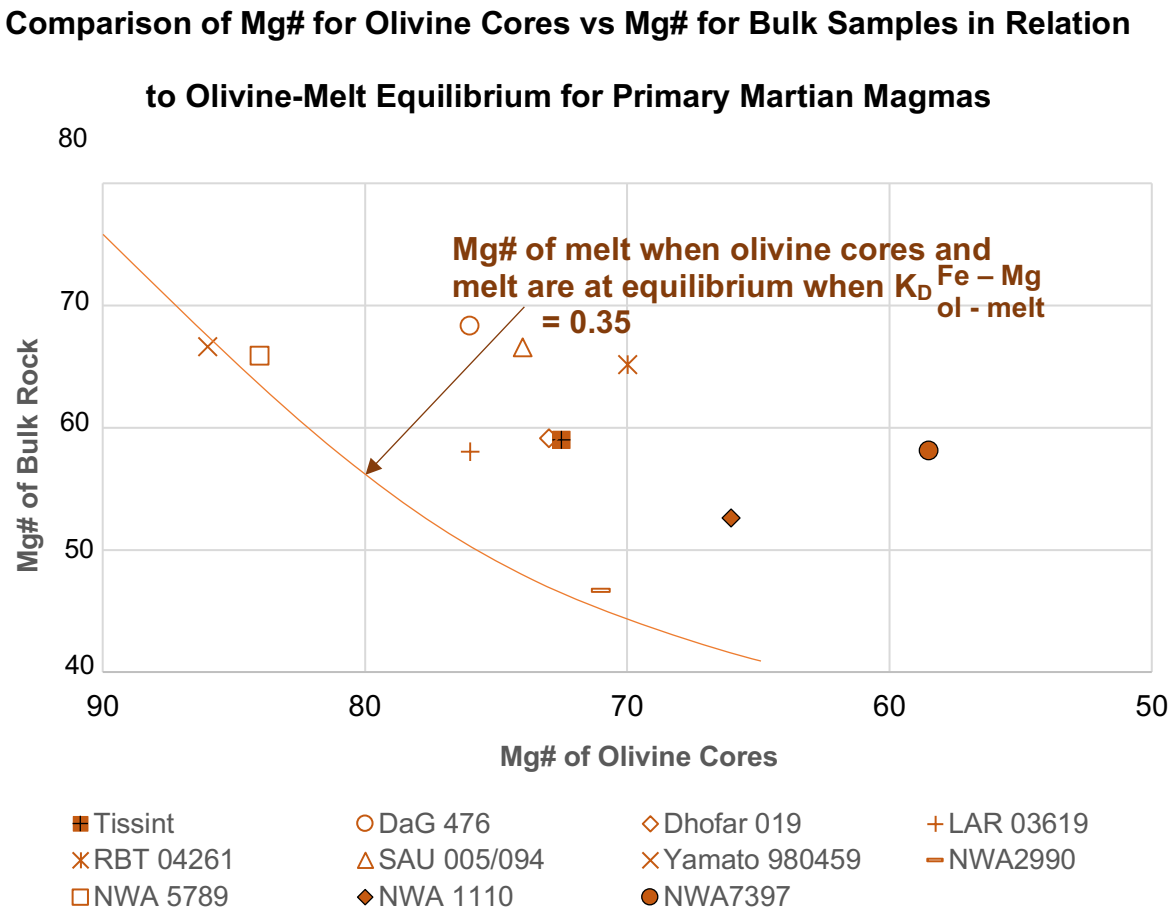

Figure 66 - Graph displaying the average Mg# of antecryst cores for NWA 1110 and Tissint, as well as olivine cores for NWA 7397 in this study compared to their bulk composition Mg#. NWA7397 was included in this plot due to the presence of olivine in this sample. Additionally, for context, average Mg# of megacryst cores for olivine-phyric Shergottites analysed in previous studies compared to their bulk Mg# composition have also been plotted in this graph (displayed by outlined markers), with data for these analyses taken from Filiberto & Dasgupta (2011) supplementary data table. The solid line represents the line of equilibrium between olivine and melt when $K_D^{Fe-Mg}_{ol-melt}$ *= 0.35, experimentally constrained by Filiberto & Dasgputa (2011).*

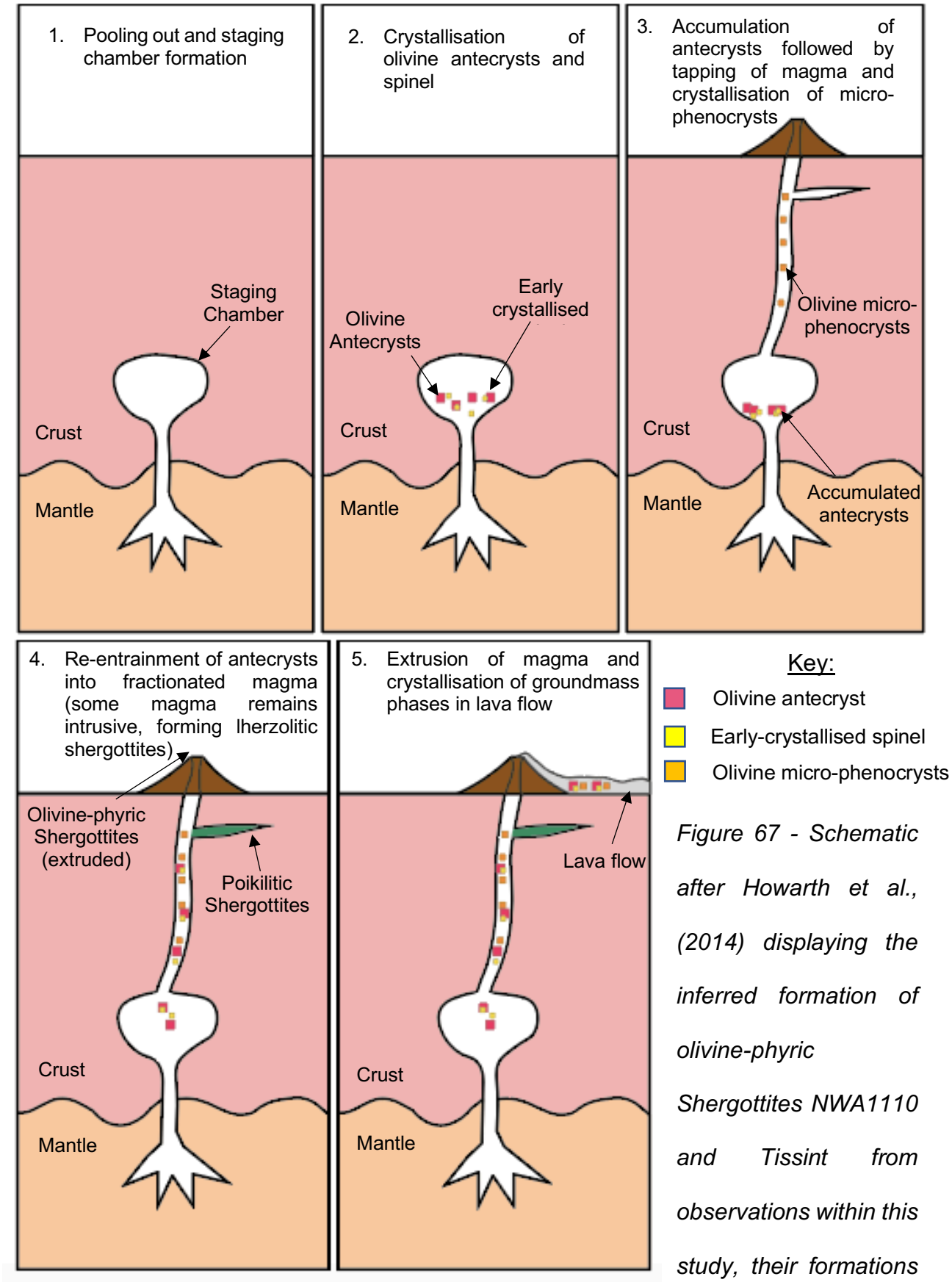

Figure 67 - Schematic after Howarth et al., (2014) displaying the inferred formation of olivine-phyric Shergottites NWA1110 and Tissint from observations within this study, their formations are discussed in detail in Chapter 5.2

5.3. An Overall Comparison of Basalts across Earth and Mars

Across all the samples analysed, there are key geochemical and petrological similarities and differences across lavas from both Earth and Mars. In this section these will be compared and discussed alongside literature data from the DVP and CRFB to identify their potential formaking accurate terrestrial analogues for Mars.

Petrological Observations:

When comparing the petrological observations of Hawaii 1 and Hawaii 2 to those of NWA7397, NWA1110 and Tissint, there are several differences that suggest these aren't the best terrestrial analogues for Mars. The presence of vesicles and infilled vesicles across both Hawaiian samples (Chapters 4.1.1 and 4.1.2) and New Mexico are noticeably absent from the Martian Shergottites, and as a result may not simulate the testing of *in situ* utilisation on Martian basalts as accurately as other, non-vesicular, analogues. The olivine micro-phenocrysts in Hawaii 1 also display a smaller grain size relative to the plagioclase laths present across the sample (Table 4), which differs greatly from the textures observed across both poikilitic and olivine-phyric Shergottites (Chapter 4.2). Additionally, the low estimated abundance of olivine within Hawaii 1 (Table 6), (and the very fine-grained nature of the groundmass) indicates that this sample would not make an accurate petrological analogue for the more olivine-rich, slightly coarser samples from Mars.

In addition to the vesicular nature of Hawaii 2, the size and abundance of plagioclase laths is largely different to those demonstrated by NWA7397, NWA1110 and Tissint (Tables 4 and 6), with plagioclase often occurring at larger sizes than olivine across the whole sample (Chapter 4.1.2, Figure 24a). Additionally, pyroxene within Hawaii 2 occurs at an incredibly fine grain size within the groundmass, resulting in a lack of pyroxene compositions collected for this sample. This also differs greatly to the abundance of pyroxene across Martian Shergottites (Table 6), occurring at much larger sizes to those observed in Hawaii 2 (Table 4). Whilst Hawaii 2 does display two phases of olivine phenocrysts (Chapter 4.2.1, Figure 24a), of which the largest phenocrysts display weak zoning (similar to olivine-phyric Shergottites NWA1110 and Tissint), the presence of vesicles, the size and abundance of plagioclase, and the scarcity of pyroxene indicates that similar to Hawaii 1, Hawaii 2 may not make the best petrological analogue for Martian basalts. Unlike Hawaii 1 and Hawaii 2, ESA01-A and New Mexico have displayed many similarities to the Martian Shergottites analysed in this study, this is discussed in more detail in the following Chapters.

Table Display the Estimated Mineral Abundances for All Samples in this Study						
	Olivine	Pyroxene	Plagioclase	Groundmass	Spinel	Carbonates
Hawaii 1	6%	8%	20%	66%	N/A	N/A
Hawaii 2	13%	(in groundmass)	60%	25%	2%	N/A
ESA01-A	15%	15%	60%	N/A	8%	2%
New Mexico	20%	(in groundmass)	30%	40%	10%	N/A
NWA7397	40%	30%	15%	N/A	10%	5%
NWA1110	20%	40%	35%	N/A	5% combined	
Tissint	20%	40%	30%	N/A	10% combined	

Table 6 - Table displaying all of the estimated mineral abundances highlighted in the 'Results' section (Chapters 4.1 and 4.2) of this study for all terrestrial and Martian samples analysed

Geochemical Observations:

Across all the Martian samples studied, NWA7397, NWA1110 and Tissint displayed similar compositions to the surface compositions analysed by the Spirit Rover in Gusev crater. The differences in geochemical composition of Martian meteorites compared to surface measurements from Gale crater (Curiosity Rover), mildly alkalic rocks from Gusev crater (Spirit Rover), TES and Pathfinder analyses (Graph 21), (mentioned in Chapter 2.3), however, has been observed, indicating further that Martian meteorites may be more representative of the rocks *in situ* utilisation may face during future space missions to Mars.

Compared to all terrestrial samples studied, Martian meteorites exhibit a substantially higher bulk content of FeO (see Table 7). This enrichment is also noticeable in olivine (Graph 21) and pyroxene compositions across the Martian meteorites, with ESA01-A being the only terrestrial sample (including literature data from the DVP) that has olivine compositions similar to the olivine (olivine micro-phenocrysts in olivine-phyric Shergottites) that crystallised in Fe-rich, fractionated magmas within Martian meteorites (discussed in Chapter 5.2). This suggests that the Martian mantle is more enriched in FeO than the terrestrial mantle (also noted by Franz *et al.,* (2019), McSween Jr (2015) and Taylor (2013)), with Taylor, (2013) suggesting this FeO rich nature is the result of oxidation of metallic iron during the accretionary process of Mars.

Alongside a higher FeO content, the Martian meteorites analysed display a lower SiO_2 content than the DVP, CRFB and all terrestrial samples studied (Figure 68). In fact, the CRFB, DVP and Hawaii 2 samples share a bulk geochemistry more similar to the Martian surface data collected by TES (Figure 68). This may indicate that these samples could make a better geochemical analogue for Martian surface compositions, however, are not analogous to the bulk geochemistry displayed by NWA7397, NWA1110 and Tissint.

The lack of plate tectonics on Mars indicates that tholeiitic lavas on Earth would be most analogous to Martian samples as they have no influence of subduction during their formation like those seen on Earth (Chapter 1.2). This is also supported by the bulk geochemistry of the Martian meteorites analysed in this study, with NWA 7397, NWA 1110 and Tissint all plotting in the tholeiitic region of TAS (Figure 68). Whilst the Spirit and Curiosity rovers did find alkalic lavas in

Gusev and Gale crater respectively, the tholeiitic composition of Martian Shergottites and their highest abundance on Earth compared to all Martian meteorites indicates further that Shergottites are more representative of material *in situ* utilisation may face on the Martian surface. As a result, terrestrial tholeiitic samples in this study (ESA01-A and Hawaii 1) would make the best analogues for bulk geochemistry in Martian Shergottites.

When analysing the bulk Mg# across Earth and Mars, terrestrial samples are considerably more evolved compared to those from Mars, with the Mg# for Earth falling consistently between 40 and 50, whilst Mg# for Shergottites are consistently above 50 (Table 7). The evolved nature of terrestrial samples could be the result of subducting lithosphere and associated surface materials causing significant heterogeneity within mantle compositions of Earth (Tatsumi & Kogisco, 2003), subsequently lowering their Mg#. This could also explain why New Mexico (the only terrestrial sample analysed in this study with a known association to subduction zones, Chapter 5.1), is the most evolved of the terrestrial samples. Additionally, the inferred lack of subduction processes, and hence lack surface material influence on Mars could explain why the Mg# for the Martian Shergottites is significantly higher, representing a less evolved melt.

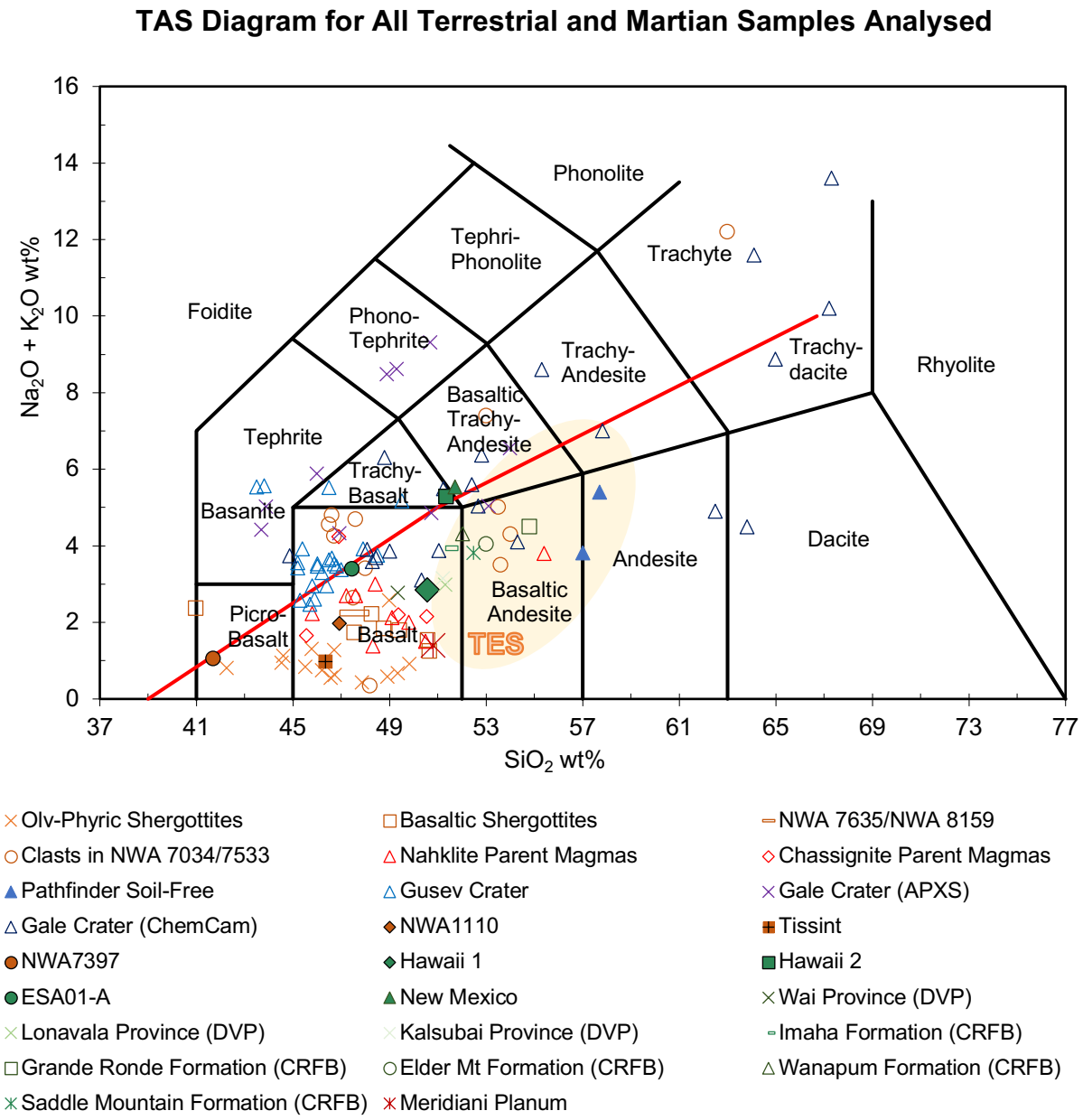

Figure 68 - TAS diagram displaying the bulk geochemical compositions of all terrestrial and Martian samples studied. For context Martian surface compositions from Gusev and Gale crater, Meridiani Planum and other Martian meteorite data from Filiberto, (2017) has also been plotted on this graph. Immediate surface compositions observed by Mar's Global Surveyor's TES (after McSween et al., 2009) have also been included, alongside literature data for the DVP and CRFB sourced from Basu et al., (2020) and Hooper & Hawkesworth, (1993) respectively. Above the red line = alkaline, below the red line = tholeiitic.

Olivine

The MgO vs FeO content within individual olivine compositions across terrestrial and Martian samples form a linear trend, with Martian samples generally being more Fe-rich than the terrestrial samples (Figure 69), (as expected given the Fe-rich nature of the bulk geochemistry, Table 7). Hawaii 1, Hawaii 2 and New Mexico are most compositionally similar to the olivine antecrysts exhibited by the olivine-phyric Shergottites, whilst ESA01-A is more Fe-rich and closer in composition to the olivine micro-phenocrysts within olivine-phyric Shergottites. The relationships between olivine in ESA01-A and New Mexico compared to the Martian Shergottites is explained further in Chapters 5.4 and 5.5. ESA01-A and Hawaii 2, however, do exhibit some olivine compositions that stray from the linear trend formed by the terrestrial and Martian samples, suggesting some variation across olivine (potentially the result of alteration) that may not be representative of the antecrysts within olivine-phyric Shergottites.

Olivine compositions across the DVP in comparison to the terrestrial samples are more varied, with olivine compositions from the Wai formation typically being most similar to Hawaii 1, Hawaii 2 and New Mexico, and hence most similar to the olivine antecrysts in NWA1110 and Tissint. The Lonavala and Kalsubai formations across the DVP exhibit more primitive compositions, comprising of the highest MgO contents in this study. This could indicate that basalts within the Wai formation of the DVP may make good geochemical analogues for the more primitive Martian magma responsible for the crystallisation of antecrysts in olivine-phyric Shergottites, however, this would not make a good analogue for poikilitic Shergottites.

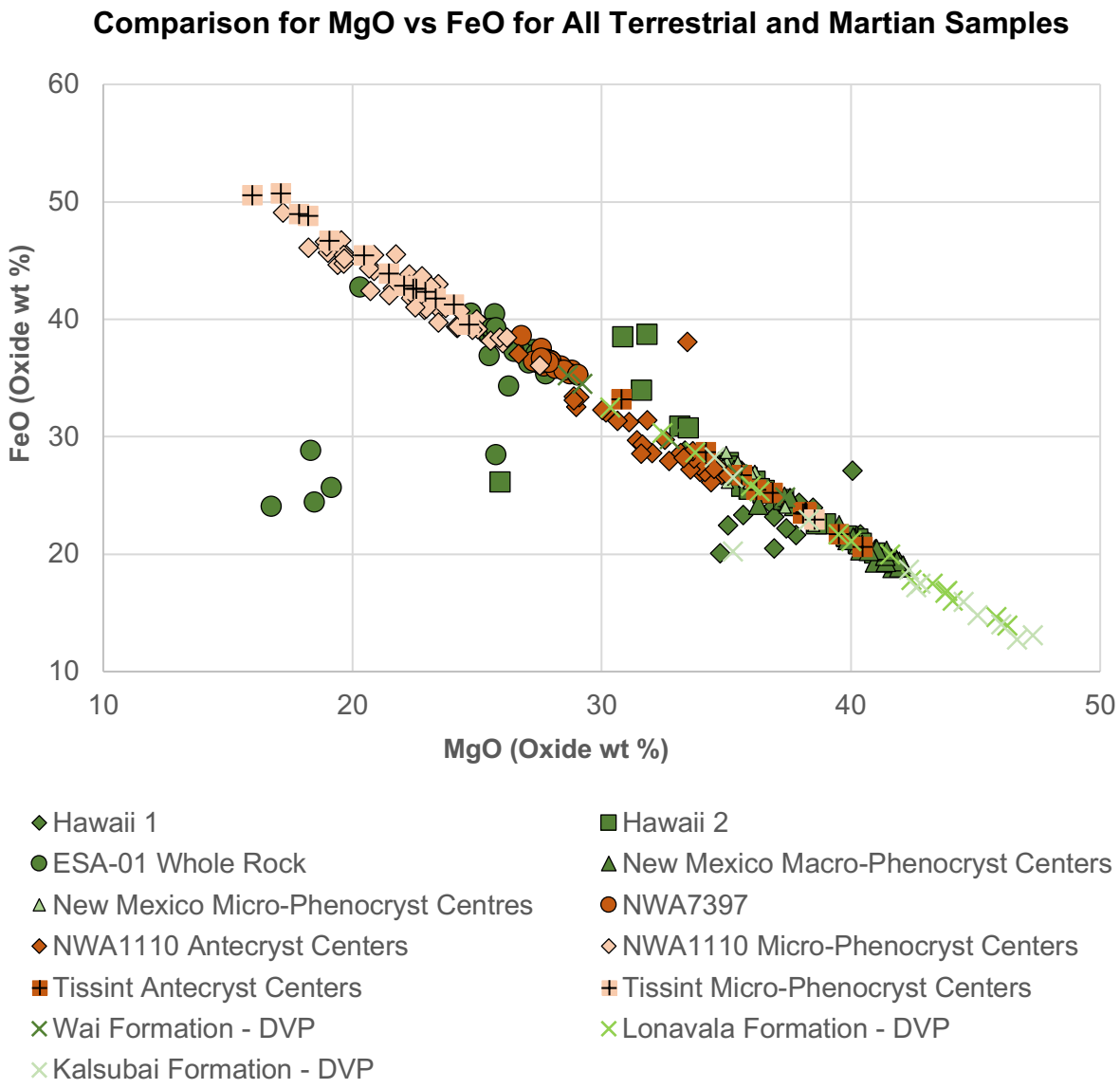

Figure 69 - Harker diagram comparing the MgO vs FeO content for every sample analysed within this study. Data on the table is also accompanied by individual olivine compositions for each formation of the Deccan Volcanic Province (DVP) sourced from Sano et al., (2001)

Pyroxene

Due to the potential shock-induced alteration of pyroxene in Martian meteorites (inferred in Chapter 5.2), whilst pyroxene compositions may appear similar in Figure 70, they may not be the most representative of pyroxene compositions on Mars. Hawaii 1 demonstrates the most similar compositions consistently across the whole sample to Martian Shergottites, with only augite compositions present (Figure 70).

Whilst this is similar to the augite compositions displayed by the Martian Shergottites, Hawaii 1 lacks any presence of pigeonite, and therefore doesn't display such varied compositions seen across NWA7397, NWA1110 and Tissint. As a result, Hawaii 1 could potentially be a good analogue for the melt that saw the crystallisation of Ca-rich pyroxene in the Martian Shergottites, but is not representative of all pyroxene compositions. New Mexico displays the widest range of pyroxene compositions across all terrestrial samples, whilst ESA01-A only comprises of diopside. Further detail on pyroxene compositions across ESA01-A and New Mexico compared to Martian Shergottites are discussed in Chapters 5.4 and 5.5.

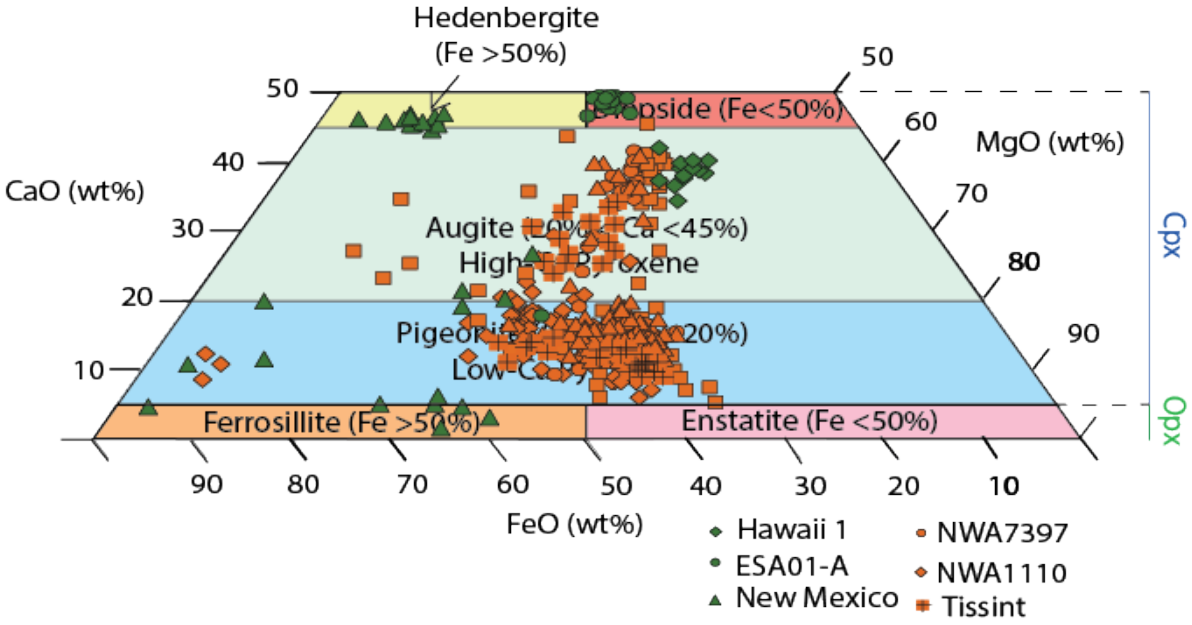

Figure 70 - Quadrilateral plot of pyroxene compositions for terrestrial and Martian samples within this study, including individual pyroxene compositions for the Wai, Lonavala and Kalsubai formations within the Deccan Traps (DVP), sourced from Sano et al., (2001)

Similar to Hawaii 1, most pyroxene compositions across the DVP are of augite composition, and therefore, may be more representative of the later stage magma that saw the crystallisation of Ca-rich pyroxene in Martian meteorites. Additionally, the Wai and Lonavala also comprise of occasional diopside, which is absent in the Martian Shergottites analysed. Despite this, of the DVP formations, the Lonavala and Kalsubai provinces display the most similar compositions of augite to the Martian Shergottites, in particular to the augitic compositions exhibited by NWA1110.

Plagioclase

Plagioclase compositions across NWA7397, NWA1110 and Tissint are very similar to the compositions exhibited by New Mexico (Figure 71, discussed further in Chapter 5.5) and Hawaii 2, with these samples all falling between An_{43-68} (Figure 71). Plagioclase compositions in Hawaii 2 are limited to An_{50-68}, and therefore are most similar to those displayed by Tissint (An_{60-68}). Hawaii 1 exhibits plagioclase of higher Anorthite content than those of Hawaii 2 and New Mexico, with compositions as high as An_{79}. Anorthite content this high was not observed in any Martian Shergottites analysed, indicating that plagioclase compositions across Hawaii 1 are not analogous to Martian Shergottites. Extensive zoning in plagioclase within ESA01-A displays a wider range of plagioclase compositions in comparison to those of Martian Shergottites, discussed further in Chapter 5.4.

Plagioclase compositions across the DVP vary greatly to the Martian Shergottites, with all three formations exhibiting compositions between An_{70-90}, differing to those exhibited by the Martian Shergottites (Figure 71). As a result, based on the literature data used, these samples would not make the most accurate analogues for individual plagioclase chemistries of Martian basalts.

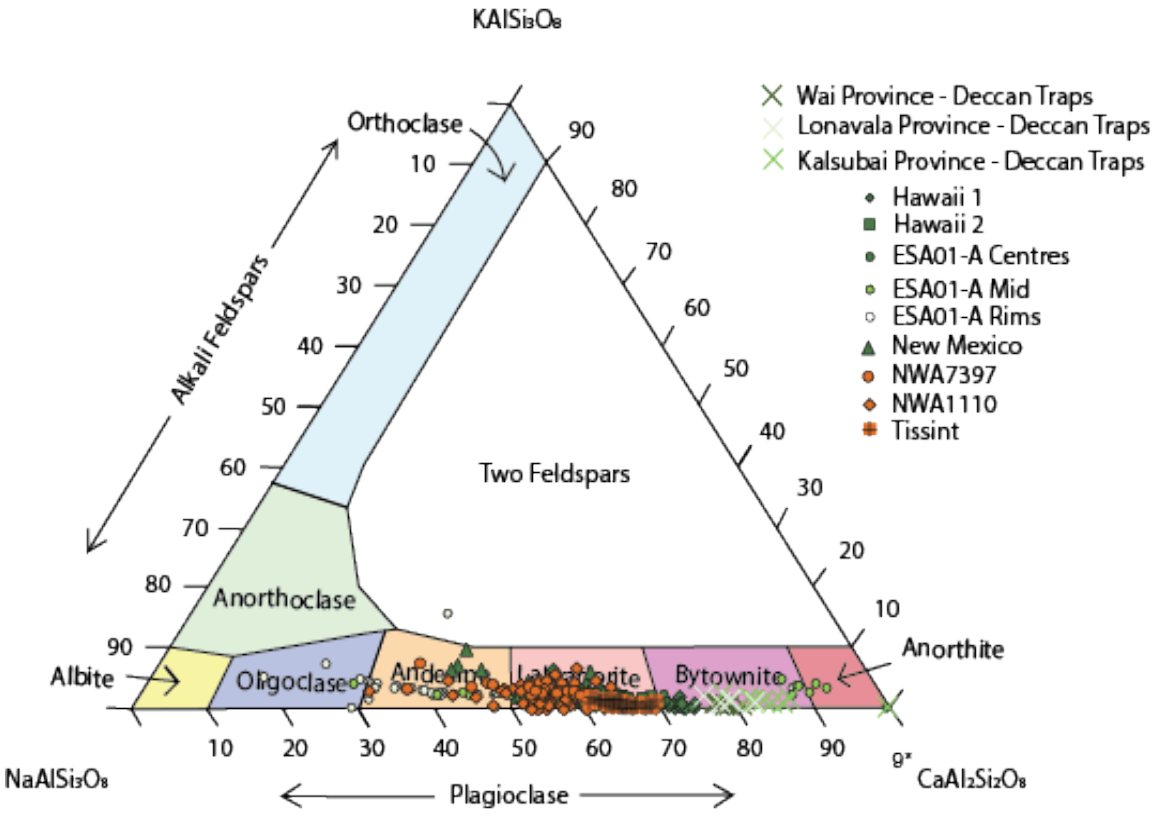

Figure 71 - Triangular plot displaying the individual plagioclase compositions for all terrestrial and Martian samples within this study, with data for the Wai, Lonavala and Kalsubai formations in the DVP source from Sano et al., (2003). All data in wt% oxide.

From these petrological and geochemical analyses, whilst Hawaii 1 displays similar pyroxene compositions to the Martian Shergottites, and olivine compositions to those of the olivine-phyric Shergottites, the plagioclase compositions vary greatly. Whilst plagioclase and olivine compositions indicate Hawaii 2 may make a good individual mineral analogue for these phases, the lack of coarser grained pyroxene indicates this sample may not make a good geochemical analogue for pyroxene in Martian basalts. Petrologically, both Hawaii 1 and Hawaii 2 would not make good analogues for the Martian Shergottites analysed, with the presence of vesicles, grain size differences and

estimated mineral phase abundances varying greatly compared to NWA7397, NWA1110 and Tissint.

Due to the current use of ESA01-A as a Martian analogue within the European Space Agency's ESA^{2}C collection (discussed in Chapter 5.4), this sample will be discussed in further detail, breaking down the individual mineral compositions and bulk geochemistry's compared to NWA7397, NWA1110 and Tissint. Additionally, of all the terrestrial samples analysed, New Mexico appears the most petrologically similar to the olivine-phyric Shergottites, and displays very similar individual mineral chemistries to NWA7397, NWA1110 and Tissint. This sample will be discussed further in Chapter 5.5.

5.4. ESA-01A as a Martian Analogue

ESA01-A is a gabion basalt sample part of the wider European Space Agency (ESA) Exploration Sample Analogue Collection (ESA^{2}C) curated by the ESA, and the Natural History Museum (NHM), (Manick *et al*., 2017). This collection was started with the aim to curate accurate chemical and mechanical analogues (Smith *et al.,* 2017), for expected geological environments across a range of planetary bodies within our Solar System (Martin & Duvet, 2019), and consisted of 82 analogue and simulant materials by 2019. Chemical similarities between these analogues include the modal mineralogy, individual mineral chemistry, bulk geochemistry and mineral phases present within the sample (ESA, 2021). The subsequent importance of these analogues is their use in supporting future

technological developments within ESA's Human and Robotic Exploration mission programme for Mars and the Moon (in addition to Phobos, Deimos (both Martian moons), and C-Type Asteroids), (Smith *et al.,* 2017). These analogues provide long-term analogue resources for mission requirements, and further resources for external research developments in planetary science (Martin & Duvet, 2019).

These analogues have previously been used in testing for future space missions, for example, the use of the Lunar dust simulant (also part of the ESA^{2}C) in testing spacecraft aiming to operate on the Lunar surface. The simulant provides indication into how the Lunar dust will interact with the moving parts of the spacecraft, (for example, if a coating of the Lunar dust on this spacecraft would cause it to overheat - an issue found on the Lunar roving vehicle during the Apollo 15, 16 and 17 missions). As a result, these analogues aid in the design of future spacecraft, aiming to reduce the effect of this Lunar dust (Martin & Duvet, 2019). Additionally, finding root petrological and chemical analogues of a known formation for these planetary bodies (an end-member analogue without requiring addition of material, (Sibille & Carpenter, 2006)) can also provide an insight into larger scale geological context of these planetary bodies and allow for testing of *in situ* utilisation for use in future space missions (Foucher *et al.,* 2021).

In addition to chemical and mechanical similarities of the suggested analogues, another requirement for analogue materials is their ability to be readily available, occurring at a large enough volume that any collection for testing will be sustainable (Smith *et al.,* 2017). Current Lunar and Martian analogues within the ESA^{2}C are commercially available to ensure a more sustainable collection. It was

also highlighted by Smith *et al.,* (2017) that the commercial availability of these samples ensures greater confidence in the operation quality during their collection.

Within the ESA^{2}C collection, the basaltic samples (including ESA01-A) are deemed suitable chemical and mineralogical analogues for both Mars and the Moon (Manick *et al.,* 2017). Despite this, whilst similarities between ESA01-A and the Martian samples previously discussed within this study have been found, so have a range of differences. Below is a more extensive comparison of ESA01-A (Chapter 4.1.3) to these Martian samples (Chapters 4.2.1, 4.2.2 and 4.2.3).

Petrological comparison:

The lack of olivine macro-phenocrysts/antecrysts in ESA01-A indicates that it is most petrologically similar to NWA7397. Despite this, the grain sizes of the major mineral phases (olivine, pyroxene and plagioclase) across ESA01-A are smaller than grain sizes across NWA7397 (possibly due to the deeper crystallisation of NWA7397 within the Martian crust (Chapter 5.2) as opposed to the emplacement on the surface inferred for ESA01-A (Chapter 5.1)), and appears more similar to the micro-phenocrysts and groundmass of olivine-phyric shergottites NWA1110 and Tissint (Table 4). Additionally, NWA7397 is cumulate in nature, displaying a non-poikilitic texture that differs from the moderately porphyritic texture exhibited by ESA01-A. The presence of un-zoned olivine micro-phenocrysts and a fine, interstitial plagioclase/pyroxene dominated groundmass within ESA01-A, however, is more similar to the olivine-phyric Shergottites if excluding the olivine antecrysts. These observations indicate that ESA01-A could be a good

petrological analogue for the Martian magma prior to the re-introduction of olivine antecrysts, however, does not make an accurate analogue for olivine-phyric Shergottites as a whole.

Despite some similarities between ESA01-A and the Martian Shergottites, spinel is petrographically different across these samples. Spinel within ESA01-A is an interstitial component, moulding around plagioclase laths. In NWA7397, NWA1110 and Tissint however, spinel appears as an early-crystallised mineral, associated with the cumulate olivine and earlier-crystallised olivine antecrysts. Spinel crystals have also experienced zoning within all Martian Shergottites analysed (typically when in contact with groundmass material), whereas in ESA01-A these crystals remain un-zoned. A comparison of textures across ESA01-A and the Martian Shergottites analysed can be seen in Figures 72a, 72b, 72c and 72d. Whilst noticeably different, it is difficult to compare plagioclase petrology across Martian meteorites and, not only ESA01-A, but all of the terrestrial samples analysed due to the likely shock-transformation of plagioclase to maskylenite across Martian meteorites.

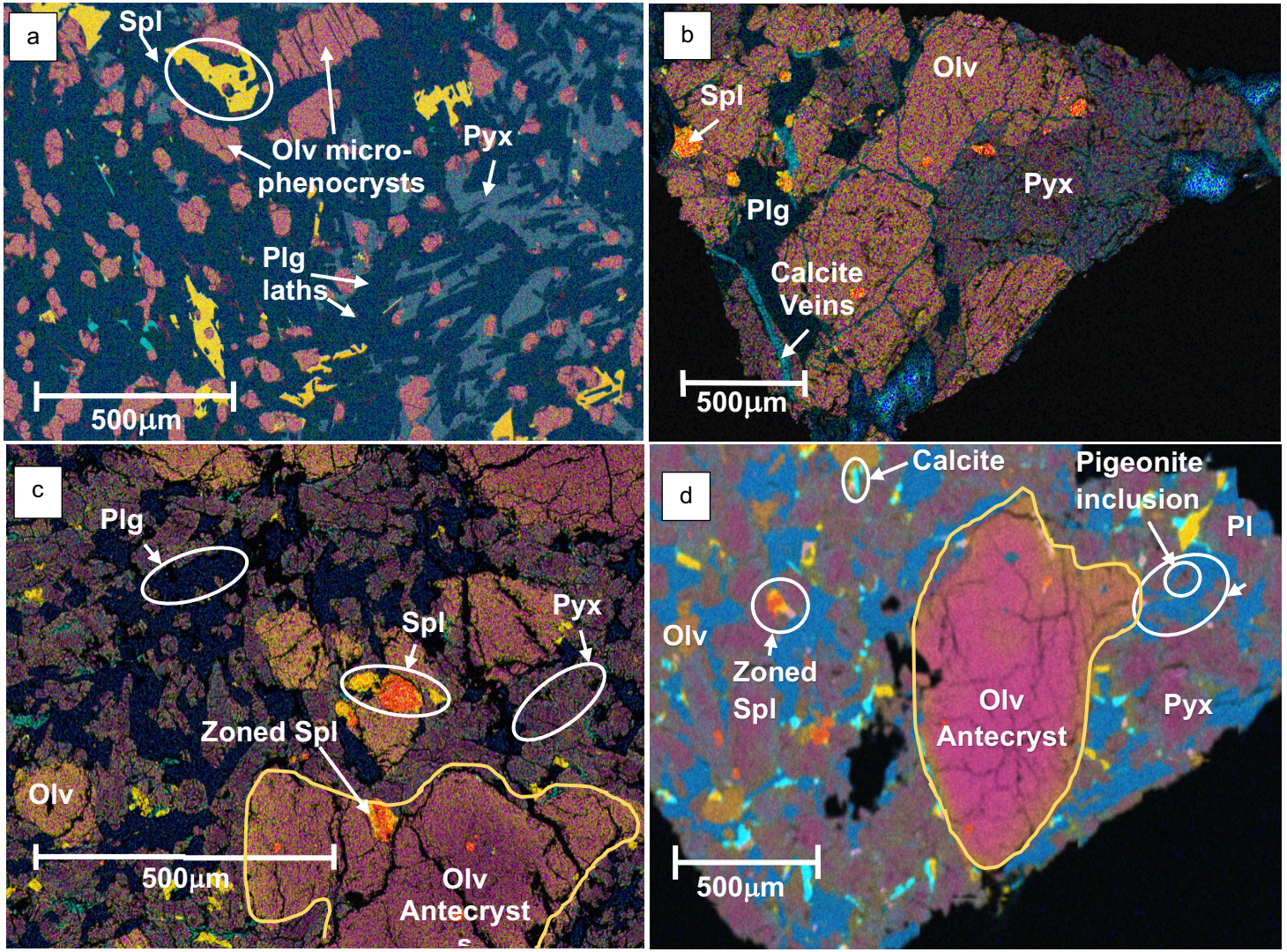

Figure 72 - a) EDS image at 75x magnification for ESA01-A - discussed in more detail within Chapter 5.1, b) EDS image at 37x magnification displaying the texture of NWA7397, discussed in Chapter 5.2, c) EDS image at 250x magnification, displaying the porphyritic texture of NWA1110 discussed in Chapter 5.2, d) EDS image at 200x magnification displaying the porphyritic texture in Tissint, discussed in Chapter 5.2. All images within this figure follow the sample key: Yellow = Iron, Orange = Titanium, Teal = Calcium, Navy Blue = Aluminium, Pink = Magnesium and Green = Sodium, Red = Chromite

When comparing the SiO_2, Na_2O and K_2O content of ESA01-A to the Martian Shergottites analysed, ESA01-A displays very similar compositions to NWA1110 and Tissint, with all three samples plotting as a basalt on a TAS diagram (Figure 73), exhibiting tholeiitic lavas. Despite this, the composition of ESA01-A is slightly more silicic than NWA7397, also displaying a higher $Na_2O + K_2O$ content in comparison.

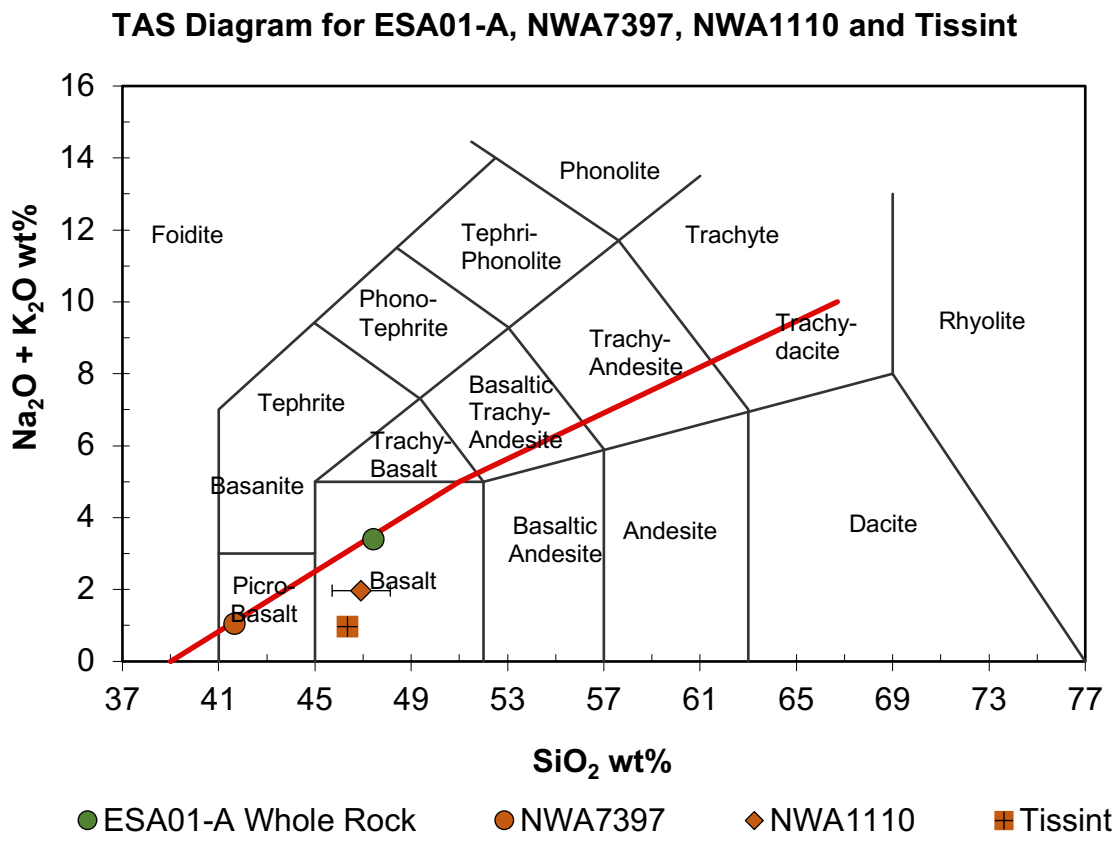

Figure 73 - TAS diagram displaying the bulk geochemistry of ESA01-A, NWA1110 and Tissint as basalt, whilst NWA7397 plots as a pico-basalt.

When comparing the total bulk geochemistry of ESA01-A relative to all other samples analysed, ESA01-A is most representative of the Martian meteorites, displaying a tholeiitic composition and lowest SiO_2 content across all terrestrial

samples relative to a high FeO and MgO content (although these values in ESA01-A are still very low compared to Martian samples). Additionally, ESA01-A has the lowest TiO_2 content of all of the terrestrial samples analysed of which is closest to the minimal TiO_2 content exhibited by the Martian meteorites.

The bulk Mg# for ESA01-A is the highest of all terrestrial samples analysed, showing greatest resemblance to the Martian meteorites. All Martian samples have a higher bulk Mg# displaying a more primitive composition despite their fractionated nature (exhibited by their larger FeO content). This FeO content could, however, be due to the more Fe-rich nature of Mars' mantle as a whole. Their larger bulk Mg#, however, could be due to the accumulated olivine antecrysts that represent an excess in olivine when compared to their associated olivine cores (Filiberto & Dasgupta, 2011, Chapter 5.2). Additionally, the accumulation of these antecrysts has been recognised as able to increase the MgO of a bulk sample (Larrea *et al.,* 2012) potentially explaining the high MgO content relative to the already high FeO content in Martian samples.

Bulk Geochemistry for All Samples												
All Data in wt% Oxide	**SiO_2**	**Al_2O_3**	**FeO**	**CaO**	**MgO**	**Na_2O**	**TiO_2**	**K_2O**	**Cr_2O_3**	**P_2O_5**	**MnO**	Mg#
Hawaii 1	50.56 ± 0.36	14.62 ± 0.78	11.77 ± 0.49	11.22 ± 0.09	6.09 ± 0.38	2.42 ± 0.07	2.64 ± 0.10	0.43 ± 0.01	0.07 ± BDL	0.19 ± BDL	0.23 ± BDL	47.98
Hawaii 2	51.36 ± 0.28	19.76 ± 1.60	8.81 ± 0.87	9.06 ±0.21	4.17 ± 0.15	4.03 ± 0.13	1.58 ± 0.22	1.25 ± 0.16	BDL	BDL	BDL	45.77
ESA01-A	47.44 ± 0.69	21.11 ± 0.03	10.61 ± 0.86	10.05 ± 0.74	5.77 ± 0.01	3.39 ± 0.16	1.49 ± 0.66	0.17 ± BDL	BDL	BDL	0.15 ± BDL	49.23
New Mexico	51.72 ± 0.08	19.21 ± 0.94	8.93 ± 0.73	9.01 ± 0.21	3.44 ± 0.57	4.18 ± 0.07	1.70 ± 0.11	1.36 ± 0.07	BDL	0.26 ± 0.01	0.15 ± 0.02	40.72
NWA 7397	41.69 ± 0.28	6.54 ± 0.30	23.48 ± 0.02	7.25 ± 0.75	18.25 ± 0.36	1.05 ± 0.08	0.48 ± BDL	BDL	0.89 ± 0.09	0.75 ± BDL	0.52 ± BDL	58.08
NWA 1110	46.92 ± 2.41	7.96 ± 2.50	22.40 ± 3.04	6.60 ± 1.78	13.93 ± 5.21	1.62 ± 0.21	BDL	0.35 ± BDL	BDL	0.82 ± BDL	BDL	52.58
Tissint	46.35 ± 0.12	7.76 ± 0.35	19.28 ± 0.16	7.41 ± 0.31	15.54 ± 0.98	0.97 ± 0.06	0.48 ± 0.15	BDL	0.58 ± BDL	0.57 ± 0.12	0.52 ± BDL	56.14
NWA 1068 (Filiberto *et al.,* 2010)	45.78	5.85	20.90	7.02	16.78	1.13	n.a.	0.20	0.58	0.50	0.42	58.87
Tissint (Basu Sarbadhikari et al., 2016)	46.20	5.18	21.10	6.92	17.50	0.74	0.64	0.02	0.60	0.52	0.53	59.66

Table 7 – Table displaying the bulk geochemical data collected for all samples within this study, error margins calculated by standard deviation of data. Where BDL is written, values detected by the SEM were either on or below the detection limit and therefore weren't included. Literature data for NWA 1068 (paired meteorite with NWA 1110, calculated using ICP-MS) and Tissint (also calculated

by ICP-MS) are also included in this table for context against bulk analyses from this study. n.a. = not analysed

Geochemical Comparison:

Olivine

When comparing olivine compositions across the terrestrial samples and olivine-phyric shergottites, the higher FeO content within olivine micro-phenocrysts is similar to olivine micro-phenocrysts in ESA01-A. This suggests that olivine in ESA01-A is geochemically most similar to the more fractionated melt responsible for these olivine micro-phenocrysts in NWA1110 and Tissint (Figure 74). Additionally, despite their differing petrology olivine in ESA01-A is also compositionally very similar to olivine in NWA7397. A potential explanation for this is the proposed similarity in origin of olivine-phyric and poikilitic Shergottites, seeing the differentiation of magma through fractional crystallisation (discussed in Chapter 5.2, Howarth *et al.,* (2014)).

If NWA7397 represents a more intrusive sample of a similar magma responsible for the Fe-rich olivine micro-phenocrysts within NWA1110 and Tissint, it could explain the additional similarity of ESA01-A to NWA7397. As a result, ESA01-A does make an accurate geochemical analogue for individual olivine compositions in NWA7397. It can also be argued that ESA01-A makes a good geochemical analogue for these compositions in NWA1110 and Tissint, although it is important to highlight this is a similarity in the olivine micro-phenocrysts and is not the case for all olivine in these meteorites.

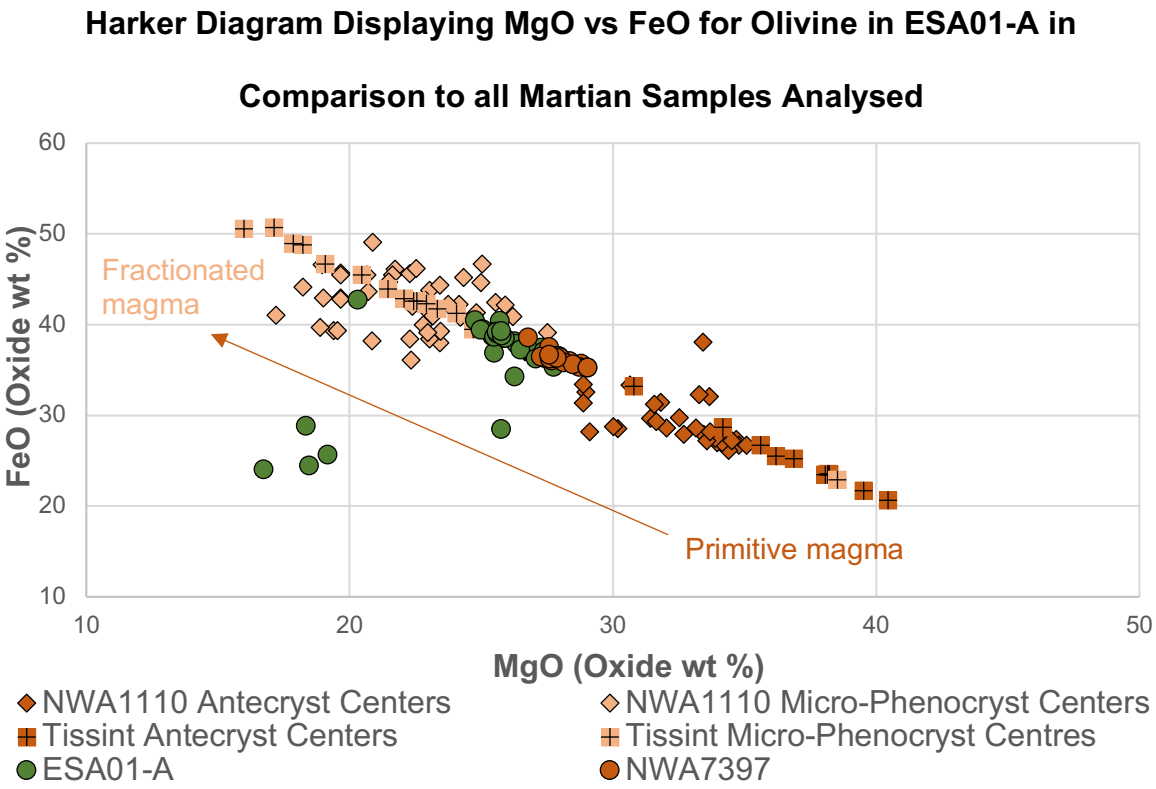

Figure 74 - Harker diagram displaying a linear trend in comparisons of MgO vs FeO (both in wt% oxide) for olivine in ESA01-A in relation to all Martian samples analysed in this study.

Pyroxene

Whilst olivine compositions across ESA01-A and the Martian Shergottites are similar, pyroxene compositions are distinctly different. It is important to note, however, that the alteration of pyroxene compositions due to shock and associated recrystallisation (Chapter 5.2), makes pyroxene compositions difficult to compare across planetary bodies.

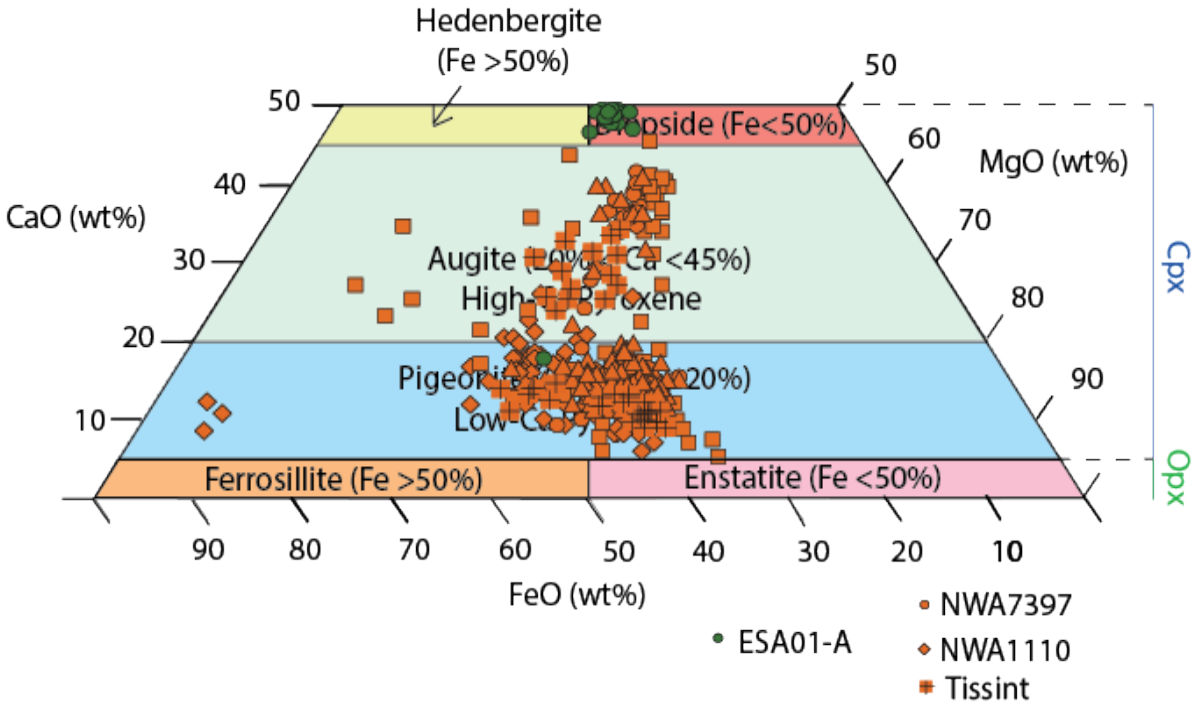

Figure 75 - Quadrilateral plot displaying the compositions of pyroxene across ESA01-A and all Martian samples analysed within this study – Further data is available in Appendix 4.

Unlike pyroxene in Martian Shergottites, pyroxene in ESA01-A is un-zoned and displays a Ca-rich, diopsidic composition. This differs greatly from the pigeonite and augite composition displayed by the Martian Shergottites (Figure 75). In fact, ESA01-A is the only terrestrial sample that comprises of diopside. This could suggest pyroxene crystallisation began earlier in ESA01-A's crystallisation history relative to NWA7397, NWA1110 and Tissint (Poldervaart & Hart, 1951), with their differing compositions indicating ESA01-A is not the best analogue for individual pyroxene compositions in any of the Martian Shergottites.

Plagioclase

Plagioclase compositions in ESA01-A are distinctly different to the Martian Shergottites analysed. This is largely due to the zoning displayed by these plagioclase crystals resulting in incredibly varied compositions (Chapter 5.1).

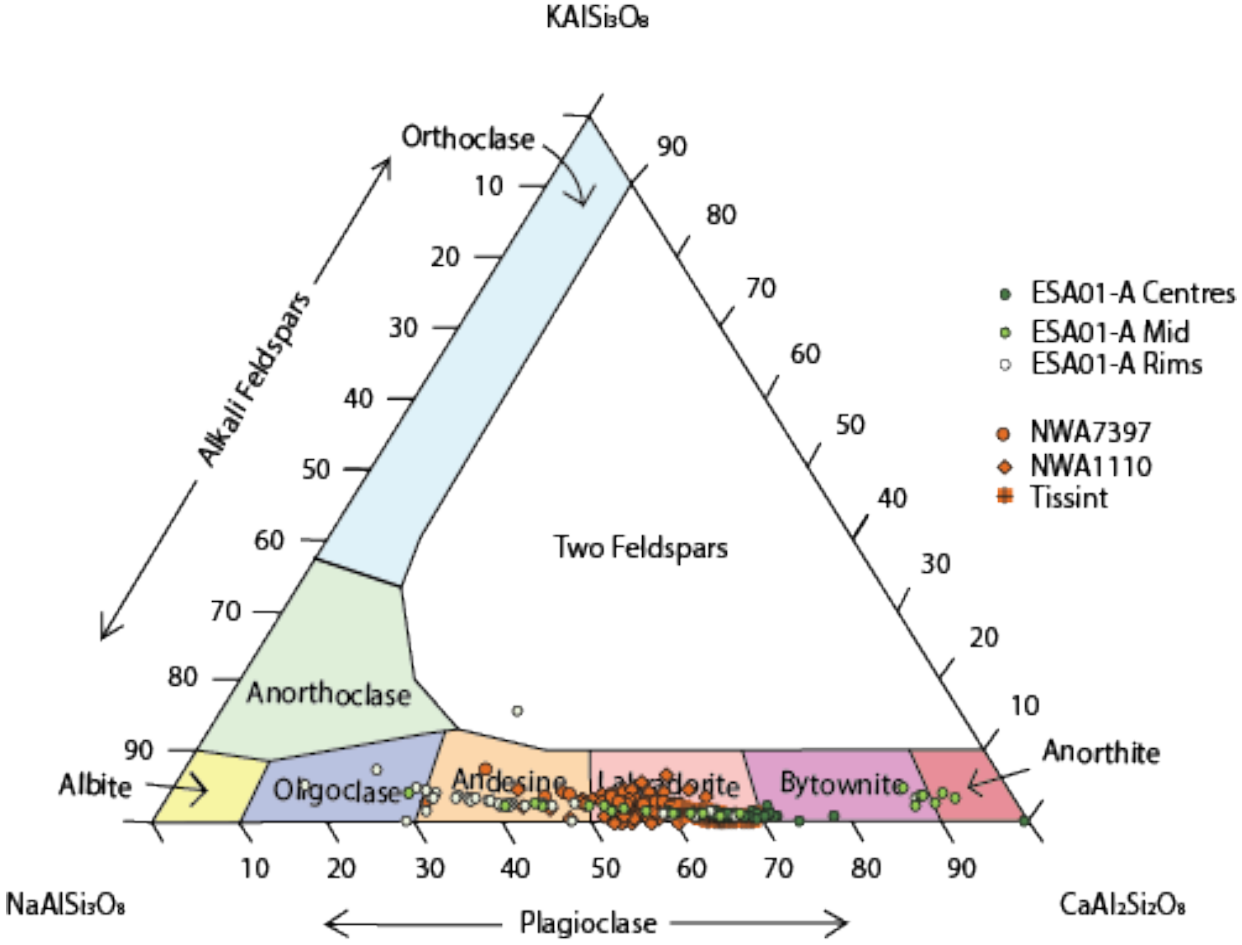

Figure 76 - Triangular plot displaying plagioclase compositions across ESA01-A and all Martian Shergottites analysed in this study, – Further data is available in Appendix 8. All data in wt% oxide.

Across NWA7397, NWA1110 and Tissint, plagioclase compositions fall between An_{30-68} (Figure 76). For ESA01-A, however, the extensive zoning present across plagioclase results in a larger range of anorthite content (Figure 76). Whilst

plagioclase in terrestrial samples may be difficult to compare to Martian meteorites due to the likely shock-transformation of plagioclase to maskylenite (mentioned in Chapter 4.2), the compositional heterogeneity in plagioclase across ESA01-A suggests that it is not geochemical analogous to Martian meteorites.

Through petrological and geochemical observations of ESA01-A, it has been inferred that ESA01-A makes an accurate bulk geochemical analogue for all Martian Shergottites in this study. Additionally, olivine compositions indicate ESA01-A is a more suited analogue for the fractionated magmas that see the crystallisation of the micro-phenocrysts and groundmass visible in NWA1110 and Tissint, and the more intrusive NWA7397. Despite this, ESA01-A becomes a less accurate analogue for pyroxene and plagioclase compositions across Martian Shergottites. This suggests that ESA01-A may not be the best analogue for all individual mineral chemistries of Martian Shergottites, a component looked for within chemical analogues (discussed previously). Petrologically, ESA01-A is not the most accurate analogue for NWA7397, NWA1110 or Tissint, despite showing some similarities in the fine-grained phases of olivine-phyric Shergottites. A full comparison of pros and cons for ESA01-A can be seen in Table 8.

Pros and Cons for ESA01-A as a Martian Analogue		
	Pros	**Cons**
ESA01-A	• Olivine compositions similar to fractionated poikilitic Shergottites and micro-phenocrysts in olivine-phyric Shergottites • Bulk geochemistry most similar to Martian samples • Already commercially available (Craig's Quarry, Northern Ireland)	• Pyroxene compositions different to all Shergottites analysed • Plagioclase is incredibly zoned, displays a large range of plagioclase that are largely absent in Shergottites • Petrologically very different to both olivine-phyric and poikilitic Shergottites (no olivine antecrysts/macro-phenocrysts. Mineral abundances as well as grains sizes vary greatly compared to poikilitic Shergottites • Olivine compositions similar to fractionated magmas on Mars, not as representative for more primitive magmas • Spinel present as an intercumulus phase with large grain sizes, differing from Shergottites

Table 8 - Table displaying the pros and cons for ESA01-A as an analogue for Mars

There is, however, one sample - New Mexico - that has displayed similar individual mineral compositions to NWA7397, NWA1110 and Tissint. This sample also exhibits a striking similarity in texture to that of the olivine-phyric Shergottites. As a result, New Mexico is proposed as a more accurate chemical and petrological analogue for olivine-phyric Shergottites. This is discussed further in the following chapter.

5.5. New Mexico: A potential analogue for Olivine-Phyric Shergottites

Despite baring minimal petrological similarity to poikilitic Shergottite NWA7397, New Mexico displayed many similarities petrologically and geochemically to olivine-phyric Shergottites NWA1110 and Tissint. In this section, these similarities (as well as differences between these samples) will be discussed.

Petrological Comparisons:

New Mexico is petrographically the most similar to the olivine-phyric Shergottites, Figure 77a, 77b and 77c (despite the crystallisation processes to get to their similar textures differing, Chapters 5.1 & 5.2). This is due to the lack of olivine antecrysts cumulate nature and larger grain size within NWA7397 (Table 4, Figure 77d). When compared to NWA1110 and Tissint, New Mexico displays a similar porphyritic texture of zoned olivine macro- and un-zoned micro-phenocrysts as the zoned olivine antecrysts and un-zoned micro-phenocrysts displayed within both these Martian meteorites (Figure 77a and 77b). Additionally, unlike the intercumulus nature in ESA01-A, spinel is present as an early-crystallised phase within New Mexico included and associated with the olivine macro-phenocrysts. This is much more similar to all of the Martian Shergottites analysed within this study.

Despite the noticeable similarities between New Mexico and the olivine-phyric Shergottites, as with ESA01-A there are some key differences. Firstly, New Mexico contains dendritic pyroxene and pyroxene overgrowths within the groundmass (Chapter 4.1.4, Figure 28b) that are absent in NWA1110 and Tissint.

This could be due to the different nature of their formation, with magma mixing processes within a subduction zone potentially being responsible for these features in New Mexico (Chapter 5.1), of which differs greatly to the closed-system fractionation experienced by NWA1110 and Tissint (Chapter 5.2). As well as this, microstructures such as symplectic and spinifex textures within the groundmass of New Mexico are absent from NWA1110 and Tissint, however, this could be due to shock effects induced by the ejection of these meteorites from Mars obscuring these textures. The patchy zoning in pyroxene present in NWA1110 and Tissint is also absent from New Mexico, although this could also be due to the potential shock origin of this zoning (Chapter 5.2).

Whilst there are some petrological differences, the overall similarity of textures across New Mexico compared to the olivine-phyric Shergottites could make New Mexico an accurate analogue for testing of *in situ* instrumentation. The presence of the olivine macro-phenocrysts in addition to the micro-phenocrysts within New Mexico provides a more accurate comparison for these meteorites, and could be more representative of how this instrumentation will be affected when testing *in situ* samples of this olivine-phyric nature.

Geochemical comparison:

Despite several petrological similarities to olivine-phyric Shergottites, ESA01-A remains as the best terrestrial analogue for the bulk geochemistry of Martian Shergottites. When plotted on a TAS diagram, the basaltic trachy andesite composition exhibited by New Mexico (Chapter 5.3, Figure 68), means that the bulk geochemistry is more alkaline than Martian Shergottites, indicating a very

different formation process to Martian Shergottites (discussed in Chapters 1.2 and 5.1.3). New Mexico therefore isn't representative of the basalt compositions exhibited by NWA7397, NWA1110 or Tissint. Additionally, of all terrestrial samples analysed, New Mexico exhibits the lowest Mg# (Table 7), representing a more evolved magma (likely due to the extent of magma mixing experienced by the sample). As a result, ESA01-A exhibits the most similar bulk geochemistry to Martian Shergottites in comparison to New Mexico.

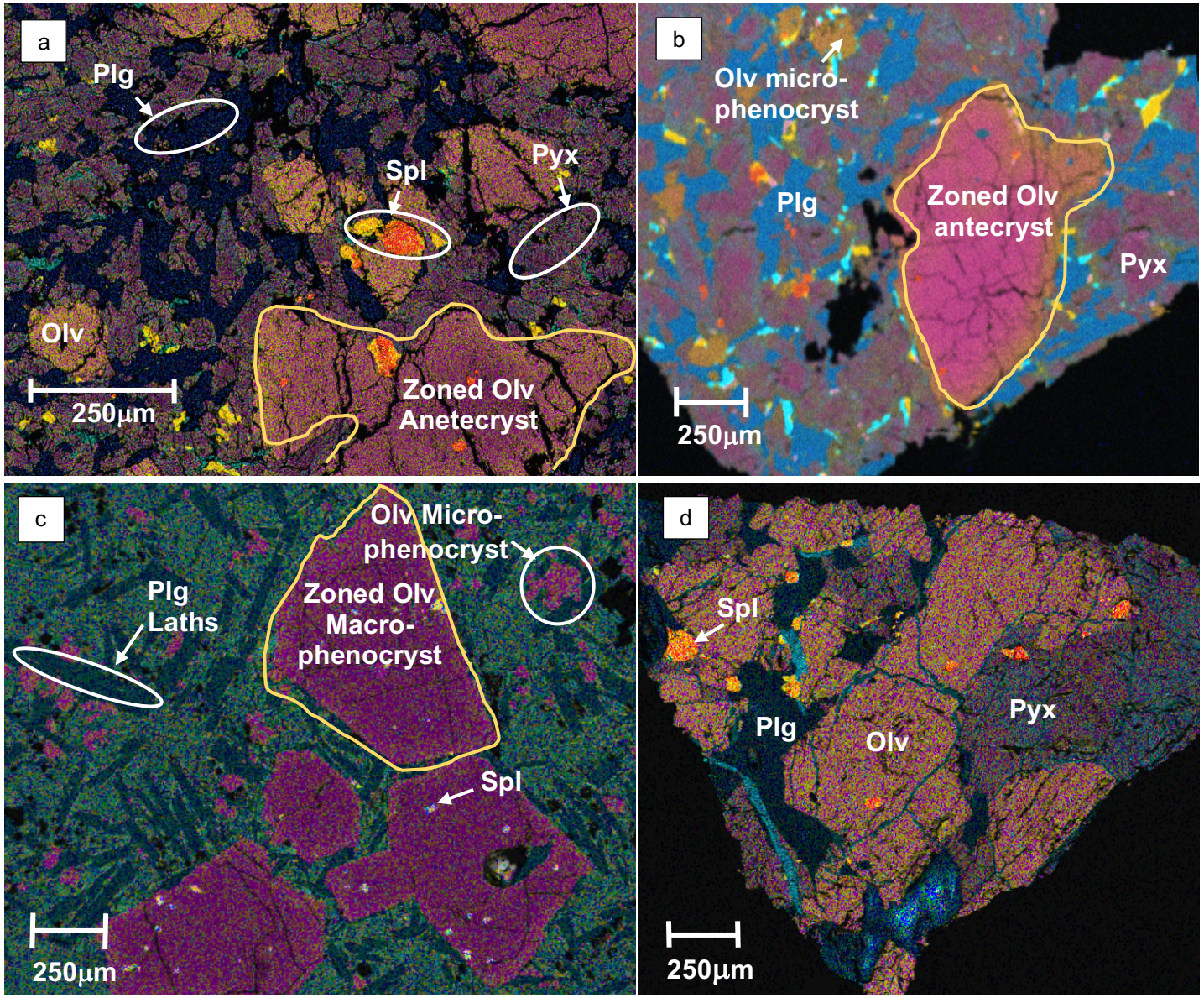

Figure 77 - a) EDS image taken at 250x magnification displaying the porphyritic texture of NWA1110, b) EDS image taken at 200x magnification displaying the porphyritic texture of Tissint, c) EDS image taken at 40x magnification for New Mexico, displaying the presence of both olivine macro- and micro-phenocrysts, d) EDS image taken at 37x magnification of NWA7397, displaying the cumulate, non-poikilitic texture. All images within this figure follow the sample key: Yellow = Iron, Orange = Titanium, Teal = Calcium, Navy Blue = Aluminium, Pink = Magnesium and Green = Sodium, Red = Chromium

Olivine

Olivine compositions in New Mexico to those of NWA7397, NWA1110 and Tissint, display more primitive compositions, with the macro-phenocryst cores displaying some of the highest MgO contents across New Mexico and all Martian meteorites analysed (Figure 78). Not only are the macro-phenocrysts within New Mexico more Mg-rich, but the micro-phenocrysts, despite being more Fe-rich relative to macro-phenocrysts in the sample, are more Mg-rich than the Fe-rich micro-phenocrysts within Martian meteorites. Whilst the Mg-rich nature of New Mexico olivine compositions (both micro-phenocrysts and macro-phenocrysts) are different to the Fe-rich nature of the micro-phenocrysts in NWA1110 and Tissint (of which ESA01-A provides a more accurate analogue, Figure 78), olivine in New Mexico is more similar to the primitive Martian antecryst cores (Figure 78) that are inferred to have crystallised deeper in the Martian crust prior to their re-introduction into the later fractionated magma (Chapter 5.2).

Olivine in New Mexico is more analogous to the antecrysts of Martian olivine-phyric Shergottites, and so may make a better analogue for the parental magma that saw the crystallisation of the antecrysts. This could also explain why, due to their Mg-rich nature, olivine compositions in New Mexico are least similar to the Fe-rich olivine compositions of NWA7397 (Figure 78), with the inferred formation of this sample involving the fractionation of this magma prior to its crystallisation (Chapter 5.2). As a result, whilst not being analogous to olivine compositions within poikilitic Shergottites, New Mexico would make a good chemical analogue for individual olivine compositions within olivine-phyric Martian meteorites, albeit the more primitive olivine crystals within these meteorites.

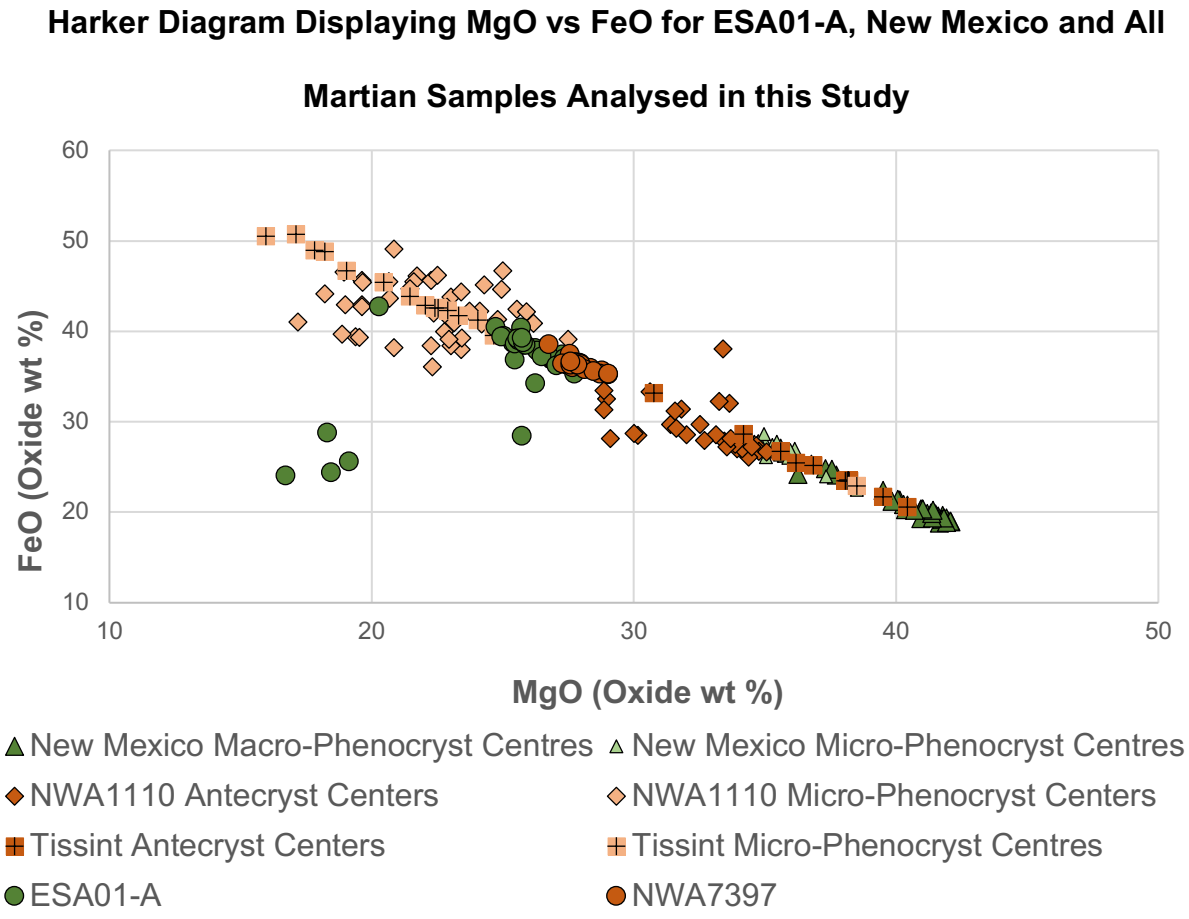

Figure 78 - Harker diagram displaying the MgO vs FeO content for olivine macro-phenocryst/ antecryst and micro-phenocryst centres in New Mexico compared to those in olivine-phyric Shergottites NWA1110 and Tissint, as well as olivine cores in NWA7397

Pyroxene

In addition to the similarity of olivine compositions to those of antecrysts within olivine-phyric Shergottites, pyroxene compositions are also more similar across New Mexico to all Martian Shergottites analysed in this study compared to those in ESA01-A.

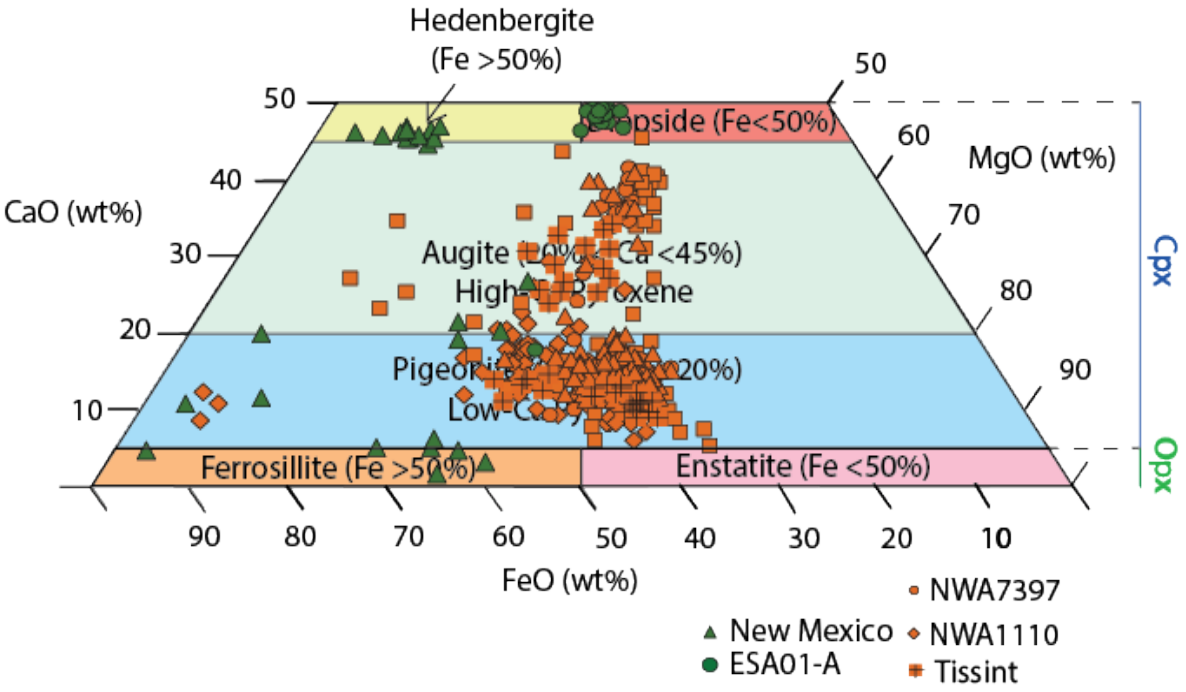

Figure 79 - Quadrilateral plot displaying the pyroxene compositions across NWA7397, NWA1110 and Tissint in comparison to those of New Mexico – Further data is available in Appendix 4.

Whilst New Mexico exhibits hedenbergite and ferrosillite (orthopyroxene) within its groundmass that are absent in NWA7397, NWA1110 and Tissint, it also comprises of pigeonite and augite, compositions that are the only two present across all Martian meteorites analysed (Figure 79). Despite the presence of this orthopyroxene suggesting inversion must have occurred between orthopyroxene and pigeonite during crystallisation, (a process that must have occurred prior to crystallisation of pyroxene in NWA7397, NWA1110 and Tissint), the presence of pigeonite could also represent an overlap of augitic and pigeonite compositions. The presence of pigeonite and augite within New Mexico compared to the lack of pigeonite in ESA01-A suggests New Mexico is a better analogue for the individual pyroxene compositions in Martian Shergottites.

Plagioclase

Whilst New Mexico exhibits some differences in composition across olivine and pyroxene compared to olivine-phyric Shergottites (although more similar than ESA01-A), plagioclase in New Mexico is geochemically the most similar to all Martian Shergottites analysed. In New Mexico, NWA7397, NWA1110 and Tissint, all plagioclase compositions fall between An_{30-68} (Figure 80). The similarity of plagioclase compositions in New Mexico (An_{43-65}) compared to the varied compositions exhibited by ESA01-A (Chapter 5.4) indicates that of these two terrestrial samples, New Mexico makes the best geochemical analogue for individual plagioclase compositions for NWA7397, NWA1110 and Tissint.

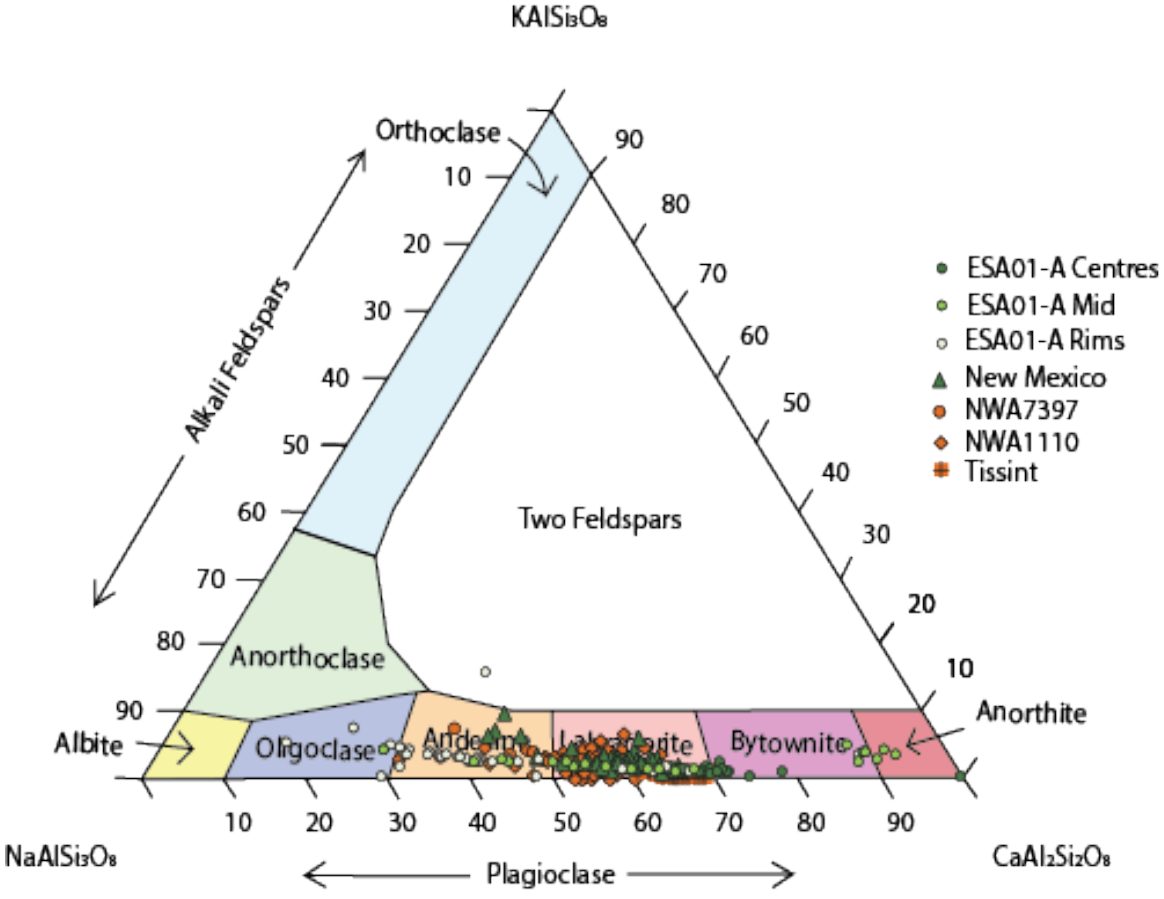

Figure 80 - Triangular plot displaying the plagioclase compositions exhibited by ESA01-A, New Mexico, NWA7397, NWA1110 and Tissint – Further data is available in Appendix 6. All data in wt% oxide.

Comparing the petrological observations of New Mexico, ESA01-A, NWA1110 and Tissint, it is evident that New Mexico is a more accurate petrological analogue for olivine-phyric Shergottites. This is shown by the presence of olivine macro-phenocrysts and micro-phenocrysts across this sample compared to the olivine antecrysts and micro-phenocrysts in the olivine-phyric Shergottites, a texture absent in ESA01-A. New Mexico does, however, differ greatly to poikilitic Shergottite NWA7397, therefore is not the best analogue for this type of Shergottite. A pros and cons list for New Mexico and its viability as an analogue for Mars can be seen in Table 9.

Additionally, individual olivine compositions of New Mexico compared to those of NWA1110 and Tissint suggest New Mexico is an accurate geochemical analogue for the parental magmas responsible for antecryst crystallisation in olivine-phyric Shergottites. Despite this, ESA01-A remains the best analogue for individual olivine compositions in poikilitic Shergottites as displayed by NWA7397 (due to the fractionated nature of this sample). ESA01-A is also the best analogue for bulk geochemistry across these samples. Whilst the individual olivine compositions across both ESA01-A and New Mexico vary in terms of accuracy across the Martian Shergottites (with ESA01-A representing the more fractionated magmas of these Shergottites), New Mexico is the best geochemical analogue for individual plagioclase and pyroxene compositions in NWA7397, NWA1110 and Tissint compared to ESA01-A.

Overall, New Mexico is proposed as the best terrestrial analogue for olivine-phyric Martian Shergottites of all terrestrial samples in this study, with ESA01-A more similar to poikilitic Shergottites. As mentioned in Chapter 1.3, olivine-phyric

Shergottites are the most common type of Martian meteorites on Earth, (e.g LAR 12095, LAR 12240, DaG 476, SaU 005, (Dunham *et al.,* 2019), Dhofar 019, NWA 1110, Tissint), and therefore could be more representative of volcanism across Mars. As a result, New Mexico may be a more applicable match for basaltic volcanism on Mars, and a more accurate petrological and geochemical analogue for testing *in situ* resource utilisation. Whilst the lavas from New Mexico aren't currently 'commercially' available, the large extent of these lavas means that, in moderation, collection of samples from this province could be sustainable and therefore, could be considered as a viable analogue for Martian volcanism.

Pros and Cons for New Mexico as a Martian Analogue		
	Pros	**Cons**
New Mexico	• Petrologically very similar to olivine-phyric Shergottites, displaying both olivine macro-and micro-phenocrysts surrounded by a fine grain plagioclase/pyroxene groundmass • Olivine compositions similar to more primitive antecrysts in olivine-phyric Shergottites • Wider range of pyroxene compositions with larger abundance of augite and pigeonite to ESA01-A • Plagioclase compositions within the same Anorthite range as Martian Shergottites. • Spinel present as an early crystallising phase more similar to Shergottites	• Not yet commercially available • Olivine compositions may be more similar to primitive magmas on Mars, however are not as representative for more fractionated magmas • Has experienced magma mixing which is absent in Martian Shergottites

Table 9 - Table displaying the pros and cons for New Mexico as a analogue for Mars

6. Conclusion

Basaltic volcanism has had a huge role in shaping planetary bodies in our Solar System, being found on Earth, the Moon and Mars. Intraplate basaltic volcanism has been prominent on all three of these planetary bodies, producing flood lavas that on Earth have created provinces such as the DVP and CRFB. This type of volcanism is particularly important on the Moon and Mars due to their lack of plate tectonics. Whilst both orbital and lander missions have allowed for the analysis of these lavas on the Moon and Mars (with *in situ* sample collection from Apollo, Luna and Chang'e 5 missions aiding studies of the Moon further), the lack of *in situ* samples from Mars means meteorites are the only direct samples available to study these Martian lavas. In particular, Shergottites (part of the wider SNC Martian meteorites) are the most common and are similar to these extrusive Martian flood lavas.

Using meteorite samples from Mars (albeit samples that are not *in situ*) and direct samples (through Apollo/Luna/Chang'e 5 missions and meteorites) from the Moon, comparison and identification of similar terrestrial analogues for the Moon and Mars are essential for the testing of *in situ* utilisation for future space missions. Agencies such as the ESA and the NHM have collaborated in the creation of analogue collections specifically for this purpose. This study utilised these Martian meteorites (as opposed to Martian surface data) and Lunar meteorites (owing to the limited availability of Apollo and Luna samples) to compare against terrestrial analogues of intraplate origin (Hawaii 1, Hawaii 2, and New Mexico) and find accurate terrestrial analogues for the Moon and Mars.

These samples were also compared to current ESA01-A analogue from Northern Ireland, of which is part of the ESA^{2}C collection by ESA and the NHM.

The scarcity of basalt clasts in the Lunar breccias analysed (as well as their extensively brecciated nature), meant petrological and geochemical analyses for Lunar Mare basalts were limited. As a result, these samples were difficult to compare to terrestrial samples and were not discussed further than the preliminary data collection. Collection and analysis of more representative Lunar samples for the Lunar Mare basalts such as Apollo or Luna samples could allow for future improvements in looking for terrestrial analogues for the Moon. Looking for more ancient examples of terrestrial flood basalt volcanism may also improve the search for terrestrial analogues for the Moon due to the inferred lack of volcanism on the Moon past 1 Ga (Chapter 2.2).

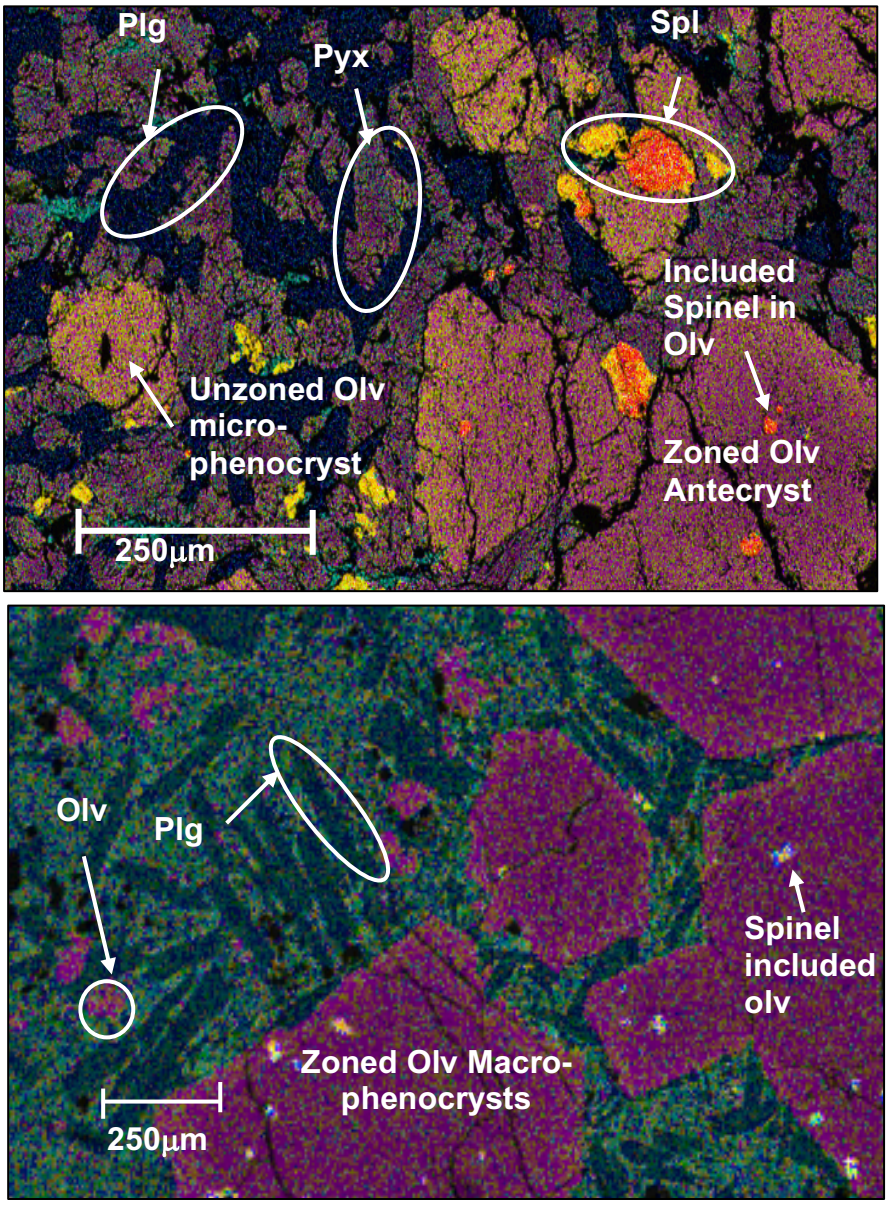

Figure 81 - a) EDS image of NWA1110 taken at 250x magnification displaying antecrysts and micro-phenocrysts of olivine, b) EDS image taken at 40x magnification of New Mexico, displaying olivine macro- and micro-phenocrysts. Both images follow the same key: Yellow = Iron, Orange = Titanium, Teal = Calcium, Navy Blue = Aluminium, Pink = Magnesium and Green = Sodium, Red = Chromium

When comparing the terrestrial samples to Martian Shergottites, ESA01-A is an accurate analogue for bulk geochemistry of all Martian meteorites in this study.

Olivine compositions within this sample may also make a good analogue for the later crystallised, fractionated magmas responsible for the fine-grained components of olivine-phyric Shergottites. The inferred similar origin of this fractionated magma for olivine-phyric Shergottites and poikilitic Shergottites explains why olivine compositions in ESA01-A are also a good geochemical analogue for NWA7397. ESA01-A is not the most accurate petrological or geochemical analogue for individual mineral chemistries across these meteorites.

Despite the involvement of a subduction zone during its inferred formation and the evidence of magma mixing, New Mexico is proposed as the best petrological analogue for olivine-phyric Shergottites, displaying both macro-phenocrysts and micro-phenocrysts of olivine similar to the antecrysts and micro-phenocrysts observed in NWA1110 and Tissint (Figure 81). A limitation for this study, however, is the magma mixing model for New Mexico being related to source region mixing rather than within the magma plumbing system, further study is needed for this model. Magma mixing is absent in the Martian Shergottites and therefore this feature in New Mexico wasn't discussed further.

Olivine-Phyric Shergottites are the most common, and therefore New Mexico is likely more representative for Martian volcanism as a whole compared to ESA01-A (Table 10). New Mexico is also a representative sample for individual mineral compositions within NWA7397, NWA1110 and Tissint, displaying a wide range of pyroxene compositions including augite and pigeonite, and plagioclase compositions within range of the Martian Shergottites. Olivine compositions in New Mexico may also represent a good geochemical analogue for more primitive

magmas responsible for the crystallisation of antecrysts in olivine-phyric Shergottites.

Pros and Cons for ESA01-A and New Mexico as Martian Analogues		
	Pros	**Cons**
ESA01-A	• Olivine compositions similar to fractionated poikilitic Shergottites and micro-phenocrysts in olivine-phyric Shergottites • Bulk geochemistry most similar to Martian samples • Already commercially available (Craig's Quarry, Northern Ireland)	• Pyroxene compositions different to all Shergottites analysed • Plagioclase is incredibly zoned, displays a large range of plagioclase that are largely absent in Shergottites • Petrologically very different to both olivine-phyric and poikilitic Shergottites (no olivine antecrysts/macro-phenocrysts. Mineral abundances as well as grains sizes vary greatly compared to poikilitic Shergottites • Olivine compositions similar to fractionated magmas on Mars, not as representative for more primitive magmas • Large, intercumulus spinel present differing from Shergottites
New Mexico	• Petrologically very similar to olivine-phyric Shergottites, displaying both olivine macro-and micro-phenocrysts surrounded by a fine grain plagioclase/pyroxene groundmass • Olivine compositions similar to more primitive antecrysts in olivine-phyric Shergottites • Wider range of pyroxene compositions with larger abundance of augite and pigeonite to ESA01-A • Plagioclase compositions within the same Anorthite range as Martian Shergottites. • Spinel present as an early crystallising phase more similar to Shergottites	• Not yet commercially available • Olivine compositions may be more similar to primitive magmas on Mars, however are not as representative for more fractionated magmas • Has experienced magma mixing which is absent in Martian Shergottites

Table 10 - Table displaying the pros and cons for both ESA01-A and New Mexico as Martian analogues from observations in this study

For future research, the Icelandic Laki 1783-1784 lava flow identified by Keszthelyi *et al.,* (2000) as a good morphological analogue for flood lavas on Mars (Chapter 1.3) could be studied to see if it would also make an accurate analogue both petrologically and geochemically to Martian Shergottites. The similarity of New Mexico to Martian Shergottites also indicates that there is a potential for accurate analogues elsewhere that aren't strictly intraplate in origin (potentially at other intra-rift arc settings similar to what's inferred for New Mexico), suggesting whilst some analogues may be similar geochemically, it is also important to consider the textural similarities of these terrestrial analogues to that of their extra-terrestrial counterparts. Finally, whilst New Mexico isn't currently commercially available, the extent of this province indicates that it could potentially be sourced sustainably if in moderation. As a result, New Mexico is proposed as an accurate and viable petrological and geochemical analogue for olivine-phyric Martian basalts.

7. References

Adcock, C. T., Udry, A., Hausrath, E. M., Tschauauner, O. (2018), 'Craters of the Moon National Monument basalts as unshocked compositional and weathering analogs for martian rocks and meteorites', *American Mineralogist*, **103**, 502-516

Agee, C. B., Wilson, N. V., McCubbin, F. M., Ziegler, K., Polyak, V. J., Sharp, Z. D., Asmerom, Y., Nunn, M. H., Shaheen, R., Thiemens, M. H., Steele, A., Fogel, M. L., Bowden, R., Glamoclija, M., Zhang, Z., Elardo, S. M. (2013), 'Unique Meteorite from

Early Amazonian Mars: Water-Rich Basaltic Breccia Northwest Africa 7034', *Science,* **339**, 780-785

Albarède, F. (2009), 'The Earth in the Solar System' in *Albarède, F. 'Geochemistry: An Introduction, Second Edition',* University Printing House, Cambridge, United Kingdom, Chapter 12, 272-276

Alexander, C, M, O'D. (2021), 'Meteorite', available at < https://www.britannica.com/science/meteorite >, (Accessed: 01/09/2021)

Anderson Jr. A. T., Swihart, G. H., Artioli, G., Geiger, C. A. (1984), 'Segregation Vesicles, Gas Filter-Pressing and Igneous Differentiation', *The Journal of Geology*, **92**, 55-72

Apollo Field Geology Investigation Team (1973), 'Apollo 16 Exploration of Descartes: A Geologic Summary', *Science*, **179**, 62-69

Armstrong, (2010), 'Northwest Africa 1110 (Martian (Shergottite))', Available at < https://www.lpi.usra.edu/meteor/get_original_photo.php?recno=5647633 >, (Accessed: 09/10/21)

Auricular, (2012), 'Tissint: Martian (Shergottite)', Available at, < https://www.lpi.usra.edu/meteor/get_original_photo.php?recno=5659903> (Accessed: 09/10/21)

Balta, J. B., Sanborn, M., McSween Jr, H. Y., Wadhwa, M. (2013), 'Magmatic history and parental melt compositions of olivine-phyric shergottite LAR06319: Important of magmatic degassing and olivine antecrysts in Martian magmatism', *Meteoritics & Planetary Science,* **48**, 1359-1382

Balta, J. B., Sanborn, M. E., Udry, A., Wadwha, M., McSween Jr, H. Y. (2015), 'Petrology and trace element geochemistry of Tissint, the newest shergottite fall', *Meteoritics & Planetary Science*, **50**, 63-85

Barnes, S. J., Mole, D. R., Le Vaillant, M., Campbell, M. J., Verrall, M. R., Roberts, M. P., Evans, N. J. (2016), 'Poikilitic Textures, Heteradcumulates and Zoned Orthopyroxenes in the Ntaka Ultramafic Complex, Tanzania: Implications for Crystallisation Mechanisms of Oikocrysts', *Journal of Petrology*, **57**, 1171-1198

Basu, A.R., Saha-Yannopoulos, A. Chakrabarty, P. (2020), 'A precise geochemical volcano-stratigraphy of the Deccan traps', *Lithos*, **376-377**, 105754

Basu Sarbadhikari, A., Babu, E. V. S. S. K., Vijaya Kumar, T., Chennaoui Adoujehane, H. (2016), 'Martian meteorite Tissint records unique petrogenesis among the depleted shergottites', *Meteoritics & Planetary Science*, **51**, 1588-1610

Baziotis, I. P., Liu, Y., DeCarli, P. S., Jay Melosh, H., McSween, H. Y., Bodnar, R. J., Taylor, L. A. (2013), 'The Tissint Martian meteorite as evidence for the largest impact excavation', *Nature Communications*, **4**, DOI: 10.1038/ncomms2414

Bogard, D. D. & Johnson, P. (1983), 'Martian Gases in an Antarctic Meteorite?', *Science*, **221**, 651-654

Bourdon, B., Turner, S., Dossetto, A. (2003), 'Dehydration and partial melting in subduction zones: Constraints from U-series disequillibria', *Journal of Geophysical Research: Solid Earth,* **108**, Issue B6

Brasser, R. (2013), 'The Formation of Mars: Building Blocks and Accretion Time Scale', *Space Science Review*, **174**, 11-25

Brooks, C. L., Stevenson, C., Raine, R., Parker, K. (2016), 'Stratigraphy of the Lower Basalt Formation, Antrim Lava Group, Northern Ireland', *Applied Earth Science*, DOI: 10.1080/03717453.2016.1166614

Canup, R. M. (2014), 'Lunar-forming impacts: processes and alternatives', *Philos Trans A Math Phys Eng Sci,* **372**, 20130175

Canup, R. M. (2019), 'Giant Impact Hypothesis: An evolving legacy of Apollo', *Astronomy*, available at < https://astronomy.com/news/2019/05/giant-impact-hypothesis-an-evolving-legacy-of-apollo >, (Accessed: 09/09/21)

Carlson, R.W. (1991), 'Physical and Chemical Evidence on the Cause and Source Characteristics of Flood Basalt Volcanism', *Australian Journal of Earth Sciences,* **38**, 525-544

Carlson, R.W. & Hart, W. (1988), 'Flood Basalt Volcanism in the Northwestern United States', in Macdougall, J.D., '*Continental Flood Basalts',* Kluwer Academic Publishers, 35-61

Carlson, R. W. (2019), 'Analysis of lunar samples: Implications for planet formation and evolution', *Science,* **365**, 240-243

Carr, M. (2006), 'Volcanism' in *Carr. M., 'The Surface of Mars',* Cambridge University Press, Chapter 3, 43-47

Chapin, C. E., Wilks, M., McIntosh, W. C. (2004), 'Space-time patterns of Late Cretaceous to present magmatism in New Mexico – comparison with Andean volcanism

and potential for future volcanism', *New Mexico Bureau of Geology & Mineral Resources, Bulletin,* **160**, 13-40

Chen, S., Ni, P., Zhang, Y., Gagnon, J. (2019), 'Element partitioning between olivine and melt inclusions in Lunar samples', *50th Lunar and Planetary Science Conference*, LPI Contribution No. 2132, 3025

Chevrel, M. O., Baratoux, D., Hess, K-U., Dingwell, D. B. (2014), 'Viscous flow behaviour of tholeiitic and alkaline Fe-rich Martian basalts', *Geochimica et Cosmochimica Acta,* **124**, 348-365

Condie, K. C. (2016), 'Chapter 3 – Tectonic Settings', in Condie, K. C. '*Earth as an Evolving Planetary System (Third Edition)', Academic Press,* 43-88

Crozaz. G., Floss, C., Wadhwa, M. (2003), 'Chemical alteration and REE mobilization in meteorites from hot and cold deserts', *Geochimica et Cosmochimica Acta*, **67**, 4727-4741

De Paor, A. (2001), 'A theory of the Earth's magnetic field and of sunspots, based on the self-excited dynamo incorporating the Hall Effect', *Nonlinear Processes in Geophysics*, **8**, 265-279

Driscoll, P. (2019), 'Geodynamo recharged', *Nature Geoscience*, **12**, 83-84

Dunham, E. T., Balta, J. B., Wadhwa, M., Sharp, T. G., McSween, Jr. H. Y. (2019), 'Petrology and geochemistry of olivine-phyric shergottites LAR12095 and LAR 12240: Implications for their petrogenetic history on Mars', *Meteorit Planet Sci.*, **54**, 811-835

Drake, M. J. & Righter, K. (2002), 'Determining the composition of the Earth', *Nature*, **416**, 39-44

Edwards, D. (2007), 'Northwest Africa 3160 (Lunar (bas. Breccia))', *Encyclopedia of Meteorites*, available at < http://www.encyclopedia-of-meteorites.com/test/NWA3160_don_edwards.jpg >, (Accessed: 22/12/21)

Eggins, S.M. (2007), 'Laser Ablation ICP-MS Analysis of Geological Materials Prepared as Lithium Borate Glasses', *Geostandards Newsletter*, **27**, 147-162

Elardo, S. (2016), 'Lunar Magma Ocean Theory, Origins, and Rationale', in *Cudnik. B. 'Encyclopaedia of Lunar Scienc',* Springer, Cham, https://doi.org/10.1007/978-3-319-05546-6_25-1

ESA (2021), 'ESA^{2}C Collection', Available at < https://sacf.esa.int/sacf-home/esa2c-collection/ >, (Accessed: 09/10/21)

Evans, C. (2016). Meteorite Classification Chart. Retrieved September 20, 2016, from https://curator.jsc.nasa.gov/education/classification.cfm

Fassett, C. I. & Minton, D. A. (2013), 'Impact bombardment of the terrestrial planets and the early history of the Solar System', *Nature Geoscience*, **6**, 520-524

Ferrari, L., Valencia-Moreno, M., and Bryan, S., 2007, Magmatism and tectonics of the Sierra Madre Occidental and its relation with the evolution of the western margin of North America, in Alaniz-Álvarez, S.A., and Nieto-Samaniego, Á.F., eds., *Geology of México: Celebrating the Centenary of the Geological Society of México*: Geological Society of America Special Paper 422, p. 1–39

Filiberto, J. (2008), 'Similarities between the shergottites and terrestrial ferropicrites', *Icarus*, **197,** 52-59

Filiberto, J. (2017), 'Geochemistry of Martian basalts with constraints on magma genesis', *Chemical Geology*, **466**, 1-14

Filiberto J., Jackson C., Le L., and Treiman A. H. (2009). Partitioning of Ni between olivine and an iron-rich basalt: Experiments, partition models, and planetary implications. *American Mineralogist* **94**: 256– 261

Filiberto J. and Dasgupta R. (2010). Fe-Mg partitioning between olivine and Martian magmas: Application to genesis of olivine-phyric shergottites and conditions of melting in the Martian interior (abstract). *Meteoritics & Planetary Science* **45**: A54

Filiberto, J., Musselwhite, D. S., Gross, J., Burgess, K., Le, L., Treiman, A. H. (2010), 'Experimental petrology, crystallisation history, and parental magma characteristics of olivine-phyric shergottite NWA1068: Implications for the petrogenesis of 'enriched' olivine-pyric shergottites', *Meteoritics & Planetary Science*, **45**, 1258-1270

Filiberto, J., Gross, J., Udry, A., Trela, J., Wittmann, A., Cannon, K. M., Penniston-Dorland, P., Ash, R., Hamilton, V. E., Meado, A. L., Carpenter, P., Jolliff, B., Ferré, E. C. (2018), 'Shergottite Northwest Africa 6963: A Pyroxene-Cumulate Martian Gabbro', *Journal of Geophysical Research: Planets*, **123**, 1823-1841

Forget, F. & Hauber, E. (2015), 'Mars' in *Gargaud, M., Irvine, W. M., Amiles, R., Cleavesll, H. J., Pinti, D. L., Quintanilla, J. C., Rouan, D., Spohn, T., Tirard, S., Viso, M., 'Encyclopedia of Astrobiology*, Springer, Berlin, https://doi.org/10.1007/978-3-662-44185-5_938

Frost, D. A., Lasbleis, M., Chandler, B., Romanowicz, B. (2021), 'Dynamic history of the inner core constrained by seismic anistropy', *Nature Geoscience*, **14**, 531-535

Foucher, F., Hickman-Lewis, K., Hutzler, A., Joy, K. H., Folco, L., Bridges, J. C., Wozniakiewicz, P., Martínez-Frías, J., Debaille, V., Zolensky, M., Yano, H., Bost, N., Ferrière, L., Lee, M., Michalski, J., Schroeven-Deceuninck, H., Kminek, G., Viso, M., Russell, S., Smith, C., Zipfel, J., Westall. (2021), 'Definition and use of functional analogues in planetary exploration', *Planetary and Space Science*, **197**, 105162

Franz, H., King, P. L., Gaillard, F. (2019), 'Chapter 6 – Sulfur on Mars from the Atmosphere to the Core' *in Filiberto, J. & Schwenzer, S. P. 'Volatiles in the Martian Crust',* Elsevier, DOI: 10.1016/C2015-0-01738-5

Ganerød, M., Smethurst, M. A., Torsvik, T. H., Prestvik, T., Rousse, S., McKenna, C., van Hinsbergen, D. J. J., Hendriks, B. W. H. (2010), 'The North Atlantic Igneous Province rescontructed and its relation to the Plume Generation Zone: the Antrim Lava Group revisted', *Geophysical Journal International*, **182**, 183-202

Geert-Jan, L. M. de Hass., Nijland, T. G., Valbracht, P. J., Maijer, C., Verschure, R., Andersen, T. (2002), 'Magmatic versus metamorphic origin of olivine-plagioclase coronas', *Contribution to Minerals Petrology*, **143**, 537-550

Gillet, P., Barrat, J. A., Beck, P., Marty, B., Greenwood, R. C., Franchi, I.A. & Cotton, J. (2005), 'Petrology, geochemistry, and cosmic ray exposure age of lherzolitic shergottite Northwest Africa 1950', *Meteoritics & Planetary Science*, **40**(8), 1175-1184

Goodrich, C. A. (2002) 'Olivine-phyric martian basalts: A new type of shergottite', *Meteoritics & Planetary Science,* **37**, B31-B34

Gordeychik, B., Churikova, T., Kronz, A., Sundermeyer, C., Simakin, A., Wörner, G. (2018), 'Growth of, and diffusion in, olivine in ultra-fast ascending basalt magmas from Shiveluch volcano', *Scientific Reports*, **8**, 11775

Graham, D.J. & Midgley, N.G. (2000), 'Graphical representation of particle shape using triangular diagrams: an Excel spreadsheet method', *Earth Surface Processes and Landforms*, **25**(13), 1473-1477

Gross, J. & Joy, K. H. (2016), 'Evolution, Lunar: From Magma Ocean to Crust Formation', in *Cudnik, B.,* '*Encyclopedia of Lunar Science*', Springer, Cham, DOI: 10.1007/978-3-319-05546-6_39-1

Gross, J., Teriman, A. H., Filiberto, J., Herd, C. D. K. (2011), 'Primitive olivine-phyric shergottite NWA5789: Petrography, mineral chemistry, and cooling history imply a magma similar to Yamato-980459', *Meteoritics & Planetary Science*, **46**, 116-133

Halliday, A. N. (2012), 'The Origin of the Moon', *Planetary Science*, **338**, 1040-1041

Hartmann, W. K. & Neukum, G. (2001), 'Cratering Chronology and the Evolution of Mars', *Space Science Reviews*, **96**, 165-194

Head III, J. W. & Wilson, L. (1992), 'Lunar Mare volcanism: Stratigraphy, eruption conditions and the evolution of secondary crusts *', *Geochemica et Cosmochimica,* **56**, 2155-2175

Helz, R. T., Clague, D. A., Sisson, T. W., Thornber, C. R. (2014), 'Petrologic Insights into Basaltic Volcanism at Historically Active Hawaiian Volcanoes', in Poland, M. P.,

Takahashi, T. J., Landowski, C. M., '*Characteristics of Hawaiian Volcanoes*', U.S. Geological Survey Professional Paper 1801, Chapter 6, p237

Herd. C. D. K. (2003), 'The oxygen fugacity of olivine-phyric martian basalts and the components within the mantle and crust of Mars', *Meteoritics & Planetary Science,* **38**, 1793-1805

Hibiya, Y., Archer, G. J., Tanaka, R., Sanborn, M. E., Sato, Y., Lizuka, T., Ozawa, K., Walker, R. J., Yamaguchi, A., Yin, Q-Z., Nakamura, T., Irving, A. J. (2018), 'The origin of the unique achondrite Northwest Africa 6704: Constraints from petrology, chemistry and Re-Os, O and Ti isotope systematics', *Geochimica et Cosmochimica Acta*, **245**, 597-627

Holness, M. B., Stripp, G., Humphreys, M. C. S., Veksler, I. V., Nielsen, T. F. D., Tegner, C. (2011), 'Silicate Liquid Immiscibility within the Crystal Mush: Late-stage Magmatic Microstructures in the Skaergaard Intrusion, East Greenland', *Journal of Petrology*, **52**, 175-222

Hooper, P. R. (1997), 'The Columbia River Flood Basalt Province: Current Status', in Mahoney, J.J & Coffin, M.F., '*Large Igenous Provinces: Continental, Oceanic, and Planetary Flood Volcanism'*, **100,** American Geophysical Union

Hooper, P.R. (1990), 'The timing of crustal extension and the eruption of continental flood basalts', *Nature*, **345**, 246-249

Hooper, P.R. & Hawkesworth, C.J. (1993), 'Isotopic and Geochemical Constraints on the Origin and Evolution of the Columbia River Flood Basalts', Journal of Petrolgy, 34, 1203-1246

Howarth, G. H., Pernet-Fisher, J., Barry, P. H. (2014), 'Petrology of the new Enriched lherzolitic Shergottite NWA7397 Formation', *45th Lunar and Planetary Science Conference, Abstract 1310*

Howarth, G. H., Pernet-Fisher, J. F., Balta, J. B.,Barry, P. H., Bodnar, R. J., Taylor, L. A. (2014), 'Two-stage polybaric formation of the new enriched, pyroxene-oikocrystic, lherzolitic Shergottite, NWA7397', *Meteoritics & Planetary Science,* **49**, 1812-1830

Hughes, S.S., Haberle, C.W., Nawotniak, S.E.K., Sehlke, A., Garry, W.B., Elphic, R.C., Payler, S.J., Stevens, A.H., Cockell, C.S., Brady, A.L., Heldmann, J.L., Lim, D.S.S. (2019), 'Basaltic Terrains in Idaho and Hawai'i as Planetary Analogs for Mars Geology and Astrobiology', *Astrobiology*, **19(3)**, 260-283

Irving, T. (2021), 'An up-to-date List of Martian Meteorites', *University of Washington*, < https://imca.cc/mars/martian-meteorites-list.htm > (Accessed: 01/09/2021)

Jennings, E. S., Gibson, S. A., Maclennan, J. (2019) 'Hot primary melts and mantle source for the Paraná-Etendeka flood basalt province: New constraints from Al-in-olivine thermometry', *Chemical Geology*, **529**, 119287

Jiang, Z., Li, S., Liu, Q., Zhang, J., Zhou, Z., Zhang, Y. (2021), 'The trials and tribulations of the Hawaii hot spot model', *Earth-Science Reviews*, **215**, 103544

Jones, R. H. (2003), 'Meteorites', in Meyers, R. A. '*Encyclopedia of Physical Science and Technology (Third Edition)',* 559-574

Jones, T. H. (2003), 'Constraints on the structure of the Martian interior determined from the chemical and isotopic systematics of SNC meteorites', *Planetary Science*, **38**, 1807-1814

Kasbohm, J. & Schoene, B. (2018), 'Rapid eruption of the Columbia River flood basalt and correlation with the mid-Miocene climate optimum', *Geology*, **4**, eaat8223

Keevil, H. A., Namur, O., Holness, M. B. (2020), 'Microstructures and Late-Stage Magmatic Processes in Layered Mafic Intrusions: Symplectites from the Sept Iles Intrusion, Quebec, Canada', *Journal of Petrology*, **61**, egaa071

Keszthelyi, L. & McEwen, A.S. (2000), 'Terrestrial analogs and thermal models for Martian flood lavas', *Journal of Geophysical Research,* **105**, 15,027-15,049

Keszthelyi, L. & McEwen, A. (2007), 'Comparison of flood lavas on Earth and Mars', in Chapman, M., '*The Geology of Mars: Evidence from Earth-Based Analogs'*, Cambridge University Press, Chapter 5, 126-145

Keszthelyi, L., Self, S., Thordarson, T. (2006), 'Flood lavas on Earth, Io and Mars', *Journal of the Geological Society*, **163**, 253-264

Khan, A. & Connolly, J. A. D. (2008), 'Constraining the composition and thermal state of Mars from inversion of geophysical data', *Journal of Geophysical Research,* **113**, E07003

Kiefer, W. S. (2010), 'Melting in the martian mantle: Shergottie formation and implications for present-day mantle convection on Mars'*, Meteoritics & Planetary Scince,* **38**, 1815-1832

Kiefer, W.S. (2013), 'Mantle Plumes and Geologically Recent Volcanism on Mars', *American Geophysical Union, Fall Meeting 2013, abstract id D121A-2263*

Kiefer, W. S. & Jones, J. H. (2015), 'Formation and Preservation of the Depleted and Enriched Shergottite Isotopic Reservoirs in a Convecting Martian Mantle', *46th Lunar and Planetary Science Conference*, Abstract 1197

Knapmeyer-Endrun, B. & Kawamura, T. (2020), 'NASA's InSight mission on Mars – first glimpses of the planets interior from seismology', *Nature Communications*, **11**, 1451

Koeberl, C. (2003), 'The Late Heavy Bombardment in the Inner Solar System: Is there any Connection to Kuiper Belt Objects', *Earth, Moon and Planets*, **92**, 79-87

Korotev, R. L. (2021), 'List of Lunar Meteorites – Feldspathic to Basaltic Order', *Washington University in St. Louis, Earth and Planetary Sciences*, available at < http://meteorites.wustl.edu/lunar/moon_meteorites_list_alumina.htm >, (Accessed: 01/09/2021)

Krot, A. N., Keil, K. Scott, E. R. D., Goodrich, C. A., Weisberg, M. K. (2014), 'Classification of Meteorites and Their Genetic Relationships', *Treatise on Geochemistry* in *Earth Systems and Environmental Sciences*, **1**, 1-63

Lapen, T. J., Righter, M., Brandon, A. D., Debaille, V., Beard, B. L., Shafer, J. T., Peslier, A. H. (2010), 'A younger age for ALH84001 and its geochemical link to shergottite sources in Mars', *Science*, **328**, 347-51

Larrea, P., Franca, Z., Lago, M., Widom, E., Galé, Ubide, T. (2012), 'Magmatic Processes and the Role of Antecrysts in the Genesis of the Corvo Island (Azores Achipelago, Portugal)', *Journal of Petrology*, **54**, 769-793

Lemelin, M., Morisset, C. E., Germain, M., Hipkin, V. (2013), 'Ilmenite mapping of the lunar regolith over Mare Australe and Mare Ingenii regions: An optimised multisource

approach based on Hapke radiative transfer theory', *The Journal of Geophysical Research Planets*, **118(2)**, DOI: 10.1002/2013JE004392

Libbey, R.B. & Williams-Jones, A.E. (2016), 'Compositions of hydrothermal silicate and carbonates as indicators of physicochemical conditions in the Reykjanes geothermal system, Iceland', *Geothermics,* **64**, 15-27

Lin, Y., Guan, Y., Wang, D., Kimura, M., Leshin, L. A. (2005), 'Petrogenesis of the new lherzolitic shergottites Grove Mountains 99027: Constraints of petrography, mineral chemistry, and rare earth elements', *Meteoritics & Planetary Science*, **40**, 1599-1619

Lofgren, G. E. & Lofgren, E. M. (1981), 'Catalog of Lunar Mare Basalts Greater Than 40 Grams: Part 1: Major and Trace Chemistry', *Lunar and Planetary Contribution,* **438,** 1-409

Lowrey, J. R., Ivanic, T. J., Wyman, D. A., Roberts, M. P. (2017), 'Platy Pyroxene: New Insights into Spinifex Texture', *Journal of Petrology*, 1-30, DOI: 10.1093/petrology/egx069

Lunine, J. I. (2006), 'Physical conditions on early Earth', *Philos Trans R Soc Lond B Biol Sci.,* **29**, 1721-1731

Macdonald, G. A., (1949), 'Petrography of the Island of Hawaii', *Geological Survey Professional Paper 214-D*

Macdougall, J.D. (1988), 'Continental Flood Basalts and MORB: A Brief Discussion of Similarities and Differences in their Petrogenesis', in Macdougall, J.D. '*Continental Flood Basalts*', Kluwer Academic Publishers, 331-344

Manick, K., Mavris, C., Duvet, L., Schroeven-Deceuninck, H., Smith, C. L. (2017), 'Starting a European Space Agency Sample Analogue Collection (ESA^{2}C) and Curation Facility for Exploration Missions: Chemical Characterisation', Lunar Planetary Science Institute Conference, Abstract No. 1220

Mari, N., Hallis, L. J., Daly, L., Lee, M. R. (2020), 'Convective activity in a Martian magma chamber recorded by , P-zoning in Tissint olivine', *Meteoritics & Planetary Science,* **55**, 1057-1072

Martin, D. J. P. & Duvet, L. (2019), 'ESA's sample analogue facility (SACF), and expanding ESA's exploration sample analogue collection (ESA^{2}C', *50th Lunar and Planetary Science Conference*, **Abstract No. 2132**

McCubbin, F. M., Boyce, J. W., Novák-Szabó, T., Santos, A. R., Tartèse, R., Muttik, N., Domokos, G., Vazquez, J., Keller, L. P., Moser, D. E., Jerolmack, D. J., Shearer, C. K., Steele, A., Elardo, S. M., Rahman, Z., Anand, M., Delhaye, T., Agee, C. B. (2016), 'Geologic history of Martian regolith breccia Northwest Africa 7034: Evidence for hydrothermal activity and lithologic diversity in the Martian crust', *Journal of Geophysical Research: Planets,* **121**, 2120-2149

McSween Jr, H. Y. (1999), 'Achondrite Parent Bodies', in *McSween Jr, H. Y., 'Meteorites and Their Parent Bodies – Second Edition',* Cambridge University Press, p174

McSween, Jr, H. Y. (2015), 'Petrology on Mars', *American Mineralogist,* **100**, 2380-2395

McSween, Jr, H. Y., Taylor, J., Wyatt, M. B. (2009), 'Elemental Composition of the Martian Crust', *Science*, **324**, 736-739

McSween, Jr. H. Y., Murchie, S. L., Bridges, N. T., Anderson, R. C., Bell III, J. F., Britt, D. T., Brückner, J., Dreibus, G., Economou, T., Ghosh, A., Golombek, P., Greenwood, J. P., Johnson, J. R., Moore, H. J., Morris, R. V., Parker, T. J., Rieder, R., Singer, R., Wänke, H. (1999), 'Chemical, multispectral, and textural constraints on the composition and origin of rocks at the Mars Pathfinder landing site', *Journal of Geophysical Research Atmospheres*, **104(E4)**, DOI: 10.1029/98JE02551

McSween, H. Y., Ruff, S. W., Morris, R. V., Bell III, J. F., Herkenhoff, K., Gellert, R., Stockstill, K. R., Tornabene, L. L., Squyres, S. W., Crisp, J. A., Christensen, P. R., McCoy, T. J., Mittlefehldt, D. W., Schmidt, M. (2006), 'Alkaline volcanic rocks from the Columbia Hills, Gusev crater, Mars', *Journal of Geophysical Research,* **111**, E9

Mezger, K., Debaille, V., Kleine, T. (2013), 'Core Formation and Mantle Differentiation on Mars', *Space Science Review*, **174**, 27-48

Mikouchi, T. & Kurihara, T. (2008), 'Mineralogy and petrology of paired lherzolitic shergottites Yamato 000027, Yamato 000047 and Yamato 000097: Another fragment from a Martian 'lherzolite' block', *Polar Science*, **2**, 175-194

Mikouchi ab, T., Miyamoto a, M., Mckay ab, G. A. (1999), 'The role of undercooling in producing igneous zoning trends in pyroxenes and maskelynites among basaltic Martian meteorites', *Earth and Planetary Science Letters*, **173**, 235-256

Mitchell, K. L. & Wilson, L. (2003), 'Mars: a geologically active planet', *Astronomy & Geophysics*, **44**, 4.16-4.20

Nagaoka, H., Takeda, H., Karouji, Y., Ohtake, M. (2014), 'Implications for the origins of pure anorthosites found in the feldspathic lunar meteorites Dhofar 489 group', *Earth, Planets and Space*, **66**(1):115

Mullis, A. M. (1993), 'A mechanism for the generation of the Lunar-Mare basalts', Geophys. J. Int, **114**, 196-208

NASA (2021), 'Viking 1 & 2', *NASA Science, MARS Exploration Program',* available at < https://mars.nasa.gov/mars-exploration/missions/viking-1-2/ >, (Accessed: 01/09/21)

NASA Earth Observatory (2006), 'Mauna Loa Oberservatory', available at < https://earthobservatory.nasa.gov/images/43182/mauna-loa-observatory >, (Accessed: 08/09/21)

NASA Photojournal (1998a), 'PIA00304: Farside View of Earth's Moon as Seen by the Celementine Spacecraft', available at < https://photojournal.jpl.nasa.gov/catalog/PIA00304 > (Accessed: 06/10/21)

NASA Photojournal (1998b), 'PIA00302: Nearside of Earth's Moon as Seen by the Clementine Spacecraft', available at < https://photojournal.jpl.nasa.gov/catalog/PIA00302 > (Accessed: 06/10/21)

Nikishin, A. M. (2011), 'The Geological History and Geodynamics of the Earth', *Moscow University Geology Bulletin*, **66**, 225-241

O'Hara, M.J. (2000), 'Flood Basalts and Lunar Petrogenesis', *Journal of Petrology,* **41**, 1121-1125

O'Hara, M. J. (2000), 'Flood Basalts, Basalt Floods or Topless Bushvelds? Lunar Petrogenesis Revisted', *Journal of Petrology,* **41**, 1545-1651

Ohtake, M., Takeda, H., Matsunaga, T., Yokota, Y., Haruyama, J., Morota, T., Yamamoto, S., Ogawa, Y., Hiroi, T., Karouji, Y., Saiki, K., Lucey, P. G. (2012), 'Asymmetric crustal growth on the Moon indicated by primitive farside highland materials', *Nature Geoscience*, **5**, 384-388

Ori, G.G. & Karna, A. (2003), 'The Uppermost Crust of Mars and Flood Basalts', *Lunar and Planetary Science XXXIV*, 1539

Papike, J. J., Karner, J. M., Shearer, C. K., Burger, P. V. (2009), 'Silicate mineralogy of Martian meteorites', *Geochimica et Cosmochimica Acta,* **73**, 7443-7485

Patterson, E. M. (1950), 'Evidence of Fissure Eruption in the Tertiary Lava Plateau of North East Ireland', *Geological Magazine*, **87**, 45-52

Patterson, E. M., Mitchell, W. A., Swaine, D. J. (1954-1956), 'The Tertiary Volcanic Succession in the Western Part of the Antrim Plateau', *Proceedings of the Royal Irish Academy. Section B: Biological, Geological, and Chemical Science,* **57**, 155-178

Pepin, R. O. (1985), 'Meteorites: Evidence of Martian Origins', *Nature*, **317**, 473-475

Pfalzner, S., Davies, M. B., Gounelle, M., Johansen, A., Münker, C., Lacerda, P., Portegies Zwart, S., Testi, L., Trieloff, M., Veras, D. (2015), 'The formation of the solar system', *Physica Scripta*, **90**, 068001

Pietruszka, A. J., Marske, J. P., Heaton, D. E., Garcia, M. O., Rhodes, J. M. (2018), 'An Isotopic Perspective into the Magmatic Evolution and Architecture of the Rift Zones of Kilauea Volcano', *Journal of Petrology*, **59**, 2311-2352

Poland, M. P., Mikilus, A., Montgomery-Brown, E. (2011), 'A refined model for Kilauea's magma plumbing system', *American Geophysical Union Fall Meeting Abstract V34A-06*

Poland, M. P., Mikilus, A., Montgomery-Brown, E. (2014), 'Magma Supply, Storage and Transport at Shield-Stage Hawaiian Volcanoes', in Poland, M. P., Takahashi, T. J., Landowski, C. L. *'Characteristics of Hawaiian Volcanoes',* U.S. Geological Survey, Reston, Virginia, Chapter 5, 179-237

Poldervaart, A. & Hess, H. H. (1951), 'Pyroxenes in the Crystallisation of Basaltic Magma', *The Journal of Geology*, **59**, 472-489

Righter, K. & O'Brien, D. P. (2011), 'Terrestrial Planet Formation', *Proceedings of the National Academy of Sciences of the United States of America,* **108**(48), 19165-19170

Rivoldini, A., Van Hoolst, T., Verhoeven, O., Mocquet, A., Dehant, V. (2011), 'Geodesy constraints on the interior structure and composition of Mars', *Icarus*, **213**, 451-472

Roeder, P. L. & Emslie, R. F. (1970), 'Olivine-Liquid Equilibrium', *Contributions to Mineralogy and Petrology,* **29**, 275-289

Ruzicka, A., Snyder, G.A., Taylor, L.A. (2000), 'Comparative geochemistry of basalts from the Moon, Earth, HED asteroid, and Mars: Implications for the origin of the Moon', *Geochimica et Cosmochimica Acta,* **65**, 979-997

Sano, T., Fujii, T., Deshmukh, S.S., Fukuoka,T., Aramaki, S. (2001), 'Differentiation Process : Contribution from Deccan Trap Basalts: Contribution from Geochemistry and Experimental Petrology', Journal of Petrology, **42**, 2175-2195

Sautter, V. & Payre, V. (2021), 'Alkali magmatism on Mars: an unexpected diversity', *Comptes Rendus Geoscience, Sciences de la Planète,* 1778-7025

Schaber, G. G. (1973), 'Lava flows in Mare Imbrium: Geologic evaluation from Apollo orbital photography', *Proceedings of the Lunar Science Conference,* **4**, 73-92

Schmidt, M. E., Campbell, J. L., Gellert, R., Perrett, G. M., Treiman, A. H., Blaney, D. L., Olilla, A., Calef, F. J., Edgar, L., Elliott, B. E., Grotzinger, J., Hurowitz, J., King, P. L., Minitti, M. E., Sautter, V., Stack, K., Berger, J. A., Bridges, J. C., Ehlmann, B. L., Forni, O., Leshin, L. A., Lewis, K. W., McLennan, S. M., Ming, D. W., Newsom, H., Pradler, I., Squyres, S. W., Stopler, E. M., Thompson, L., VanBommel, S., Wiens, R. C. (2014), 'Geochemical diversity in first rocks examined by the Curiosity Rover in Gale Crater: Evidence for and significance of an alkali and volatile-rich igneous source', *Journal of Geophysical Research: Planets,* **119**, 64-81

Schulz, T., Povinec, P. P., Ferrière, L., Timothy Jull, A. J., Kováčik, A., Sykora, I., Tusch, J., Münker, C., Topa, D., Koeberl, C. (2020), 'The history of the Tissint meteorite, from its crystallisation on Mars to its exposure in space: New geochemical, isotopic, and cosmogenic nuclide data', *Meteoritics & Planetary Science*, **55**, 294-311

Self, S., Coffin, M.F., Rampino, M.R., Wolff, J.A. (2015), 'Large Igneous Provinces and Flood Basalt Volcanism' in Sigurdsson, H. *'The Encyclopaedia of Volcanoes (Second Edition)',* Academic Press, Chapter 24, 441-455

Shahar, A., Hillgren, V. J., Horan, M. F., Mesa-Garcia, J., Kaufman, L. A., Mock, T. D. (2015), 'Sulfur-controlled iron isotope fractionation experiments of core formation in planetary bodies', *Geochimica et Cosmochimica Acta*, **150**, 253-264

Shearer, C. K., Burger, P. V., Papike, J. J., Borg, L. E., Irving, A. J., Herd, C. D. K. (2007), ''Petrogenic linkages among Martian basalts: Implications based on trace element chemistry of olivine', *Lunar and Planetary Science XXXVIII*, **Abstract 1140**

Shearer, C. K., Burger, P. V., Papike, J. J., Borg, L. E., Irving, A. J., Herd, C. (2008), 'Petrogenic linkages among Martian basalts: Implications based on trace element chemistry of olivine', *Meteoritics & Planetary Science,* **43**,1241-1258

Sibille, L. & Carpenter, P. K. (2006), 'Standard Lunar regolith simulants for space resource utilisation technologies development: Effects of materials choices', *Planetary Science XXXVII*, **1789**

Silver. P.G., Behn, M.D., Kelley, K., Schmitz, M., Savage, B. (2006), 'Understanding Cratonic Flood Basalts', *Earth and Planetary Science Letters,* **245**, 190-201

Simms, M. J. (2000), 'The sub-basaltic surface in northeast Ireland and its significance in interpreting the Tertiary history of the region', *Proceedings of the Geologists' Association*, **111**, 321-333

Smith, C., Russell, S., Almeida, N. (2018), 'Meteorites: The Story of Our Solar System', Natural History Museum, London

Smith, C. L., Rumsey, M. S., Manick, K., Gill, S-J., Mavris, C., Schroeven-Deceuninck, H., Duvet, L. (2017), 'Starting a European Space Agency Sample Analogue Collection

(ESA^{2}C) and Curation Facility for Exploration Missions', *European Planetary Science Congress Abstracts*, **11**, EPSC2017-671-1

Solomon, S. C. (1975), 'Mare volcanism and lunar crustal structure', *Proceedings of Lunar Science Conference 6th',* **1**, 1021-1042

Spudis, P. D. (2015), 'Volcanism on the Moon', in Sigurdsson, H. *'The Encyclopedia of Volcanoes', Academic Press,* Chapter 39, 689-700

Stern, R. J. (2002), 'Subduction Zones', *Rev. Geophys.,* **40**(4), 1012, DOI: 10.1029/2001RG000108

Thompson, J. O. & Ramsey, M. S. (2020), 'Spatiotemporal variability of active lava surface radiative properties using ground-based multispectral thermal infrared data', *Journal of Volcanology and Geothermal Research*, **208**(47): 107077

Stewart, A. J., Schmidt, M. W., Van Westrenen, W., Liebske, C. (2007), 'Mars: A New Core-Crystallisation Regime', *Science*, **316**, 1323-1325

Stikrude, L., Scipioni, R., Desjarlais, M. P. (2020), 'A silicate dynamo in the early Earth', *Nature Communications*, **11**, Article Number: 935

Storey, W. C. (1973), 'Volatization Studies on a Terrestrial Basalt and their Applicability to Volatization from the Lunar Surface', *Nature Physical Science*, **241**, 154-157

Susko, D., Karunatillake, S., Kodikara, G., Skok, J.R., Wray, J., Heldmann, J., Cousin, A., Judice, T. (2017), 'A record of igneous evolution in Elysium, a major martian volcanic province', *Scientific Reports*, **7**, 43177

Stoeckli, (2013), 'Northwest Africa 7397 (Martian (Shergottite))', Available at < https://www.lpi.usra.edu/meteor/get_original_photo.php?recno=5663353 > (Accessed: 09/10/21)

Tatsumi, Y. & Kogiso, T. (2003), 'The subduction factory: its role in the evolution of the Earth's crust and mantle', in *Larter, R. D. & Leat., P. T. 'Intra-Oceanic Subduction Systems: Tectonic and Magmatic Processes'* , Geological Society, London, Special Publications, **219**, 55-80

Taylor, G. J. (2020), 'Explaining the Compositional Heterogeneities of the Martian Mantle by Late Accretion of Large Projectiles', *Planetary Science Research Discoveries*, available at < http://www.psrd.hawaii.edu/May20/martian-mantle.html >, (Accessed: 30/09/21)

Taylor, G. J., (2013), 'The bulk composition of Mars', *Chemie der Erde*, **73**, 401-420

Taylor, S. R. (1982), 'Chapter 6 – Basaltic Volcanism', in *Taylor, S. R. 'Planetary Sceince: A Lunar Perspective',* 263-342

The Meteoritical Society (2021), 'Recommended Classifications', available at < https://www.lpi.usra.edu/meteor/metbullclass.php?sea=Lunar+%28bas.+breccia%29 >, (Accessed: 02/09/2021)

Thompson, R. N., Ottley, C. J., Smith, P. M., Pearson, D. G., Dickin, A.P., Morrison, M. A., Leat, P. T., Gibson, S. A. (2005), 'Source of the Quaternary Alkalic Basalts, Picrites and Basanites of the Potrillo Volcanic Field, New Mexico, USA: Lithosphere or Convecting Mantle', *Journal of Petrology,* **46**, 1603-1643

Tomkeieff, S. J. (1940), 'The basalt lavas of the Giant's Causeway district of Northern Ireland', *Bulletin of Volcanology,* **6**, 89-143

Tomkeieff, S. J. (1934), 'Differentiation in Basalt Lava, Island Magee, Co. Antrim', *Geological Magazine*, **71**(11), 501-512

Tsuchiyama, A. (1986), 'Experimental Study of Olivine-Melt Reaction and it's Petrological Implications', *Journal of Volcanology and Geothermal Research,* **29,** 245-264

Udry, A., Howarth, G. H., Herd, C. D. K., Day, J. M. D., Lapen, T. J., Filiberto, J. (2020), 'What martian meteorites reveal about the interior and surface of Mars', *Journal of Geophysical Research: Planets*, **125**, e2020JE006523

United States Central Intelligence Agency (2019), '*Political Map of the World*', scale 1:35,000,000, available at: < https://geology.com/world/cia-world-map.shtml >, (Accessed: 24/03/21)

USGS a (2021), 'Kilauea', available at: < https://www.usgs.gov/volcanoes/kilauea >, (Accessed: 04/07/21)

USGS b (2021), 'Evolution of Hawaiian Volcanoes', available at: < https://www.usgs.gov/observatories/hawaiian-volcano-observatory/evolution-hawaiian-volcanoes >, (Accessed: 04/07/21)

Valencia, S. N., Jolliff, B. L., Korotev, R. L. (2019), 'Petrography, relationships, and petrogenesis of the gabbroic lithologies in Northwest Africa 773 clan members Northwest Africa 773, 2727, 3160, 3170, 7007 and 10656', *Meteoritics & Planetary Science,* **54**, 2083-2115

Verma, O. & Khosla, A. (2019), 'Developments in the stratigraphy of the Deccan Volcanic Province, peninsular India', *Internal Geophysics (Vulcanology)*, **351**, 461-476

Vermeesch, P. & Pease, V. (2021), 'A genetic classification of the tholeiitic and calc-alkaline magma series', *Geochemical Perspectives Letters,* **19**, 1-6

Ward, K. M., Delph, J. R., Zandt, G., Beck, S. L., Ducea, M. N. (2017), 'Magmatic evolution of a Cordilleran flare-up and its role in the creation of silicic crust', *Scientific Reports,* **7**, 9047

Walker, G. P. L. (1959), 'Some Observations on the Antrim Basalts and Associated Dolerite Intrusions', *Proceedings of the Geologists' Association,* **70**, 179-205

White, W.M. (2016), 'Hot Spots and Mantle Plumes' in Hariff, J., Meschede, M., Petersen, S., Thiede, J. '*Encyclopedia of Marine Geosciences'*, Springer, Dordrecht, H, p316-328

White, R.S. & McKenzie, D. (1995), 'Mantle Plumes and Flood Basalts', *Journal of Geophysical Research*, **100**, 17,543-17,585

Whitten, J. L. & Head III, J. W. (2013), 'Detecting volcanic resurfacing of heavily cratered terrain: Flooding simulations on the Moon using Lunar Orbiter Laser Altimeter (LOLA) data', *Planetary and Space Science*, **85**, 24-37

Wilkinson, C. M., Ganerød, M., Hendriks, B. W. H., Eide, E. A. (2017), 'Compilation and appraisal of geochronological data from the North Atlantic Igneous Province (NAIP)', *Geological Society, London, Special Publications,* **447**, 69-103

Williams, D. R. (2020), 'Earth Fact Sheet', *NASA*, available at < https://nssdc.gsfc.nasa.gov/planetary/factsheet/earthfact.html >

Williams, J-P. (2021), 'Geologic Time Scales for Mercury, Moon, Mars, Venus and Earth', The Planetary Society, available at < https://www.planetary.org/space-images/geologic-time-scales-for >, (Accessed: 26/08/21)

Williams, J-P., Nimmo, F., Moore, W.B., Paige, D. A. (2018), 'The formation of Tharsis on Mars: What the line-of-sight gravity is telling us', *Journal of Geophysical Research: Planets,* **113**, E10, DOI: 10.1029/2007JE003050

Witze, A. (2021), 'First peek inside Mars reveals a crust with cake-likelayers', *Nature,* **589**, 13

Wolff, J.A., Ramos, F.C., Hart, G.L., Patterson, J.D., Brandon, A.D. (2008), 'Columbia River Flood Basalts from a centralised crustal magmatic system', *Nature Geoscience,* **1**, 177-180

Wright, T. L. (1971), 'Chemistry of Kilauea and Mauna Loa Lava in Space and Time', *Geological Survey Professional Paper 735,* United States Government Printing Office, Washington

Wright, T. L. & Fiske, R. S. (1971), 'Origin of the Differentiated and Hybrid Lavas of Kilauea Volcano, Hawaii', *Journal of Petrology*, **12**, 1-66

Wyatt, M. B. & McSween Jr, H. Y. (2002), 'Spectral evidence for weathered basalt as an alternative to andesite in the northern lowlands of Mars', *Nature*, **417**, 263-266

Xue, Z., Xiao, L., Neal, C.L., Xu, Y. (2019), 'Oldest high-Ti basalt and magnesian crustal materials in feldspathic lunar meteorite Dhofar1428', *Geochimica et Cosmochimica Acta,* **266**, 74-108

Yang, F., Huang, X-L., Xu, Y-G., He, P-L. (2019), 'Magmatic Processes Associated with Oceanic Crustal Accretion at Slow-spreading Ridges: Evidence from Plagioclase in Mid-Ocean Ridge Basalts from the South China Sea', *Journal of Petrology*, **60**, 1135-1162

Yaxley, G.M. (2000), 'Experimental study of phase and letting relations of homogenous basalt + peridotite mixtures and implications for the petrogenesis of flood basalts', *Contributions to Mineralogy and Petrology,* **139**, 326-338

Zakharova, N.V., Goldberg, D.S., Sullivan, C., Herron, M.M., Grau, J.M. (2012), 'Petrophysical and geochemical properties of Columbia River flood basalt: Implications for carbon sequestration', *Geochemistry, Geophysics, Geosystems,* **13**

Zhu, M-H., Wünnemann, K., Potter, R. W. K., Kleine, T., Morbidelli, A. (2019), 'Are the Moon's Nearside-Farside Asymmetries the Result of a Giant Impact, *Journal of Geophysical Research: Planets,* **124**, 2117-2140

Zeigler, R.A., Korotev, R. L., Irving, A. J., Jolliff, B. L., Kuehner, S. M., Hupé, A. C. (2006), 'Petrography and composition of Lunar basaltic meteorite NWA3160', *Lunar and Planetary Science XXXVII Conference,* Abstract: 1804

Zimbelman, J. R., Garry, W. B., Bleacher, J. E., Crown, D. A. (2015), 'Volcanism on Mars', in *Sigurdsson, H. 'The Encyclopedia of Volcanoes (Second Edition)',* Elservier, Chapter 41, 717-728

List of Publications Produced during Period of Study:

Willcocks, F., Grimes, S. T., Stephen, N. R. (2021), 'Comparative Planetology of the Inner Solar System; Using Flood Basalts on the Moon (Lunar Maria), Mars (Tharsis and Elysium), and Earth to Investigate the Magmatic Evolution of Our Solar System', *84th Annual Meeting of The Meteoritical Society 2021 (LPI Contrib. No. 2609),* **Abstract #6061**

8. Appendix

Pyroxene Compositions

Appendix 1

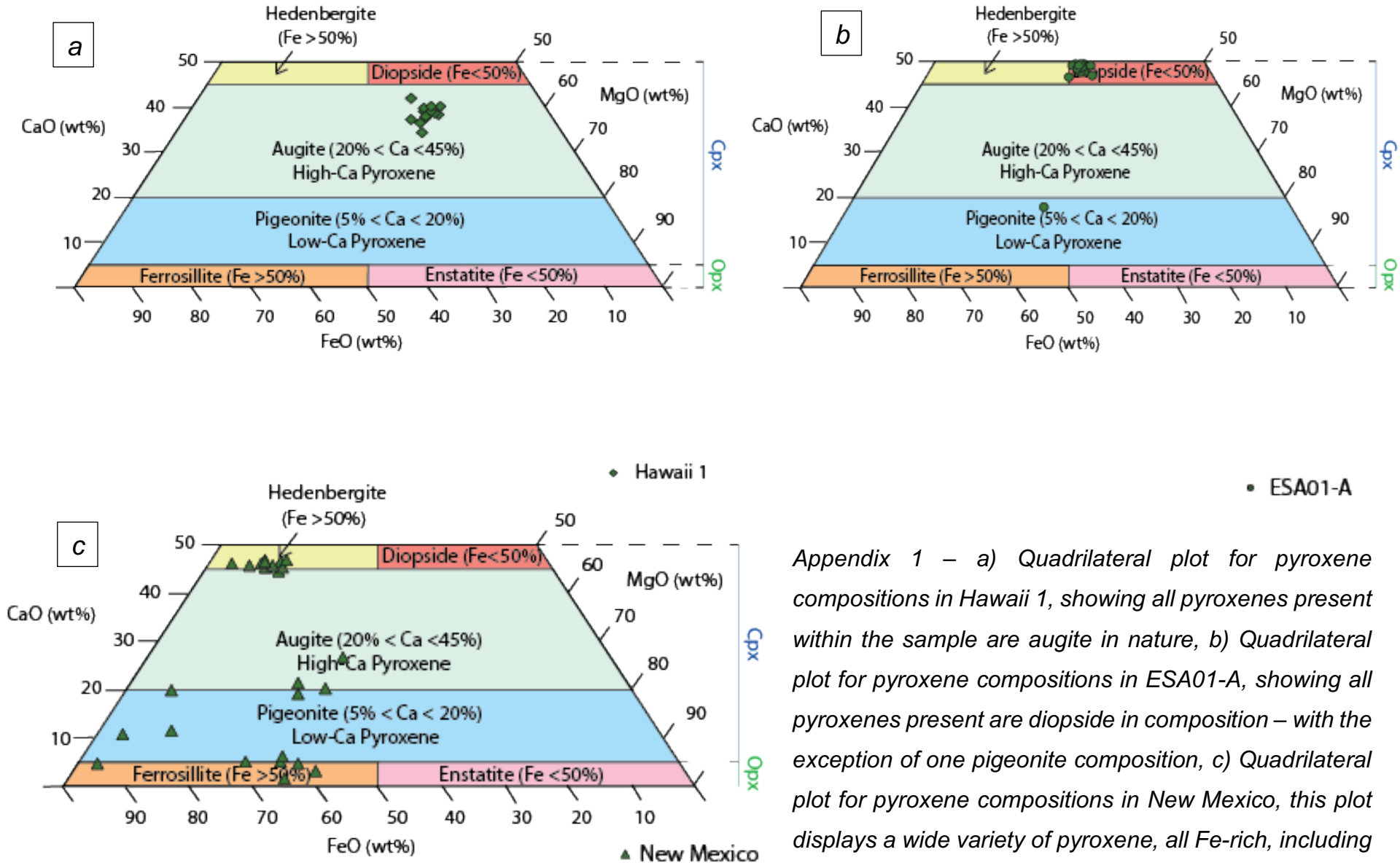

Appendix 1 – a) Quadrilateral plot for pyroxene compositions in Hawaii 1, showing all pyroxenes present within the sample are augite in nature, b) Quadrilateral plot for pyroxene compositions in ESA01-A, showing all pyroxenes present are diopside in composition – with the exception of one pigeonite composition, c) Quadrilateral plot for pyroxene compositions in New Mexico, this plot displays a wide variety of pyroxene, all Fe-rich, including ferrosillite, pigeonite, augite and hedenbergite.

Appendix 2

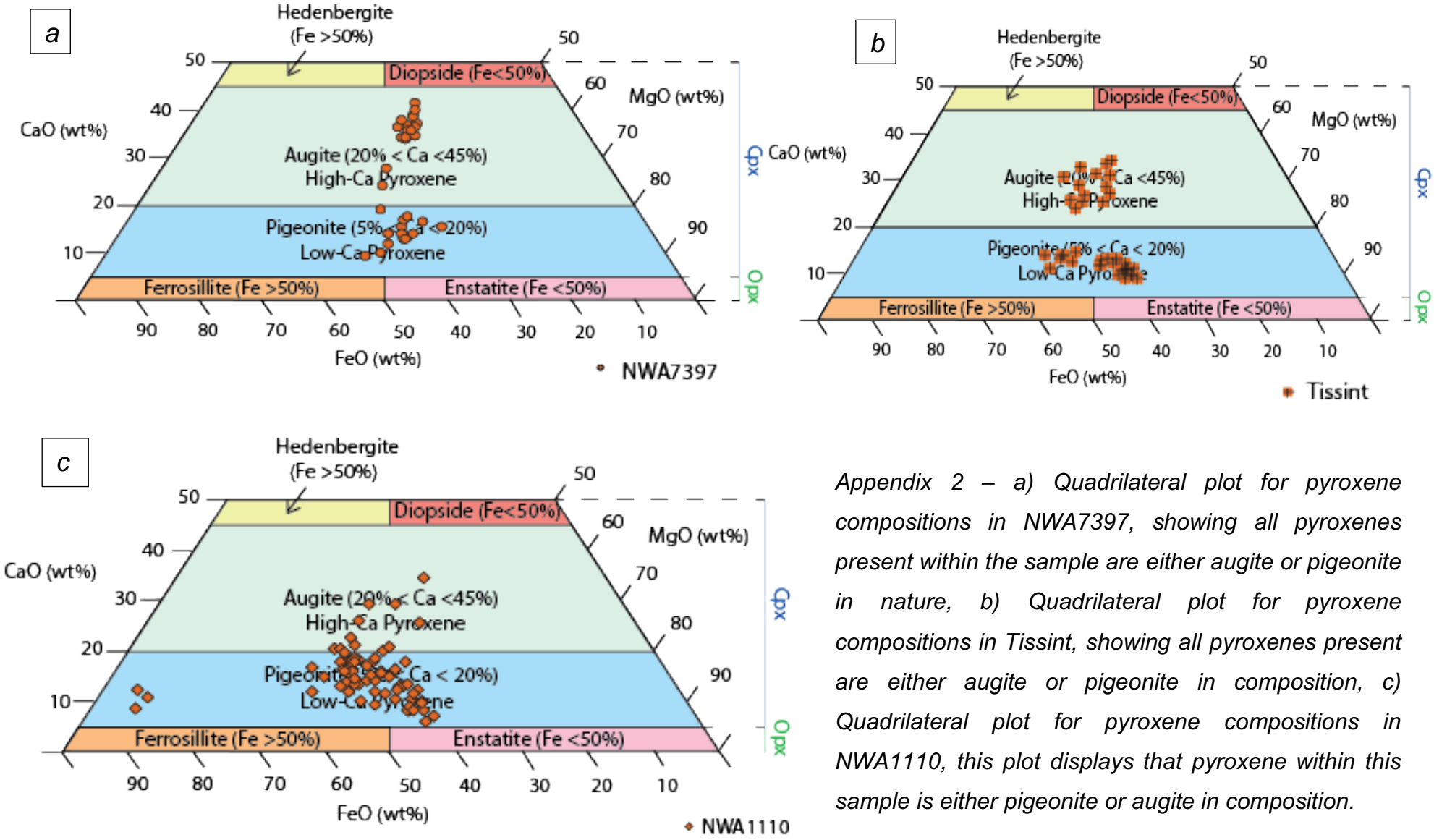

Appendix 2 – a) Quadrilateral plot for pyroxene compositions in NWA7397, showing all pyroxenes present within the sample are either augite or pigeonite in nature, b) Quadrilateral plot for pyroxene compositions in Tissint, showing all pyroxenes present are either augite or pigeonite in composition, c) Quadrilateral plot for pyroxene compositions in NWA1110, this plot displays that pyroxene within this sample is either pigeonite or augite in composition.

Appendix 3

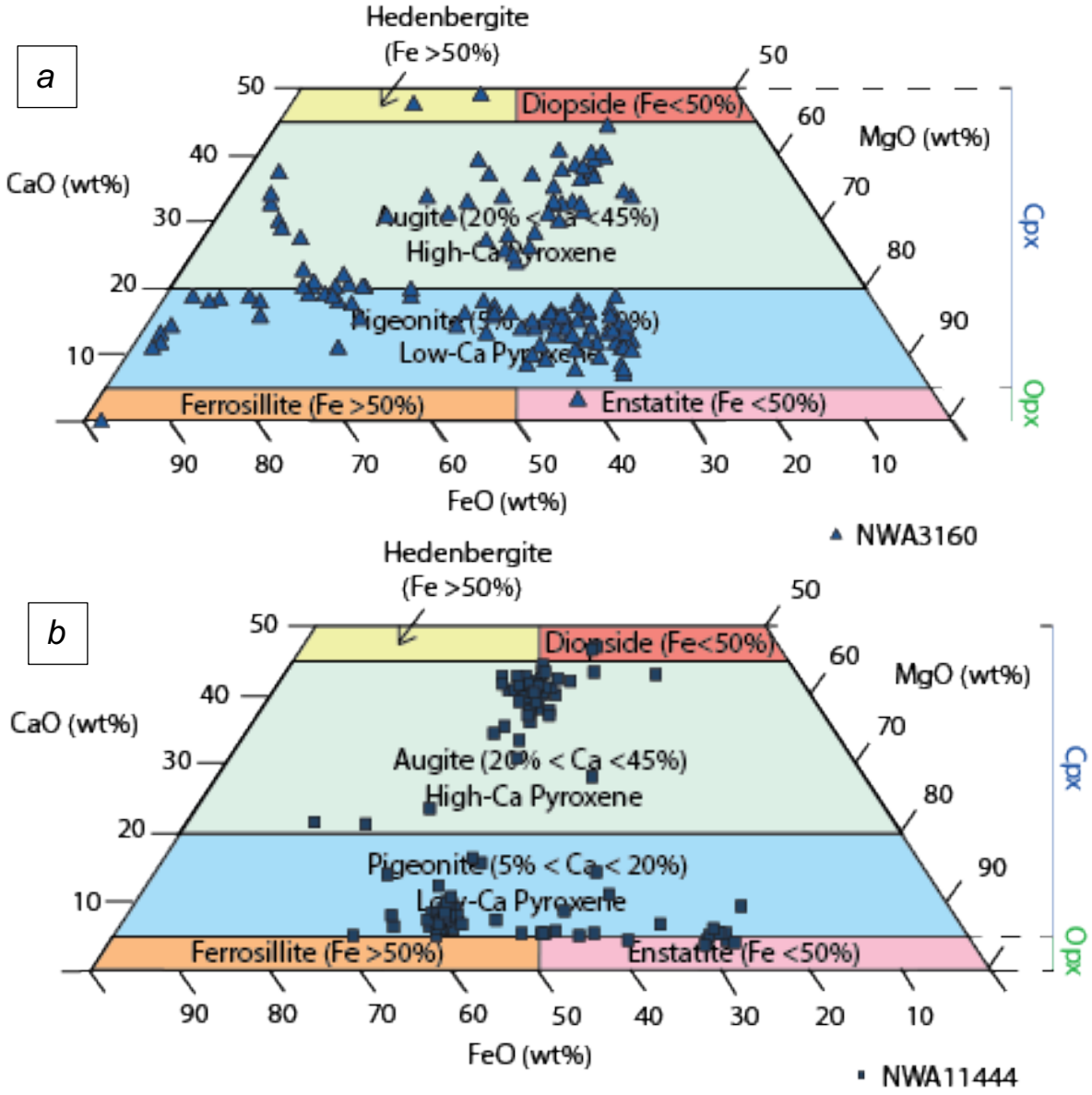

Appendix 3 – a) Quadrilateral plot for pyroxene compositions in NWA3160, this plot displays a range of pyroxenes, all Fe-rich, mainly representing a pigeonite or augite composition, with some examples of hedenbergite, ferrosillite and enstatite b) Quadrilateral plot for pyroxene compositions in NWA11444, showing almost all pyroxenes present are either augite or pigeonite in composition, there are also examples of enstatite across this sample

Appendix 4 – Pyroxene Compositions

For all data tables, where N/A is written, values detected by the SEM were either on or below the detection limit and therefore weren't included.

Hawaii 1												
Data in Wt % Oxide		SiO_2	Al_2O_3	CaO	Na_2O	FeO	MgO	TiO_2	Total	Wo	Ens	Fs
Site 1	Augite 1	42.45	10.12	17.23	N/A	10.24	19.96	N/A	100.00	36.33	42.08	21.59
	Augite 2	50.93	3.28	19.63	N/A	8.60	17.57	N/A	100.01	42.86	38.36	18.78
	Augite 3	51.52	5.82	17.84	N/A	10.15	14.67	N/A	100.00	41.82	34.39	23.79
	Augite 4	56.29	N/A	18.46	N/A	7.67	17.58	N/A	100.00	42.23	40.22	17.55
	Augie 5	54.31	6.25	15.83	N/A	8.14	15.47	N/A	100.00	40.14	39.22	20.64
Site 2	Augite 1	52.00	3.13	18.33	N/A	8.40	16.96	1.17	99.99	41.95	38.82	19.23
	Augite 2	51.27	5.34	15.94	0.65	9.92	15.39	1.50	100.01	38.64	37.31	24.05
	Augite 3	51.67	2.26	18.51	N/A	9.57	17.00	1.00	100.01	41.06	37.71	21.23
	Augite 4	51.65	2.91	17.66	N/A	9.38	17.28	1.11	99.99	39.85	38.99	21.16
	Augite 5	51.39	2.94	18.17	N/A	9.41	16.96	1.14	100.01	40.79	38.08	21.13
	Augite 6	49.87	4.65	17.80	N/A	10.12	16.21	1.34	9.99	40.34	36.73	22.93
Site 3	Augite 1	52.08	2.98	17.31	N/A	9.06	17.46	1.08	99.97	39.49	39.84	20.67
	Augite 2	51.74	3.13	18.10	N/A	8.75	17.22	1.06	100.00	41.07	39.07	19.85
Site 5	Augite 1	52.20	2.79	17.97	N/A	8.43	17.64	0.97	100.00	40.80	40.05	19.14
	Standard Deviation	3.00	2.18	0.99	N/A	0.82	1.27	0.17				
	Average	51.38	4.28	17.77	0.65	9.13	16.96	1.15				

a) – Graph displaying the geochemical data for pyroxene in Hawaii 1

ESA01-A											
Data in Wt % Oxide		SiO_2	Al_2O_3	CaO	FeO	MgO	TiO_2	Total	Wo	Ens	Fs
Site 1	Diopside 1	48.13	4.32	21.63	10.83	12.15	2.94	100.00	48.49	27.24	24.28
	Diopside 2	48.79	4.10	21.52	10.28	12.85	2.46	100.00	48.20	28.78	23.02
	Diopside 3	49.61	3.15	22.00	10.26	12.39	2.58	99.99	49.27	27.75	22.98
	Diopside 4	48.42	3.89	21.56	10.66	12.58	2.89	100.00	48.13	28.08	23.79
Site 2	Diopside 1	48.74	3.80	21.09	9.82	13.6	2.96	100.01	47.38	30.55	22.06
	Diopside 2	48.07	5.32	20.52	11.54	11.51	3.03	99.99	47.10	26.42	26.49
	Diopside 3	49.01	3.66	21.95	10.56	11.59	3.24	100.01	49.77	26.28	23.95
	Pigeonite 1	42.81	16.81	7.15	18.48	14.75	N/A	100.00	17.71	36.53	45.77
Site 4	Diopside 1	50.31	3.20	22.16	9.90	12.32	2.11	100.00	49.93	27.76	22.31
	Diopside 2	49.99	3.13	22.20	10.05	12.46	2.18	100.01	49.65	27.87	22.48
	Diopside 3	49.64	3.09	22.21	10.31	12.52	2.23	100.00	49.31	27.80	22.89
	Diopside 4	50.90	2.65	22.17	9.51	12.94	1.83	100.00	49.69	29.00	21.31
Site 8	Diopside 1	47.99	3.91	22.39	11.06	11.56	3.08	99.99	49.74	25.68	24.57
	Diopside 2	48.75	3.34	22.03	10.85	12.31	2.73	100.01	48.75	27.24	24.01
	Diopside 3	48.90	3.53	21.95	10.72	12.25	2.65	100.00	48.86	27.27	23.86
	Diopside 4	48.68	3.58	22.19	10.35	12.50	2.71	100.01	49.27	27.75	22.98
	Diopside 5	48.78	3.56	22.01	10.75	12.16	2.74	100.00	49.00	27.07	23.93
	Diopside 6	49.33	2.97	22.42	10.49	12.2	2.59	100.00	49.70	27.05	23.25
	Standard Deviation	1.67	3.17	3.50	1.95	0.76	0.38				
	Average	48.71	4.33	21.06	10.91	12.48	2.64				

b) – Graph displaying the geochemical data for pyroxene in ESA01-A

New Mexico													
Data in Wt % Oxide		SiO_2	Al_2O_3	CaO	FeO	MgO	Na_2O	K_2O	TiO_2	**Total**	**Wo**	**Ens**	**Fs**
LAM	Pigeonite 1	53.70	17.88	4.74	13.39	6.94	3.35	N/A	N/A	100.00	18.91	37.68	53.41
	Augite 2	54.75	15.40	6.05	9.59	7.04	3.79	N/A	3.37	99.99	26.68	31.04	42.28
	Augite 3	52.70	16.25	5.80	14.01	7.14	4.09	N/A	N/A	99.99	21.52	26.49	51.99
	Augite 4	54.06	18.61	4.63	11.09	7.23	4.38	N/A	N/A	100.00	20.17	31.50	48.32
Site 3	Hedenbergite 1	53.55	12.07	12.06	11.38	2.21	2.30	2.71	3.72	100.00	47.02	8.62	44.37
	Hedenbergite 2	55.57	12.68	10.07	10.95	0.80	2.29	3.19	4.44	99.99	46.15	3.67	50.18
	Hedenbergite 3	55.70	13.94	9.97	9.86	2.10	2.46	3.10	2.87	100.00	45.46	9.58	44.96
	Augite 1	51.62	7.25	14.09	13.76	3.82	1.54	2.12	5.80	100.00	44.49	12.06	43.45
	Hedenbergite 4	55.10	8.15	13.25	11.99	3.22	1.85	2.56	3.86	99.98	46.56	11.31	42.13
	Hedenbergite 5	52.00	8.62	13.72	13.81	2.85	1.96	2.24	4.80	100.00	45.16	9.38	45.46
	Hedenbergite 6	51.29	7.29	14.99	14.03	3.99	1.64	2.03	4.73	99.99	45.41	12.09	42.50
	Ferrosillite 1	41.94	3.95	2.50	33.11	12.72	N/A	1.40	4.38	100.00	5.17	26.32	68.51
	Hedenbergite 7	53.62	8.28	13.52	13.03	3.04	2.05	2.54	3.91	99.99	45.69	10.27	44.04
Site 4	Pigeonite 1	29.40	11.42	3.28	26.08	1.26	4.24	N/A	24.32	100.00	10.71	4.11	85.17
	Pigeonite 2	33.39	7.62	3.63	24.30	3.62	3.10	1.30	23.04	100.00	11.51	11.47	77.02
	Ferrosillite 1	26.21	8.38	1.46	29.92	0.97	2.48	1.21	29.37	100.00	4.51	3.00	92.49
	Hedenbergite 1	55.43	11.14	11.14	11.05	2.00	2.45	2.81	3.99	100.01	46.05	8.27	45.68
	Hedenbergite 2	52.24	10.48	12.74	13.36	1.85	2.01	2.58	4.73	99.99	45.58	6.62	47.80
	Hedenbergite 3	55.53	10.69	11.73	11.32	2.18	1.86	2.74	3.97	100.02	46.49	8.64	44.87
	Hedenbergite 4	53.13	10.11	13.51	11.99	3.45	1.97	2.13	3.71	100.00	46.67	11.92	41.42
	Pigeonite 3	38.06	8.51	6.12	22.62	2.29	2.42	1.28	18.69	99.99	19.72	7.38	72.90
Site 7	Ferrosillite 1	39.43	1.74	2.94	37.11	18.79	N/A	N/A	N/A	100.01	5.00	31.93	63.07
	Pieonite 1	38.49	1.47	3.69	37.27	19.08	N/A	N/A	N/A	100.00	6.15	31.78	62.08
	Ferrosillite 2	39.82	2.77	2.71	34.68	20.02	N/A	N/A	N/A	100.00	4.72	34.87	60.41
	Ferrosillite 3	43.54	3.51	0.84	33.31	17.80	N/A	N/A	N/A	99.00	1.62	34.26	64.12
	Ferrosillite 4	40.05	3.55	1.68	32.02	20.95	0.95	0.80	N/A	100.00	3.07	38.33	58.59

Standard Deviation	9.02	4.77	4.85	9.94	6.75	0.94	0.72	8.77
Average	47.32	9.30	7.73	19.42	6.82	2.53	2.16	8.37

c) – Graph displaying the geochemical data for pyroxene in New Mexico

			NWA7397 – Ca-Rich Pyroxene											
	Data in Wt % Oxide		SiO_2	Al_2O_3	CaO	FeO	MgO	Cr_2O_3	P_2O_4	Mg#	Total	Wo	Ens	Fs
Grain 1	Site 1	Pigeonite 1	51.43	1.95	16.70	12.71	16.25	0.97	N/A	69.51	100.01	36.57	35.59	27.84
	Site 2													
	Site 3	Augite 1	51.71	1.68	15.34	13.53	16.81	0.92	N/A	68.90	99.99	33.58	36.80	29.62
		Augite 2	51.38	1.93	15.85	14.14	16.70	N/A	N/A	67.80	100.00	33.95	35.77	30.28
		Augite 3	52.31	1.79	16.20	13.09	16.61	N/A	N/A	69.35	100.00	35.29	36.19	28.52
		Augite 4	52.08	1.66	16.70	11.95	16.66	0.96	N/A	71.31	100.01	36.86	36.77	26.37
		Augite 5	52.25	1.60	16.29	12.15	16.76	0.95	N/A	71.09	100.00	36.04	37.08	26.88
	Site 4	Augite 1	52.41	1.71	17.80	11.84	16.24	N/A	N/A	70.98	100.00	38.80	35.40	25.81
		Augite 2	52.06	1.94	15.65	13.54	16.81	N/A	N/A	68.88	100.00	34.02	36.54	29.43
		Augite 3	51.85	1.95	19.05	11.25	15.91	N/A	N/A	71.60	100.01	41.22	34.43	24.35
Grain 2	Site 1	Augite 1	52.77	1.66	17.50	11.94	16.14	N/A	N/A	70.67	100.01	38.39	35.41	26.20
		Augite 2	51.85	1.50	16.91	13.84	15.90	N/A	N/A	67.19	100.00	36.25	34.08	29.67
		Augite 3	41.09	3.09	11.37	18.29	18.03	N/A	8.13	63.74	100.00	23.84	37.81	38.35
	Site 2	Augite 1	51.25	2.46	17.37	13.18	15.74	N/A	N/A	68.04	100.00	37.52	34.00	28.47
		Augite 2	54.06	N/A	18.32	11.44	16.18	N/A	N/A	71.60	100.00	39.88	35.22	24.90
		Augite 3	53.41	N/A	15.98	12.89	17.71	N/A	N/A	71.01	99.99	34.31	38.02	27.67
		Augite 4	53.88	N/A	16.39	12.80	16.93	N/A	N/A	70.22	100.00	35.54	36.71	27.75
		Standard Deviation	2.93	0.43	1.69	1.64	0.62	0	0					
		Average	51.61	1.92	16.46	13.04	16.59	0.95	8.13					

d) – Graph displaying the geochemical data for Ca-rich pyroxene in NWA7397

NWA7397 – Fe/Mg-Rich Pyroxene												
Data in Wt % Oxide			SiO_2	Al_2O_3	CaO	FeO	MgO	Mg#	Total	Wo	Ens	Fs
Grain 1	Site 1	Pigeonite 1	51.62	1.01	6.51	20.14	20.71	64.71	99.99	13.75	43.73	42.53
	Site 2	Pigeonite 1	52.08	0.98	8.80	19.36	18.78	63.36	100.00	18.75	40.01	41.24
		Pigeonite 2	51.02	0.97	4.32	23.29	20.39	60.95	99.99	9.00	42.48	48.52
	Site 3	Pigeonite 1	53.56	1.05	5.84	18.03	21.53	68.04	100.01	12.86	47.42	39.71
		Pigeonite 2	52.90	2.09	6.71	17.89	20.41	67.04	100.00	14.91	45.35	39.75
		Augite 6	48.69	1.16	13.82	17.96	18.37	64.58	100.00	27.56	36.63	35.81
		Pigeonite 3	54.64	1.22	6.64	14.66	22.84	73.53	100.00	15.04	51.74	33.21
	Site 4	Pigeonite 1	53.11	1.13	5.70	18.53	21.54	67.45	100.01	12.45	47.06	40.49
		Pigeonite 2	53.44	1.12	6.11	18.43	20.91	66.92	100.01	13.44	46.01	40.55
		Pigeonite 3	54.41	1.29	7.23	15.74	21.32	70.72	99.99	16.32	48.14	35.54
Grain 2	Site 1	Pigeonite 1	53.38	N/A	5.26	20.40	20.96	64.69	100.00	11.28	44.96	43.76
		Pigeonite 2	53.31	N/A	4.51	21.28	20.90	63.65	100.00	9.66	44.76	45.58
		Pigeonite 3	53.88	N/A	5.77	18.52	21.82	67.75	99.99	12.51	47.32	40.16
	Site 2	Pigeonite 1	54.74	N/A	6.16	17.44	21.66	68.89	100.00	13.61	47.86	38.53
		Pigeonite 2	57.29	N/A	7.02	16.48	19.21	67.51	100.00	16.44	44.98	38.59
		Pigeonite 3	53.24	N/A	8.02	17.57	21.17	68.24	100.00	17.15	45.27	37.57
		Pigeonite 4	53.84	N/A	6.29	19.58	20.28	64.87	99.99	13.63	43.94	42.43
		Standard Deviation	1.81	0.33	2.14	2.06	1.13					
		Average	53.24	1.19	6.75	18.55	20.75					

e) – Graph displaying the geochemical data for Fe/Mg-rich pyroxene in NWA7397

NWA1110												
Data in Wt % Oxide		SiO_2	Al_2O_3	CaO	FeO	MgO	TiO_2	K_2O	Total	Wo	Ens	Fs
Site 1	Augite 1	52.72	1.37	9.17	18.93	17.80	N/A	N/A	99.99	19.98	38.78	41.24
	Pigeonite 1	56.49	N/A	3.72	18.72	21.07	N/A	N/A	100.00	8.55	48.43	43.02
	Pigeonite 2	52.57	N/A	3.93	20.46	23.04	N/A	N/A	100.00	8.29	48.58	43.14
	Pigeonite 3	51.13	1.77	8.47	22.90	15.73	N/A	N/A	100.00	17.98	33.40	48.62
	Pigeonite 4	51.21	1.91	6.98	24.81	15.10	N/A	N/A	100.01	14.89	32.20	52.91
	Pigeonite 5	51.24	2.18	8.55	21.28	16.74	N/A	N/A	99.99	18.36	35.95	45.69
	Pigeonite 6	51.17	1.48	7.99	22.65	16.71	N/A	N/A	100.00	16.87	35.29	47.84
Site 2	Pigeonite 1	55.67	N/A	3.59	18.19	22.56	N/A	N/A	100.01	8.10	50.88	41.02
	Pigeonite 2	53.83	N/A	3.80	19.99	22.38	N/A	N/A	100.00	8.23	48.47	43.30
	Augite 1	53.01	3.93	8.72	20.92	13.42	N/A	N/A	100.00	20.25	31.17	48.58
	Pigeonite 3	53.70	N/A	8.20	20.32	17.78	N/A	N/A	100.00	17.71	38.40	43.89
	Pigeonite 4	53.97	N/A	4.72	19.25	22.06	N/A	N/A	100.00	10.25	47.93	41.82
	Pigeonite 5	53.07	N/A	4.32	22.55	20.06	N/A	N/A	100.00	9.21	42.74	48.05
	Pigeonite 6	53.66	N/A	4.68	18.68	22.98	N/A	N/A	100.00	10.10	49.59	40.31
	Pigeonite 7	54.20	N/A	5.96	19.31	20.53	N/A	N/A	100.00	13.01	44.83	42.16
	Pigeonite 8	54.08	N/A	5.96	19.18	20.79	N/A	N/A	100.01	12.98	45.26	41.76
	Pigeonite 9	55.27	N/A	5.46	17.79	21.47	N/A	N/A	99.99	12.21	48.01	39.78
	Pigeonite 10	52.86	N/A	5.67	26.39	15.08	N/A	N/A	100.00	12.03	31.99	55.98
	Pigeonite 11	52.00	N/A	6.67	23.03	18.31	N/A	N/A	100.01	13.89	38.14	47.97
	Pigeonite 12	50.33	N/A	7.31	23.51	17.25	1.59	N/A	99.99	15.21	35.89	48.91
	Pigeonite 13	49.59	N/A	6.97	25.10	18.34	N/A	N/A	100.00	13.83	36.38	49.79
	Pigeonite 14	56.03	N/A	7.93	20.78	15.26	N/A	N/A	100.00	18.04	34.71	47.26
	Pigeonite 15	52.13	N/A	5.72	24.19	17.96	N/A	N/A	100.00	11.95	37.52	50.53
	Pigeonite 16	54.50	N/A	7.24	19.88	18.39	N/A	N/A	100.01	15.91	40.41	43.68
	Pigeonite 17	53.00	N/A	8.35	22.19	16.46	N/A	N/A	100.00	17.77	35.02	47.21
	Pigeonite 18	49.40	N/A	6.62	25.85	18.13	N/A	N/A	100.00	13.08	35.83	51.09

	Pigeonite 19	55.35	N/A	4.22	18.10	22.34	N/A	N/A	100.01	9.45	50.02	40.53
	Pigeonite 20	54.52	N/A	5.16	20.61	19.71	N/A	N/A	100.00	11.35	43.34	45.32
Site 3	Pigeonite 1	55.25	N/A	6.28	20.85	17.61	N/A	N/A	99.99	14.04	39.36	46.60
	Pigeonite 2	51.78	N/A	5.69	22.47	20.07	N/A	N/A	100.00	11.80	41.61	46.59
	Pigeonite 3	50.82	2.29	6.66	21.28	18.94	N/A	N/A	100.01	14.21	40.40	45.39
	Pigeonite 4	52.91	N/A	6.22	22.81	18.07	N/A	N/A	99.99	13.21	38.37	48.43
	Augite 1	50.50	N/A	10.46	22.33	16.71	N/A	N/A	100.01	21.13	33.76	45.11
	Pigeonite 5	54.18	N/A	8.17	17.86	19.79	N/A	N/A	100.00	17.83	43.19	38.98
	Pigeonite 6	52.29	N/A	7.30	21.76	18.65	N/A	N/A	100.00	15.30	39.09	45.61
	Pigeonite 7	54.18	2.03	7.79	21.28	14.72	N/A	N/A	100.00	17.79	33.61	48.60
	Pigeonite 8	53.05	N/A	7.06	20.13	19.76	N/A	N/A	100.00	15.04	42.09	42.88
	Pigeonite 9	54.50	N/A	6.68	19.62	19.21	N/A	N/A	100.00	14.68	42.21	43.11
	Pigeonite 10	52.55	N/A	8.10	21.43	17.92	N/A	N/A	100.01	17.07	37.77	45.16
Site 4	Pigeonite 1	53.74	1.41	3.95	19.23	21.68	N/A	N/A	100.00	8.81	48.33	42.87
	Pigeonite 2	54.43	1.47	3.08	17.61	23.41	N/A	N/A	100.01	6.98	53.08	39.93
	Pigeonite 3	51.92	1.25	8.63	20.29	17.91	N/A	N/A	100.00	18.43	38.24	43.33
	Pigeonite 4	51.02	2.16	8.42	22.90	15.50	N/A	N/A	100.00	17.98	33.11	48.91
	Augite 1	51.51	2.50	15.86	12.77	17.32	N/A	N/A	100.00	34.52	37.69	27.79
	Augite 2	47.87	2.17	11.39	22.42	16.15	N/A	N/A	100.00	22.80	32.33	44.88
	Pigeonite 5	52.07	2.18	7.29	21.91	16.54	N/A	N/A	99.99	15.94	36.16	47.90
	Pigeonite 6	53.29	1.79	4.59	19.89	20.44	N/A	N/A	100.00	10.22	45.50	44.28
	Augite 3	54.62	N/A	13.32	17.63	14.43	N/A	N/A	100.00	29.35	31.80	38.85
	Pigeonite 7	54.17	N/A	7.11	20.13	18.59	N/A	N/A	100.00	15.51	40.56	43.92
	Pigeonite 8	51.00	2.02	5.76	20.21	21.01	N/A	N/A	100.00	12.26	44.72	43.02
	Pigeonite 9	50.27	1.30	8.97	22.46	17.00	N/A	N/A	100.00	18.52	35.10	46.38
	Pigeonite 10	50.71	2.17	6.32	23.07	17.73	N/A	N/A	100.00	13.41	37.63	48.96
	Augite 4	56.75	2.87	10.34	13.27	16.76	N/A	N/A	99.99	25.61	41.52	32.87
	Pigeonite 11	54.23	N/A	2.70	19.10	23.97	N/A	N/A	100.00	5.90	52.37	41.73

	Pigeonite 12	51.95	N/A	6.96	23.23	17.86	N/A	N/A	100.00	14.48	37.17	48.35
	Augite 5	51.42	2.38	13.53	16.12	16.54	N/A	N/A	99.99	29.29	35.81	34.90
Site 5	Pigeonite 1	44.35	5.80	4.23	42.20	3.37	N/A	N/A	99.95	8.49	6.77	84.74
	Pigeonite 2	45.48	7.54	5.07	38.36	3.55	N/A	N/A	100.00	10.79	7.56	81.65
	Augite 1	52.34	4.32	8.78	20.70	13.86	N/A	N/A	100.00	20.26	31.98	47.76
	Pigeonite 3	55.54	N/A	4.42	22.15	17.89	N/A	N/A	100.00	9.94	40.24	49.82
	Pigeonite 4	54.14	N/A	6.08	18.84	20.94	N/A	N/A	100.00	13.26	45.66	41.08
	Augite 2	55.32	N/A	9.24	17.91	17.53	N/A	N/A	100.00	20.68	39.23	40.09
	Pigeonite 5	54.67	N/A	3.62	19.34	22.37	N/A	N/A	100.00	7.99	49.35	42.66
	Pigeonite 6	54.71	N/A	5.14	18.55	21.60	N/A	N/A	100.00	11.35	47.69	40.96
	Augite 3	51.22	2.08	9.23	22.07	15.39	N/A	N/A	99.99	19.77	32.96	47.27
	Pigeonite 7	53.38	N/A	7.54	19.30	19.78	N/A	N/A	100.00	16.17	42.43	41.40
	Pigeonite 8	51.03	2.06	7.59	23.20	16.12	N/A	N/A	100.00	16.18	34.36	49.46
	Pigeonite 9	53.28	3.05	7.77	20.41	15.48	N/A	N/A	99.99	17.80	35.46	46.75
	Pigeonite 10	51.49	2.55	7.35	22.63	15.98	N/A	N/A	100.00	15.99	34.77	49.24
	Pigeonite 11	50.53	1.99	7.86	25.51	14.11	N/A	N/A	100.00	16.55	29.72	53.73
	Augite 4	49.81	2.80	12.37	19.87	15.15	N/A	N/A	100.00	26.17	31.87	41.97
	Pigeonite 12	44.59	8.48	5.53	37.54	2.34	N/A	1.52	100.00	12.18	5.15	82.67
	Standard Deviation	2.51	1.74	2.28	4.44	4.05	N/A	N/A				
	Average	52.51	2.69	6.91	21.62	17.74	1.59	1.52				

f) – Graph displaying the geochemical data for Fe/Mg-rich pyroxene in NWA1110

Tissint – Ca Rich - Pyroxene										
Data in Wt % Oxide		SiO_2	Al_2O_3	CaO	FeO	MgO	Total	Wo	Ens	Fs
Site 4	Augite 1	52.02	N/A	14.64	19.42	13.92	100.00	30.51	29.01	40.48
	Augite 2	51.64	N/A	11.47	20.2	16.7	100.01	23.71	34.53	41.76
	Augite 3	54.33	N/A	11.38	16.57	17.72	100.00	24.92	38.80	36.28
	Augite 4	53.11	N/A	13.33	15.79	17.77	100.00	28.43	37.90	33.6
Site 5	Augite 1	52.85	N/A	15.87	14.70	16.58	100.00	33.66	35.16	31.18
	Augite 2	52.77	N/A	15.44	17.16	14.63	100.00	32.69	30.98	36.33
	Augite 3	52.61	6.29	10.41	17.17	13.51	99.99	25.33	32.88	41.79
	Augite 4	53.57	N/A	15.43	14.53	16.47	100.00	33.23	35.47	31.29
	Augite 5	53.3	N/A	14.34	15.00	17.36	100.00	30.71	37.17	32.12
	Augite 6	52.78	9.00	11.00	14.76	12.45	99.99	28.79	32.58	38.63
	Augite 7	52.9	N/A	16.08	14.18	16.84	100.00	34.14	35.75	30.11
	Augite 8	51.4	N/A	12.89	18.77	16.94	100.00	26.52	34.86	38.62
	Augite 9	52.91	N/A	14.61	16.12	16.36	100.00	31.03	34.74	34.23
	Augite 10	53.68	N/A	12.39	15.71	18.22	100.00	26.75	39.34	33.92
	Standard Deviation	0.78	1.92	1.94	1.91	1.76				
	Average	52.85	7.65	13.52	16.43	16.11				

g) Graph displaying the geochemical data for Ca-rich pyroxene in Tissint

Tissint – Fe/Mg Rich Pyroxene										
Data in Wt % Oxide		SiO2	Al2O3	CaO	FeO	MgO	Total	Wo	Ens	Fs
Site 1	Augite 1	52.62	6.27	10.37	16.33	14.40	99.99	25.23	35.04	39.73
	Pigeonite 1	54.74	N/A	3.95	17.20	24.10	99.99	8.73	53.26	38.01
	Pigeonite 2	54.16	N/A	5.03	17.69	23.13	100.01	10.97	50.45	38.58
	Pigeonite 3	54.55	N/A	4.67	17.78	23.00	100.00	10.28	50.61	39.12
	Pigeonite 4	51.53	0.95	6.50	24.80	16.21	99.99	13.68	34.12	52.20
Site 2	Pigeonite 1	52.19	0.95	6.02	23.31	17.52	99.99	12.85	37.40	49.75
	Pigeonite 2	54.17	N/A	4.34	18.89	22.6	100.00	9.47	49.31	41.22
	Pigeonite 3	53.5	N/A	5.35	20.15	21.01	100.01	11.50	45.17	43.32
	Pigeonite 4	54.40	N/A	4.35	17.56	23.69	100.00	9.54	51.95	38.51
	Pigeonite 5	52.17	1.1	6.36	22.83	17.55	100.01	13.61	37.55	48.84
Site 4	Pigeonite 1	53.79	N/A	5.92	18.36	21.93	100.00	12.81	47.46	39.73
	Pigeonite 2	53.68	N/A	4.05	18.64	23.63	100.00	8.74	51.01	40.24
	Pigeonite 3	54.10	N/A	5.38	17.82	22.70	100.00	11.72	49.46	38.82
	Pigeonite 4	54.39	N/A	4.67	18.16	22.77	99.99	10.24	49.93	39.82
	Pigeonite 5	54.00	N/A	5.30	19.8	20.9	100.00	11.52	45.43	43.04
Site 5	Pigeonite 1	54.56	N/A	4.19	17.55	23.69	99.99	9.22	52.15	38.63
	Pigeonite 2	54.55	N/A	4.28	17.52	23.66	100.01	9.41	52.05	38.54
	Pigeonite 3	54.30	N/A	4.86	17.30	23.54	100.00	10.63	51.51	37.86
	Pigeonite 4	54.58	N/A	4.43	18.04	22.95	100.00	9.75	50.53	39.72
	Pigeonite 5	53.18	2.07	5.25	18.33	21.17	100.00	11.73	47.31	40.96
	Pigeonite 6	52.12	N/A	5.14	25.32	17.42	100.00	10.74	36.38	52.88
	Pigeonite 7	53.88	N/A	4.82	18.38	22.92	100.00	10.45	49.70	39.85
	Pigeonite 8	54.55	N/A	4.89	17.62	22.93	99.99	10.76	50.46	38.78
	Pigeonite 9	54.59	N/A	4.94	17.83	22.64	100.00	10.88	49.86	39.26
	Pigeonite 10	54.27	N/A	5.81	18.15	21.76	99.99	12.71	47.59	39.70

	Pigeonite 11	53.63	N/A	5.8	19.75	20.82	100.00	12.51	44.90	42.59
	Pigeonite 12	53.54	N/A	6.08	19.17	21.21	100.00	13.09	45.65	41.26
	Pigeonite 13	52.22	N/A	6.53	23.54	17.71	100.00	13.67	37.07	49.27
	Pigeonite 14	52.57	N/A	5.83	22.75	18.85	100.00	12.29	39.74	47.97
	Pigeonite 15	53.11	N/A	6.73	21.75	18.41	100.00	14.35	39.26	46.39
	Standard Deviation	0.93	2.29	1.23	2.48	2.64				
	Average	53.65	2.27	5.39	19.41	21.16				

h) – Graph displaying the geochemical data for Fe/Mg-rich pyroxene in Tissint

NWA3160 - Ca Rich Pyroxene												
Data in Wt % Oxide		SiO_2	Al_2O_3	CaO	FeO	MgO	Cr_2O_3	TiO_2	Total	Wo	Ens	Fs
LAM	Augite 1	53.95	N/A	16.34	12.98	16.73	N/A	N/A	100.00	35.68	36.33	28.19
	Augite 2	54.83	N/A	17.10	11.80	16.26	N/A	N/A	99.99	37.87	36.01	26.13
	Augite 3	53.18	2.81	16.12	10.80	17.08	N/A	N/A	99.99	36.64	38.82	24.55
	Melt Pocket 1	62.38	15.33	13.40	6.27	2.61	N/A	N/A	99.99	60.14	11.71	28.14
	Melt Pocket 2	63.86	14.01	13.56	5.74	2.82	N/A	N/A	99.99	61.30	12.75	25.95
	Augite 4	53.71	2.52	16.69	9.91	17.16	N/A	N/A	99.99	38.14	39.21	22.65
	Augite 5	52.09	2.85	14.96	12.25	17.85	N/A	N/A	100.00	33.20	39.61	27.19
	Augite 6	54.06	N/A	18.34	9.29	18.31	N/A	N/A	100.00	39.92	39.86	20.22
	Melt Pocket 3	64.95	9.59	12.81	5.88	6.77	N/A	N/A	100.00	50.31	26.59	23.10
Site 1	Augite 1	53.58	N/A	20.76	8.16	17.50	N/A	N/A	100.00	44.72	37.70	17.58
	Augite 2	54.05	3.69	13.84	12.11	16.31	N/A	N/A	100.00	32.75	38.59	28.66
Site 2	Melt Pocket 1	52.38	13.05	16.28	11.10	3.92	N/A	3.26	99.99	52.01	12.52	35.46
	Augite 1	54.30	2.15	13.80	11.68	18.07	N/A	N/A	100.00	31.69	41.49	26.82
	Augite 2	53.69	3.06	16.33	9.86	17.06	N/A	N/A	100.00	37.76	39.45	22.80
	Augite 3	54.94	3.01	14.21	8.49	19.35	N/A	N/A	100.00	33.79	46.02	20.19
	Augite 4	53.63	2.37	17.32	9.61	17.08	N/A	N/A	100.01	39.35	38.81	21.84
Site 3	Diopside 1	48.12	24.09	13.76	8.26	5.78	N/A	N/A	100.01	49.50	20.79	29.71
	Augite 1	52.07	16.30	14.21	12.76	16.30	1.41	N/A	100.00	32.84	37.67	29.49
	Augite 2	52.24	16.55	14.70	13.14	16.55	N/A	N/A	100.00	33.12	37.28	29.60
	Augite 3	49.64	20.13	11.45	10.21	7.40	N/A	1.18	100.01	39.40	25.46	35.13
	Diopside 2	50.27	21.75	12.87	10.26	3.72	N/A	1.14	100.01	47.93	13.85	38.21
Site 4	Melt Pocket 1	61.99	16.25	13.32	6.15	2.29	N/A	N/A	100.00	61.21	10.52	28.26
	Melt Pocket 2	60.04	15.10	13.47	6.56	2.71	N/A	2.11	99.99	59.23	11.92	28.85
Site 6	Augite 1	54.77	N/A	18.48	11.35	15.40	N/A	N/A	100.00	40.86	34.05	25.09
	Augite 2	51.97	N/A	17.91	14.32	15.80	N/A	N/A	100.00	37.29	32.90	29.81

	Augite 3	53.24	N/A	18.19	11.27	17.31	N/A	N/A	100.01	38.89	37.01	24.10
Site 8	Augite 1	53.05	N/A	19.06	10.12	17.77	N/A	N/A	100.00	40.60	37.85	21.55
	Augite 2	55.01	N/A	16.65	10.35	17.99	N/A	N/A	100.00	37.01	39.99	23.01
	Augite 3	51.04	2.72	17.73	10.83	17.68	N/A	N/A	100.00	38.34	38.24	23.42
	Augite 4	53.05	3.95	17.56	8.67	16.78	N/A	N/A	100.01	40.83	39.01	20.16
	Standard Deviation	4.07	7.57	2.27	2.30	6.16	N/A	1.00				
	Average	54.54	10.06	15.71	10.01	13.28	1.41	1.92				

f) – Graph displaying the geochemical data for Ca-rich pyroxene in NWA3160

NWA3160 – Fe/Mg Rich Pyroxene												
Data in Wt % Oxide		SiO_2	Al_2O_3	CaO	FeO	MgO	Cr_2O_3	Na_2O	Total	Wo	Ens	Fs
LAM	Pigeonite 1	54.41	N/A	6.72	18.23	20.64	N/A	N/A	100.00	14.74	45.27	39.99
	Pigeonite 2	55.61	N/A	5.31	13.86	25.22	N/A	N/A	100.00	11.96	56.81	31.22
	Pigeonite 3	53.53	N/A	3.94	20.81	21.71	N/A	N/A	99.99	8.48	46.73	44.79
	Pigeonite 4	53.87	2.14	6.98	16.16	20.85	N/A	N/A	100.00	15.87	47.40	36.74
	Pigeonite 5	54.11	N/A	6.79	17.42	21.67	N/A	N/A	99.99	14.80	47.23	37.97
	Pigeonite 6	52.43	N/A	8.46	28.76	10.34	N/A	N/A	99.99	17.79	21.74	60.47
	Augite 7	51.85	N/A	10.00	28.48	9.67	N/A	N/A	100.00	20.77	20.08	59.15
	Augite 8	48.76	N/A	10.40	29.46	11.38	N/A	N/A	100.00	20.30	22.21	57.49
	Pigeonite 7	55.47	2.01	5.46	16.83	20.23	N/A	N/A	100.00	12.84	47.58	39.58
	Pigeonite 8	51.80	N/A	8.75	16.43	23.02	N/A	N/A	100.00	18.15	47.76	34.09
	Augite 9	50.87	N/A	11.19	31.15	6.79	N/A	N/A	100.00	22.78	13.82	63.40
	Augite 10	54.32	N/A	12.76	17.12	15.80	N/A	N/A	100.00	27.93	34.59	37.48
	Augite 11	51.11	N/A	9.99	31.21	7.69	N/A	N/A	100.00	20.43	15.73	63.84
	Pigeonite 9	56.60	N/A	5.59	16.43	21.38	N/A	N/A	100.00	12.88	49.26	37.86
	Pigeonite 10	55.36	N/A	6.04	14.41	24.20	N/A	N/A	100.01	13.53	54.20	32.27
	Pigeonite 11	55.59	N/A	5.84	13.89	24.67	N/A	N/A	99.99	13.15	55.56	31.28
	Pigeonite 12	53.71	N/A	8.94	29.03	8.32	N/A	N/A	100.00	19.31	17.97	62.71
	Pigeonite 13	54.97	N/A	8.44	23.95	12.64	N/A	N/A	100.00	18.74	28.07	53.19
	Pigeonite 14	56.18	N/A	3.04	15.07	25.71	N/A	N/A	100.00	6.94	58.67	34.39
	Pigeonite 15	49.97	7.72	6.73	15.99	19.60	N/A	N/A	100.01	15.90	46.31	37.78
	Pigeonite 16	54.08	N/A	7.90	20.38	17.64	N/A	N/A	100.00	17.20	38.41	44.38
	Augite 12	51.78	N/A	14.68	30.06	3.48	N/A	N/A	100.00	30.44	7.22	62.34
	Pigeonite 17	55.39	N/A	5.17	14.76	24.68	N/A	N/A	100.00	11.59	55.32	33.09
	Augite 13	48.24	14.15	9.74	14.51	13.37	N/A	N/A	100.01	25.89	35.54	38.57
	Pigeonite 17	54.59	N/A	6.37	17.54	21.50	N/A	N/A	100.00	14.03	47.35	38.63

	Augite 14	50.18	N/A	10.38	31.19	7.81	N/A	N/A	100.01	21.02	15.82	63.16
	Pigeonite 18	49.51	N/A	6.73	42.66	1.10	N/A	N/A	100.00	13.33	2.18	84.49
	Pigeonite 19	53.23	N/A	6.57	17.47	22.73	N/A	N/A	100.00	14.05	48.60	37.35
	Pigeonite 20	54.11	N/A	7.30	20.76	17.83	N/A	N/A	100.00	15.91	38.85	45.24
	Augite 15	51.23	N/A	18.35	28.63	1.79	N/A	N/A	100.00	37.63	3.67	58.70
	Pigeonite 21	55.30	N/A	6.16	15.62	22.92	N/A	N/A	100.00	13.78	51.28	34.94
	Pigeonite 22	54.02	1.84	5.80	14.72	23.62	N/A	N/A	100.00	13.14	53.51	33.35
	Pigeonite 23	53.08	N/A	7.58	22.57	16.78	N/A	N/A	100.01	16.15	35.76	48.09
	Pigeonite 24	53.47	N/A	5.33	19.47	21.72	N/A	N/A	99.99	11.46	46.69	41.85
	Pigeonite 25	53.88	N/A	6.73	14.46	24.94	N/A	N/A	100.01	14.59	54.06	31.35
	Pigeonite 26	50.00	N/A	9.53	32.36	8.11	N/A	N/A	100.00	19.06	16.22	64.72
	Augite 16	46.96	N/A	14.75	32.48	5.81	N/A	N/A	100.00	27.81	10.95	61.24
	Pigeonite 27	55.35	N/A	6.41	13.63	24.61	N/A	N/A	100.00	14.36	55.12	30.53
	Pigeonite 28	37.17	N/A	1.90	26.25	34.68	N/A	N/A	100.00	3.02	55.20	41.78
	Pigeonite 29	52.28	N/A	6.91	23.88	16.92	N/A	N/A	99.99	14.48	35.46	50.05
	Pigeonite 30	56.04	N/A	3.67	15.06	25.23	N/A	N/A	100.00	8.35	57.39	34.26
	Pigeonite 31	52.63	N/A	8.57	21.41	17.39	N/A	N/A	100.00	18.09	36.71	45.20
	Pigeonite 32	56.48	N/A	3.31	14.88	25.34	N/A	N/A	100.01	7.60	58.21	34.18
	Augite 17	54.76	N/A	11.87	16.18	17.19	N/A	N/A	100.00	26.24	38.00	35.76
	Augite 18	52.65	N/A	14.60	23.62	9.13	N/A	N/A	100.00	30.83	19.28	49.88
	Augite 19	48.14	7.76	16.47	15.37	12.26	N/A	N/A	100.00	37.35	27.80	34.85
	Pigeonite 33	56.45	N/A	7.31	13.58	22.67	N/A	N/A	100.01	16.78	52.04	31.18
	Augite 20	50.96	N/A	9.90	28.41	10.73	N/A	N/A	100.00	20.19	21.88	57.93
	Augite 21	51.00	5.13	14.84	15.33	13.70	N/A	N/A	100.00	33.83	31.23	34.94
	Pigeonite 34	50.19	N/A	8.92	35.22	5.68	N/A	N/A	100.01	17.90	11.40	70.69
	Pigeonite 35	54.78	N/A	5.90	21.37	17.94	N/A	N/A	99.99	13.05	39.68	47.27
	Augite 22	48.62	N/A	16.88	31.93	2.57	N/A	N/A	100.00	32.85	5.00	62.14
	Augite 23	50.41	N/A	16.84	21.56	11.19	N/A	N/A	100.00	33.96	22.57	43.48
	Pigeonite 36	51.55	N/A	8.97	36.47	3.01	N/A	N/A	100.00	18.51	6.21	75.27

	Augite 24	50.87	N/A	10.78	29.11	9.24	N/A	N/A	100.00	21.94	18.81	59.25
	Pigeonite 37	55.33	N/A	4.81	17.05	22.80	N/A	N/A	99.99	10.77	51.05	38.18
	Pigeonite 38	56.31	N/A	3.29	17.38	23.02	N/A	N/A	100.00	7.53	52.69	39.78
Site 1	Pigeonite 1	53.19	N/A	7.67	17.8	21.34	N/A	N/A	100.00	16.39	45.59	38.03
	Pigeonite 2	56.95	N/A	8.57	22.60	11.88	N/A	N/A	100.00	19.91	27.60	52.50
	Pigeonite 3	52.85	N/A	7.20	28.63	11.32	N/A	N/A	100.00	15.27	24.01	60.72
	Augite 3	56.08	4.30	12.42	12.30	14.90	N/A	N/A	100.00	31.35	37.61	31.04
	Augite 4	55.48	15.06	9.20	12.49	7.77	N/A	N/A	100.00	31.23	26.37	42.40
	Pigeonite 4	56.02	N/A	4.80	14.44	24.74	N/A	N/A	100.00	10.91	56.25	32.83
	Pigeonite 5	57.59	N/A	7.90	12.50	22.01	N/A	N/A	100.00	18.63	51.90	29.47
	Pigeonite 6	56.70	N/A	8.78	26.42	8.10	N/A	N/A	100.00	20.28	18.71	61.02
	Augite 5	58.31	N/A	11.91	14.10	15.69	N/A	N/A	100.01	28.56	37.63	33.81
	Pigeonite 7	51.93	1.27	7.58	20.89	18.32	N/A	N/A	99.99	16.20	39.15	44.65
Site 2	Augite 5	55.69	N/A	17.82	26.49	0	N/A	N/A	100.00	40.22	0.00	59.78
	Pigeonite 1	48.11	N/A	9.40	39.71	2.78	N/A	N/A	100.00	18.12	5.36	76.53
	Augite 6	48.75	13.40	9.01	14.58	14.26	N/A	N/A	100.00	23.80	37.68	38.52
	Pigeonite 2	50.56	N/A	7.06	40.96	1.42	N/A	N/A	100.00	14.28	2.87	82.85
	Pigeonite 3	54.59	2.07	7.52	14.92	20.90	N/A	N/A	100.00	17.35	48.22	34.43
	Pigeonite 4	54.68	1.65	5.18	15.41	23.08	N/A	N/A	100.00	11.86	52.85	35.29
	Pigeonite 5	53.90	1.72	5.36	16.04	22.99	N/A	N/A	100.01	12.07	51.79	36.13
	Pigeonite 6	47.74	2.34	5.85	42.62	1.45	N/A	N/A	100.00	11.72	2.90	85.38
	Pigeonite 7	46.21	5.91	9.05	34.26	4.57	N/A	N/A	100.00	18.90	9.54	71.55
	Augite 7	48.53	N/A	22.77	28.70	0	N/A	N/A	100.00	44.24	0.00	55.76
	Augite 8	52.91	N/A	11.73	17.99	17.37	N/A	N/A	100.00	24.91	36.89	38.20
Site 3	Pigeonite 1	51.93	N/A	9.02	37.54	1.51	N/A	N/A	100.00	18.76	3.14	78.09
	Pigeonite 2	49.95	N/A	5.42	43.44	1.19	N/A	N/A	100.00	10.83	2.38	86.79
	Pigeonite 3	55.08	2.16	6.99	14.46	21.31	N/A	N/A	100.00	16.35	49.84	33.82
	Ferrosillite 1	30.33	N/A	0	68.42	1.25	N/A	N/A	100.00	0.00	1.79	98.21

	Pigeonite 4	49.41	1.09	16.92	30.36	2.22	N/A	N/A	100.00	34.18	4.48	61.33
	Augite 4	49.75	0.99	14.31	30.99	3.95	N/A	N/A	99.99	29.06	8.02	62.92
	Pigeonite 5	54.13	1.99	7.22	14.85	21.81	N/A	N/A	100.00	16.45	49.70	33.84
	Pigeonite 6	46.73	2.49	4.57	21.53	24.68	N/A	N/A	100.00	9.00	48.60	42.40
	Pigeonite 7	54.30	1.63	6.06	14.21	23.79	N/A	N/A	99.99	13.75	53.99	32.25
	Pigeonite 8	54.67	1.58	4.14	15.77	23.84	N/A	N/A	100.00	9.46	54.49	36.05
	Pigeonite 9	54.87	1.55	4.82	14.11	24.66	N/A	N/A	100.01	11.06	56.57	32.37
	Pigeonite 10	54.52	1.74	5.64	16.43	21.66	N/A	N/A	99.99	12.90	49.53	37.57
	Augite 5	51.68	2.85	14.59	17.45	12.08	N/A	1.36	100.01	33.07	27.38	39.55
	Augite 6	48.44	1.02	10.2	32.75	7.59	N/A	N/A	100.00	20.18	15.02	64.80
	Pigeonite 11	52.66	2.38	4.96	29.38	10.61	N/A	N/A	99.99	11.03	23.60	65.36
Site 6	Pigeonite 1	53.36	N/A	6.56	19.21	20.88	N/A	N/A	100.01	14.06	44.76	41.18
	Pigeonite 2	54.52	N/A	6.38	19.47	19.62	N/A	N/A	99.99	14.03	43.15	42.82
	Pigeonite 3	53.95	1.70	6.82	17.37	20.16	N/A	N/A	100.00	15.38	45.46	39.17
	Pigeonite 4	53.84	1.66	7.19	17.07	20.24	N/A	N/A	100.00	16.16	45.48	38.36
	Augite 4	53.62	1.71	13.56	13.48	17.63	N/A	N/A	100.00	30.36	39.47	30.18
	Pigeonite 5	56.22	N/A	4.38	19.03	20.37	N/A	N/A	100.00	10.00	46.53	43.47
Site 7	Pigeonite 1	55.12	N/A	7.09	16.74	21.04	N/A	N/A	99.99	15.80	46.89	37.31
	Augite 1	54.02	1.34	12.12	18.00	14.52	N/A	N/A	100.00	27.15	32.53	40.32
	Pigeonite 2	51.29	1.82	7.63	20.09	19.16	N/A	N/A	99.99	16.28	40.87	42.85
	Pigeonite 3	51.02	1.08	8.70	29.55	9.65	N/A	N/A	100.00	18.16	20.15	61.69
	Pigeonite 4	54.28	1.67	6.57	15.77	21.70	N/A	N/A	99.99	14.92	49.27	35.81
	Augite 2	53.63	2.64	13.82	11.12	17.18	1.06	0.55	100.00	32.81	40.79	26.40
	Pigeonite 5	48.66	7.73	8.16	27.07	8.37	N/A	N/A	99.99	18.72	19.20	62.09
Site 8	Pigeonite 1	54.85	N/A	7.07	14.37	23.71	N/A	N/A	100.00	15.66	52.51	31.83
	Pigeonite 2	51.96	N/A	7.6	34.52	5.92	N/A	N/A	100.00	15.82	12.32	71.86
	Hedenbergite 1	50.79	N/A	17.02	32.19	0	N/A	N/A	100.00	34.59	0.00	65.41
	Pigeonite 3	55.28	N/A	4.71	14.59	25.42	N/A	N/A	100.00	10.53	56.84	32.63

	Pigeonite 4	55.92	2.21	6.38	12.34	23.15	N/A	N/A	100.00	15.24	55.29	29.47
	Augite 5	53.44	N/A	10.94	17.05	18.57	N/A	N/A	100.00	23.50	39.88	36.62
	Standard Deviation	3.72	3.67	3.92	9.19	8.14	N/A	0.57				
	Average	52.61	3.51	8.54	22.20	15.42	1.06	0.96				

g) – Graph displaying the geochemical data for Ca-rich pyroxene in NWA3160

NWA3160 Basalt Clast Pyroxene												
Data in Wt% Oxide		**MgO**	**Al_2O_3**	**SiO_2**	**CaO**	**Cr_2O_3**	**FeO**	**TiO_2**	**Total**	**Ens**	**Wo**	**Fs**
Site 1	Spectrum 6	23.71	1.82	55.48	4.70	N/A	14.29	0.00	100.00	55.53	11.01	33.47
	Spectrum 8	23.07	1.97	53.69	6.68	0.86	13.72	0.00	99.99	53.07	15.37	31.56
	Spectrum 9	19.71	0.91	51.20	7.11	0.95	20.11	0.00	99.99	42.00	15.15	42.85
	Spectrum 10	13.83	2.46	50.85	15.83	0.94	16.09	0.00	100.00	30.23	34.60	35.17
	Spectrum 11	19.43	LLD	53.76	5.21	N/A	21.60	0.00	100.00	42.02	11.27	46.71
	Spectrum 12	24.34	1.19	53.48	3.79	0.88	16.32	0.00	100.00	54.76	8.53	36.72
Site 2	Spectrum 29	1.84	1.15	47.11	18.57	1.11	30.20	0.00	99.98	3.64	36.69	59.67
	Spectrum 30	5.78	1.81	46.61	13.27	1.73	30.80	0.00	10.00	11.59	26.62	61.79
	Spectrum 33	23.50	2.10	54.48	5.25	N/A	14.67	0.00	100.00	54.12	12.09	33.79
	Spectrum 36	N/A	2.38	48.45	9.28	0.92	38.98	0.00	100.01	0.00	19.23	80.77
Site 3	Spectrum 37	2.18	1.28	48.32	9.70	0.00	38.53	0.00	100.01	4.32	19.24	76.43
	Spectrum 39	6.33	1.83	47.94	12.79	0.00	29.51	1.59	99.99	13.02	26.30	60.68
	Spectrum 40	3.37	1.84	46.68	15.12	0.00	31.38	1.61	100.00	6.76	30.32	62.92
	Spectrum 43	3.34	1.27	46.55	10.22	0.00	37.39	1.22	99.99	6.56	20.06	73.39
	Spectrum 45	N/A	1.84	48.84	8.47	0.00	39.95	0.91	100.01	0.00	17.49	82.51
	Spectrum 46	9.57	N/A	49.64	7.72	0.00	32.15	0.91	99.99	19.36	15.61	65.03
	Spectrum 49	6.52	2.51	37.00	1.44	0.00	52.53	N/A	100.00	10.78	2.38	86.84
	Spectrum 50	1.96	4.35	24.83	2.51	0.00	49.93	16.42	100.00	3.60	4.61	91.78
	Spectrum 52	8.74	1.96	49.90	7.81	0.00	30.41	1.18	100.00	18.61	16.63	64.76

	Spectrum 53	3.94	1.91	47.88	14.30	0.00	30.39	1.58	100.00	8.10	29.41	62.49
	Spectrum 54	10.67	17.40	46.83	10.55	0.00	13.51	1.05	100.01	30.72	30.38	38.90
Site 4	Spectrum 57	21.79	0.97	52.69	2.76	0.00	21.80	N/A	100.01	47.01	5.95	47.03
	Spectrum 61	1.31	2.22	44.32	13.60	0.00	36.76	1.79	100.00	2.54	26.32	71.14
	Spectrum 65	12.69	2.12	48.80	16.45	1.07	18.87	N/A	100.00	26.43	34.26	39.30
	Spectrum 66	16.94	N/A	23.38	8.89	0.00	50.79	N/A	100.00	22.11	11.60	66.29
	Spectrum 67	17.07	2.39	52.71	11.43	0.00	16.40	N/A	100.00	38.02	25.46	36.53
	Spectrum 68	17.12	1.12	53.86	6.10	0.00	21.79	N/A	99.99	38.04	13.55	48.41
	Spectrum 85	15.96	3.18	51.16	16.80	0.00	12.90	N/A	100.00	34.95	36.79	28.25
	Spectrum 75	1.10	1.09	47.15	10.41	N/A	39.25	1.00	100.00	2.17	20.51	77.32
	Spectrum 77	10.23	45.60	33.99	4.69	N/A	5.49	N/A	100.00	50.12	22.98	26.90
	Spectrum 78	16.46	2.67	52.07	18.23	0.98	8.47	1.13	100.01	38.14	42.24	19.62
	Spectrum 79	17.38	2.65	52.87	18.50	N/A	7.39	1.20	99.99	40.17	42.75	17.08
	Spectrum 81	13.00	1.37	49.87	10.76	N/A	24.02	0.96	99.98	27.21	22.52	50.27
	Spectrum 82	18.38	1.12	52.86	5.98	N/A	21.67	N/A	100.01	39.93	12.99	47.08
	Spectrum 83	15.93	1.95	49.11	18.89	1.30	12.81	LLD	99.99	33.45	39.66	26.89
	Spectrum 84	13.76	5.33	48.96	13.61	1.08	15.37	1.89	100.00	32.19	31.84	35.96
	Standard Deviation	7.44	8.02	7.29	5.05	0.57	12.57	3.15				
	Average	12.38	3.81	47.87	10.21	0.51	25.45	1.32				

h) – Graph displaying the geochemical data for Ca-rich pyroxene in NWA3160

NWA11444 – Ca Rich - Pyroxene												
Data in Wt % Oxide		SiO_2	Al_2O_3	CaO	FeO	MgO	Cr_2O_3	TiO_2	Total	Wo	Ens	Fs
Site 1	Augite 1	52.38	1.18	20.19	12.93	13.31	N/A	N/A	99.99	43.48	28.67	27.85
	Augite 2	52.37	1.48	19.13	13.50	13.51	N/A	N/A	99.99	41.46	29.28	29.26
	Augite 3	52.82	1.38	17.30	14.29	14.21	N/A	N/A	100.00	37.77	31.03	31.20
	Augite 4	54.04	1.53	17.79	12.50	14.14	N/A	N/A	100.00	40.04	31.83	28.13
	Augite 5	53.11	1.35	18.63	12.86	14.06	N/A	N/A	100.01	40.90	30.87	28.23
Site 3	Augite 1	52.50	1.07	17.80	14.72	13.91	N/A	N/A	100.00	38.34	29.96	31.70
	Augite 2	52.23	1.25	20.16	12.97	13.39	N/A	N/A	100.00	43.34	28.78	27.88
	Augite 3	53.32	1.26	18.19	13.38	13.85	N/A	N/A	100.00	40.05	30.49	29.46
	Augite 4	51.66	1.20	19.37	13.60	13.30	N/A	N/A	100.00	41.86	28.74	29.39
	Augite 5	52.63	N/A	15.80	16.85	14.72	N/A	N/A	100.00	33.35	31.07	35.57
	Augite 6	52.37	1.32	18.83	14.09	13.39	N/A	N/A	100.00	40.66	28.91	30.43
	Augite 7	52.24	1.49	19.55	13.31	13.42	N/A	N/A	100.01	42.24	29.00	28.76
	Augite 8	53.46	1.11	17.11	13.64	14.68	N/A	N/A	100.00	37.66	32.31	30.02
Site 4	Augite 1	51.24	3.08	16.02	14.69	13.73	1.23	N/A	99.99	36.05	30.90	33.06
	Augite 2	51.62	1.45	19.93	15.36	11.62	N/A	N/A	99.98	42.49	24.77	32.74
	Augite 3	51.88	1.23	18.96	15.51	12.42	N/A	N/A	100.00	40.44	26.49	33.08
	Augite 4	46.99	25.80	11.66	4.26	11.29	N/A	N/A	100.00	42.85	41.49	15.66
	Augite 5	51.03	1.11	16.93	17.28	13.63	N/A	N/A	99.98	35.39	28.49	36.12
	Augite 6	52.86	1.36	18.46	13.49	13.84	N/A	N/A	100.01	40.31	30.22	29.46
	Augite 7	51.73	2.02	18.85	13.54	12.98	N/A	N/A	100.00	41.55	28.61	29.84
	Augite 8	50.22	1.50	19.03	15.24	12.79	1.23	N/A	100.01	40.44	27.18	32.38
	Augite 9	52.06	1.31	19.15	14.28	13.19	N/A	N/A	99.99	41.08	28.29	30.63
Site 5	Diopside 1	50.92	2.30	21.10	9.06	14.77	N/A	1.52	99.97	46.96	32.87	20.16
Site 7	Augite 1	52.07	1.54	20.46	12.79	13.15	N/A	N/A	100.01	44.09	28.34	27.56
	Augite 2	51.32	1.39	19.23	14.09	13.06	N/A	0.91	100.00	41.46	28.16	30.38

	Augite 3	52.79	1.41	19.85	12.65	13.29	N/A	N/A	99.99	43.35	29.02	27.63
	Augite 4	51.67	1.31	20.08	14.11	12.83	N/A	N/A	100.00	42.71	27.29	30.01
LAM	Augite 1	45.45	17.31	12.77	14.08	10.39	N/A	N/A	100.00	34.29	27.90	37.81
	Augite 2	45.37	17.43	10.38	11.18	15.64	N/A	N/A	100.00	27.90	42.04	30.05
	Augite 3	48.77	N/A	10.72	30.11	10.40	N/A	N/A	100.00	20.93	20.30	58.77
	Augite 4	51.86	N/A	20.49	15.02	12.63	N/A	N/A	100.00	42.56	26.24	31.20
	Augite 5	52.15	N/A	18.80	15.04	14.01	N/A	N/A	100.00	39.29	29.28	31.43
	Augite 6	52.87	N/A	19.54	13.97	13.61	N/A	N/A	99.99	41.47	28.88	29.65
	Augite 7	51.44	N/A	20.22	14.47	13.88	N/A	N/A	100.01	41.63	28.58	29.79
	Augite 8	48.92	N/A	20.92	16.04	14.11	N/A	N/A	99.99	40.96	27.63	31.41
	Augite 9	52.21	N/A	19.10	15.21	13.38	N/A	N/A	99.99	40.05	28.06	31.89
	Augite 10	52.29	N/A	18.73	15.25	13.73	N/A	N/A	100.00	39.26	28.78	31.96
	Augite 11	51.01	N/A	20.26	15.41	13.30	N/A	N/A	99.98	41.37	27.16	31.47
	Augite 12	51.90	N/A	20.04	14.50	13.56	N/A	N/A	100.00	41.66	28.19	30.15
	Augite 13	51.87	N/A	19.10	15.27	13.76	N/A	N/A	100.00	39.68	28.59	31.73
	Augite 14	53.44	N/A	17.53	15.01	14.03	N/A	N/A	100.01	37.64	30.13	32.23
	Augite 15	52.71	N/A	19.42	13.59	14.27	N/A	N/A	99.99	41.07	30.18	28.74
	Augite 16	53.20	N/A	18.81	14.37	13.62	N/A	N/A	100.00	40.19	29.10	30.71
	Augite 17	52.95	N/A	18.35	14.43	14.28	N/A	N/A	100.01	38.99	30.34	30.66
	Augite 18	52.14	N/A	19.68	14.13	14.05	N/A	N/A	100.00	41.12	29.36	29.52
	Augite 19	51.60	2.68	14.02	16.93	14.77	N/A	N/A	100.00	30.66	32.31	37.02
	Augite 20	52.38	N/A	18.56	15.59	13.47	N/A	N/A	100.00	38.98	28.29	32.74
	Augite 21	51.38	N/A	20.19	16.24	12.19	N/A	N/A	100.00	41.53	25.07	33.40
	Augite 22	52.42	N/A	19.15	14.51	13.93	N/A	N/A	100.01	40.24	29.27	30.49
	Augite 23	52.19	1.86	16.95	13.96	15.05	N/A	N/A	100.01	36.88	32.75	30.37
	Diopside 1	52.76	N/A	21.92	9.90	15.42	N/A	N/A	100.00	46.40	32.64	20.96
	Augite 25	48.33	1.32	10.72	32.35	7.28	N/A	N/A	100.00	21.29	14.46	64.25
	Augite 26	52.20	2.22	19.71	10.18	15.69	N/A	N/A	100.00	43.24	34.42	22.33
	Augite 27	53.13	N/A	19.68	11.92	15.27	N/A	N/A	100.00	41.99	32.58	25.43

	Augite 28	52.61	N/A	19.94	12.77	14.68	N/A	N/A	100.00	42.08	30.98	26.95
	Augite 24	52.25	2.08	16.83	14.98	13.86	N/A	N/A	100.00	36.85	30.35	32.80
	Standard Deviation	1.76	5.59	2.62	3.85	1.37	0	0				
	Average	51.70	3.25	18.25	14.49	13.51	1.23	1.12				

i) – Graph displaying the geochemical data for Ca-rich pyroxene in NWA11444

NWA11444 – Fe/Mg Rich Pyroxene												
Data in Wt % Oxide		SiO_2	Al_2O_3	CaO	FeO	MgO	Cr_2O_3	TiO_2	Total	Wo	Ens	Fs
Site 1	Pigeonite 1	52.17	N/A	3.75	27.25	16.83	N/A	N/A	100.00	7.84	35.19	56.97
	Pigeonite 2	52.22	N/A	4.21	26.20	17.37	N/A	N/A	100.00	8.81	36.35	54.83
	Pigeonite 3	52.90	N/A	3.21	26.20	17.69	N/A	N/A	100.00	6.82	37.56	55.63
	Pigeonite 4	57.50	N/A	2.08	19.89	20.53	N/A	N/A	100.00	4.89	48.31	46.80
Site 3	Pigeonite 1	52.20	N/A	2.92	27.50	17.38	N/A	N/A	100.00	6.11	36.36	57.53
	Pigeonite 2	52.56	N/A	4.21	26.21	17.01	N/A	N/A	99.99	8.88	35.86	55.26
	Pigeonite 3	52.24	N/A	3.14	27.08	17.55	N/A	N/A	100.01	6.57	36.74	56.69
	Pigeonite 4	52.02	N/A	2.68	27.93	17.36	N/A	N/A	99.99	5.59	36.19	58.22
	Pigeonite 5	49.75	1.94	2.88	30.55	14.88	N/A	N/A	100.00	5.96	30.80	63.24
	Pigeonite 6	52.09	N/A	3.29	27.57	17.05	N/A	N/A	100.00	6.87	35.59	57.55
	Pigeonite 7	52.78	N/A	7.17	23.10	16.94	N/A	N/A	99.99	15.19	35.88	48.93
	Enstatite 1	52.43	N/A	2.26	28.03	17.28	N/A	N/A	100.00	4.75	36.33	58.92
	Pigeonite 8	52.15	N/A	2.69	27.65	17.51	N/A	N/A	100.00	5.62	36.59	57.78
	Pigeonite 9	52.12	N/A	3.68	27.05	17.15	N/A	N/A	100.00	7.69	35.82	56.50
	Pigeonite 10	52.48	1.70	7.38	22.64	15.81	N/A	N/A	100.01	16.10	34.50	49.40
	Enstatite 2	48.38	N/A	2.39	35.24	13.99	N/A	N/A	100.00	4.63	27.10	68.27
	Pigeonite 11	41.16	2.25	10.70	23.22	12.10	5.4	5.17	100.00	23.25	26.29	50.46
	Pigeonite 12	56.22	N/A	2.12	21.68	19.99	N/A	N/A	100.01	4.84	45.65	49.51
	Pigeonite 13	57.82	N/A	2.26	19.22	20.69	N/A	N/A	99.99	5.36	49.06	45.58
Site 4	Enstatite 1	54.12	1.42	1.78	16.59	25.16	N/A	0.92	99.99	4.09	57.80	38.11
	Enstatite 2	54.86	1.35	1.69	12.59	28.60	N/A	0.91	100.00	3.94	66.70	29.36
	Pigeonite 1	49.82	1.19	3.82	30.58	14.59	N/A	N/A	100.00	7.80	29.78	62.42
	Pigeonite 2	51.61	N/A	3.60	27.99	16.79	N/A	N/A	99.99	7.44	34.70	57.85
	Pigeonite 3	52.33	N/A	2.69	27.72	17.26	N/A	N/A	100.00	5.64	36.21	58.15
	Pigeonite 4	51.10	1.44	3.72	27.52	16.23	N/A	N/A	100.01	7.84	34.19	57.97

Site 5	Pigeonite 1	59.35	1.95	3.47	8.96	26.28	N/A	N/A	100.01	8.96	67.89	23.15
	Enstatite 1	55.75	1.70	1.66	11.64	29.25	N/A	N/A	100.00	3.90	68.74	27.36
	Pigeonite 2	50.39	0.97	6.62	29.18	12.84	N/A	N/A	100.00	13.61	26.40	59.99
	Pigeonite 3	52.27	N/A	2.63	27.14	17.96	N/A	N/A	100.00	5.51	37.63	56.86
	Pigeonite 4	51.98	N/A	2.92	28.3	16.79	N/A	N/A	99.99	6.08	34.97	58.95
	Pigeonite 5	54.55	1.66	1.73	19.28	22.77	N/A	N/A	99.99	5.12	67.41	27.47
	Pigeonite 6	55.76	1.30	2.15	11.45	29.35	N/A	N/A	100.01	5.01	68.34	26.66
	Pigeonite 7	55.77	1.62	2.19	11.62	28.81	N/A	N/A	100.01	5.14	67.60	27.26
	Pigeonite 8	51.90	1.03	5.59	26.03	15.45	N/A	N/A	100.00	11.88	32.82	55.30
	Pigeonite 9	52.52	0.96	3.24	23.89	19.39	N/A	N/A	100.00	6.96	41.68	51.35
	Pigeonite 10	53.53	N/A	2.31	21.98	22.18	N/A	N/A	100.00	4.97	47.73	47.30
Site 7	Pigeonite 1	54.71	N/A	4.87	16.73	23.70	N/A	N/A	100.01	10.75	52.32	36.93
	Pigeonite 2	53.76	1.58	2.18	18.50	23.98	N/A	N/A	100.00	4.88	53.69	41.42
	Pigeonite 3	52.64	2.90	3.69	19.12	21.65	N/A	N/A	100.00	8.30	48.70	43.00
	Pigeonite 4	52.22	N/A	2.63	28.00	17.15	N/A	N/A	100.00	5.50	35.89	58.60
	Pigeonite 5	52.25	N/A	3.31	27.14	17.31	N/A	N/A	100.01	6.93	36.24	56.83
	Pigeonite 6	51.53	0.96	4.13	26.78	16.62	N/A	N/A	100.02	8.69	34.97	56.34
	Pigeonite 7	52.26	N/A	3.14	27.21	17.40	N/A	N/A	100.01	6.58	36.44	56.98
LAM	Enstatite 1	55.70	N/A	2.02	12.81	29.47	N/A	N/A	100.00	4.56	66.52	28.92
	Pigeonite 1	53.63	N/A	6.41	16.99	22.97	N/A	N/A	100.00	13.82	49.54	36.64
	Pigeonite 2	52.95	N/A	3.25	27.67	16.13	N/A	N/A	100.00	6.91	34.28	58.81
	Pigeonite 3	50.67	N/A	3.85	27.97	17.52	N/A	N/A	100.01	7.80	35.51	56.69
	Pigeonite 4	50.85	N/A	3.23	28.31	17.62	N/A	N/A	100.01	6.57	35.84	57.59
	Pigeonite 5	52.40	N/A	3.81	27.34	16.45	N/A	N/A	100.00	8.00	34.56	57.44
	Pigeonite 6	51.29	N/A	4.15	27.06	17.50	N/A	N/A	100.00	8.52	35.93	55.55
	Pigeonite 7	52.17	N/A	3.59	26.49	17.75	N/A	N/A	100.00	7.51	37.11	55.38
	Pigeonite 8	51.81	N/A	3.63	27.02	17.54	N/A	N/A	100.00	7.53	36.40	56.07
	Pigeonite 9	51.74	N/A	3.72	27.48	17.07	N/A	N/A	100.01	7.71	35.36	56.93

	Pigeonite 10	51.27	N/A	3.91	27.74	17.07	N/A	N/A	99.99	8.03	35.04	56.94
	Pigeonite 11	51.95	N/A	3.43	27.54	17.07	N/A	N/A	99.99	7.14	35.53	57.33
	Pigeonite 12	52.81	N/A	3.48	26.80	16.91	N/A	N/A	100.00	7.37	35.83	56.79
	Pigeonite 13	51.63	N/A	4.65	26.80	16.93	N/A	N/A	100.01	9.61	34.99	55.39
	Enstatite 2	55.67	N/A	1.55	13.20	29.59	N/A	N/A	100.01	3.50	66.73	29.77
	Pigeonite 14	51.77	N/A	3.08	27.92	17.24	N/A	N/A	100.01	6.38	35.74	57.88
	Pigeonite 15	51.84	N/A	4.52	26.71	16.94	N/A	N/A	100.01	9.38	35.17	55.45
	Pigeonite 16	52.25	N/A	3.85	26.91	16.99	N/A	N/A	100.00	8.06	35.58	56.36
	Enstatite 3	56.48	N/A	1.65	11.48	30.39	N/A	N/A	100.00	3.79	69.83	26.38
	Pigeonite 17	54.64	2.66	2.15	29.30	11.25	N/A	N/A	100.00	6.48	38.26	55.26
	Enstatite 4	51.40	N/A	3.15	26.86	18.60	N/A	N/A	100.01	4.79	52.02	43.19
	Pigeonite 18	54.12	N/A	2.20	19.82	23.87	N/A	N/A	100.00	4.97	47.96	47.07
	Pigeonite 19	53.54	N/A	2.31	21.87	22.28	N/A	N/A	100.00	5.50	66.70	27.80
	Pigeonite 20	55.79	N/A	2.43	12.29	29.49	N/A	N/A	100.00	10.42	34.99	54.59
	Pigeonite 21	51.24	N/A	5.08	26.62	17.06	N/A	N/A	100.01	6.38	60.24	33.38
	Standard Deviation	5.23	0.69	1.55	6.29	4.54	0	0				
	Average	52.24	1.66	3.44	23.43	19.46	5.40	2.33				

j) – Graph displaying the geochemical data for Fe/Mg-rich pyroxene in NWA11444

Plagioclase Compositions

Appendix 5

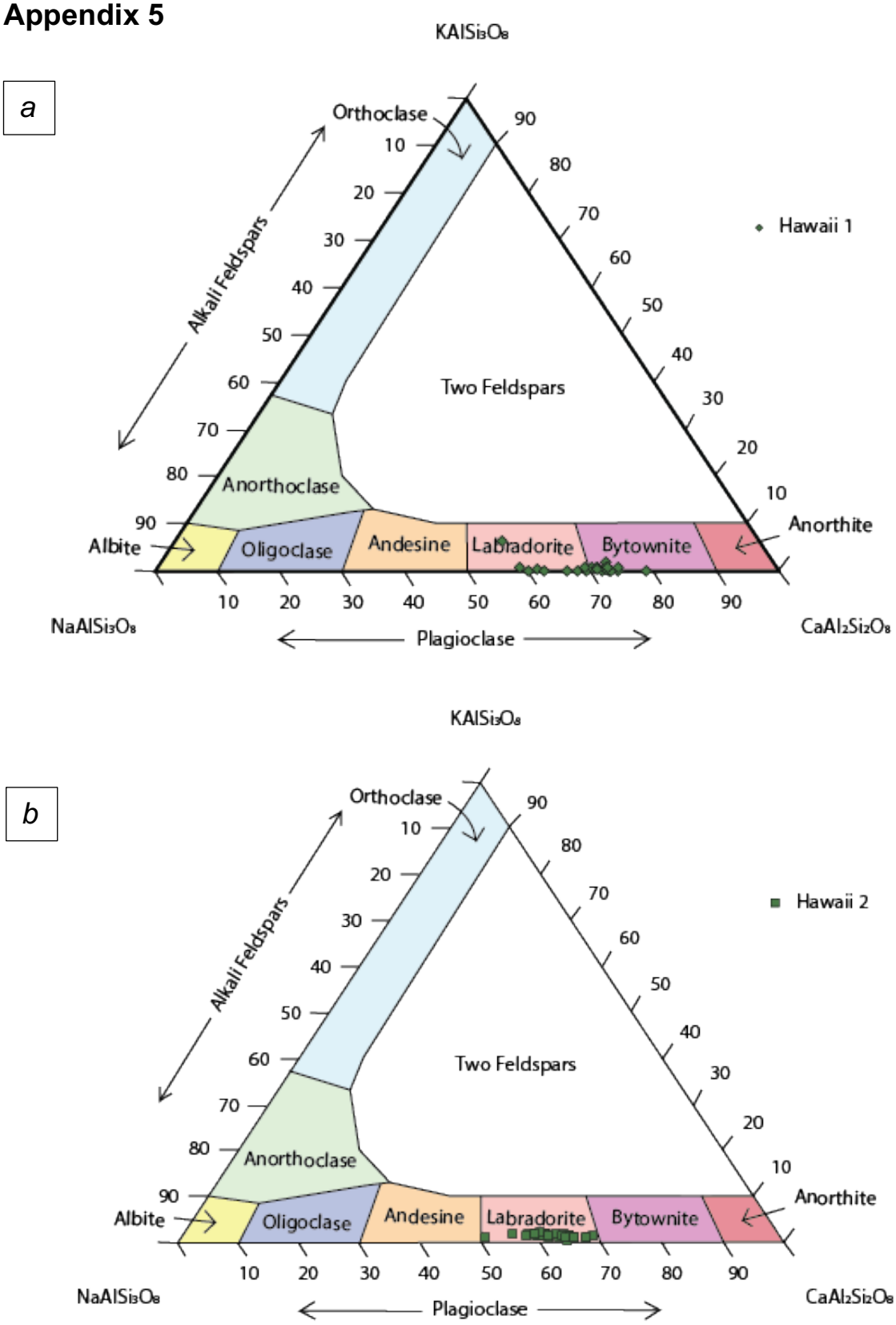

Appendix 5 – a) Triangular plot displaying plagioclase compositions within Hawaii 1, showing Hawaii 1 comprises of both bytownite and labradorite plagioclase, b) Triangular plot displaying plagioclase compositions within Hawaii 2. This sample only contains plagioclase of labradorite composition. All data in wt% oxide.

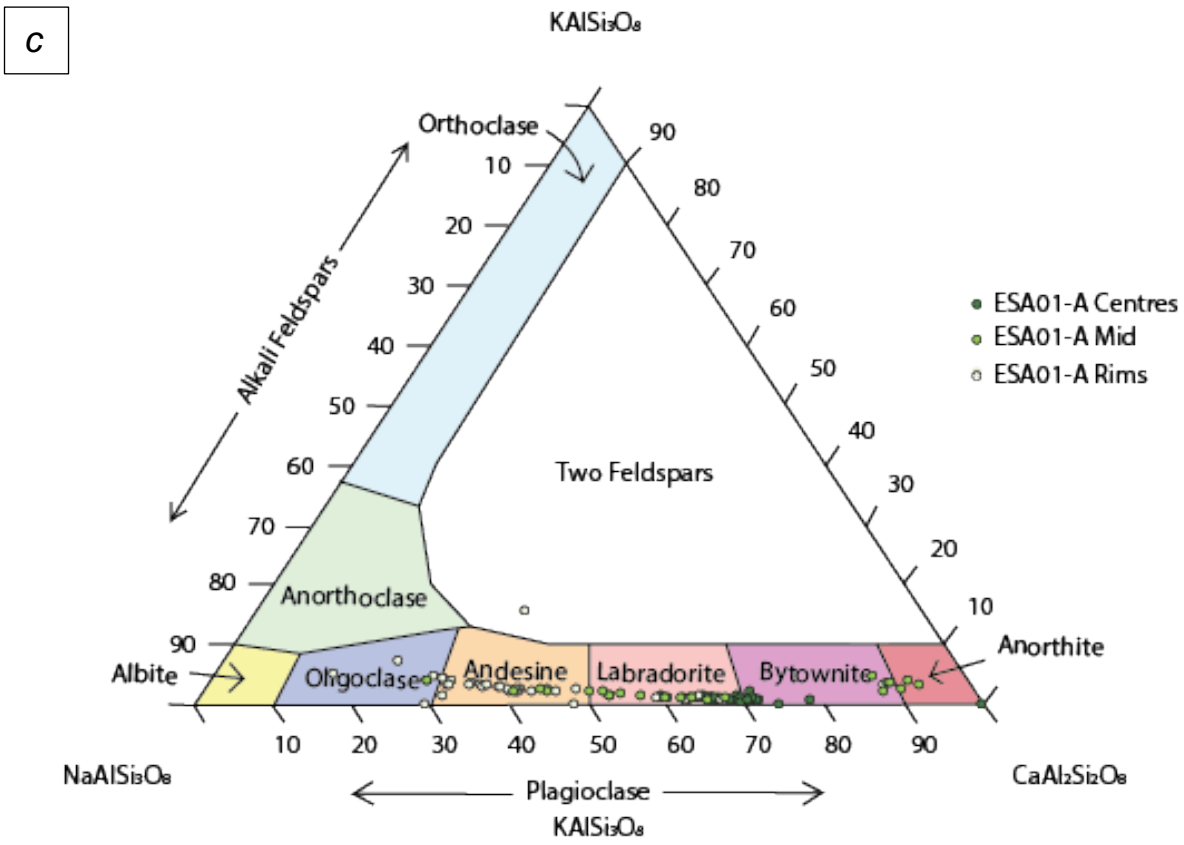

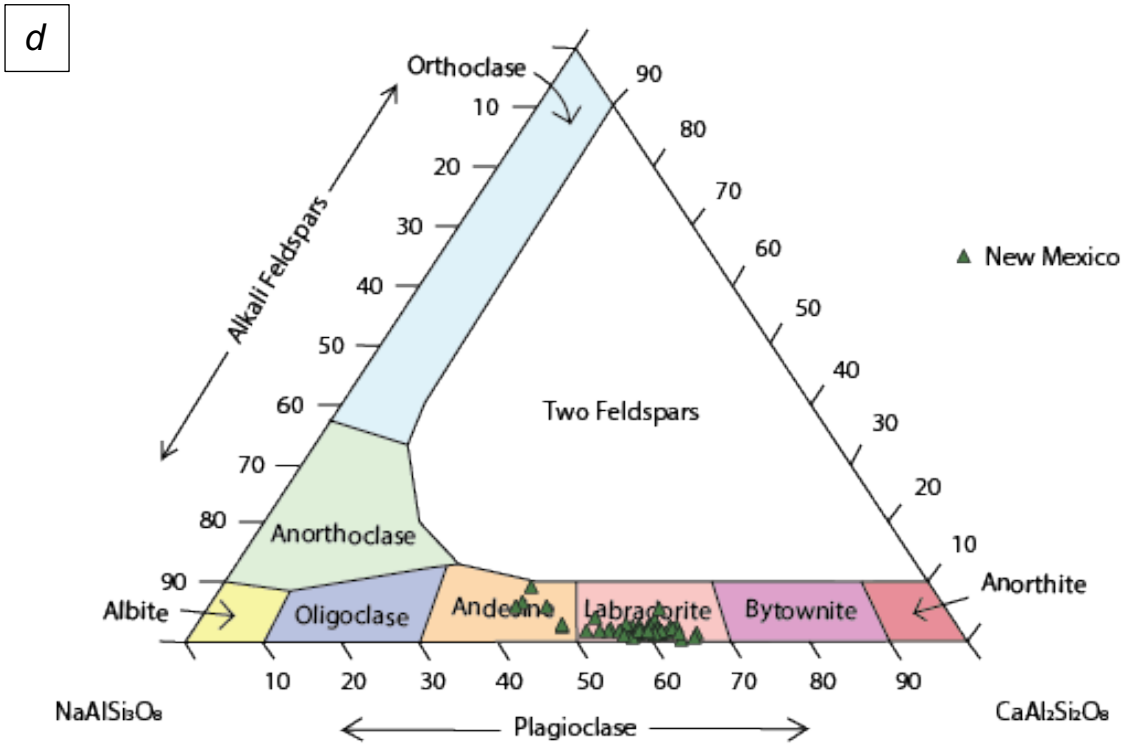

Appendix 5 – c) Triangular plot displaying plagioclase compositions within ESA01-A showing ESA01-A comprises of a range of oligoclase, andesine, labradorite, bytownite and anorthite due to the strong zoning present in plagioclase within the sample, b) Triangular plot displaying plagioclase compositions within New Mexico. This sample only contains plagioclase of both andesine and labradorite composition. All data in wt% oxide.

Appendix 6

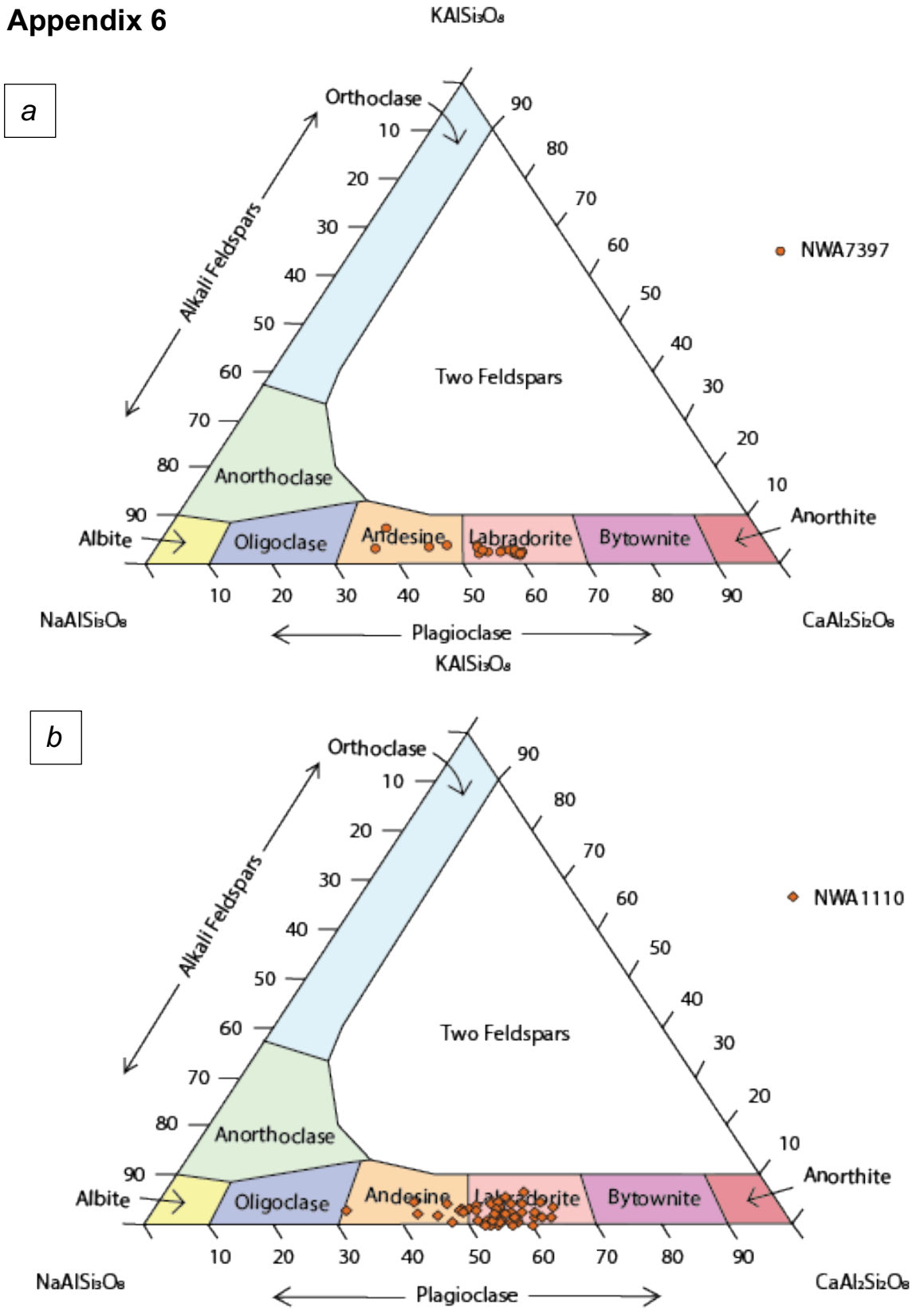

Appendix 6 – a) Triangular plot displaying plagioclase compositions within NWA7397, showing NWA7397 comprises of both andesine and labradorite, b) Triangular plot displaying plagioclase compositions within NWA1110. This sample also contains plagioclase of both andesine and labradorite composition. All data in wt% oxide.

c

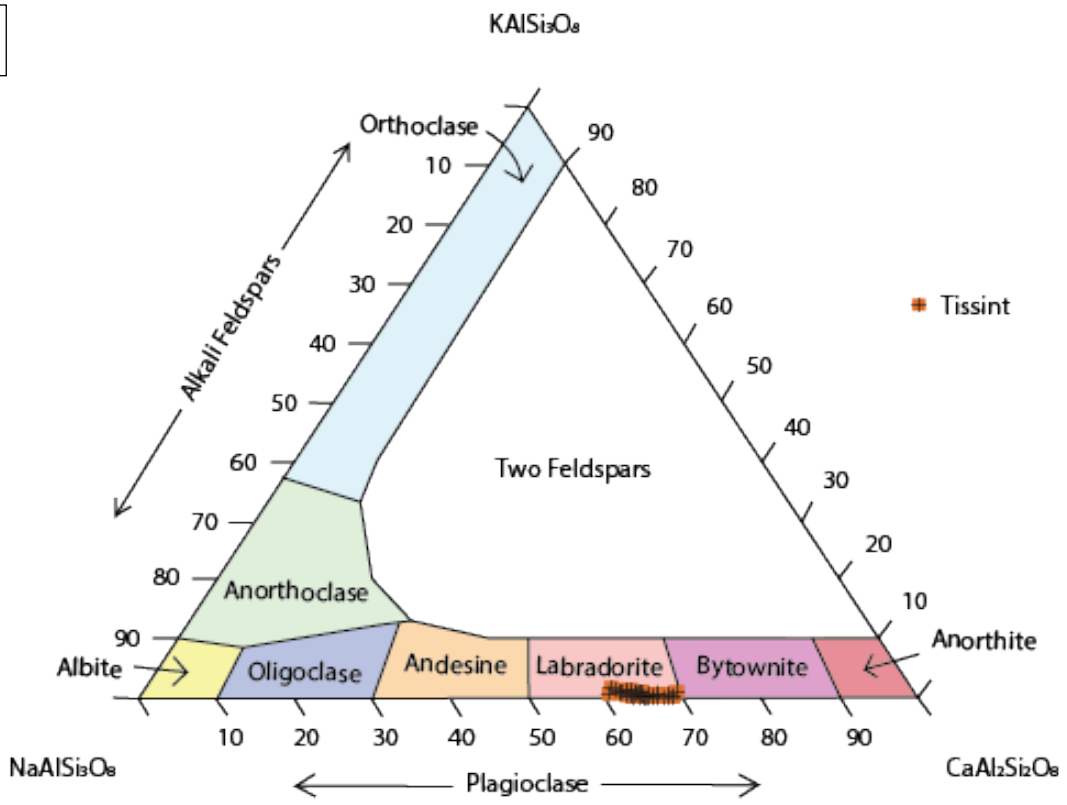

Appendix 6 – c) Triangular plot displaying plagioclase compositions within Tissint, showing, unlike the previous two Martian samples, Tissint comprises of only labradorite. All data in wt% oxide.

Appendix 7

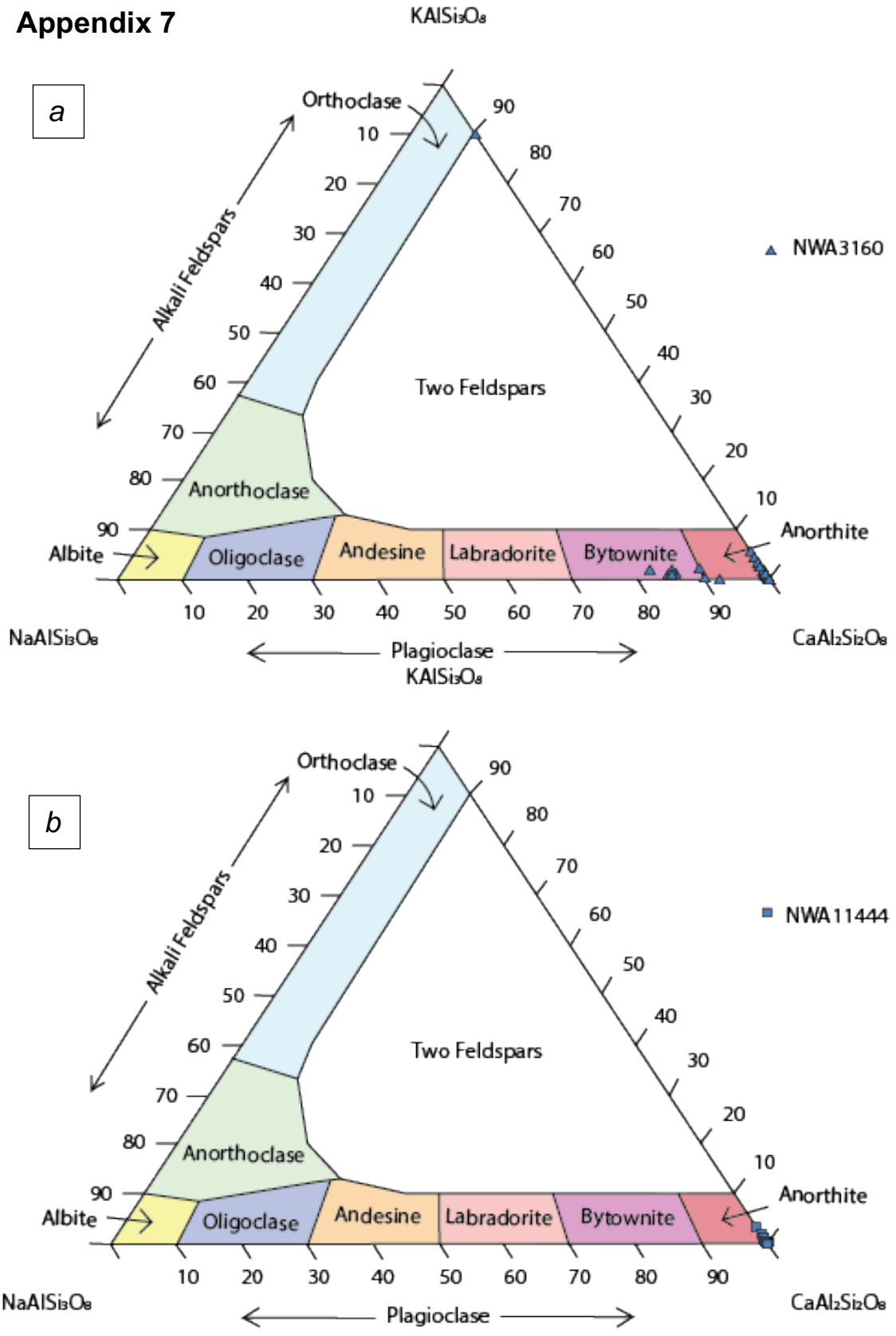

Appendix 7 – a) Triangular plot displaying plagioclase compositions within NWA3160, showing this sample comprises of both bytownite and anorthite compositions, b) Triangular plot displaying plagioclase compositions within NWA11444. This sample also contains plagioclase that is only anorthite composition. All data in wt% oxide.

Appendix 8 – Plagioclase Compositions

For all data tables, where N/A is written, values detected by the SEM were either on or below the detection limit and therefore weren't included.

Hawaii 1												
Data in Wt % Oxide		SiO_2	Al_2O_3	CaO	Na_2O	FeO	K_2O	MgO	An	Ab	Or	Total
Site 1	Plagioclase 1	51.95	29.82	13.97	3.93	0.33	N/A	N/A	66.27	33.73	0.00	100.00
	Plagioclase 2	49.33	32.44	13.08	4.54	0.55	0.07	N/A	61.18	38.43	0.39	100.01
	Plagioclase 3	49.63	31.22	15.51	3.38	N/A	N/A	0.26	71.72	28.28	0.00	100.00
	Plagioclase 4	49.54	29.46	13.60	4.50	2.60	N/A	0.29	62.55	37.45	0.00	99.99
	Plagioclase 5	51.05	29.06	13.56	5.01	0.71	N/A	0.60	59.93	40.07	0.00	99.99
	Plagioclase 6	49.43	31.58	15.47	3.21	N/A	0.31	N/A	71.46	26.83	1.71	100.00
	Plagioclase 7	49.63	33.98	12.29	3.21	0.88	N/A	N/A	67.90	32.10	0.00	99.99
	Plagioclase 8	56.61	26.12	11.19	4.82	0.14	1.11	N/A	52.70	41.08	6.22	99.99
	Plagioclase 9	54.50	27.69	13.76	3.36	0.69	N/A	N/A	69.35	30.64	0.00	100.00
	Plagioclase 10	51.45	30.16	15.04	3.08	0.26	N/A	N/A	72.96	27.04	0.00	99.99
	Plagioclase 11	51.68	28.78	15.88	3.03	0.34	N/A	0.29	74.33	25.67	0.00	100.00
	Plagioclase 12	50.78	31.25	15.65	2.33	N/A	N/A	N/A	78.78	21.22	0.00	100.01
Site 2	Plagioclase 1	49.93	30.64	15.37	3.09	0.74	N/A	0.23	73.32	26.68	0.00	100.00
	Plagioclase 2	52.60	30.71	11.36	4.41	0.53	0.10	0.29	58.38	41.01	0.61	100.00
	Plagioclase 3	50.82	30.74	14.05	3.30	0.68	0.13	0.28	69.64	29.60	0.77	100.00
	Plagioclase 4	51.02	30.54	14.25	3.18	0.71	0.13	0.17	70.69	28.55	0.77	100.00
	Plagioclase 5	51.08	29.92	14.48	3.25	0.85	0.16	0.26	70.46	28.62	0.93	100.00
	Plagioclase 6	50.25	30.48	14.85	3.11	0.97	0.12	0.21	72.01	27.29	0.69	99.99
	Plagioclase 7	50.83	30.10	14.47	3.06	1.09	0.09	0.36	71.94	27.53	0.53	100.00
Site 3	Plagioclase 1	50.30	30.80	14.70	3.09	0.74	0.09	0.28	72.06	27.41	0.53	100.00
	Plagioclase 2	51.41	29.69	13.80	3.42	1.15	0.15	0.38	68.43	30.69	0.89	100.00

Site 5	Plagioclase 3	49.73	31.23	15.03	2.86	0.80	0.10	0.26	73.95	25.46	0.59	100.01
	Plagioclase 4	50.68	31.18	14.71	3.04	N/A	0.11	0.27	72.31	27.04	0.64	99.99
	Plagioclase 5	50.77	30.51	14.37	3.24	0.79	0.08	0.25	70.69	28.84	0.47	100.01
	Standard Deviation	1.75	1.53	1.24	0.68	0.50	0.27	0.10				
	Average	51.04	30.34	14.19	3.48	0.78	0.20	0.29				

a) – Graph displaying the geochemical data for plagioclase in Hawaii 1

Hawaii 2												
Data in Wt % Oxide		SiO_2	Al_2O_3	CaO	Na_2O	FeO	MgO	K_2O	An	Ab	Or	Total
Site 1	Plagioclase 1	51.99	29.87	12.96	4.15	0.66	0.15	0.23	62.40	36.20	1.32	100.01
	Plagioclase 2	52.06	29.82	13.09	3.98	0.6	0.15	0.30	63.39	34.88	1.73	100.00
	Plagioclase 3	52.28	29.53	13.2	3.97	0.56	0.15	0.30	63.64	34.64	1.72	99.99
	Plagioclase 4	51.98	29.92	13.14	4.02	0.52	0.13	0.29	63.88	35.37	0.75	100.00
	Plagioclase 5	53.41	28.83	12.06	4.47	0.79	0.11	0.32	58.74	39.40	1.86	99.99
	Plagioclase 6	53.02	29.17	12.18	4.31	0.82	0.16	0.34	59.75	38.26	1.98	100.00
	Plagioclase 7	53.28	28.91	12.19	4.38	0.72	0.15	0.38	59.27	38.54	2.20	100.01
	Plagioclase 8	52.83	29.13	12.42	4.4	0.71	0.16	0.36	59.68	38.26	2.06	100.01
	Plagioclase 9	52.98	29.28	12.16	4.43	0.75	0.09	0.31	59.18	39.02	1.80	100.00
	Plagioclase 10	52.61	29.77	13.21	3.95	N/A	0.18	0.29	63.81	34.53	1.67	100.01
	Plagioclase 11	52.05	29.71	13.38	3.92	0.51	0.16	0.26	64.38	34.13	1.49	99.99
	Plagioclase 12	52.08	29.63	13.17	4.03	0.62	0.16	0.30	63.26	35.03	1.72	99.99
	Plagioclase 13	53.68	29.13	11.45	4.58	0.68	0.15	0.33	56.88	41.17	1.95	100.00
	Plagioclase 14	53.56	29.12	11.84	4.45	0.51	0.21	0.31	58.43	39.74	1.82	100.00
	Plagioclase 15	53.04	28.98	12.85	4.01	0.69	0.09	0.33	62.68	35.40	1.92	99.99
	Plagioclase 16	53.79	29.5	11.18	4.51	0.64	0.11	0.27	56.86	41.51	1.64	100.00
	Plagioclase 17	53.87	29.82	10.02	5.37	0.53	0.15	0.23	50.07	48.56	1.37	99.99
	Plagioclase 18	53.72	28.75	11.84	4.51	0.68	0.14	0.37	57.92	39.92	2.16	100.01
	Plagioclase 19	51.90	28.47	13.92	4.17	0.69	0.53	0.31	63.75	34.56	1.69	99.99
	Plagioclase 20	54.12	29.31	10.88	4.84	0.53	N/A	0.32	54.35	43.75	1.90	100.00
	Plagioclase 21	51.59	30.29	13.64	3.6	0.52	0.13	0.22	66.81	31.91	1.28	99.99
	Plagioclase 22	50.78	29.58	14.8	3.69	0.69	0.13	0.34	67.63	30.52	1.85	100.01
	Plagioclase 23	53.19	29.18	12.51	4.15	0.46	0.16	0.34	61.25	36.77	1.98	99.99
	Plagioclase 24	53.11	29.12	12.26	4.37	0.67	0.11	0.35	59.56	38.42	2.02	99.99
	Plagioclase 25	51.89	30.07	13.35	3.85	0.61	N/A	0.23	64.83	33.84	1.33	100.00

Site 2	Plagioclase 1	52.38	29.79	12.89	4.05	0.51	0.10	0.29	62.68	35.64	1.68	100.01
	Plagioclase 2	52.07	30.01	13.01	4.00	0.53	0.13	0.26	63.28	35.21	1.51	100.01
	Plagioclase 3	51.62	30.16	13.35	3.87	0.55	0.18	0.26	64.61	33.89	1.50	99.99
	Plagioclase 4	51.75	29.54	13.62	3.58	1.09	0.19	0.23	66.86	31.80	1.34	100.00
Site 4	Plagioclase 1	53.17	29.24	12.35	4.28	0.52	0.13	0.30	60.63	38.02	1.34	99.99
	Plagioclase 2	53.51	29.16	11.98	4.35	0.59	0.12	0.29	59.32	38.98	1.71	100.00
	Plagioclase 3	53.1	29.13	12.08	4.45	0.66	0.18	0.40	58.61	39.07	2.31	100.00
	Plagioclase 4	53.06	29.14	12.46	4.31	0.64	0.09	0.31	60.40	37.81	1.79	100.01
	Plagioclase 5	53.3	28.53	11.93	4.53	1.11	0.28	0.34	58.1	39.93	1.97	100.02
	Standard Deviation	0.81	0.46	0.93	0.36	0.15	0.08	0.05				
	Average	52.73	29.40	12.57	4.22	0.65	0.16	0.30				

b) – Graph displaying the geochemical data for plagioclase in Hawaii 2

ESA01-A – Centres												
Data in Wt % Oxide		SiO_2	Al_2O_3	CaO	Na_2O	FeO	MgO	K_2O	An	Ab	Or	Total
Site 1	Plagioclase 1	50.11	31.46	14.48	3.31	0.53	N/A	0.12	70.25	29.06	0.69	100.01
	Plagioclase 2	49.83	31.57	14.68	3.25	0.52	N/A	0.16	70.46	28.62	0.93	100.01
	Plagioclase 3	50.36	31.29	14.45	3.31	0.47	N/A	0.11	70.25	29.12	0.64	99.99
	Plagioclase 4	49.89	30.81	14.19	3.14	1.28	0.50	0.19	70.60	28.27	1.13	100.00
	Plagioclase 5	51.12	30.46	13.72	3.80	0.76	N/A	0.13	66.12	33.14	0.75	99.99
	Plagioclase 6	51.28	30.46	13.65	3.74	0.71	N/A	0.16	66.23	32.84	0.92	100.00
	Plagioclase 7	49.90	31.50	14.37	3.52	0.51	N/A	0.20	68.50	30.36	1.14	100.00
	Plagioclase 8	51.78	29.31	12.36	4.04	1.81	0.47	0.23	68.38	30.31	1.30	100.00
	Plagioclase 9	48.57	28.91	12.24	3.31	1.29	2.47	0.15	62.04	37.06	0.91	100.00
	Plagioclase 10	52.61	29.44	11.91	4.44	1.35	N/A	0.25	58.84	39.69	1.47	100.00
Site 2	Plagioclase 1	52.69	29.55	12.78	2.42	1.77	0.79	N/A	74.48	25.52	0.00	100.00
	Plagioclase 2	48.66	31.56	15.13	3.39	0.88	N/A	0.39	69.63	28.23	2.14	100.01
	Plagioclase 3	56.45	29.71	11.88	N/A	1.96	N/A	N/A	100.00	0.00	0.00	100.00
Site 4	Plagioclase 1	49.82	31.56	14.43	3.24	0.71	0.13	0.10	70.69	28.72	0.58	99.99
	Plagioclase 2	50.71	27.66	11.93	3.33	3.94	2.31	0.11	65.96	33.32	0.72	99.99
	Plagioclase 3	53.00	29.22	12.20	4.57	0.81	N/A	0.21	58.88	39.91	1.21	100.01
	Plagioclase 4	50.54	31.20	14.08	3.44	0.63	N/A	0.12	68.86	30.44	0.70	100.01
	Plagioclase 5	50.97	30.69	13.36	3.77	0.91	0.12	0.19	65.46	33.43	1.11	100.01
	Plagioclase 6	52.37	28.84	12.61	4.02	1.33	0.65	0.18	62.74	36.19	1.07	100.00
	Plagioclase 7	52.15	29.93	12.81	4.14	0.82	N/A	0.15	62.55	36.58	0.87	100.00
	Plagioclase 8	51.76	30.19	13.28	3.80	0.80	N/A	0.18	65.19	33.76	1.05	100.01
Site 5	Plagioclase 1	51.40	30.04	13.16	3.93	1.20	0.11	0.16	64.31	34.76	0.93	100.00
	Plagioclase2	51.28	30.29	13.37	3.85	0.93	0.09	0.20	64.98	33.86	1.16	100.01
	Plagioclase 3	51.76	30.23	13.63	4.03	N/A	0.10	0.25	64.23	34.37	1.40	100.00
	Plagioclase 4	51.49	30.88	13.64	3.84	N/A	N/A	0.14	65.72	33.48	0.80	99.99

	Plagioclase 5	50.50	30.95	13.79	3.52	0.97	0.14	0.13	67.88	31.36	0.76	100.00
	Plagioclase 6	51.16	30.37	13.34	3.77	1.21	N/A	0.17	65.51	33.50	0.99	100.02
Site 8	Plagioclase 1	49.79	31.87	14.60	3.12	0.52	N/A	0.10	71.69	27.72	0.58	100.00
	Plagioclase 2	55.13	27.76	10.65	5.22	0.85	0.11	0.27	52.16	46.26	1.57	99.99
	Plagioclase 3	49.89	31.34	14.86	3.23	0.55	N/A	0.13	71.24	28.02	0.74	100.00
	Plagioclase 4	51.87	30.05	13.37	3.73	0.73	0.09	0.16	65.83	33.23	0.94	100.00
	Plagioclase 5	50.22	31.36	14.36	3.42	0.47	N/A	0.16	69.24	29.84	0.92	99.99
	Plagioclase 6	50.52	31.02	14.09	3.39	0.80	0.09	0.09	69.30	30.17	0.53	100.00
	Plagioclase 7	52.45	30.21	12.42	4.14	0.58	N/A	0.19	61.67	37.20	1.12	99.99
	Plagioclase 8	51.87	30.26	12.95	4.12	0.65	N/A	0.16	62.88	36.20	0.92	100.01
	Plagioclase 9	51.37	29.86	13.38	4.07	0.79	0.32	0.21	63.73	35.08	1.19	100.00
	Plagioclase 10	51.59	30.21	13.26	3.99	0.75	N/A	0.19	64.04	34.87	1.09	99.99
Site 9	Plagioclase 1	49.81	31.49	14.72	3.28	0.51	N/A	0.19	70.49	28.42	1.08	100.00
	Plagioclase 2	52.41	29.55	12.17	4.43	0.97	0.30	0.16	59.78	39.28	0.93	99.99
	Plagioclase 3	47.25	23.64	10.19	1.54	10.12	7.18	0.09	77.88	21.30	0.82	100.01
	Plagioclase 4	50.16	31.11	14.61	3.36	0.65	N/A	0.11	70.17	29.20	0.63	100.00
	Standard Deviation	1.62	1.45	1.13	0.60	1.59	1.73	0.06				
	Average	51.13	30.19	13.34	3.65	1.21	0.89	0.17				

c) – Graph displaying the geochemical data for plagioclase centres in ESA01-A

ESA01-A – Rims													
Data in Wt % Oxide		SiO_2	Al_2O_3	CaO	Na_2O	FeO	MgO	K_2O	TiO_2	An	Ab	Or	Total
Site 1	Plagioclase 11	58.67	23.95	6.50	6.67	2.46	1.19	0.56	N/A	33.79	62.74	3.47	100.00
	Plagioclase 12	60.52	24.56	6.36	7.32	0.55	N/A	0.69	N/A	31.13	64.84	4.02	100.00
	Plagioclase 13	59.31	25.26	7.16	6.94	0.77	N/A	0.56	N/A	35.12	61.61	3.27	100.00
	Plagioclase 14	58.18	26.15	7.96	6.52	0.68	0.10	0.40	N/A	39.34	58.31	2.35	99.99
	Plagioclase 15	54.77	24.72	7.18	5.68	4.58	2.69	0.38	N/A	34.75	49.75	15.50	100.00
	Plagioclase 16	60.55	24.77	6.10	7.42	0.45	N/A	0.72	N/A	29.92	65.87	4.21	100.01
	Plagioclase 17	49.79	27.08	11.05	3.38	5.54	2.96	0.20	N/A	63.49	35.14	1.40	100.00
Site 2	Plagioclase 4	57.01	25.40	8.79	6.95	1.42	N/A	0.43	N/A	40.18	57.48	2.34	100.00
	Plagioclase 5	59.52	26.49	5.80	6.92	1.05	N/A	0.22	N/A	31.21	67.38	1.41	100.00
	Plagioclase 6	60.37	24.15	8.94	5.22	1.32	N/A	N/A	N/A	48.62	51.38	0.00	100.00
Site 4	Plagioclase 9	57.40	25.00	7.29	6.37	2.14	1.33	0.48	N/A	37.60	59.45	2.95	100.01
	Plagioclase 10	60.26	25.05	6.30	7.37	0.44	N/A	0.57	N/A	31.01	65.65	3.34	99.99
	Plagioclase 11	58.88	25.79	7.23	6.92	0.68	N/A	0.50	N/A	35.53	61.54	2.93	100.00
	Plagioclase 12	58.22	25.96	8.11	6.73	0.56	N/A	0.42	N/A	38.98	58.62	2.40	100.00
	Plagioclase 13	59.54	25.06	6.90	7.14	0.68	0.12	0.56	N/A	33.68	63.07	3.25	100.00
	Plagioclase 14	61.91	22.76	4.61	7.83	1.03	0.36	1.24	0.26	22.76	29.95	7.29	100.00
	Plagioclase 15	60.23	24.54	6.40	7.44	0.61	0.24	0.54	N/A	31.21	65.66	3.14	100.00
	Plagioclase 16	57.65	26.25	8.38	6.49	0.81	N/A	0.42	N/A	40.63	56.94	2.42	100.00
	Plagioclase 17	58.43	25.45	7.75	6.80	0.87	N/A	0.45	0.25	47.64	59.76	2.60	100.00
	Plagioclase 18	56.55	19.62	2.95	8.29	9.35	2.43	0.83	N/A	15.58	79.21	5.22	100.02
Site 5	Plagioclase 7	61.58	24.31	5.73	7.66	N/A	N/A	0.71	N/A	28.04	67.83	4.14	99.99
	Plagioclase 8	57.16	26.59	8.84	5.97	0.97	N/A	0.46	N/A	43.78	53.51	2.71	99.99
	Plagioclase 9	58.46	25.41	7.32	6.86	1.14	0.27	0.55	N/A	35.90	60.89	3.21	100.01
	Plagioclase 10	52.11	29.26	12.67	4.17	1.55	0.12	0.15	N/A	62.12	37.00	0.88	100.03
	Plagioclase 11	58.18	25.04	7.61	6.58	1.40	0.73	0.47	N/A	37.90	59.31	2.79	100.01

	Plagioclase 12	57.65	26.13	8.23	6.46	1.18	N/A	0.36	N/A	40.44	57.45	2.11	100.01
Site 8	Plagioclase 11	54.84	23.58	7.27	5.32	5.85	2.84	0.31	N/A	42.11	55.76	2.14	100.01
	Plagioclase 12	51.35	29.66	13.36	3.58	1.35	0.56	0.13	N/A	66.82	32.40	0.77	99.99
	Plagioclase 13	56.27	27.03	9.44	6.07	0.79	N/A	0.39	N/A	45.19	52.59	2.22	99.99
	Plagioclase 14	52.99	28.80	11.68	4.49	1.60	0.27	0.17	N/A	58.38	40.61	1.01	100.00
	Plagioclase 15	58.26	25.84	8.18	6.52	0.67	0.10	0.43	N/A	39.92	57.58	2.50	100.00
	Plagioclase 16	60.60	24.01	5.70	7.41	1.05	0.45	0.81	N/A	28.40	66.80	4.80	100.03
	Plagioclase 17	60.41	24.42	6.11	7.44	0.74	0.11	0.76	N/A	29.84	65.75	4.42	99.99
	Plagioclase 18	61.64	23.86	5.74	7.53	1.24	N/A	N/A	N/A	29.64	70.36	0.00	100.01
	Plagioclase 19	55.08	27.64	14.16	0.97	1.35	0.34	0.46	N/A	86.01	10.66	3.33	100.00
	Standard Deviation	2.96	1.85	2.39	1.49	1.89	1.03	0.23	0.01				
	Average	57.84	25.42	7.82	6.33	1.67	0.91	0.49	0.26				

d) – Graph displaying the geochemical data for plagioclase rims in ESA01-A

ESA01-A – Mid Plagioclase													
Data in Wt % Oxide		SiO_2	Al_2O_3	CaO	Na_2O	FeO	MgO	K_2O	TiO_2	An	Ab	Or	Total
Site 4	Plagioclase 19	51.74	30.26	13.01	4.10	0.64	0.09	0.18	N/A	63.02	35.94	1.04	100.02
	Plagioclase 20	54.61	28.29	10.79	5.28	0.78	N/A	0.25	N/A	52.27	46.49	1.44	100.00
	Plagioclase 21	56.97	26.58	9.16	6.14	0.77	N/A	0.38	N/A	44.20	53.62	2.18	100.00
	Plagioclase 22	54.91	27.87	10.74	5.45	0.67	N/A	0.37	N/A	51.04	46.87	2.09	100.01
	Plagioclase 23	54.18	28.72	11.46	4.77	0.62	N/A	0.25	N/A	56.21	42.33	1.46	100.00
	Plagioclase 24	52.57	29.34	12.45	4.53	0.91	N/A	0.21	N/A	59.58	39.23	1.20	100.01
	Plagioclase 25	51.57	30.36	13.14	3.84	0.84	0.10	0.14	N/A	64.87	34.31	0.82	99.99
	Plagioclase 26	55.30	27.30	10.11	5.44	0.92	0.25	0.37	0.30	49.57	48.27	2.16	99.99
Site 5	Plagioclase 13	57.61	25.78	8.26	6.64	1.12	0.17	0.41	N/A	39.78	57.87	2.35	99.99
Site 8	Plagioclase 20	52.62	29.06	12.48	4.19	1.20	0.28	0.16	N/A	61.62	37.44	0.94	99.99
	Plagioclase 21	50.23	28.83	12.92	3.39	2.76	1.70	0.16	N/A	67.13	31.88	0.99	99.99
	Plagioclase 22	55.29	27.86	14.21	0.91	0.84	0.40	0.49	N/A	86.43	10.02	3.55	100.00
	Plagioclase 23	56.47	27.74	14.36	0.55	0.43	N/A	0.46	N/A	90.30	6.26	3.44	100.01
	Plagioclase 24	55.92	28.17	14.18	1.03	0.39	N/A	0.30	N/A	86.46	11.36	2.18	99.99
	Plagioclase 25	54.07	28.33	14.19	0.79	1.80	0.47	0.36	N/A	88.42	8.91	2.67	100.01
Site 9	Plagioclase 5	54.26	28.19	11.09	5.09	1.02	N/A	0.34	N/A	53.56	44.49	1.96	99.99
	Plagioclase 6	61.06	24.41	5.71	7.66	0.49	N/A	0.67	N/A	28.03	68.05	3.92	100.00
	Plagioclase 7	57.29	25.89	8.64	5.99	1.40	0.37	0.42	N/A	43.24	54.25	2.50	100.00
	Plagioclase 8	54.90	27.67	13.54	0.85	1.64	0.93	0.46	N/A	86.65	9.84	3.51	99.99
	Plagioclase 9	56.75	27.27	14.52	0.65	0.30	N/A	0.56	N/A	88.74	7.19	4.07	100.05
	Plagioclase 10	55.50	27.60	14.09	1.08	0.85	0.22	0.65	N/A	83.78	11.62	4.60	99.99
	Standard Deviation	2.43	1.42	2.42	2.30	0.56	0.47	0.15	N/A				
	Average	54.94	27.88	11.86	3.73	0.97	0.45	0.36	0.30				

e) – Graph displaying the geochemical data for mid-plagioclase in ESA01-A

New Mexico												
Data in Wt % Oxide		SiO_2	Al_2O_3	CaO	Na_2O	FeO	MgO	K_2O	An	Ab	Or	Total
LAM	Plagioclase 1	52.18	28.86	11.26	5.20	1.37	0.73	0.40	53.25	44.50	2.25	100.00
	Plagioclase 2	56.52	27.27	10.23	4.19	1.17	0.17	0.44	55.79	41.35	2.86	99.99
	Plagioclase 3	52.26	29.53	11.71	5.00	0.77	0.37	0.36	55.27	42.71	2.02	100.00
	Plagioclase 4	53.55	28.44	12.14	4.31	0.77	0.49	0.30	59.81	38.43	1.76	100.00
	Plagioclase 5	53.55	28.93	12.23	4.24	0.51	0.25	0.30	60.37	37.87	1.76	100.01
	Plagioclase 6	54.72	28.52	11.00	4.01	0.91	0.22	0.62	57.91	38.20	3.89	100.00
	Plagioclase 7	53.50	28.76	12.57	4.05	0.69	N/A	0.44	61.55	35.89	2.57	100.01
	Plagioclase 8	53.62	28.46	12.80	3.73	0.97	0.14	0.27	64.41	33.97	1.62	99.99
	Plagioclase 9	52.72	29.64	12.21	4.12	0.93	N/A	0.37	60.73	37.08	2.19	99.99
	Plagioclase 10	52.50	28.87	12.43	4.19	1.15	0.39	0.46	60.46	36.88	2.66	99.99
	Plagioclase 11	53.59	28.98	12.18	4.62	0.32	N/A	0.32	58.22	39.96	1.82	100.01
	Plagioclase 12	52.40	30.00	11.53	4.92	0.68	N/A	0.47	54.92	42.41	2.67	100.00
	Plagioclase 13	53.97	28.16	12.08	4.32	0.74	0.41	0.32	59.57	38.55	1.88	100.00
	Plagioclase 14	52.79	28.92	12.36	4.54	0.94	0.16	0.29	57.10	41.30	1.60	100.00
	Plagioclase 15	53.23	29.47	12.25	4.08	0.57	N/A	0.41	60.88	36.69	2.43	100.01
	Plagioclase 16	53.80	27.95	11.77	4.80	1.23	0.22	0.23	56.78	41.90	1.32	100.00
	Plagioclase 17	54.65	27.54	11.57	4.61	1.16	N/A	0.47	56.52	40.75	2.73	100.00
	Plagioclase 18	52.97	29.16	12.13	4.36	0.80	0.15	0.42	59.11	38.45	2.44	99.99
	Plagioclase 19	53.83	28.83	12.74	4.05	0.22	0.25	0.09	63.14	36.32	0.53	100.01
	Plagioclase 20	52.24	29.57	12.57	4.92	0.33	N/A	0.37	57.36	40.63	2.01	100.00
	Plagioclase 21	52.53	29.66	12.07	4.58	0.71	N/A	0.46	57.74	39.64	2.62	100.01
	Plagioclase 22	52.30	29.39	13.16	3.87	0.83	0.30	0.14	64.73	34.45	0.82	99.99
	Plagioclase 23	53.43	29.37	12.19	4.34	0.38	N/A	0.28	59.82	38.54	1.64	99.99
	Plagioclase 24	53.63	28.79	11.66	4.38	0.74	0.36	0.46	57.91	39.37	2.72	100.02
	Plagioclase 25	53.38	28.73	12.31	4.35	0.72	0.15	0.35	59.76	38.22	2.02	99.99
	Plagioclase 26	53.45	28.78	12.04	4.89	0.57	N/A	0.27	56.76	41.72	1.52	100.00

	Plagioclase 27	53.04	18.89	11.52	4.04	9.90	1.64	0.98	57.61	36.56	5.83	100.01
Site 3	Plagioclase 1	53.89	29.19	11.32	4.54	0.70	N/A	0.36	56.70	41.15	2.15	100.00
	Plagioclase 2	53.70	29.13	11.68	4.59	0.60	N/A	0.31	57.38	40.81	1.81	100.01
	Plagioclase 3	53.95	29.03	11.79	4.16	0.62	0.13	0.32	59.85	38.22	1.93	100.00
	Plagioclase 4	54.66	28.13	10.87	5.09	0.76	0.12	0.37	52.97	44.88	2.15	100.00
	Plagioclase 5	53.65	29.16	11.84	4.35	0.76	N/A	0.24	59.21	39.36	1.43	100.00
	Plagioclase 6	59.47	22.99	7.93	5.93	2.13	0.41	1.13	39.64	52.64	6.73	99.99
	Plagioclase 7	59.37	23.82	7.81	6.04	1.62	0.32	1.02	39.14	54.68	6.09	100.00
	Plagioclase 8	55.51	27.57	10.33	5.09	0.93	0.21	0.36	51.73	46.13	2.15	100.00
	Plagioclase 9	54.54	28.78	11.03	4.71	0.58	0.11	0.25	55.56	42.94	1.50	100.00
	Plagioclase 10	53.93	28.89	11.33	4.57	0.84	0.13	0.31	56.74	41.41	0.85	100.00
	Plagioclase 11	53.56	29.05	11.45	4.60	0.82	0.12	0.35	56.71	41.23	2.60	99.95
	Plagioclase 12	56.14	27.22	9.30	5.53	1.11	0.24	0.47	46.81	50.37	2.82	100.01
	Plagioclase 13	53.43	29.44	11.80	4.34	0.61	0.10	0.28	59.04	39.29	1.67	100.00
	Plagioclase 14	53.99	29.23	10.32	5.42	0.60	0.09	0.34	50.27	47.77	1.97	99.99
	Plagioclase 15	53.69	29.11	11.63	4.43	0.76	0.13	0.26	58.28	40.17	1.55	100.01
	Plagioclase 16	56.15	26.15	11.04	4.71	0.98	0.48	0.50	54.77	42.28	2.95	100.01
Site 4	Plagioclase 1	58.13	25.10	8.05	6.16	1.67	0.18	0.70	50.19	55.65	4.16	99.99
	Plagioclase 2	56.85	26.39	9.38	5.61	1.04	0.20	0.53	46.52	50.35	3.13	100.00
	Plagioclase 3	59.58	18.54	8.44	6.06	5.01	0.69	1.67	39.45	51.26	9.29	99.99
	Plagioclase 4	58.26	22.28	8.97	5.86	2.99	0.60	1.04	43.10	50.95	5.95	100.00
Site 6	Plagioclase 1	54.60	28.18	10.94	4.85	0.89	0.23	0.31	54.47	43.70	1.84	100.00
	Plagioclase 2	53.89	28.68	11.22	4.83	0.97	0.18	0.23	55.45	43.20	1.35	100.00
	Plagioclase 3	53.20	29.11	12.44	4.00	0.79	0.15	0.29	62.13	36.15	1.72	99.98
	Plagioclase 4	53.62	29.10	11.39	4.54	0.91	0.10	0.34	56.92	41.06	2.02	100.00
	Plagioclase 5	53.35	29.21	11.72	4.45	0.77	0.18	0.33	58.12	39.93	1.95	100.01
	Standard Deviation	1.87	2.69	1.28	0.60	1.43	N/A	0.28				
	Average	54.26	27.77	11.32	4.68	1.15	N/A	0.43				

f) – Graph displaying the geochemical data for plagioclase in New Mexico

NWA7397												
Data in Wt % Oxide			**SiO_2**	**Al_2O_3**	**CaO**	**Na_2O**	**FeO**	**MgO**	**K_2O**	An	Ab	Or	Total
Grain 1	**Site 1**	Plagioclase 1	55.88	27.87	10.30	5.08	0.51	N/A	0.36	51.70	46.15	2.15	100.00
		Plagioclase 2	54.80	28.48	10.66	4.93	0.55	0.20	0.38	53.21	44.53	2.26	100.00
		Plagioclase 3	55.01	28.26	11.10	4.70	0.47	N/A	0.45	55.11	42.23	2.66	99.99
		Plagioclase 4	57.18	26.83	9.21	5.61	0.43	0.10	0.65	45.74	50.42	3.84	100.01
	Site 2	Plagioclase 1	55.84	27.54	10.14	5.07	0.79	N/A	0.62	50.57	45.75	3.68	100.00
		Plagioclase 2	54.15	28.64	11.83	4.39	0.54	N/A	0.44	58.28	39.14	2.58	99.99
		Plagioclase 3	54.08	28.51	11.66	4.71	0.55	N/A	0.50	56.12	41.02	2.87	100.01
		Plagioclase 4	55.95	27.31	10.39	5.16	0.57	N/A	0.61	50.80	45.65	3.55	99.99
		Plagioclase 5	57.28	27.30	8.47	5.81	0.48	0.11	0.56	43.10	53.05	3.39	100.01
		Plagioclase 6	54.71	28.85	10.42	5.01	0.55	N/A	0.46	52.01	45.25	2.73	100.00
		Plagioclase 7	60.41	24.42	6.91	6.44	0.59	N/A	1.22	34.52	58.22	7.26	99.99
		Plagioclase 8	58.69	26.18	7.13	7.01	0.44	N/A	0.56	34.81	61.93	3.26	100.01
Grain 2	**Site 1**	Plagioclase 1	54.87	28.12	11.26	4.81	0.52	N/A	0.42	55.02	42.53	2.44	100.00
		Plagioclase 2	54.17	27.21	11.24	4.20	2.13	0.68	0.37	58.30	39.42	2.28	100.00
		Plagioclase 3	54.42	28.46	11.59	4.52	0.55	0.12	0.34	57.45	40.54	2.01	100.00
		Plagioclase 4	54.16	28.49	11.90	4.51	0.63	N/A	0.32	58.21	39.92	1.86	100.01
		Plagioclase 5	54.46	28.28	11.77	4.52	0.60	N/A	0.36	57.76	40.14	2.10	99.99
	Site 2	Plagioclase 1	54.61	28.37	11.50	4.49	0.60	N/A	0.44	57.07	40.33	2.60	100.01
		Plagioclase 2	54.23	28.55	11.65	4.41	0.72	0.08	0.36	58.08	39.78	2.14	100.00
		Standard Deviation	1.74	1.08	1.53	0.73	0.37	N/A	0.20				
		Average	55.52	27.77	10.48	5.02	0.64	0.22	0.50				

g) – Graph displaying the geochemical data for plagioclase in NWA7397

NWA1110												
Data in Wt % Oxide		SiO_2	Al_2O_3	CaO	Na_2O	FeO	MgO	K_2O	An	Ab	Or	Total
Site 1	Plagioclase1	55.21	27.05	11.42	4.75	1.03	0.41	0.13	56.62	42.62	0.77	100.00
	Plagioclase 2	55.87	25.72	9.35	6.25	2.46	N/A	0.35	44.36	53.66	1.98	100.00
	Plagioclase 3	55.34	26.37	11.32	5.06	1.03	0.45	0.44	53.90	43.60	2.49	100.01
	Plagioclase 4	56.16	26.17	10.12	4.79	1.80	0.76	0.21	53.16	45.53	1.31	100.01
	Plagioclase 5	54.17	26.25	10.81	4.67	2.35	0.78	0.97	52.95	41.39	5.66	100.00
Site 2	Plagioclase 1	55.98	26.67	11.17	4.06	1.87	N/A	0.25	59.37	39.05	1.58	100.00
	Plagioclase 2	56.24	25.97	10.00	5.26	1.02	0.78	0.72	49.08	46.72	4.21	99.99
	Plagioclase 3	55.92	27.24	10.47	4.20	1.60	0.47	0.10	57.56	41.78	0.65	100.00
	Plagioclase 4	56.50	26.36	10.05	4.91	1.65	0.44	0.08	52.81	46.69	0.50	99.99
	Plagioclase 5	56.79	25.33	10.27	4.70	2.20	0.72	N/A	54.70	45.30	0.00	100.01
	Plagioclase 6	53.99	27.93	10.82	4.99	1.45	0.44	0.37	53.33	44.50	2.17	99.99
	Plagioclase 7	54.47	26.89	11.64	4.89	1.64	N/A	0.46	55.33	42.06	2.60	99.99
	Plagioclase 8	57.84	26.80	8.95	5.67	N/A	N/A	0.74	44.55	51.07	4.39	100.00
	Plagioclase 9	58.13	25.74	7.92	6.21	1.17	N/A	0.83	39.31	55.78	4.91	100.00
	Plagioclase 10	55.67	26.68	11.70	4.69	0.66	0.48	0.11	56.45	42.91	0.64	99.99
	Plagioclase 11	55.52	27.04	10.90	4.87	1.17	0.33	0.16	54.76	44.23	0.96	99.99
	Plagioclase 12	56.67	26.54	10.38	4.03	1.38	0.33	0.67	56.20	39.48	4.32	100.00
Site 3	Plagioclase 1	57.69	25.28	10.03	5.47	0.79	0.15	0.59	48.62	47.08	3.40	100.00
	Plagioclase 2	53.75	29.01	10.41	4.88	0.69	0.49	0.78	51.61	43.78	4.60	100.01
	Plagioclase 3	56.05	25.79	11.32	5.34	1.02	0.27	0.21	53.31	45.51	1.18	100.00
	Plagioclase 4	54.97	27.05	11.10	4.97	0.88	0.39	0.65	53.19	43.10	3.71	100.01
	Plagioclase 5	54.12	27.84	11.73	4.92	1.20	0.20	N/A	56.85	43.15	0.00	100.01
	Plagioclase 6	57.20	25.90	10.88	4.55	0.73	N/A	0.74	54.41	41.18	4.41	100.00
	Plagioclase 7	54.71	25.08	13.10	5.34	1.42	0.09	0.26	56.78	41.88	1.34	100.00
	Plagioclase 8	54.28	27.67	10.76	5.62	1.11	N/A	0.55	29.85	47.12	3.03	99.99
	Plagioclase 9	55.07	28.65	10.34	4.90	0.28	N/A	0.76	51.41	44.09	4.50	100.00

	Plagioclase 10	53.43	27.41	9.19	7.00	2.11	0.40	0.46	41.02	56.54	2.44	100.00
Site 4	Plagioclase 1	56.50	27.04	10.05	4.84	1.01	0.45	N/A	53.43	46.57	0.00	99.89
	Plagioclase 2	55.72	27.19	11.66	4.19	0.81	N/A	0.42	59.06	38.41	2.53	99.99
	Plagioclase 3	54.23	26.08	12.47	3.95	2.07	0.59	0.61	61.29	35.14	3.57	100.00
	Plagioclase 4	54.47	27.44	11.07	5.76	1.10	N/A	0.16	51.05	48.07	0.88	100.00
	Plagioclase 5	57.34	27.16	10.06	3.45	0.52	0.77	0.70	58.70	36.43	4.86	100.00
	Plagioclase 6	56.14	26.26	10.21	4.63	1.72	0.26	0.78	52.31	42.93	4.76	100.00
	Plagioclase 7	54.79	27.20	9.99	4.90	2.36	0.62	0.13	52.55	46.64	0.81	99.99
Site 5	Plagioclase 1	56.61	25.48	11.20	5.17	0.42	0.52	0.59	52.69	44.01	3.30	99.99
	Plagioclase 2	54.03	27.73	11.58	5.74	0.91	N/A	N/A	52.71	47.29	0.00	99.99
	Plagioclase 3	55.17	25.52	11.29	6.52	0.83	N/A	0.67	47.27	49.40	3.34	100.00
	Plagioclase 4	55.67	25.41	10.54	4.77	2.90	0.58	0.13	54.54	44.66	0.80	100.00
	Plagioclase 5	57.36	24.17	9.50	3.90	2.86	1.98	0.22	56.48	41.96	1.56	99.99
	Plagioclase 6	55.79	24.88	10.14	3.95	2.98	1.88	0.39	57.12	40.27	2.62	100.01
	Plagioclase 7	52.44	25.93	13.43	4.36	3.20	0.37	0.28	62.02	36.44	1.54	100.01
	Plagioclase 8	56.79	25.14	9.94	5.76	1.08	0.75	0.54	47.32	49.62	3.06	100.00
	Plagioclase 9	55.08	27.31	11.52	4.24	1.48	0.37	N/A	60.02	39.98	0.00	100.00
	Plagioclase 10	53.85	27.02	10.93	5.19	1.30	0.56	0.16	53.28	45.79	0.93	99.01
	Plagioclase 11	55.58	27.20	10.31	5.38	0.67	0.34	0.51	49.92	47.14	2.94	99.99
	Plagioclase 12	54.17	27.90	11.36	5.30	0.86	N/A	0.41	52.99	44.74	2.28	100.00
	Plagioclase 13	54.59	28.73	10.59	4.60	1.08	N/A	0.41	54.58	42.90	2.52	100.00
	Plagioclase 14	57.77	25.62	11.15	3.84	1.21	0.12	0.28	60.49	37.70	1.81	99.99
	Plagioclase 15	54.16	29.86	9.62	5.87	0.38	N/A	0.11	47.22	52.14	0.64	100.00
	Plagioclase 16	54.14	27.41	10.83	6.17	0.95	N/A	0.51	47.91	49.40	2.69	100.01
	Plagioclase 17	53.69	27.62	11.10	4.24	1.53	0.67	1.15	55.11	38.09	6.80	100.00
	Standard Deviation	1.32	1.13	0.97	0.74	N/A	N/A	N/A				
	Average	55.45	26.70	10.72	4.97	1.38	0.55	0.45				

h) – Graph displaying the geochemical data for plagioclase in NWA1110

Tissint												
Data in Wt % Oxide		SiO_2	Al_2O_3	CaO	Na_2O	FeO	MgO	K_2O	An	Ab	Or	Total
Site 1	Plagioclase 1	52.43	29.69	13.05	3.88	0.74	0.21	N/A	65.02	34.98	0.00	100.00
	Plagioclase 2	53.34	29.25	12.37	4.23	0.54	0.17	0.10	61.41	38.00	0.59	100.00
	Plagioclase 3	52.11	29.99	13.10	3.73	0.81	0.18	0.08	65.68	33.84	0.48	100.00
	Plagioclase 4	53.21	29.08	12.47	4.15	0.85	0.18	0.07	62.15	37.43	0.42	100.01
	Plagioclase 5	53.52	29.28	12.05	4.15	0.69	0.12	0.19	60.90	37.96	1.14	100.00
Site 2	Plagioclase 1	52.12	30.06	13.41	3.62	0.79	N/A	N/A	67.18	32.82	0.00	100.00
	Plagioclase 2	52.51	29.76	12.73	4.09	0.77	0.14	N/A	63.23	36.77	0.00	100.00
	Plagioclase 3	52.34	29.57	12.94	3.93	0.91	0.26	0.06	64.30	35.34	0.36	100.01
	Plagioclase 4	53.03	29.45	12.34	4.24	0.67	0.10	0.17	61.04	37.96	1.00	100.00
	Plagioclase 5	53.08	29.13	12.57	4.07	0.91	0.17	0.07	62.79	36.79	0.42	100.00
Site 4	Plagioclase 1	52.33	28.91	13.06	3.96	1.56	0.12	0.07	64.30	35.28	0.41	100.01
	Plagioclase 2	52.63	29.35	13.23	3.70	0.72	0.26	0.12	65.92	33.36	0.71	100.01
	Plagioclase 3	51.89	28.74	12.71	3.92	2.35	0.21	0.18	63.49	35.44	1.07	100.00
	Plagioclase 4	52.37	29.01	12.60	4.18	1.44	0.23	0.16	61.90	37.16	0.94	99.99
	Plagioclase 5	53.21	28.21	12.96	4.28	0.93	0.19	0.23	61.78	36.92	1.31	100.01
	Plagioclase 6	53.78	28.75	12.22	4.27	0.54	0.21	0.23	60.43	38.21	1.35	100.00
	Plagioclase 7	51.67	30.17	13.02	3.75	0.93	0.45	N/A	65.74	34.26	0.00	99.99
	Plagioclase 8	50.96	28.78	12.27	3.97	3.71	0.21	0.10	62.69	36.70	0.61	100.00
	Plagioclase 9	52.58	29.03	12.88	3.95	1.06	0.32	0.18	63.63	35.31	1.06	100.00
	Plagioclase 10	52.13	29.28	13.00	3.94	1.41	0.24	N/A	64.58	35.42	0.00	100.00
Site 5	Plagioclase 1	52.05	29.40	13.19	3.86	1.50	0.23	0.14	64.84	34.34	0.82	100.37
	Plagioclase 2	52.86	29.34	12.82	3.99	0.65	0.20	0.15	63.41	35.71	0.88	100.01
	Plagioclase 3	51.25	29.57	12.87	4.05	1.85	0.30	0.11	63.31	36.05	0.64	100.00
	Plagioclase 4	52.63	27.98	12.06	3.89	2.25	0.94	0.24	62.21	36.31	1.47	99.99
	Plagioclase 5	53.43	28.86	12.26	4.38	0.62	0.13	0.31	59.64	38.56	1.80	99.99

	Plagioclase 6	52.18	30.10	13.35	3.40	0.70	0.27	N/A	68.45	31.55	0.00	100.00
	Plagioclase 7	53.29	28.84	12.15	4.41	1.04	0.16	0.12	59.93	39.36	0.70	100.01
	Plagioclase 8	51.79	29.94	13.53	3.35	1.07	0.13	0.18	68.31	30.61	1.08	99.99
	Plagioclase 9	52.77	29.21	12.87	3.89	0.94	0.33	N/A	64.64	35.36	0.00	100.01
	Plagioclase 10	52.38	29.27	13.21	4.16	0.76	0.09	0.14	63.19	36.01	0.80	100.01
	Plagioclase 11	51.83	29.51	12.99	3.84	1.67	0.15	N/A	65.15	34.85	0.00	99.99
	Plagioclase 12	51.68	30.49	13.29	3.39	0.89	0.17	0.08	68.08	31.43	0.49	99.99
	Plagioclase 13	52.91	29.24	12.92	3.98	0.63	0.32	N/A	64.21	35.79	0.00	100.00
	Plagioclase 14	53.16	28.82	12.90	4.09	0.77	0.09	0.17	62.92	36.10	0.99	100.00
	Plagioclase 15	52.64	29.61	13.14	3.45	0.91	0.12	0.13	67.25	31.95	0.79	100.00
	Plagioclase 16	53.09	29.55	12.28	4.14	0.75	N/A	0.19	61.41	37.46	1.13	100.00
	Plagioclase 17	52.20	29.19	13.37	3.51	1.30	0.43	N/A	67.79	32.21	0.00	100.00
	Plagioclase 18	52.80	28.95	13.36	3.70	0.76	0.28	0.13	66.10	33.13	0.77	99.98
	Plagioclase 19	52.25	28.90	13.25	4.01	1.20	0.23	0.16	64.02	35.06	0.92	100.00
	Plagioclase 20	52.81	29.13	13.35	3.73	0.77	0.21	N/A	66.42	33.58	0.00	100.00
	Standard Deviation	0.63	0.51	0.42	0.27	N/A	N/A	N/A				
	Average	52.53	29.28	12.85	3.93	1.08	0.23	0.15				

i) – Graph displaying the geochemical data for plagioclase in Tissint

NWA3160												
Data in Wt % Oxide		SiO_2	Al_2O_3	CaO	Na_2O	FeO	MgO	K_2O	An	Ab	Or	Total
LAM	Plagioclase 1	47.56	34.77	17.26	N/A	0.41	N/A	N/A	100.00	0.00	0.00	100.00
	Plagioclase 2	64.36	20.76	1.74	N/A	0.27	0.13	12.74	10.29	0.00	89.71	100.00
	Plagioclase 3	46.32	34.84	17.72	N/A	0.88	0.15	0.09	99.40	0.00	0.60	100.00
	Plagioclase 4	44.75	36.85	17.85	N/A	0.48	N/A	0.06	99.60	0.00	0.40	99.99
	Plagioclase 5	47.70	33.93	17.07	N/A	1.14	0.17	N/A	100.00	0.00	0.00	100.01
	Plagioclase 6	47.26	34.83	16.64	N/A	0.99	0.29	N/A	100.00	0.00	0.00	100.01
	Plagioclase 7	47.68	34.59	17.08	N/A	0.17	0.41	0.08	99.45	0.00	0.55	100.01
	Plagioclase 8	46.07	35.22	17.62	N/A	0.49	0.50	0.10	99.33	0.00	0.67	100.00
	Plagioclase 9	44.26	35.33	19.31	N/A	1.02	N/A	0.09	99.45	0.00	0.55	100.01
	Plagioclase 10	45.03	35.65	19.09	N/A	0.23	N/A	N/A	100.00	0.00	0.00	100.00
	Plagioclase 11	46.68	34.47	17.26	N/A	1.10	0.35	0.13	99.11	0.00	0.89	99.99
	Plagioclase 12	47.61	34.55	17.11	N/A	0.63	N/A	0.11	99.24	0.00	0.76	100.01
	Plagioclase 13	49.90	34.38	15.09	N/A	0.22	0.41	N/A	100.00	0.00	0.00	100.00
	Plagioclase 14	47.53	33.85	16.51	N/A	1.50	0.53	0.08	99.43	0.00	0.57	100.00
	Plagioclase 15	43.74	36.66	18.85	N/A	0.74	N/A	N/A	100.00	0.00	0.00	99.99
	Plagioclase 16	46.00	35.19	17.94	N/A	0.45	0.27	0.15	99.01	0.00	0.99	100.00
	Plagioclase 17	47.99	33.64	17.05	N/A	0.57	0.30	0.46	96.89	0.00	3.11	100.01
	Plagioclase 18	44.53	36.49	18.34	N/A	0.26	0.38	N/A	100.00	0.00	0.00	100.00
	Plagioclase 19	45.76	36.00	17.55	N/A	0.57	N/A	0.11	99.26	0.00	0.74	99.99
	Plagioclase 20	48.30	33.94	16.99	N/A	0.40	0.26	0.11	99.24	0.00	0.76	100.00
	Plagioclase 21	47.11	34.24	17.25	N/A	0.40	0.35	0.65	95.71	0.00	4.29	100.00
	Plagioclase 22	48.08	34.67	16.21	N/A	0.81	N/A	0.22	98.41	0.00	1.59	99.99
	Plagioclase 23	44.91	35.55	18.53	N/A	0.78	0.24	N/A	100.00	0.00	0.00	100.01
	Plagioclase 24	46.82	34.62	17.24	N/A	0.50	0.58	0.23	98.44	0.00	1.56	99.99
	Plagioclase 25	44.87	35.30	19.24	N/A	0.40	N/A	0.19	98.84	0.00	1.16	100.00
	Plagioclase 26	46.57	34.55	17.90	N/A	0.44	0.44	0.09	99.40	0.00	0.60	99.99

	Plagioclase 27	45.37	36.08	17.65	N/A	0.57	0.32	N/A	100.00	0.00	0.00	99.99
	Plagioclase 28	46.17	35.32	17.98	N/A	0.38	0.14	N/A	100.00	0.00	0.00	99.99
	Plagioclase 29	45.13	35.40	18.77	N/A	0.45	0.12	0.13	99.18	0.00	0.82	100.00
	Plagioclase 30	51.96	31.43	15.17	N/A	0.57	0.87	N/A	100.00	0.00	0.00	100.00
	Plagioclase 31	66.18	21.10	N/A	N/A	0.12	N/A	12.60	0.00	0.00	100.00	100.00
	Plagioclase 32	76.42	13.93	N/A	N/A	0.82	0.58	8.35	0.00	0.00	100.00	100.10
Site 1	Plagioclase 1	47.41	34.23	17.80	N/A	0.18	N/A	0.38	97.52	0.00	2.48	100.00
	Plagioclase 2	44.64	35.09	17.98	N/A	1.03	0.97	0.29	98.12	0.00	1.88	100.00
	Plagioclase 3	47.21	33.26	19.38	N/A	N/A	N/A	0.15	99.09	0.00	0.91	100.00
Site 2	Plagioclase 1	45.94	34.14	17.79	1.08	0.48	0.00	0.37	88.14	9.68	2.18	99.80
	Plagioclase 2	47.09	34.64	16.25	0.97	0.68	0.30	0.07	89.84	9.70	0.46	100.00
	Plagioclase 3	46.27	35.40	16.94	0.78	0.47	0.13	N/A	92.31	7.69	0.00	99.99
	Plagioclase 4	44.63	36.40	18.52	N/A	0.45	N/A	N/A	100.00	0.00	0.00	100.00
Site 3	Plagioclase 1	49.37	32.70	15.34	1.50	0.87	0.10	0.13	84.24	14.91	0.85	100.01
	Plagioclase 2	45.94	35.21	18.00	N/A	0.46	0.23	0.16	98.95	0.00	1.05	100.00
	Plagioclase 3	46.29	35.68	17.08	N/A	0.69	0.26	N/A	100.00	0.00	0.00	100.00
	Plagioclase 4	47.19	34.32	15.35	1.37	1.25	0.33	0.20	84.96	13.72	1.32	100.01
	Plagioclase 5	45.56	35.32	18.23	N/A	0.59	0.22	0.08	99.48	0.00	0.52	100.00
	Plagioclase 6	48.74	32.71	15.50	1.40	1.33	N/A	0.31	84.23	13.77	2.01	99.99
	Plagioclase 7	48.34	32.99	15.65	1.48	0.95	0.43	0.16	84.51	14.46	1.03	100.00
	Plagioclase 8	46.02	35.17	17.49	N/A	0.93	0.30	0.10	99.32	0.00	0.68	100.01
Site 6	Plagioclase 1	45.60	35.60	17.04	N/A	1.10	0.42	0.24	98.35	0.00	1.65	100.00
	Plagioclase 2	47.96	33.64	15.23	N/A	1.14	1.27	0.75	94.46	0.00	5.54	99.99
	Plagioclase 3	64.99	21.02	N/A	N/A	0.26	0.51	13.22	0.00	0.00	100.00	100.00
	Plagioclase 4	64.85	24.89	N/A	N/A	0.54	N/A	9.72	0.00	0.00	100.00	100.00
	Plagioclase 5	46.70	35.07	16.56	N/A	1.05	N/A	0.63	95.67	0.00	4.33	100.01
	Plagioclase 6	47.75	34.62	14.99	1.76	0.56	N/A	0.31	80.83	17.17	1.99	99.99
	Plagioclase 7	65.33	20.46	N/A	N/A	0.76	N/A	13.45	0.00	0.00	100.00	100.00

Site 7	Plagioclase 1	46.87	34.51	17.48	N/A	0.58	0.46	0.10	99.32	0.00	0.68	100.00
	Plagioclase 2	47.67	35.15	16.32	N/A	0.41	0.30	0.14	98.99	0.00	1.01	99.99
Site 8	Plagioclase 1	45.25	35.04	17.99	N/A	0.70	0.73	0.29	98.12	0.00	1.88	100.00
	Plagioclase 2	49.18	32.89	16.56	N/A	0.92	0.45	N/A	100.00	0.00	0.00	100.00
	Plagioclase 3	45.22	35.56	18.04	N/A	0.62	0.35	0.20	98.70	0.00	1.30	99.99
	Plagioclase 4	45.41	36.54	17.08	N/A	0.45	N/A	0.51	96.57	0.00	3.43	99.99
	Plagioclase 5	43.20	34.64	20.88	N/A	0.97	0.30	N/A	100.00	0.00	0.00	99.99
	Plagioclase 6	45.05	37.76	15.96	N/A	N/A	0.87	0.36	97.38	0.00	2.62	100.00
	Standard Deviation	6.43	4.56	2.39	0.32	N/A	N/A	3.97				
	Average	48.55	33.43	17.04	1.29	0.65	0.39	1.72				

j) – Graph displaying the geochemical data for plagioclase in NWA3160

NWA3160 Basalt Clast									
Data in Wt% Oxide		Na2O	Al2O3	SiO2	CaO	FeO	Total	Ab	An
Site 1	Spectrum 2	1.11	33.78	47.03	18.08	N/A	100.00	5.78	94.22
	Spectrum 3	N/A	35.08	45.86	19.06	N/A	100.00	0.00	100.00
	Spectrum 4	N/A	35.51	45.25	19.24	N/A	100.00	0.00	100.00
	Spectrum 7	0.78	34.66	45.49	19.08	N/A	100.01	3.93	96.07
	Spectrum 13	N/A	19.12	71.61	9.27	N/A	100.00	0.00	100.00
	Spectrum 14	N/A	34.23	45.82	19.95	N/A	100.00	0.00	100.00
Site 2	Spectrum 23	1.29	34.47	47.99	16.25	N/A	100.00	7.35	92.65
	Spectrum 24	N/A	34.77	45.78	19.45	N/A	100.00	0.00	100.00
	Spectrum 25	N/A	34.51	46.55	18.94	N/A	100.00	0.00	100.00
	Spectrum 26	N/A	35.66	42.88	21.46	N/A	100.00	0.00	100.00
	Spectrum 27	N/A	36.02	44.43	19.55	N/A	100.00	0.00	100.00
	Spectrum 28	1.59	32.60	46.96	18.85	N/A	100.00	7.78	92.22
	Spectrum 32	1.31	34.09	47.29	17.32	N/A	100.01	7.03	92.97
	Spectrum 35	1.68	31.47	51.6	14.23	1.03	100.01	10.56	89.44
Site 3	Spectrum 38	1.34	29.98	49.76	16.85	2.08	100.01	7.37	92.63
	Spectrum 41	1.21	31.49	49.61	16.33	1.37	100.01	6.90	93.10
	Spectrum 44	1.40	30.90	50.47	15.73	1.50	100.00	8.17	91.83
	Spectrum 47	1.15	32.25	49.18	15.85	1.58	100.01	6.76	93.24
	Spectrum 48	1.23	30.26	50.80	16.19	1.51	99.99	7.06	92.94

	Spectrum 51	1.41	30.01	50.88	16.22	1.47	99.99	8.00	92.00
Site 4	Spectrum 58	N/A	34.8	46.61	18.58	N/A	99.99	0.00	100.00
	Spectrum 59	1.30	34.06	46.06	18.59	N/A	100.01	6.54	93.46
	Spectrum 60	N/A	36.83	44.27	18.89	N/A	99.99	0.00	100.00
	Spectrum 63	0.80	23.66	62.76	11.19	1.59	100.00	6.67	93.33
	Spectrum 69	N/A	35.79	45.13	19.08	N/A	100.00	0.00	100.00
	Standard Deviation	0.25	3.98	6.13	2.73	0.77			
	Average	1.26	32.64	48.80	17.37	0.58			

k) - Graph displaying the geochemical data for plagioclase in NWA3160 Basalt Clast

NWA11444												
Data in Wt % Oxide		SiO_2	Al_2O_3	CaO	Na_2O	FeO	MgO	K_2O	An	Ab	Or	Total
Site 1	Plagioclase 1	43.32	36.29	19.88	N/A	0.38	0.13	N/A	100.00	0.00	0.00	100.00
	Plagioclase 2	44.29	36.62	18.74	N/A	0.35	N/A	N/A	100.00	0.00	0.00	100.00
	Plagioclase 3	44.15	35.80	19.32	N/A	0.55	0.09	0.09	99.45	0.00	0.55	100.00
	Plagioclase 4	43.84	35.85	19.49	N/A	0.65	0.11	0.07	99.57	0.00	0.43	100.01
	Plagioclase 5	43.77	36.44	19.39	N/A	0.40	N/A	N/A	100.00	0.00	0.00	100.00
	Plagioclase 6	43.79	35.50	19.85	N/A	0.48	0.23	0.14	99.17	0.00	0.83	99.99
	Plagioclase 7	44.25	35.91	18.67	N/A	0.60	0.37	0.21	98.68	0.00	1.32	100.01
	Plagioclase 8	43.88	36.11	19.61	N/A	0.40	N/A	N/A	100.00	0.00	0.00	100.00
	Plagioclase 9	43.61	36.37	19.94	N/A	N/A	N/A	0.08	99.52	0.00	0.48	100.00
	Plagioclase 10	42.76	37.17	19.59	N/A	0.36	N/A	0.12	99.29	0.00	0.71	100.00
	Plagioclase 11	43.66	36.33	19.49	N/A	0.52	N/A	N/A	100.00	0.00	0.00	100.00
	Plagioclase 12	43.69	36.63	19.09	N/A	0.15	0.30	0.14	99.13	0.00	0.87	100.00
Site 2	Plagioclase 1	43.92	36.33	19.30	N/A	0.34	0.11	N/A	100.00	0.00	0.00	100.00
	Plagioclase 2	43.71	36.14	19.93	N/A	0.23	N/A	N/A	100.00	0.00	0.00	100.01
	Plagioclase 3	44.05	36.05	19.67	N/A	0.12	0.12	N/A	100.00	0.00	0.00	100.01
	Plagioclase 4	44.40	35.82	19.18	N/A	0.40	0.20	N/A	100.00	0.00	0.00	100.00
	Plagioclase 5	43.37	36.55	19.54	N/A	0.30	0.16	0.07	99.58	0.00	0.42	99.99
	Plagioclase 6	43.04	36.38	20.23	N/A	0.23	0.13	N/A	100.00	0.00	0.00	100.01
	Plagioclase 7	43.83	36.75	19.22	N/A	N/A	N/A	0.20	98.78	0.00	1.22	100.00
	Plagioclase 8	42.76	36.26	19.70	N/A	0.44	0.21	0.64	96.28	0.00	3.72	100.01
	Plagioclase 9	43.51	35.39	20.75	N/A	0.35	N/A	N/A	100.00	0.00	0.00	100.00
	Plagioclase 10	43.72	35.71	19.85	N/A	0.72	N/A	N/A	100.00	0.00	0.00	100.00
Site 3	Plagioclase 1	44.20	35.74	19.18	N/A	0.63	0.12	0.13	99.20	0.00	0.80	100.00
	Plagioclase 2	43.64	35.97	19.67	N/A	0.50	0.10	0.12	99.28	0.00	0.72	100.00
	Plagioclase 3	43.32	36.15	20.04	N/A	0.38	0.12	N/A	100.00	0.00	0.00	100.01
	Plagioclase 4	43.01	36.25	20.31	N/A	0.35	N/A	0.08	99.53	0.00	0.47	100.00

	Plagioclase 5	43.54	36.07	19.80	N/A	0.44	0.15	N/A	100.00	0.00	0.00	100.00
	Plagioclase 6	43.50	35.90	19.92	N/A	0.49	0.09	0.10	99.41	0.00	0.59	100.00
	Plagioclase 7	44.18	35.78	19.27	N/A	0.56	0.12	0.09	99.88	0.00	0.55	100.00
	Plagioclase 8	42.99	36.61	19.84	N/A	0.42	N/A	0.15	99.11	0.00	0.89	100.01
	Plagioclase 9	43.64	36.04	19.35	N/A	0.98	N/A	N/A	100.00	0.00	0.00	100.01
	Plagioclase 10	43.45	36.15	19.61	N/A	0.61	0.17	N/A	100.00	0.00	0.00	99.99
	Plagioclase 11	44.31	34.52	20.58	N/A	0.39	N/A	0.21	98.80	0.00	1.00	100.01
	Plagioclase 12	43.77	34.77	20.34	N/A	0.74	0.28	0.09	99.48	0.00	0.52	99.99
	Plagioclase 13	44.14	35.64	19.91	N/A	N/A	0.31	N/A	100.00	0.00	0.00	100.00
	Plagioclase 14	44.03	35.73	19.43	N/A	0.11	0.34	0.35	97.90	0.00	2.10	99.99
	Plagioclase 15	43.84	35.25	19.85	N/A	0.83	N/A	0.23	98.64	0.00	1.36	100.00
	Plagioclase 16	44.72	34.50	20.13	N/A	0.55	N/A	0.11	99.35	0.00	0.65	100.01
	Plagioclase 17	43.12	35.57	19.57	N/A	1.24	0.50	N/A	100.00	0.00	0.00	100.00
Site 4	Plagioclase 1	43.40	36.13	20.23	N/A	0.24	N/A	N/A	100.00	0.00	0.00	100.00
	Plagioclase 2	43.13	36.16	20.33	N/A	0.26	0.12	N/A	100.00	0.00	0.00	100.00
	Plagioclase 3	43.23	36.10	20.09	N/A	0.32	0.20	0.06	99.65	0.00	0.35	100.00
	Plagioclase 4	43.39	36.15	19.99	N/A	0.26	0.13	0.08	99.53	0.00	0.47	100.00
	Plagioclase 5	43.83	36.08	19.03	N/A	0.81	N/A	0.26	98.40	0.00	1.60	100.01
	Plagioclase 6	43.22	35.40	20.51	N/A	0.39	0.26	0.22	98.74	0.00	1.26	100.00
	Plagioclase 7	42.63	37.30	19.43	N/A	0.30	0.12	0.22	98.67	0.00	1.33	100.00
	Plagioclase 8	43.12	36.10	20.25	N/A	0.37	0.15	N/A	100.00	0.00	0.00	99.99
Site 5	Plagioclase 1	43.24	36.21	20.32	N/A	0.23	N/A	N/A	100.00	0.00	0.00	100.00
	Plagioclase 2	43.62	36.09	20.21	N/A	0.09	N/A	N/A	100.00	0.00	0.00	100.01
	Plagioclase 3	43.56	35.30	19.49	N/A	0.75	0.84	0.06	99.63	0.00	0.37	100.00
Site 7	Plagioclase 1	43.56	35.96	19.96	N/A	0.39	0.13	N/A	100.00	0.00	0.00	100.00
	Plagioclase 2	43.41	36.12	19.91	N/A	0.41	0.08	0.08	99.52	0.00	0.48	100.01
	Plagioclase 3	43.44	36.08	20.10	N/A	0.38	N/A	N/A	100.00	0.00	0.00	100.00
	Plagioclase 4	43.76	35.51	19.65	N/A	0.72	0.26	0.10	99.40	0.00	0.60	100.00

	Plagioclase 5	43.07	36.62	19.94	N/A	0.37	N/A	N/A	100.00	0.00	0.00	100.00
	Plagioclase 6	43.70	35.72	20.02	N/A	0.35	0.14	0.06	99.64	0.00	0.36	99.99
LAM	Plagioclase 1	43.68	36.01	19.94	N/A	0.27	0.10	N/A	100.00	0.00	0.00	100.00
	Plagioclase 2	43.34	36.38	19.97	N/A	0.31	N/A	N/A	100.00	0.00	0.00	100.00
	Plagioclase 3	43.80	36.15	19.70	N/A	0.28	N/A	0.07	99.58	0.00	0.42	100.00
	Plagioclase 4	43.76	35.98	19.89	N/A	0.26	0.11	N/A	100.00	0.00	0.00	100.00
	Plagioclase 5	43.57	36.17	19.92	N/A	0.24	0.10	N/A	100.00	0.00	0.00	100.00
	Plagioclase 6	43.74	36.17	19.77	N/A	0.19	0.13	N/A	100.00	0.00	0.00	100.00
	Plagioclase 7	44.04	35.86	19.61	N/A	0.37	0.11	N/A	100.00	0.00	0.00	99.99
	Plagioclase 8	43.61	36.16	20.00	N/A	0.24	N/A	N/A	100.00	0.00	0.00	100.01
	Plagioclase 9	43.20	36.15	20.24	N/A	0.31	0.10	N/A	100.00	0.00	0.00	100.00
	Plagioclase 10	43.63	35.97	20.04	N/A	0.26	0.10	N/A	100.00	0.00	0.00	100.00
	Plagioclase 11	43.68	35.98	19.97	N/A	0.25	0.11	N/A	100.00	0.00	0.00	99.99
	Plagioclase 12	43.27	35.94	20.23	N/A	0.39	0.17	N/A	100.00	0.00	0.00	100.00
	Plagioclase 13	43.92	35.79	19.65	N/A	0.44	0.14	0.06	99.64	0.00	0.36	100.00
	Plagioclase 14	43.70	36.25	19.83	N/A	0.22	N/A	N/A	100.00	0.00	0.00	100.00
	Plagioclase 15	44.38	35.20	19.55	N/A	0.55	0.24	0.08	99.52	0.00	0.48	100.00
	Plagioclase 16	43.66	35.78	19.94	N/A	0.44	0.18	N/A	100.00	0.00	0.00	100.00
	Plagioclase 17	43.62	36.08	20.12	N/A	0.18	N/A	N/A	100.00	0.00	0.00	100.00
	Plagioclase 18	43.88	35.91	20.03	N/A	0.18	N/A	N/A	100.00	0.00	0.00	100.00
	Plagioclase 19	43.67	35.93	20.09	N/A	0.16	0.15	N/A	100.00	0.00	0.00	100.00
	Plagioclase 20	43.54	35.76	20.33	N/A	0.21	0.17	N/A	100.00	0.00	0.00	100.01
	Plagioclase 21	43.58	36.24	19.96	N/A	0.21	N/A	N/A	100.00	0.00	0.00	99.99
	Plagioclase 22	43.68	36.02	19.90	N/A	0.22	0.18	N/A	100.00	0.00	0.00	100.00
	Plagioclase 23	44.22	35.55	19.54	N/A	0.50	0.13	0.07	99.58	0.00	0.42	100.01
	Plagioclase 24	45.18	34.49	19.05	N/A	0.82	0.35	0.11	99.32	0.00	0.68	100.00
	Plagioclase 25	43.79	35.37	19.82	N/A	0.79	0.13	0.10	99.40	0.00	0.60	100.00
	Plagioclase 26	43.63	35.51	20.35	N/A	0.40	0.12	N/A	100.00	0.00	0.00	100.01
	Plagioclase 27	43.74	35.58	19.53	N/A	0.67	0.25	0.22	98.68	0.00	1.32	99.99

	Plagioclase 28	44.04	35.24	19.51	N/A	0.82	0.24	0.15	99.09	0.00	0.91	100.00
	Plagioclase 29	43.46	36.29	19.58	N/A	0.57	N/A	0.10	99.40	0.00	0.60	100.00
	Plagioclase 30	43.74	35.90	19.67	N/A	0.69	N/A	N/A	100.00	0.00	0.00	100.00
	Plagioclase 31	43.75	36.30	19.41	N/A	0.42	N/A	0.12	99.27	0.00	0.73	100.00
	Plagioclase 32	43.64	36.23	19.82	N/A	0.20	0.11	N/A	100.00	0.00	0.00	100.00
	Plagioclase 33	43.47	36.33	19.84	N/A	0.26	0.10	N/A	100.00	0.00	0.00	100.00
	Plagioclase 34	43.59	36.13	19.71	N/A	0.34	0.15	0.09	99.46	0.00	0.54	100.01
	Plagioclase 35	44.08	35.73	19.65	N/A	0.33	0.13	0.07	99.58	0.00	0.42	99.99
	Plagioclase 36	43.48	36.21	19.94	N/A	0.37	N/A	N/A	100.00	0.00	0.00	100.00
	Plagioclase 37	44.33	35.61	19.92	N/A	0.14	N/A	N/A	100.00	0.00	0.00	100.00
	Plagioclase 38	43.65	36.02	19.58	N/A	0.53	0.15	0.07	99.58	0.00	0.42	100.00
	Plagioclase 39	43.70	35.94	19.66	N/A	0.61	N/A	0.09	99.46	0.00	0.54	100.00
	Plagioclase 40	44.66	34.93	19.77	N/A	0.64	N/A	N/A	100.00	0.00	0.00	100.00
	Plagioclase 41	43.42	36.29	20.08	N/A	0.11	0.11	N/A	100.00	0.00	0.00	100.01
	Plagioclase 42	43.15	35.94	19.73	N/A	0.18	N/A	N/A	100.00	0.00	0.00	99.00
	Plagioclase 43	43.74	35.81	20.10	N/A	0.22	0.13	N/A	100.00	0.00	0.00	100.00
	Plagioclase 44	43.39	35.66	20.73	N/A	0.11	0.11	N/A	100.00	0.00	0.00	100.00
	Plagioclase 45	43.41	36.60	19.80	N/A	0.08	0.11	N/A	100.00	0.00	0.00	100.00
	Plagioclase 46	43.42	36.06	20.07	N/A	0.35	N/A	0.10	99.41	0.00	0.59	100.00
	Plagioclase 47	43.32	36.39	20.15	N/A	0.14	N/A	N/A	100.00	0.00	0.00	100.00
	Plagioclase 48	43.64	36.01	20.11	N/A	0.11	0.13	N/A	100.00	0.00	0.00	100.00
	Plagioclase 49	43.96	36.00	19.87	N/A	0.17	N/A	N/A	100.00	0.00	0.00	100.00
	Plagioclase 50	43.88	35.20	19.83	N/A	0.48	0.52	0.09	99.46	0.00	0.54	100.00
	Plagioclase 51	43.79	35.91	19.84	N/A	0.13	0.33	N/A	100.00	0.00	0.00	100.00
	Plagioclase 52	43.70	35.86	20.08	N/A	0.27	0.09	N/A	100.00	0.00	0.00	100.00
	Plagioclase 53	43.64	36.03	20.11	N/A	0.09	0.14	N/A	100.00	0.00	0.00	100.01
	Plagioclase 54	43.75	35.86	20.08	N/A	0.31	N/A	N/A	100.00	0.00	0.00	100.00
	Plagioclase 55	43.74	35.92	20.04	N/A	0.15	0.16	N/A	100.00	0.00	0.00	100.01
	Plagioclase 56	43.45	35.91	20.15	N/A	0.22	0.27	N/A	100.00	0.00	0.00	100.00

	Plagioclase 57	43.75	35.98	20.11	N/A	N/A	0.09	0.06	99.65	0.00	0.35	99.99
	Plagioclase 58	43.68	36.03	20.11	N/A	N/A	0.18	N/A	100.00	0.00	0.00	100.00
	Plagioclase 59	43.98	35.78	19.84	N/A	0.14	0.18	0.08	99.52	0.00	0.48	100.00
	Plagioclase 60	43.06	36.44	20.19	N/A	0.17	0.14	N/A	100.00	0.00	0.00	100.00
	Plagioclase 61	43.28	35.74	20.34	N/A	0.57	N/A	0.07	99.59	0.00	0.41	100.00
	Plagioclase 62	43.64	36.14	19.71	N/A	0.23	0.28	N/A	100.00	0.00	0.00	100.00
	Plagioclase 63	43.30	36.22	20.17	N/A	0.19	0.13	N/A	100.00	0.00	0.00	100.01
	Plagioclase 64	43.77	36.06	19.99	N/A	0.10	N/A	0.08	99.53	0.00	0.47	100.00
	Plagioclase 65	43.89	35.60	19.98	N/A	0.37	0.16	N/A	100.00	0.00	0.00	100.00
	Plagioclase 66	43.45	36.21	20.17	N/A	N/A	0.17	N/A	100.00	0.00	0.00	100.00
	Plagioclase 67	43.67	36.00	20.05	N/A	0.19	0.09	N/A	100.00	0.00	0.00	100.00
	Plagioclase 68	44.54	35.51	19.38	N/A	0.25	0.21	0.11	99.33	0.00	0.67	100.00
	Plagioclase 69	43.50	35.93	20.18	N/A	0.28	0.11	N/A	100.00	0.00	0.00	100.00
	Plagioclase 70	43.58	35.93	20.12	N/A	0.28	0.09	N/A	100.00	0.00	0.00	100.00
	Plagioclase 71	43.53	36.16	20.21	N/A	N/A	N/A	0.10	99.41	0.00	0.59	100.00
	Plagioclase 72	43.51	35.93	20.29	N/A	0.27	N/A	N/A	100.00	0.00	0.00	100.00
	Plagioclase 73	43.50	36.12	20.02	N/A	0.28	0.08	N/A	100.00	0.00	0.00	100.00
	Plagioclase 74	43.91	35.93	19.99	N/A	0.10	N/A	0.07	99.58	0.00	0.42	100.00
	Plagioclase 75	43.62	36.12	19.95	N/A	0.18	0.13	N/A	100.00	0.00	0.00	100.00
	Plagioclase 76	43.49	36.06	19.98	N/A	0.25	0.22	N/A	100.00	0.00	0.00	100.00
	Plagioclase 77	43.51	36.32	19.97	N/A	0.07	0.13	N/A	100.00	0.00	0.00	100.00
	Plagioclase 78	44.17	35.68	19.85	N/A	0.30	N/A	N/A	100.00	0.00	0.00	100.00
	Plagioclase 79	43.82	36.04	19.92	N/A	0.11	0.12	N/A	100.00	0.00	0.00	100.01
	Plagioclase 80	43.80	35.95	19.83	N/A	0.29	0.13	N/A	100.00	0.00	0.00	100.00
	Plagioclase 81	43.51	36.13	19.87	N/A	0.38	0.12	N/A	100.00	0.00	0.00	100.01
	Plagioclase 82	43.89	35.89	19.83	N/A	0.25	0.13	N/A	100.00	0.00	0.00	99.99
	Plagioclase 83	43.94	35.87	19.96	N/A	0.23	N/A	N/A	100.00	0.00	0.00	100.00
	Plagioclase 84	43.65	36.02	19.98	N/A	0.24	0.12	N/A	100.00	0.00	0.00	100.01
	Plagioclase 85	43.84	35.76	19.73	N/A	0.42	0.11	0.14	99.16	0.00	0.84	100.00

	Plagioclase 86	43.42	36.23	19.89	N/A	0.38	0.08	N/A	100.00	0.00	0.00	100.00
	Plagioclase 87	43.77	36.14	19.63	N/A	0.46	N/A	N/A	100.00	0.00	0.00	100.00
	Plagioclase 88	43.85	36.31	19.47	N/A	0.27	0.10	N/A	100.00	0.00	0.00	100.00
	Plagioclase 89	43.65	35.91	20.04	N/A	0.27	0.13	N/A	100.00	0.00	0.00	100.00
	Standard Deviation	0.37	0.42	0.35	0	0	0	0				
	Average	43.67	35.96	19.86	0	0.36	0.17	0.13				

l) – Graph displaying the geochemical data for plagioclase in NWA11444

Olivine Compositions

For all data tables, where N/A is written, values detected by the SEM were either on or below the detection limit and therefore weren't included.

Hawaii 1							
Data in Wt % Oxide		SiO_2	MgO	FeO	Al_2O_3	CaO	Total
Site 1	Olivine 1	40.59	37.79	21.63	N/A	N/A	100.01
	Olivine 2	37.88	33.32	28.80	N/A	N/A	100.00
	Olivine 3	39.06	36.88	24.05	N/A	N/A	99.99
	Olivine 4	37.95	40.37	21.68	N/A	N/A	100.00
	Olivine 5	39.90	36.92	23.18	N/A	N/A	100.00
	Olivine 6	32.82	40.04	27.14	N/A	N/A	100.00
Site 2	Olivine 1	37.74	37.91	24.36	N/A	N/A	100.01
	Olivine 2	39.98	34.74	20.10	2.66	2.51	99.99
	Olivine 3	38.75	37.40	22.20	1.04	0.61	100.00
	Olivine 4	36.79	35.60	27.11	N/A	0.49	99.99
	Olivine 5	37.58	38.47	23.95	N/A	N/A	100.00
	Olivine 6	42.44	35.07	22.48	N/A	N/A	99.99
Site 3	Olivine 1	38.91	36.91	20.48	1.21	2.49	100.00
	Olivine 2	37.30	35.67	23.33	2.52	1.17	99.99
	Standard Deviation	2.20	1.97	2.57	0.85	0.99	
	Average	38.41	36.94	23.61	1.86	1.45	

a) – Graph displaying the geochemical data for olivine in Hawaii 1

Hawaii 2							
Data in Wt % Oxide		SiO_2	MgO	FeO	Al_2O_3	CaO	Total
Site 1	Olivine 1	38.76	40.29	20.96	N/A	N/A	100.01
	Olivine 2	38.47	38.98	22.55	N/A	N/A	100.00
	Olivine 3	38.57	40.14	21.28	N/A	N/A	99.99
	Olivine 4	37.69	36.16	26.16	N/A	N/A	100.01
	Olivine 5	37.13	35.08	27.79	N/A	N/A	100.00
	Olivine 6	37.62	35.81	26.57	N/A	N/A	100.00
	Olivine 7	38.08	36.53	25.39	N/A	N/A	100.00
	Olivine 8	35.96	33.13	30.91	N/A	N/A	100.00
	Olivine 9	34.49	31.59	33.92	N/A	N/A	100.00
	Olivine 10	38.33	36.48	25.19	N/A	N/A	100.00
	Olivine 11	38.12	36.33	25.56	N/A	N/A	100.01
	Olivine 12	38.06	37.29	24.65	N/A	N/A	100.00
	Olivine 13	37.65	35.84	26.50	N/A	N/A	99.99
	Olivine 14	38.83	38.62	22.55	N/A	N/A	100.00
	Olivine 15	38.59	35.91	25.51	N/A	N/A	100.01
	Olivine 16	37.77	35.80	26.43	N/A	N/A	100.00
	Olivine 17	38.77	40.30	20.92	N/A	N/A	99.99
	Olivine 18	38.96	40.95	20.09	N/A	N/A	100.00
	Olivine 19	38.45	40.27	21.29	N/A	N/A	100.01
	Olivine 20	38.68	39.83	21.49	N/A	N/A	100.00
	Olivine 21	27.57	31.82	38.72	0.96	0.94	100.01
	Olivine 22	30.11	30.85	38.49	N/A	0.56	100.01
	Olivine 23	37.04	35.04	27.48	N/A	0.44	100.00
	Olivine 24	37.87	33.92	28.22	N/A	N/A	100.01
	Olivine 25	38.62	35.61	25.77	N/A	N/A	100.00

Site 2	Olivine 1	38.61	39.89	21.50	N/A	N/A	100.00
	Olivine 2	38.69	40.42	20.89	N/A	N/A	100.00
	Olivine 3	37.94	35.92	26.13	N/A	N/A	99.99
	Olivine 4	35.32	33.48	30.73	N/A	0.47	100.00
Site 4	Olivine 1	38.66	39.82	21.51	N/A	N/A	99.99
	Olivine 2	37.94	35.94	25.49	N/A	0.64	100.01
	Standard Deviation	2.51	2.87	4.77	N/A	0.20	
	Average	37.33	36.71	25.83	0.96	0.61	

b) – Graph displaying the geochemical data for olivine in Hawaii 2

ESA01-A								
Data in Wt % Oxide		SiO_2	MgO	FeO	Al_2O_3	CaO	TiO_2	Total
Site 1	Olivine 1	35.44	27.42	37.14	N/A	N/A	N/A	100.00
	Olivine 2	35.74	27.13	37.13	N/A	N/A	N/A	100.00
	Olivine 3	36.26	27.46	36.28	N/A	N/A	N/A	100.00
	Olivine 4	35.75	25.69	38.57	N/A	N/A	N/A	100.01
	Olivine 5	36.13	26.83	37.04	N/A	N/A	N/A	100.00
	Olivine 6	34.74	24.75	40.51	N/A	N/A	N/A	100.00
	Olivine 7	35.75	26.90	37.35	N/A	N/A	N/A	100.00
	Olivine 8	35.97	26.71	37.31	N/A	N/A	N/A	99.99
	Olivine 9	35.98	26.58	37.44	N/A	N/A	N/A	100.00
Site 2	Olivine 1	35.31	27.27	37.42	N/A	N/A	N/A	100.00
	Olivine 2	33.84	25.71	40.44	N/A	N/A	N/A	99.99
	Olivine 3	35.35	25.53	39.12	N/A	N/A	N/A	100.00
	Olivine 4	46.72	16.74	24.05	12.50	N/A	N/A	100.01
	Olivine 5	39.46	26.26	34.28	N/A	N/A	N/A	100.00
Site 4	Olivine 1	35.61	26.53	37.86	N/A	N/A	N/A	100.00
	Olivine 2	35.70	25.81	38.49	N/A	N/A	N/A	100.00
	Olivine 3	35.62	26.26	38.12	N/A	N/A	N/A	100.00
	Olivine 4	35.78	26.34	37.88	N/A	N/A	N/A	100.00
Site 5	Olivine 1	35.62	25.79	38.59	N/A	N/A	N/A	100.00
	Olivine 2	35.37	25.46	39.17	N/A	N/A	N/A	100.00
	Olivine 3	35.64	25.66	38.70	N/A	N/A	N/A	100.00
	Olivine 4	35.99	26.79	37.22	N/A	N/A	N/A	100.00
	Olivine 5	35.85	25.41	38.74	N/A	N/A	N/A	100.00
	Olivine 6	35.81	25.50	38.69	N/A	N/A	N/A	100.00
	Olivine 7	35.44	25.05	39.51	N/A	N/A	N/A	100.00

	Olivine 8	36.50	25.48	36.87	1.15	N/A	N/A	100.00
	Olivine 9	35.59	24.97	39.44	N/A	N/A	N/A	100.00
	Olivine 10	39.61	18.33	28.82	13.24	N/A	N/A	100.00
	Olivine 11	35.31	25.48	38.64	N/A	0.56	N/A	99.99
	Olivine 12	36.91	27.74	35.35	N/A	N/A	N/A	100.00
	Olivine 13	22.29	20.30	42.73	1.88	N/A	12.79	99.99
	Olivine 14	36.26	26.49	37.24	N/A	N/A	N/A	99.99
	Olivine 15	35.42	25.61	38.97	N/A	N/A	N/A	100.00
	Olivine 16	35.59	25.90	38.51	N/A	N/A	N/A	100.00
	Olivine 17	40.68	19.16	25.65	12.79	1.71	N/A	99.99
Site 8	Olivine 1	35.19	25.58	39.23	N/A	N/A	N/A	100.00
	Olivine 2	35.39	25.79	38.82	N/A	N/A	N/A	100.00
	Olivine 3	35.00	25.75	39.25	N/A	N/A	N/A	100.00
	Olivine 4	36.67	27.07	36.26	N/A	N/A	N/A	100.00
	Olivine 5	35.62	27.35	37.03	N/A	N/A	N/A	100.00
Site 9	Olivine 1	42.48	18.46	24.45	12.52	2.09	N/A	100.00
	Standard Deviation	3.19	2.65	4.24	5.82	0.80	N/A	
	Average	36.15	25.25	36.68	9.01	1.45	12.79	

c) – Graph displaying the geochemical data for olivine in ESA01-A

New Mexico Macro-phenocryst Centres						
Data in Wt % Oxide		SiO_2	MgO	FeO	Al_2O_3	Total
LAM	Olivine Centre Large 1	39.02	41.53	19.45	N/A	100.00
	Olivine Centre Large 2	38.93	41.19	19.88	N/A	100.00
	Olivine Centre Large 3	38.53	41.79	19.68	N/A	100.00
	Olivine Centre Large 4	38.95	41.44	19.62	N/A	100.01
	Olivine Centre Large 5	38.78	41.61	19.62	N/A	100.01
	Olivine Centre Large 6	38.92	42.01	19.07	N/A	100.00
	Olivine Centre Large 7	38.70	41.93	19.37	N/A	100.00
	Olivine Centre Large 8	38.90	42.11	18.99	N/A	100.00
	Olivine Centre Large 9	38.87	41.86	19.28	N/A	100.01
	Olivine Centre Large 10	38.71	41.49	19.80	N/A	100.00
	Olivine Centre Large 11	39.06	41.77	19.17	N/A	100.00
	Olivine Centre Large 12	38.65	41.51	19.84	N/A	100.00
	Olivine Centre Large 13	38.92	41.39	19.68	N/A	99.99
	Olivine Centre Large 14	38.75	40.43	20.82	N/A	100.00
	Olivine Centre Large 15	38.57	41.01	20.42	N/A	100.00
	Olivine Centre Large 16	38.68	41.35	19.97	N/A	100.00
	Olivine Centre Large 17	38.50	40.14	21.36	N/A	100.00
	Olivine Centre Large 18	38.68	40.95	20.37	N/A	100.00
	Olivine Centre Large 19	39.33	41.03	19.64	N/A	100.00
	Olivine Centre Large 20	38.31	40.36	21.34	N/A	100.01
	Olivine Centre Large 21	38.83	40.29	20.88	N/A	100.00
	Olivine Centre Large 22	38.48	40.08	21.44	N/A	100.00
Site 6	Olivine Centre Large 1	39.34	41.76	18.90	N/A	100.00
	Olivine Centre Large 2	38.78	41.55	19.67	N/A	100.00
	Olivine Centre Large 3	38.88	42.07	19.05	N/A	100.00

	Olivine Centre Large 4	39.48	41.66	18.86	N/A	100.00
	Olivine Centre Large 5	39.00	41.75	19.26	N/A	100.01
	Olivine Centre Large 6	39.18	41.94	18.88	N/A	100.00
	Olivine Centre Large 7	39.39	41.06	19.55	N/A	100.00
	Olivine Centre Large 8	38.98	41.43	19.60	N/A	100.01
	Olivine Centre Large 9	38.72	40.95	20.33	N/A	100.00
	Olivine Centre Large 10	39.76	40.95	19.30	N/A	100.01
	Olivine Centre Large 11	38.75	41.83	19.43	N/A	100.01
Site 9	Olivine Centre Large 1	39.24	41.39	19.38	N/A	100.01
	Olivine Centre Large 2	38.77	41.37	19.86	N/A	100.00
	Olivine Centre Large 3	38.31	41.42	20.27	N/A	100.00
	Olivine Centre Large 4	38.60	41.02	20.38	N/A	100.00
	Olivine Centre Large 5	39.01	40.72	20.27	N/A	100.00
Site 10	Olivine Centre Large 1	38.15	37.72	24.13	N/A	100.00
	Olivine Centre Large 2	38.93	39.85	21.23	N/A	100.01
	Olivine Centre Large 3	38.04	39.52	22.44	N/A	100.00
	Olivine Centre Large 4	37.81	37.32	24.87	N/A	100.00
	Olivine Centre Large 5	38.48	36.27	24.24	1.00	99.99
	Olivine Centre Large 6	37.68	37.55	24.77	N/A	100.00
	Standard Deviation	0.41	1.33	3.12	N/A	
	Average	38.78	40.87	19.89	1.00	

d) – Graph displaying the geochemical data for olivine macro-phenocryst centres in New Mexico

New Mexico Macro-phenocryst Rims								
Data in Wt % Oxide		SiO_2	MgO	FeO	Al_2O_3	CaO	Na_2O	Total
LAM	Olivine Rim 1 Large	37.02	36.90	26.07	N/A	N/A	N/A	99.99
	Olivine Rim 2 Large	37.24	36.45	26.31	N/A	N/A	N/A	100.00
	Olivine Rim 3 Large	37.16	36.15	26.69	N/A	N/A	N/A	100.00
	Olivine Rim 4 Large	37.91	36.96	25.13	N/A	N/A	N/A	100.00
	Olivine Rim 5 Large	37.65	35.22	27.13	N/A	N/A	N/A	100.00
	Olivine Rim 6 Large	38.11	35.57	26.32	N/A	N/A	N/A	100.00
	Olivine Rim 7 Large	37.72	35.33	26.96	N/A	N/A	N/A	100.01
	Olivine Rim 8 Large	37.31	36.15	26.55	N/A	N/A	N/A	100.01
	Olivine Rim 9 Large	36.89	36.07	27.05	N/A	N/A	N/A	100.01
	Olivine Rim 10 Large	39.62	34.58	25.80	N/A	N/A	N/A	100.00
	Olivine Rim 11 Large	36.21	36.82	26.97	N/A	N/A	N/A	100.00
	Olivine Rim 12 Large	36.63	36.72	26.64	N/A	N/A	N/A	99.99
	Olivine Rim 13 Large	37.71	37.30	24.99	N/A	N/A	N/A	100.00
	Olivine Rim 14 Large	38.78	37.65	23.57	N/A	N/A	N/A	100.00
	Olivine Rim 15 Large	37.62	37.01	25.38	N/A	N/A	N/A	100.01
	Olivine Rim 16 Large	37.54	36.57	25.89	N/A	N/A	N/A	100.00
	Olivine Rim 17 Large	37.62	37.09	25.29	N/A	N/A	N/A	100.00
	Olivine Rim 18 Large	37.41	37.28	25.31	N/A	N/A	N/A	100.00
	Olivine Rim 19 Large	36.38	36.46	27.16	N/A	N/A	N/A	100.00
Site 6	Olivine Rim Large 1	38.24	37.10	24.66	N/A	N/A	N/A	100.00
	Olivine Rim Large 2	38.09	37.10	24.81	N/A	N/A	N/A	100.00
	Olivine Rim Large 3	37.74	34.80	27.46	N/A	N/A	N/A	100.00
	Olivine Rim Large 4	38.68	39.10	22.22	N/A	N/A	N/A	100.00
	Olivine Rim Large 5	38.14	38.10	23.76	N/A	N/A	N/A	100.00
	Olivine Rim Large 6	38.14	37.08	24.79	N/A	N/A	N/A	100.01
	Olivine Rim Large 7	38.49	38.98	22.53	N/A	N/A	N/A	100.00

	Olivine Rim Large 8	44.61	26.10	13.05	10.61	3.12	2.51	100.00
	Olivine Rim Large 9	37.82	36.48	25.69	N/A	N/A	N/A	99.99
	Standard Deviation	1.50	2.27	2.73	N/A	N/A	N/A	
	Average	37.95	36.33	25.15	10.61	3.12	2.51	

e) – Graph displaying the geochemical data for olivine macro-phenocryst rims in New Mexico

New Mexico Micro-Phenocryst Centres					
Data in Wt % Oxide		SiO_2	MgO	FeO	Total
LAM	Olivine Centre Small 1	37.98	34.92	27.10	100.00
	Olivine Centre Small 2	38.84	35.04	26.11	99.99
	Olivine Centre Small 3	37.33	34.75	27.91	99.99
	Olivine Center Small 4	36.82	36.14	27.04	100.00
	Olivine Center Small 5	37.72	34.85	27.43	100.00
	Olivine Centre Small 6	37.78	35.44	26.78	100.00
	Olivine Centre Small 7	37.90	34.99	27.11	100.00
	Olivine Centre Small 8	37.73	35.55	26.71	99.99
	Olivine Centre Small 9	38.74	33.58	27.68	100.00
	Olivine Centre Small 10	38.04	35.72	26.24	100.00
	Olivine Centre Small 11	37.70	34.58	27.72	100.00
	Olivine Centre Small 12	38.03	35.23	26.74	100.00
	Olivine Centre Small 13	37.59	34.61	27.80	100.00
	Olivine Centre Small 14	38.33	34.83	26.84	100.00
	Olivine Centre Small 15	37.13	35.98	26.89	100.00
	Olivine Centre Small 16	37.12	35.00	27.88	100.00
	Olivine Centre Small 17	37.56	34.86	27.58	100.00
	Olivine Centre Small 18	37.30	35.43	27.26	99.99
	Olivine Centre Small 19	38.62	37.34	24.03	99.99
	Olivine Centre Small 20	38.52	34.15	27.33	100.00
	Olivine Centre Small 21	37.00	35.60	27.40	100.00
	Olivine Centre Small 22	37.84	34.73	27.42	99.99
	Olivine Centre Small 23	36.33	34.98	28.69	100.00
	Olivine Centre Small 24	37.21	35.30	27.49	100.00
	Olivine Centre Small 25	38.82	33.66	27.52	100.00

	Olivine Centre Small 26	37.44	35.41	27.15	100.00
	Olivine Centre Small 27	37.60	36.78	25.62	100.00
	Olivine Centre Small 28	37.30	34.24	28.46	100.00
	Olivine Centre Small 29	36.70	35.45	27.85	100.00
	Olivine Centre Small 30	37.78	35.73	26.49	100.00
Site 7	Olivine Centre Small 1	37.98	35.58	26.43	99.99
	Olivine Centre Small 2	38.02	35.91	26.08	100.01
	Standard Deviation	0.65	0.96	1.18	
	Average	37.75	35.30	26.95	

f) – Graph displaying the geochemical data for olivine micro-phenocryst centres in New Mexico

	NWA7397								
	Data in Wt % Oxide		SiO_2	MgO	FeO	Al_2O_3	CaO	TiO_2	Total
Grain 1	Site 1	Olivine 1	36.30	27.67	36.03	N/A	N/A	N/A	100.00
		Olivine 2	34.92	27.57	37.51	N/A	N/A	N/A	100.00
		Olivine 3	35.60	27.98	36.42	N/A	N/A	N/A	100.00
	Site 2	Olivine 1	35.61	27.92	36.47	N/A	N/A	N/A	100.00
		Olivine 2	35.75	27.93	36.32	N/A	N/A	N/A	100.00
		Olivine 3	35.66	27.79	36.56	N/A	N/A	N/A	100.01
		Olivine 4	35.83	27.83	36.34	N/A	N/A	N/A	100.00
		Olivine 5	35.56	27.94	36.50	N/A	N/A	N/A	100.00
		Olivine 6	35.88	27.57	36.55	N/A	N/A	N/A	100.00
		Olivine 7	53.47	21.03	22.03	N/A	3.48	N/A	100.01
		Olivine 8	53.11	20.49	21.70	N/A	4.71	N/A	100.01
		Olivine 9	53.12	20.53	21.15	N/A	5.19	N/A	99.99
	Site 3	Olivine 1	36.30	27.27	36.43	N/A	N/A	N/A	100.00
		Olivine 2	35.93	28.08	35.99	N/A	N/A	N/A	100.00
		Olivine 3	35.54	28.79	35.67	N/A	N/A	N/A	100.00
		Olivine 4	35.99	28.36	35.66	N/A	N/A	N/A	100.01
		Olivine 5	35.62	27.98	36.41	N/A	N/A	N/A	100.01
		Olivine 6	35.94	28.72	35.34	N/A	N/A	N/A	100.00
Grain 2	Site 1	Olivine 1	34.65	26.77	38.59	N/A	N/A	N/A	100.01
		Olivine 2	36.06	28.13	35.82	N/A	N/A	N/A	100.01
		Olivine 3	35.90	28.47	35.63	N/A	N/A	N/A	100.00
	Site 2	Olivine 1	35.46	27.60	36.28	N/A	0.66	N/A	100.00
		Olivine 2	35.80	27.86	36.34	N/A	N/A	N/A	100.00
		Olivine 3	35.71	29.03	35.26	N/A	N/A	N/A	100.00
		Olivine 4	35.67	29.04	35.29	N/A	N/A	N/A	100.00
		Olivine 5	35.72	27.59	36.69	N/A	N/A	N/A	100.00

Standard Deviation	5.72	2.44	4.82	N/A	2.03	N/A
Average	37.73	27.15	34.58	N/A	3.51	N/A

g) – Graph displaying the geochemical data for olivine in NWA7397

NWA1110 Macro-Phenocryst Centres					
Data in Wt % Oxide		SiO_2	MgO	FeO	Total
Site 1	Olivine Centre Large 1	37.93	34.68	27.39	100.00
	Olivine Centre Large 2	38.50	34.78	26.73	100.01
	Olivine Centre Large 3	38.89	34.17	26.93	99.99
	Olivine Centre Large 4	37.95	34.31	27.74	100.00
	Olivine Centre Large 5	39.47	34.38	26.15	100.00
	Olivine Centre Large 6	38.19	34.16	27.65	100.00
	Olivine Centre Large 7	38.24	35.07	26.69	100.00
	Olivine Centre Large 8	36.76	31.82	31.42	100.00
	Olivine Centre Large 9	38.49	33.42	38.09	110.00
	Olivine Centre Large 10	39.04	33.94	27.02	100.00
	Olivine Centre Large 11	38.83	34.14	27.03	100.00
	Olivine Centre Large 12	38.24	34.50	27.25	99.99
Site 2	Olivine Centre Large 1	39.38	32.02	28.61	100.01
Site 3	Olivine Centre Large 1	38.47	28.96	32.57	100.00
	Olivine Centre Large 2	38.86	31.41	29.72	99.99
	Olivine Centre Large 3	37.68	28.87	33.45	100.00
	Olivine Centre Large 4	36.31	26.66	37.03	100.00
Site 4	Olivine Centre Large 1	38.61	33.88	27.51	100.00
	Olivine Centre Large 2	38.66	33.45	27.89	100.00
	Olivine Centre Large 3	39.22	33.55	27.23	100.00
	Olivine Centre Large 4	38.14	33.69	28.17	100.00
	Olivine Centre Large 5	38.23	33.15	28.63	100.01
	Olivine Centre Large 6	39.05	31.63	29.32	100.00
	Olivine Centre Large 7	37.74	32.52	29.74	100.00
	Olivine Centre Large 8	39.38	32.69	27.94	100.01

Site 5	Olivine Centre Large 1	37.69	31.08	31.23	100.00
	Olivine Centre Large 2	39.86	31.57	28.56	99.99
	Olivine Centre Large 3	37.74	30.17	32.09	100.00
	Olivine Centre Large 4	37.58	33.65	28.77	100.00
	Olivine Centre Large 5	37.70	30.01	32.30	100.01
	Olivine Centre Large 6	38.53	33.27	28.20	100.00
	Olivine Centre Large 7	37.53	29.10	33.37	100.00
	Olivine Centre Large 8	38.00	30.63	31.37	100.00
	Olivine Centre Large 9	38.00	28.86	33.14	100.00
	Standard Deviation	0.76	2.14	2.97	
	Average	38.32	32.36	29.62	

h) – Graph displaying the geochemical data for olivine 'macro-phenocryst' centres in NWA1110

NWA1110 Macro-Phenocryst Rims					
Data in Wt % Oxide		SiO_2	MgO	FeO	Total
Site 1	Olivine Rim Large 1	36.68	25.07	38.25	100.00
	Olivine Rim Large 2	36.89	27.04	36.07	100.00
	Olivine Rim Large 3	36.40	24.15	39.45	100.00
	Olivine Rim Large 4	36.64	24.41	38.95	100.00
	Olivine Rim Large 5	35.89	25.91	38.20	100.00
	Olivine Rim Large 6	36.88	26.88	36.24	100.00
	Olivine Rim Large 7	34.70	22.62	42.69	100.01
	Olivine Rim Large 8	36.48	26.66	36.86	100.00
	Olivine Rim Large 9	36.87	26.65	36.48	100.00
	Olivine Rim Large 10	35.77	24.60	39.63	100.00
	Olivine Rim Large 11	35.51	27.71	36.78	100.00
Site 2	Olivine Rim Large 1	35.57	23.40	41.03	100.00
	Olivine Rim Large 2	34.18	25.28	40.54	100.00
Site 3	Olivine Rim Large 1	35.92	19.56	44.52	100.00
	Olivine Rim Large 2	35.50	27.42	37.08	100.00
	Olivine Rim Large 3	35.87	23.27	40.86	100.00
	Olivine Rim Large 4	35.93	21.6	42.47	100.00
Site 4	Olivine Rim Large 1	35.73	28.30	35.97	100.00
	Olivine Rim Large 2	38.98	25.85	35.17	100.00
	Olivine Rim Large 3	35.69	26.61	37.70	100.00
	Olivine Rim Large 4	37.23	24.86	37.91	100.00
	Olivine Rim Large 5	35.87	26.12	38.01	100.00
	Olivine Rim Large 6	37.78	25.01	37.20	99.99
	Olivine Rim Large 7	36.44	27.88	35.69	100.01
	Olivine Rim Large 8	34.28	24.05	41.66	99.99
	Olivine Rim Large 9	37.95	28.86	33.19	100.00

	Olivine Rim Large 10	37.27	29.48	33.25	100.00
	Olivine Rim Large 11	38.22	29.60	32.18	100.00
Site 5	Olivine Rim Large 1	36.21	26.55	37.24	100.00
	Olivine Rim Large 2	36.88	23.57	39.54	99.99
	Standard Deviation	1.08	2.31	2.88	
	Average	36.34	25.63	38.03	

i) – Graph displaying the geochemical data for olivine 'micro-phenocryst' centres in NWA1110

NWA1110 Micro-Phenocryst Centres					
Data in Wt % Oxide		SiO_2	MgO	FeO	Total
Site 1	Olivine Centre Small 1	35.19	23.07	41.74	100.00
	Olivine Centre Small 2	34.68	19.64	45.68	100.00
Site 2	Olivine Centre Small 1	35.99	26.01	38.00	100.00
	Olivine Centre Small 2	35.69	23.43	40.88	100.00
	Olivine Centre Small 3	36.47	24.25	39.28	100.00
	Olivine Centre Small 4	33.58	23.44	42.98	100.00
	Olivine Centre Small 5	35.33	19.00	45.67	100.00
	Olivine Centre Small 6	33.89	22.28	43.82	99.99
	Olivine Centre Small 7	34.71	23.03	42.26	100.00
	Olivine Centre Small 8	36.47	24.14	39.39	100.00
	Olivine Centre Small 9	35.95	19.39	44.66	100.00
Site 3	Olivine Centre Small 1	35.01	24.97	40.01	99.99
	Olivine Centre Small 2	33.55	22.79	43.66	100.00
	Olivine Centre Small 3	36.86	20.70	42.44	100.00
	Olivine Centre Small 4	36.26	25.54	38.20	100.00
	Olivine Centre Small 5	35.01	20.85	44.14	100.00
	Olivine Centre Small 6	35.67	18.22	46.11	100.00
	Olivine Centre Small 7	32.76	21.73	45.51	100.00
	Olivine Centre Small 8	35.74	21.61	42.65	100.00
Site 5	Olivine Centre Small 1	36.30	22.88	40.82	100.00
	Olivine Centre Small 2	36.41	24.21	39.38	100.00
	Olivine Centre Small 3	33.76	19.54	46.70	100.00
	Olivine Centre Small 4	35.81	25.02	39.17	100.00
	Olivine Centre Small 5	36.41	27.5	36.08	99.99
	Olivine Centre Small 6	35.87	22.33	41.79	99.99

	Olivine Centre Small 7	34.93	22.87	42.20	100.00
	Olivine Centre Small 8	35.66	25.91	38.43	100.00
	Olivine Centre Small 9	35.62	23.03	41.35	100.00
	Olivine Centre Small 10	36.06	24.81	39.13	100.00
	Olivine Centre Small 11	36.12	22.96	40.92	100.00
	Olivine Centre Small 12	35.36	26.19	38.46	100.01
	Olivine Centre Small 13	34.78	22.28	42.94	100.00
	Olivine Centre Small 14	35.61	19.65	44.74	100.00
	Olivine Centre Small 15	33.81	21.47	42.07	99.99
	Olivine Centre Small 16	35.42	22.37	42.22	100.01
	Olivine Centre Small 17	35.26	23.74	41.00	100.00
	Olivine Centre Small 18	34.08	23.15	42.78	100.01
	Olivine Centre Small 19	34.88	19.64	45.48	100.00
	Olivine Centre Small 20	34.99	20.66	44.35	100.00
	Olivine Centre Small 21	36.86	23.43	39.71	100.00
	Olivine Centre Small 22	34.52	18.88	46.60	100.00
	Olivine Centre Small 23	34.83	18.95	46.22	100.00
	Olivine Centre Small 24	35.62	22.51	41.03	100.00
	Olivine Centre Small 25	33.71	17.20	49.09	100.00
	Olivine Centre Small 26	33.68	20.86	45.46	100.00
	Olivine Centre Small 27	35.15	19.66	45.18	99.99
	Olivine Centre Small 28	34.99	24.31	40.70	100.00
	Standard Deviation	0.97	2.36	2.85	
	Average	35.22	22.34	42.36	

j) – Graph displaying the geochemical data for olivine 'micro-phenocryst' centres in NWA1110

Tissint Macro-Phenocryst Centres					
Data in Wt % Oxide		**SiO_2**	**MgO**	**FeO**	Total
Site 1	Olivine Centre Large 1	38.23	38.2	23.57	100.00
	Olivine Centre Large 2	38.28	38.16	23.56	100.00
	Olivine Centre Large 1	38.33	36.18	25.49	100.00
Site 3	Olivine Centre Large 1	38.93	40.45	20.62	100.00
	Olivine Centre Large 2	38.32	38.21	23.47	100.00
Site 4	Olivine Centre Large 1	38.79	39.51	21.71	100.01
	Olivine Centre Large 2	38.46	38.06	23.49	100.01
	Olivine Centre Large 3	37.66	35.60	26.75	100.01
	Olivine Centre Large 4	36.01	30.78	33.21	100.00
Site 5	Olivine Centre Large 1	37.15	34.18	28.67	100.00
	Olivine Centre Large 2	38.38	38.15	23.47	100.00
	Olivine Centre Large 3	37.93	36.86	25.22	100.01
	Standard Deviation	0.80	2.60	3.37	
	Average	38.04	37.03	24.94	

k) – Graph displaying the geochemical data for olivine 'macro-phenocryst' centres in Tissint

Tissint Macro-Phenocryst Rims					
Data in Wt % Oxide		**SiO_2**	**MgO**	**FeO**	Total
Site 1	Olivine Rim Large 1	34.88	24.27	40.84	99.99
	Olivine Rim Large 2	38.28	38.16	23.56	100.00
Site 2	Olivine Rim Large 1	36.65	24.91	38.44	100.00
	Olivine Rim Large 2	35.50	25.00	39.50	100.00
Site 4	Olivine Rim Large 1	38.13	30.99	30.88	100.00
	Olivine Rim Large 2	35.95	24.92	39.13	100.00
Site 5	Olivine Rim Large 1	34.56	22.91	42.53	100.00
	Olivine Rim Large 2	34.82	23.78	41.41	100.01
	Olivine Rim Large 3	34.34	22.51	43.15	100.00
	Olivine Rim Large 4	34.44	21.48	44.08	100.00
	Olivine Rim Large 5	34.75	22.14	43.11	100.00
	Standard Deviation	1.44	4.89	6.21	
	Average	35.66	25.55	38.78	

I) – Graph displaying the geochemical data for olivine 'macro-phenocryst' rims in Tissint

Tissint Micro-Phenocryst Centres					
Data in Wt % Oxide		SiO_2	MgO	FeO	Total
Site 1	Olivine Centre Small 1	33.47	15.98	50.55	100.00
Site 2	Olivine Centre Small 1	34.98	22.43	42.58	99.99
	Olivine Centre Small 2	38.55	38.52	22.93	100.00
Site 4	Olivine Centre Small 1	34.91	23.32	41.77	100.00
	Olivine Centre Small 2	34.85	22.54	42.61	100.00
	Olivine Centre Small 3	35.79	24.68	39.53	100.00
	Olivine Centre Small 4	34.08	20.46	45.46	100.00
	Olivine Centre Small 5	34.67	24.06	41.27	100.00
Site 5	Olivine Centre Small 1	34.63	21.46	43.91	100.00
	Olivine Centre Small 2	32.95	18.22	48.83	100.00
	Olivine Centre Small 3	35.08	22.06	42.86	100.00
	Olivine Centre Small 4	34.75	22.92	42.34	100.01
	Olivine Centre Small 5	33.19	17.84	48.96	99.99
	Olivine Centre Small 6	34.25	19.06	46.69	100.00
	Olivine Centre Small 7	32.15	17.12	50.73	100.00
	Standard Deviation	1.46	5.28	6.68	
	Average	34.76	22.65	42.58	

m) – *Graph displaying the geochemical data for olivine 'micro-phenocryst' centres in Tissint*

NWA3160								
Data in Wt % Oxide		SiO_2	MgO	FeO	Al_2O_3	CaO	TiO_2	Total
LAM	Olivine 1	37.79	29.44	32.77	N/A	N/A	N/A	100.00
	Olivine 2	37.45	28.26	34.29	N/A	N/A	N/A	100.00
	Olivine 3	37.59	28.25	34.16	N/A	N/A	N/A	100.00
	Olivine 4	36.23	28.03	35.74	N/A	N/A	N/A	100.00
	Olivine 5	37.23	28.17	34.6	N/A	N/A	N/A	100.00
	Olivine 6	37.01	28.96	34.03	N/A	N/A	N/A	100.00
	Olivine 7	37.27	29.10	33.63	N/A	N/A	N/A	100.00
	Olivine 8	36.84	27.40	35.75	N/A	N/A	N/A	99.99
	Olivine 10	37.71	31.25	31.04	N/A	N/A	N/A	100.00
	Olivine 11	58.96	26.27	14.77	N/A	N/A	N/A	100.00
	Olivine 12	39.10	34.42	26.48	N/A	N/A	N/A	100.00
	Olivine 13	36.99	29.68	33.33	N/A	N/A	N/A	100.00
	Olivine 14	37.2	36.02	26.78	N/A	N/A	N/A	100.00
	Olivine 15	37.59	30.99	31.42	N/A	N/A	N/A	100.00
	Olivine 16	38.64	33.33	28.04	N/A	N/A	N/A	100.01
	Olivine 17	38.25	33.29	28.46	N/A	N/A	N/A	100.00
	Olivine 18	37.61	34.03	28.35	N/A	N/A	N/A	99.99
	Olivine 19	38.10	30.89	31.01	N/A	N/A	N/A	100.00
	Olivine 20	37.36	30.98	31.66	N/A	N/A	N/A	100.00
	Olivine 21	38.77	36.17	25.06	N/A	N/A	N/A	100.00
	Olivine 22	38.37	36.27	25.36	N/A	N/A	N/A	100.00
	Olivine 23	38.78	37.11	24.1	N/A	N/A	N/A	99.99
	Olivine 24	38.85	35.45	25.71	N/A	N/A	N/A	100.01
	Olivine 25	37.92	29.80	32.28	N/A	N/A	N/A	100.00
	Olivine 26	37.51	30.39	32.1	N/A	N/A	N/A	100.00

	Olivine 27	38.79	36.75	24.46	N/A	N/A	N/A	100.00
	Olivine 28	37.48	30.92	31.60	N/A	N/A	N/A	100.00
	Olivine 29	39.13	37.51	23.36	N/A	N/A	N/A	100.00
	Olivine 30	38.82	36.03	25.15	N/A	N/A	N/A	100.00
	Olivine 31	36.04	28.6	35.36	N/A	N/A	N/A	100.00
	Olivine 32	38.29	35.46	26.25	N/A	N/A	N/A	100.00
	Olivine 33	38.81	35.16	26.03	N/A	N/A	N/A	100.00
	Olivine 34	38.37	35.97	25.66	N/A	N/A	N/A	100.00
	Olivine 35	38.35	32.92	28.73	N/A	N/A	N/A	100.00
	Olivine 36	38.76	35.8	25.44	N/A	N/A	N/A	100.00
	Olivine 37	36.48	28.09	35.43	N/A	N/A	N/A	100.00
	Olivine 38	38.17	33.51	28.32	N/A	N/A	N/A	100.00
	Olivine 39	38.84	36.98	24.18	N/A	N/A	N/A	100.00
	Olivine 40	38.73	36.91	24.36	N/A	N/A	N/A	100.00
	Olivine 41	38.80	36.92	24.28	N/A	N/A	N/A	100.00
	Olivine 42	56.38	25.66	17.96	N/A	N/A	N/A	100.00
	Olivine 43	38.06	36.74	25.21	N/A	N/A	N/A	100.01
	Olivine 44	39.53	35.18	25.29	N/A	N/A	N/A	100.00
	Olivine 45	39.14	33.04	27.82	N/A	N/A	N/A	100.00
	Olivine 46	37.48	34.31	28.21	N/A	N/A	N/A	100.00
	Olivine 47	38.41	32.86	28.74	N/A	N/A	N/A	100.01
Site 1	Olivine 1	37.38	38.37	24.25	N/A	N/A	N/A	100.00
	Olivine 2	35.33	29.76	34.90	N/A	N/A	N/A	99.99
	Olivine 3	35.43	28.27	36.29	N/A	N/A	N/A	99.99
	Olivine 4	30.72	33.10	36.19	N/A	N/A	N/A	100.01
	Olivine 5	37.88	34.46	27.66	N/A	N/A	N/A	100.00
	Olivine 6	37.81	34.50	27.69	N/A	N/A	N/A	100.00
	Olivine 7	39.65	35.27	25.08	N/A	N/A	N/A	100.00
	Olivine 8	38.38	29.57	32.05	N/A	N/A	N/A	100.00

	Olivine 9	39.18	30.25	30.57	N/A	N/A	N/A	100.00
	Olivine 10	41.40	31.38	27.22	N/A	N/A	N/A	100.00
	Olivine 11	38.23	33.12	28.66	N/A	N/A	N/A	100.01
	Olivine 12	40.15	36.61	23.25	N/A	N/A	N/A	100.01
	Olivine 13	31.87	24.25	43.88	N/A	N/A	N/A	100.00
Site 2	Olivine 1	36.96	28.16	34.88	N/A	N/A	N/A	100.00
	Olivine 2	37.11	28.26	34.63	N/A	N/A	N/A	100.00
	Olivine 3	37.39	30.88	31.73	N/A	N/A	N/A	100.00
	Olivine 4	38.68	36.13	25.19	N/A	N/A	N/A	100.00
	Olivine 5	43.53	32.37	24.10	N/A	N/A	N/A	100.00
Site 3	Olivine 1	37.29	27.25	35.46	N/A	N/A	N/A	100.00
	Olivine 2	38.02	30.78	31.21	N/A	N/A	N/A	100.01
	Olivine 3	37.40	26.20	36.41	N/A	N/A	N/A	100.01
	Olivine 4	36.52	30.20	33.28	N/A	N/A	N/A	100.00
	Olivine 5	38.62	34.18	27.20	N/A	N/A	N/A	100.00
	Olivine 6	38.99	34.28	26.73	N/A	N/A	N/A	100.00
	Olivine 7	37.25	33.52	23.76	5.47	N/A	N/A	100.00
	Olivine 8	37.73	34.5	27.77	N/A	N/A	N/A	100.00
	Olivine 9	39.32	36.52	24.16	N/A	N/A	N/A	100.00
	Olivine 10	39.4	36.51	24.09	N/A	N/A	N/A	100.00
Site 4	Olivine 1	36.82	28.02	35.16	N/A	N/A	N/A	100.00
	Olivine 2	36.68	28.46	34.86	N/A	N/A	N/A	100.00
	Olivine 3	37.37	27.96	34.67	N/A	N/A	N/A	100.00
	Olivine 4	37.36	29.49	33.15	N/A	N/A	N/A	100.00
	Olivine 5	37.00	28.77	34.23	N/A	N/A	N/A	100.00
	Olivine 6	37.07	27.99	34.94	N/A	N/A	N/A	100.00
	Olivine 7	36.47	29.14	34.39	N/A	N/A	N/A	100.00
	Olivine 8	37.44	28.47	34.09	N/A	N/A	N/A	100.00

Site 6	Olivine 1	38.13	29.42	32.45	N/A	N/A	N/A	100.00
	Olivine 2	37.25	27.63	35.13	N/A	N/A	N/A	100.01
	Olivine 3	37.56	28.69	33.75	N/A	N/A	N/A	100.00
	Olivine 4	37.77	27.52	34.71	N/A	N/A	N/A	100.00
Site 7	Olivine 1	38.00	34.52	27.48	N/A	N/A	N/A	100.00
	Olivine 2	37.82	33.98	28.20	N/A	N/A	N/A	100.00
	Olivine 3	41.70	26.78	31.52	N/A	N/A	N/A	100.00
	Olivine 4	38.27	31.36	30.36	N/A	N/A	N/A	99.99
	Olivine 6	38.35	34.91	26.74	N/A	N/A	N/A	100.00
	Olivine 7	39.03	35.16	25.81	N/A	N/A	N/A	100.00
	Olivine 8	38.75	35.27	25.98	N/A	N/A	N/A	100.00
Site 8	Olivine 1	35.75	32.05	32.20	N/A	N/A	N/A	100.00
	Olivine 2	36.95	31.24	31.82	N/A	N/A	N/A	100.01
	Olivine 3	39.97	36.65	23.38	N/A	N/A	N/A	100.00
	Olivine 4	37.50	34.47	28.03	N/A	N/A	N/A	100.00
	Olivine 5	37.98	24.78	37.24	N/A	N/A	N/A	100.00
	Standard Deviation	3.45	4.99	5.80	N/A	N/A	N/A	
	Average	38.03	31.18	29.89	N/A	N/A	N/A	

n) – *Graph displaying the geochemical data for olivine in NWA3160 (whole rock)*

NWA3160 Basalt Clast					
Data in Wt % Oxide		**SiO_2**	**MgO**	**FeO**	**Total**
Site 1	Spectrum 1	34.63	37.73	27.64	100.00
	Spectrum 5	36.20	38.57	25.23	100.00
	Spectrum 15	32.00	35.72	32.29	100.01
	Spectrum 16	36.03	37.73	26.25	100.01
	Spectrum 17	32.27	37.07	30.66	100.00
Site 2	Spectrum 18	31.87	36.85	31.28	100.00
	Spectrum 19	35.45	38.62	25.93	100.00
	Spectrum 20	34.05	37.76	28.19	100.00
	Spectrum 21	34.53	37.94	27.54	100.01
	Spectrum 22	35.12	38.28	26.6	100.00
	Spectrum 34	36.49	38.92	24.59	100.00
Site 3	Spectrum 72	35.65	38.71	25.64	100.00
	Spectrum 73	36.72	38.48	24.79	99.99
	Spectrum 74	24.96	34.58	40.46	100.00
	Spectrum 80	28.67	35.39	35.93	99.99
	Standard Deviation	3.50	1.57	5.02	
	Average	33.26	37.26	29.48	

o) – *Graph displaying the geochemical data for olivine in the basalt clast of NWA3160*

NWA11444						
Data in Wt % Oxide		SiO_2	MgO	FeO	Cr_2O_3	Total
Site 1	Olivine 1	34.18	19.80	46.02	N/A	100.00
	Olivine 2	35.47	20.70	43.83	N/A	100.00
	Olivine 3	34.08	19.68	46.25	N/A	100.01
	Olivine 4	35.81	21.35	42.84	N/A	100.00
Site 2	Olivine 1	35.19	24.5	40.31	N/A	100.00
	Olivine 2	31.23	20.07	48.70	N/A	100.00
	Olivine 3	35.02	23.84	41.15	N/A	100.01
	Olivine 4	38.84	40.32	20.83	N/A	99.99
	Olivine 5	39.35	43.28	17.37	N/A	100.00
	Olivine 6	32.95	16.20	50.85	N/A	100.00
	Olivine 7	37.67	35.53	26.80	N/A	100.00
	Olivine 8	35.92	20.71	43.37	N/A	100.00
	Olivine 9	38.43	35.61	25.96	N/A	100.00
Site 3	Olivine 1	35.23	20.93	43.84	N/A	100.00
	Olivine 2	33.78	19.21	47.01	N/A	100.00
	Olivine 3	34.21	19.54	46.24	N/A	99.99
	Olivine 4	34.10	19.45	46.45	N/A	100.00
Site 4	Olivine 1	39.33	42.17	18.50	N/A	100.00
	Olivine 2	39.44	41.59	18.97	N/A	100.00
	Olivine 3	40.08	43.24	16.68	N/A	100.00
	Olivine 4	39.17	41.98	18.85	N/A	100.00
	Olivine 5	34.69	20.83	44.48	N/A	100.00
	Olivine 6	40.84	43.82	15.33	N/A	99.99
	Olivine 7	39.72	42.63	17.65	N/A	100.00
	Olivine 8	39.50	42.26	18.24	N/A	100.00
	Olivine 9	39.08	41.70	19.23	N/A	100.01

	Olivine 10	33.81	19.14	47.05	N/A	100.00
	Olivine 11	32.03	17.37	50.60	N/A	100.00
	Olivine 12	34.41	19.29	46.30	N/A	100.00
	Olivine 13	33.85	19.34	46.82	N/A	100.01
	Olivine 14	33.89	19.36	46.75	N/A	100.00
	Olivine 15	33.98	19.35	46.67	N/A	100.00
	Olivine 16	34.04	19.23	46.74	N/A	100.01
Site 5	Olivine 1	34.61	32.18	33.21	N/A	100.00
	Olivine 2	41.74	44.45	13.82	N/A	100.01
	Olivine 3	39.25	41.90	18.86	N/A	100.01
	Olivine 4	42.78	39.49	17.73	N/A	100.00
	Olivine 5	39.19	40.65	20.15	N/A	99.99
	Olivine 6	39.07	42.30	18.62	N/A	99.99
	Olivine 7	34.41	20.04	45.55	N/A	100.00
	Olivine 8	38.96	41.55	19.49	N/A	100.00
	Olivine 9	38.01	38.35	23.64	N/A	100.00
	Olivine 10	40.33	44.75	14.92	N/A	100.00
	Olivine 11	31.39	33.76	34.85	N/A	100.00
LAM	Olivine 1	33.64	19.77	46.59	N/A	100.00
	Olivine 2	35.18	24.40	40.41	N/A	99.99
	Olivine 3	34.99	23.98	41.03	N/A	100.00
	Olivine 4	36.86	35.69	27.45	N/A	100.00
	Olivine 5	37.41	36.46	26.14	N/A	100.01
	Olivine 6	39.56	42.83	17.61	N/A	100.00
	Olivine 7	39.02	41.88	19.10	N/A	100.00
	Olivine 8	39.00	34.31	26.69	N/A	100.00
	Olivine 9	38.40	39.81	21.80	N/A	100.01
	Olivine 10	39.02	39.24	21.74	N/A	100.00
	Olivine 11	34.94	24.05	41.01	N/A	100.00

	Olivine 12	33.2	19.94	46.86	N/A	100.00
	Olivine 13	39.34	43.15	17.51	N/A	100.00
	Olivine 14	39.04	42.89	18.07	N/A	100.00
	Olivine 15	55.76	27.97	16.27	N/A	100.00
	Olivine 16	32.72	16.53	50.75	N/A	100.00
	Olivine 17	38.97	43.52	17.51	N/A	100.00
	Olivine 18	54.79	17.21	28.00	N/A	100.00
	Olivine 19	33.61	20.61	45.79	N/A	100.01
	Olivine 20	33.52	19.71	46.77	N/A	100.00
	Olivine 21	34.08	19.60	46.32	N/A	100.00
	Olivine 22	52.92	17.52	29.56	N/A	100.00
	Olivine 23	36.89	24.24	38.87	N/A	100.00
	Olivine 24	54.57	17.58	27.85	N/A	100.00
	Olivine 25	33.82	20.41	45.77	N/A	100.00
	Olivine 26	33.87	19.09	47.04	N/A	100.00
	Olivine 27	54.13	18.36	27.51	N/A	100.00
	Olivine 28	33.38	19.82	46.80	N/A	100.00
	Olivine 29	34.34	18.90	46.76	N/A	100.00
	Olivine 30	34.32	20.10	45.58	N/A	100.00
	Olivine 31	34.57	19.85	45.57	N/A	99.99
	Olivine 32	34.64	20.03	45.33	N/A	100.00
	Olivine 33	33.77	19.25	46.98	N/A	100.00
	Olivine 34	33.55	19.38	47.07	N/A	100.00
	Olivine 35	33.60	20.20	46.20	N/A	100.00
	Olivine 36	32.84	20.57	46.59	N/A	100.00
	Olivine 37	34.10	19.44	46.46	N/A	100.00
	Olivine 38	46.17	34.96	18.87	N/A	100.00
	Olivine 39	39.86	43.78	16.36	N/A	100.00
	Olivine 40	39.97	42.21	17.82	N/A	100.00

	Olivine 41	57.21	31.11	11.69	N/A	100.01
	Olivine 42	38.81	35.92	25.27	N/A	100.00
	Olivine 43	38.24	36.30	25.46	N/A	100.00
	Olivine 44	38.06	35.16	26.78	N/A	100.00
	Olivine 45	39.20	42.01	18.80	N/A	100.01
	Olivine 46	33.62	19.07	47.31	N/A	100.00
	Olivine 47	47.32	37.00	15.68	N/A	100.00
	Olivine 48	39.44	43.27	17.29	N/A	100.00
	Olivine 49	39.71	42.31	17.98	N/A	100.00
	Olivine 50	38.95	41.93	19.12	N/A	100.00
	Olivine 51	34.68	23.17	42.16	N/A	100.00
	Olivine 52	37.58	35.87	26.55	N/A	100.00
	Olivine 53	39.12	42.18	18.70	N/A	100.00
	Olivine 54	32.53	19.69	47.79	N/A	100.01
	Olivine 55	40.50	46.28	13.22	N/A	100.00
	Olivine 56	57.86	30.33	11.82	N/A	100.01
	Olivine 57	38.77	40.97	20.25	N/A	99.99
	Olivine 58	57.22	30.14	12.64	N/A	100.00
	Olivine 59	39.52	42.24	18.24	N/A	100.00
	Olivine 60	34.25	19.39	46.36	N/A	100.00
	Olivine 61	39.05	40.15	20.80	N/A	100.00
	Olivine 62	39.27	41.11	19.62	N/A	100.00
	Olivine 63	38.60	35.67	25.73	N/A	100.00
	Olivine 64	37.12	35.74	27.14	N/A	100.00
	Olivine 65	39.10	43.59	17.30	N/A	99.99
	Olivine 66	32.11	25.24	36.62	6.04	100.01
	Olivine 67	38.57	42.44	18.99	N/A	100.00
	Olivine 68	38.93	41.81	19.26	N/A	100.00
	Olivine 69	39.19	42.89	17.92	N/A	100.00

	Olivine 70	38.74	42.15	19.11	N/A	100.00
	Olivine 71	37.40	27.08	35.52	N/A	100.00
	Olivine 72	38.60	41.86	19.54	N/A	100.00
	Olivine 73	57.38	30.43	12.19	N/A	100.00
	Olivine 74	57.83	31.19	10.98	N/A	100.00
	Olivine 75	39.51	42.08	18.42	N/A	100.01
	Olivine 76	40.76	48.38	10.86	N/A	100.00
	Olivine 77	38.99	37.79	23.23	N/A	100.01
	Olivine 78	38.57	38.38	23.04	N/A	99.99
	Olivine 79	38.18	38.11	23.71	N/A	100.00
	Olivine 80	39.00	40.39	20.71	N/A	100.10
	Olivine 81	38.40	41.72	19.88	N/A	100.00
	Olivine 82	34.92	24.36	40.72	N/A	100.00
	Olivine 83	34.32	23.72	41.96	N/A	100.00
	Olivine 84	39.05	41.97	18.98	N/A	100.00
	Olivine 85	34.92	20.63	44.45	N/A	100.00
	Standard Deviation	5.66	10.22	13.31	0.00	
	Average	38.18	31.14	30.54	6.04	

p) *- Graph displaying the geochemical data for olivine in NWA11444*